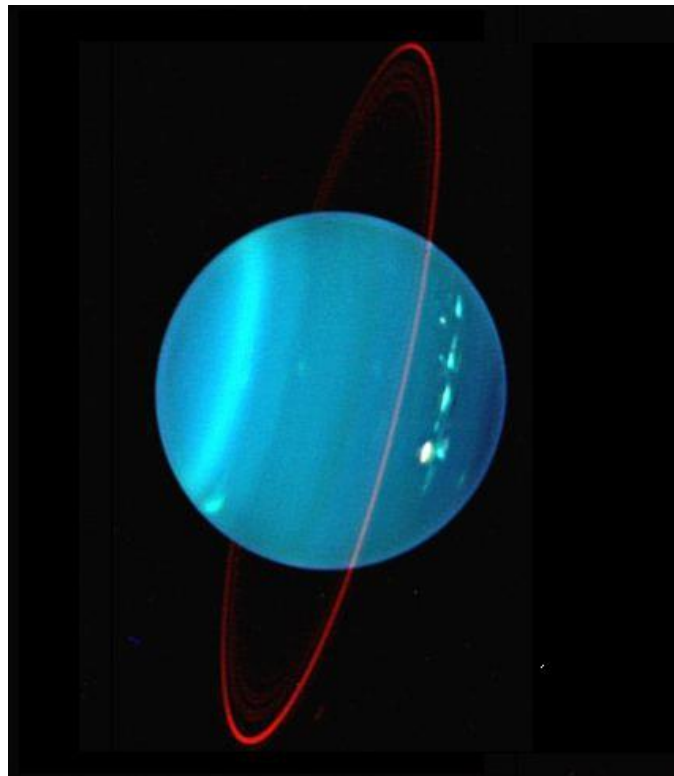

Optimization of interplanetary trajectories with deep space maneuvers - Model development and application to a Uranus orbiter mission

Thesis Report



Sjoerd Molenaar

August 2009

Optimization of interplanetary trajectories with deep space maneuvers - Model development and application to a Uranus orbiter mission

Thesis Report

Sjoerd Molenaar

August 2009

Preface

This report concludes the work that has been performed for my Master of Science thesis research at the Faculty of Aerospace Engineering of Delft University of Technology in The Netherlands. During the course of the study my interest in space engineering, in particular interplanetary trajectories, started to grow. When I was searching for a thesis subject, I looked at previous interplanetary missions. I found that Uranus has never been (or will be in the near future) the main target for a scientific mission. Uranus is considered a boring planet, but I found out that there are many interesting features at Uranus, its rings and its moons. Therefore I chose Uranus to be the target planet for this thesis research. At the end of the literature study I did prior to this thesis research, which was focused on the Uranus mission, the concept of deep space maneuvers came up. The addition of these maneuvers that are performed between planetary encounters is a recent topic in the field of optimizing interplanetary trajectories. I considered it a challenge to add these maneuvers to already existing software used at the Faculty.

Readers who are primarily interested in the planet Uranus, previously flown outer planet missions and the layout of the spacecraft are referred to part I of this report. If the reader is more interested in the orbital mechanics required for interplanetary trajectories with deep space maneuvers, part II of the report is of most value. The software package and optimization method used are the subject of part III of the report. Finally, if the reader would like to view the results obtained in this thesis, together with the conclusions and recommendations, please refer to part IV.

I would like to express my gratitude to my thesis supervisor Ron Noomen for his help during my thesis work. I appreciated the critical questions and suggestions during the weekly meetings. I would also like to thank all the students on the ninth floor for the wonderful time I have had doing my literature study and thesis research there. It was well worth it to travel from Amsterdam to Delft and back almost every day. Last, but certainly not least, I would like to thank my parents, my brother, my friends and family for supporting me during this period of hard work.

Contents

Preface	vi
Glossary	xix
Abstract	xxii
1 Introduction	1
1.1 Document overview	2
2 Mission definition	5
2.1 Assumptions for the Uranus orbiter mission	5
2.2 Time and reference systems	6
2.2.1 Julian epochs	6
2.2.2 Heliocentric reference frame	7
3 Uranus and its surroundings	11
3.1 The planet Uranus	11
3.1.1 The giant planets	12
3.1.2 Planet data	12
3.1.3 Planetary interior	13
3.1.4 Configuration	13
3.1.5 Atmosphere and meteorology	14
3.1.6 Magnetic field	15
3.2 The ring system of Uranus	17
3.3 The moons of Uranus	17
3.4 Possible scientific objectives for a mission to Uranus	20

3.5	Science orbit	20
4	Previous missions to the outer planets	23
4.1	Previous mission to Uranus: Voyager 2	23
4.1.1	Mission overview	23
4.1.2	Spacecraft overview	24
4.1.3	Trajectory	25
4.2	Jupiter mission: Galileo	25
4.2.1	Mission overview	25
4.2.2	Spacecraft overview	26
4.2.3	Trajectory	27
4.3	Saturn mission: Cassini-Huygens	28
4.3.1	Mission overview	28
4.3.2	Spacecraft overview	29
4.3.3	Trajectory	30
4.4	Pluto Mission: New Horizons	31
4.4.1	Mission overview	31
4.4.2	Spacecraft overview	32
4.4.3	Trajectory	32
4.5	Implications for a mission to Uranus	33
5	Characteristics of the Uranus orbiter spacecraft	35
5.1	Chemical propulsion systems	35
5.1.1	Propellant types	36
5.1.2	Characteristics	36
5.2	Generating electrical power	37
5.3	Payload science instruments	39
5.4	Preliminary layout of the spacecraft	40

6	Principles of orbital mechanics	45
6.1	The many-body problem	45
6.1.1	Newton's laws of motion and gravitational law	45
6.1.2	A system of n bodies	46
6.1.3	Motion of a body with respect to another body	47
6.2	The two-body problem	48
6.2.1	Conic sections	48
6.2.2	Elliptical orbits	49
6.2.3	Hyperbolic orbits	51
6.2.4	Sphere of influence	53
7	Orbit perturbations	57
7.1	Radially non-symmetric mass distribution	57
7.2	Aerodynamic forces	59
7.3	Attraction forces from other bodies	59
7.4	Solar radiation pressure	61
7.5	Electromagnetic forces	62
7.6	Implications	64
8	High thrust interplanetary trajectories	65
8.1	Two-dimensional interplanetary trajectories	65
8.1.1	Example: Hohmann transfer to Uranus	67
8.1.2	Three-dimensional interplanetary trajectories	68
8.2	Lambert's problem	68
8.3	Calculating the ΔV needed for launch and capture	74
8.4	Unpowered gravity assists	76
8.4.1	Principle of gravity assists	76
8.4.2	Heliocentric energy increase	77
8.5	Powered gravity assists	80

9	Deep Space Maneuvers	85
9.1	Basic principles of deep space maneuvers	85
9.2	Trajectory model	87
9.2.1	Randomly generating $\bar{V}_{\infty L}$	89
9.2.2	Random rotation of $\bar{V}_{\infty in}$ at an unpowered swingby	90
9.2.3	Consequences on the size of the search space	92
10	Propagation along a Kepler orbit	95
10.1	Introducing the Kepler problem	95
10.1.1	Kepler's equation for elliptical orbits	95
10.1.2	Kepler's equation for hyperbolic orbits	97
10.1.3	Kepler's equation for parabolic orbits	98
10.2	Position and velocity at a certain point in time	100
10.2.1	Solution of Kepler's problem for elliptical orbits	101
10.2.2	Solution of Kepler's problem for hyperbolic orbits	101
10.2.3	Solution of Kepler's problem for parabolic orbits	103
10.3	Universal variable formulation	103
10.3.1	The Sundman transformation	103
10.3.2	Kepler's equation using the universal variable formulation	105
10.3.3	Solving the universal variable form of Kepler's problem	108
11	Optimization	113
11.1	Overview of optimization methods	113
11.2	The simple GA	114
11.2.1	The working principle of a simple GA	114
11.2.2	Structure of the simple GA	115
11.3	Some advanced genetic operators	120
11.3.1	Elitism	120
11.3.2	Immigration	120
11.3.3	Constraint handling	120
11.4	Random number generator	121

12 GALOMUSIT	123
12.1 History and development of GALOMUSIT	123
12.2 Original version of GALOMUSIT	124
12.2.1 Program structure	124
12.2.2 Generation of individuals	125
12.2.3 Creating new generations	126
12.2.4 Multi-objective optimization	127
12.2.5 Convergence	127
12.3 Adaptations made to GALOMUSIT for this thesis	127
12.3.1 Adaptations prior to the thesis research	128
12.3.2 Setting up the program	129
12.3.3 Generating individuals for DSM trajectories	129
12.3.4 New subroutines added to GALOMUSIT	130
12.3.5 New output files	132
13 Benchmark runs for GALOMUSIT	133
13.1 Verification of results produced by previous users of GALOMUSIT	133
13.1.1 Pluto flyby with gravity assist at Jupiter	133
13.1.2 Trajectory to Neptune with multiple swingbys	134
13.2 Verification of GAMOLUSIT for an Earth-DSM-Mars transfer . . .	135
13.2.1 Problem description and results from literature	135
13.2.2 Results for the EdM test case using GALOMUSIT	137
13.2.3 Additional tests for the Earth-DSM-Mars test case	143
13.3 Verification of GALOMUSIT for an Earth-Venus-DSM-Mars transfer	146
13.3.1 Search space and results from literature	146
13.3.2 Results for the EVdM test case using GALOMUSIT	147
13.3.3 Additional tests for the EVdM test case	152

14 Results for the Uranus orbiter mission without DSMs	157
14.1 Direct transfer from Earth to Uranus	157
14.2 Results for trajectories from Earth to Uranus with swingbys	159
14.2.1 Mission specific settings in GALOMUSIT	160
14.2.2 Initial GA settings in GALOMUSIT	161
14.2.3 Results for 10% elitism, 5% immigration and 0.1% mutation	162
14.2.4 Additional tests	164
14.3 Sequences when a Venus swingby is allowed after an Earth swingby	166
14.3.1 Results for 15% elitism, 15% immigration	167
15 Results for trajectories with DSMs	169
15.1 Earth-Uranus transfer without swingbys	169
15.1.1 Results of an EdU transfer with a complete search space . .	169
15.1.2 Results of an EdU transfer with a constrained search space	172
15.2 Trajectories to Uranus with one swingby	179
15.2.1 No DSM on trajectories to Uranus with one swingby	180
15.2.2 DSM on the first leg of trajectories to Uranus with one swingby	181
15.2.3 DSM on the second leg of trajectories to Uranus with one swingby	189
15.3 Trajectories to Uranus with two swingbys	195
15.3.1 No DSMs on trajectories to Uranus with two swingbys . . .	195
15.3.2 DSM on the first leg of trajectories with two swingbys . . .	195
15.3.3 DSM on the second leg of trajectories with two swingbys . .	202
15.3.4 DSM on the third leg of trajectories with two swingbys . . .	203
16 Conclusions	205
17 Recommendations	209
Bibliography	211
A The Hohmann transfer to Uranus	I

B Benchmark tests for the EdM test case	V
B.1 EdM test case, extra test I	VI
B.2 EdM test case, extra test II	VIII
B.3 EdM test case, extra test III	X
B.4 EdM test case, extra test IV	XII
B.5 EdM test case, extra test V	XIV
B.6 EdM test case, extra test VI	XVI
B.7 EdM test case, extra test VII	XVIII
C Benchmark tests for the EVdM test case	XXI
C.1 Extra test I: $t_0 \in [4200, 4600]$ MJD2000	XXI
C.2 Extra test II: $t_0 \in [6600, 7000]$ MJD2000	XXIII
C.3 Extra test III: Complete search space, $N_{pop} = 2000$	XXIV
C.4 Extra test IV: $h_p \in [0, 0.75]$ R_V , $t_0 \in [4200, 4600]$ MJD2000	XXVI
C.5 Extra test V: $\zeta \in [4.75, 6.00]$ rad, $t_0 \in [4200, 4600]$ MJD2000	XXVII
C.6 Extra test VI: $\eta \in [0.45, 0.65]$, $t_0 \in [4200, 4600]$ MJD2000	XXVIII
C.7 Extra test VII Combination of extra tests IV, V and VI	XXIX
D Results for trajectories to Uranus without DSMs	XXXI
D.1 Elitism: 0.10, Immigration: 0.05, No Mutation	XXXII
D.2 Elitism: 0.10, Immigration: 0.20, No Mutation	XXXIII
D.3 Elitism: 0.15, Immigration: 0.15, No Mutation	XXXIV
D.4 Elitism: 0.20, Immigration: 0.05, No Mutation	XXXV
E Trajectories with DSMs and one swingby	XXXVII
E.1 EdVU, complete search space for all variables	XXXVII
E.2 EdSU, complete search space for all variables	XL
E.3 EMdU, complete search space for all variables	XLIII

Glossary

Symbols

a	Semi-major axis	[m]
B	Impact parameter	[m]
B	Magnetic field strength	[T]
c	Speed of light: $2.9979 \cdot 10^8$	[m/s]
C_3	Launch energy	[m ² /s ²]
C_D	Drag coefficient	[-]
e	Eccentricity	[-]
E	Eccentric anomaly	[°]
\mathcal{E}	Total energy	[m ² /s ²]
f	Fitness	[-]
f	Objective function	[-]
F	Force	[N]
F	Hyperbolic anomaly	[-]
g_0	Gravitational acceleration at sea level: 9.80665	[m/s ²]
G	Universal gravitational constant: $6.668 \cdot 10^{-11}$	[Nm ² /kg ²]
h	Altitude above surface	[-]
H	Angular momentum	[m ² /s]
i	Inclination	[°]
I_{sp}	Specific impulse	[s]
J_n^m	Constants of the gravitational field	[-]
m	Mass	[kg]
\dot{m}	Mass flow	[kg/s]
N_{pop}	Population size	[-]
N	Number of revolutions	[-]
p	Semi-latus rectum	[m]
p	Probability	[-]
P_n^m	Legendre polynomials	
q	Electric charge	[C]
Q	Power density of incoming radiation	[W/m ²]
r	Radial distance	[m]
R	Radius	[m]
RC	Reflection coefficient	[-]
s	Semi-parameter of a triangle	[m]
S	Reference surface area	[m ²]

t	Epoch	[MJD]/[MJD2000]
t	Time	[s]
T	Period	[s]
T	Temperature	[K]
T	Non-dimensional time	[-]
U	Voltage	[V]
V	Velocity	[m/s]
w	Exhaust velocity	[m/s]
x	Position in the x-direction	[m]
x	Non-dimensional semi-major axis	[-]
x	Universal variable	[-]
\bar{x}	Decision vector	[-]
y	Position in the y-direction	[m]
z	Position in the z-direction	[m]
β	Hyperbolic encounter angle	[°]
γ	Flight path angle	[°]
δ	Gravity assist bending angle	[°]
ε	Tolerance	[-]
ζ	Out of plane angle at unpowered swingby	[rad]
η	Angle of incidence for the incoming solar radiation	[°]
η	Fraction of time of flight for application of DSM	[-]
θ	True anomaly	[°]
θ	Directional angle for $\bar{V}_{\infty L}$	[rad]
λ_n^m	Constants of the gravity field	[°]
μ	Gravitational parameter	[m ³ /s ²]
ρ	Density	[kg/m ³]
σ	Constant of Stefan-Boltzmann: $5.67 \cdot 10^{-8}$	[W/(m ² K ⁴)]
φ	Directional angle for $\bar{V}_{\infty L}$	[rad]
ω	Argument of pericenter	[°]
ω	Angular velocity	[rad/s]
ΔV	Velocity change	[m/s]
Φ	Magnetic latitude	[°]
Ω	Right ascension of the ascending node	[°]

Subscripts

0	Initial
0	Just after impulsive shot at Earth on Hohmann orbit
1, 2, 3	With respect to body 1, 2 or 3
3	At pericenter of target planet centered hyperbola
<i>a</i>	Apocenter
<i>aero</i>	Aerodynamic
<i>alb</i>	Albedo
<i>c</i>	Circular
<i>C</i>	Capture
<i>cum</i>	Cumulative
<i>d</i>	Disturbing
<i>dry</i>	Spacecraft dry mass
<i>D</i>	Drag
<i>DSM</i>	Deep space maneuver
<i>ecl</i>	Ecliptic
<i>eff</i>	Effective
<i>eq</i>	Equatorial
<i>esc</i>	Escape
<i>E</i>	Earth
<i>f</i>	Final
<i>hyp</i>	Hyperbolic
<i>H</i>	Hohmann transfer orbit
<i>HC</i>	Heliocentric
<i>i, j, k</i>	Identifiers for different bodies
<i>i, in</i>	Initial
<i>in</i>	Incoming
<i>ir</i>	Irradiance
<i>L</i>	Launch
<i>L</i>	Lorentz
<i>Lam</i>	Lambert
<i>m</i>	Main body
<i>max</i>	Maximum
<i>min</i>	Minimal
<i>out</i>	Outgoing
<i>p</i>	Pericenter
<i>par</i>	Parabolic
<i>pl</i>	Planet
<i>pop</i>	Population
<i>r</i>	Radial direction
<i>rot</i>	Rotational
<i>s</i>	Spacecraft/Satellite
<i>s</i>	Selection
<i>sd</i>	From the spacecraft to the disturbing body
<i>sp</i>	Specific
<i>syn</i>	Synodic
<i>S</i>	Sun
<i>SB</i>	Swingby
<i>SoI</i>	Sphere of influence

t	Target planet
th	Thermal
tot	Total
tr	Truncation
U	Uranus
UC	Uranus-centered
x	In the x-direction
y	In the y-direction
z	In the z-direction
∞	At infinity
δ	Latitudinal direction

Abbreviations

ASI	Agenzia Spatiale Italiana (Italian Space Agency)
AU	Astronomical Unit
BA	Bond Albedo
DSM	Deep Space Maneuver
DSN	Deep Space Network
EADS	European Aeronautics, Defense & Space Company
EPPS	Energetic Particles and Plasma Spectrometer
ESA	European Space Agency
GALOMUSIT	Genetic ALgorithm Optimization of a MULTiple Swing-by Interplanetary Trajectory
GRC	Glenn Research Center
GSE	Gravity Science Experiment
GSFC	Goddard Space Flight Center
GTO	Geostationary Transfer Orbit
J2000	Julian Date 2451545.0
JD	Julian Date
JPL	Jet Propulsion Laboratory
LEO	Low Earth Orbit
MJD	Modified Julian Date
MMH	Monomethyl Hydrazine
NASA	National Aeronautics and Space Administration
NMP	New Millennium Program
RTG	Radioisotope Thermoelectric Generator
SOIR	Solar Occultation at InfraRed
SPICAV	SPectroscopy for Investigation of Characteristics of the Atmosphere of Venus
SRG	Stirling Radioisotope Generator
VEEGA	Venus Earth Earth Gravity Assist
VGA	Visual Geometric Albedo
VVEJGA	Venus Venus Earth Jupiter Gravity Assist

Abstract

Since the dawn of the space age many space missions have been carried out in order to explore the solar system. Only one spacecraft has ever had the privilege to travel to the distant planet Uranus, namely Voyager 2. However, Voyager 2 has only been the tip of the iceberg when it comes to uncovering the mysteries of Uranus, its rings and moons. An orbiter mission to Uranus is a logical step in the range of planetary explorers, as it could provide insight in for example the formation process of ice giants and in atmospheric phenomena.

Optimization of the interplanetary trajectory is a major part of the analysis of a mission to Uranus. Many different techniques can be applied to go from Earth to another planet. Of course a direct flight is possible, where one engine burn is applied at a parking orbit around Earth and another burn is performed to get into orbit around the target planet. It is also possible, however, to use the gravity of other planets to change the trajectory in such a way that it could save fuel with respect to the direct interplanetary transfer. It is also possible to perform an engine burn somewhere along the interplanetary orbit. Such a deep space maneuver (DSM) may also improve the total fuel consumption for the mission.

The mission to Uranus and the addition of deep space maneuvers to the trajectory form the backbone of this thesis. Therefore the following thesis objectives can be formulated:

- I *Develop a method to optimize interplanetary trajectories with deep space maneuvers and integrate this method in the software package GALOMUSIT.*
- II *Apply the developed method to optimize the trajectory for a Uranus orbiter mission.*

Based on the literature study prior to this thesis a number of assumptions are made regarding the mission to Uranus. First of all, in this thesis only high thrust trajectories are used. Secondly, planets can be used to perform either a powered or an unpowered gravity assist, but aerogravity assists are not applied. Finally, the optimization of the trajectory is done only with respect to the total ΔV , so single-objective optimization is used.

The spacecraft is assumed to start at a parking orbit around Earth. The parking orbit that is used is a Geostationary Transfer Orbit (GTO) with a

pericenter altitude of 185 km. The final science orbit around Uranus is a polar orbit, with an eccentricity of 0.90 and a pericenter altitude of 2500 km. For the trajectory towards Uranus, the spacecraft is allowed to perform a maximum of five swingbys. Mercury and Neptune are not used as a swingby planet. Venus and Earth can be used multiple times for a swingby, Venus three times and Earth twice.

The trajectory that produces the lowest total ΔV for trajectories without DSMs is EVVEJU. The total ΔV that is required for this trajectory is 2.892 km/s. The launch date is 12 September 2015 and the arrival date is 16 July 2034, giving a total time of flight of 6882.2 days.

The VVEJ trajectory was present in a set of 77 swingby sequences used by *Melman* [2007] for his thesis research on a mission to Neptune. A number of assumptions was made to come to this set of sequences, one of which was that it was not possible to perform a swingby at Venus after a swingby at Earth. The inner part of the solar system is often used to gain enough velocity to travel to the outer parts of the solar system. Therefore, a new set of 77 possible swingby sequences was created by allowing a swingby at Venus after a swingby at Earth. The best result out of the new sequences is EVVEJ, with a total ΔV of 5.005 km/s. The launch date is 17 January 2017 and the arrival date is 15 November 2034. This results in a total time of flight of 6518.7 days. The total ΔV in this case is more than 2 km/s higher than the VVEJ trajectory. It can therefore be concluded that the new swingby sequences do not provide better results in terms of the total ΔV with respect to the original set of sequences.

The addition of DSMs to the trajectory meant that some changes had to be made in GALOMUSIT. First of all, a method had to be developed to propagate a spacecraft along a Kepler orbit. An interplanetary leg with a DSM can not be analyzed using Lambert targeting alone. Lambert targeting is the backbone of GALOMUSIT, ensuring that the spacecraft encounters a target planet at a specified time instant. The first part of the leg is now based on Kepler's problem, where both the initial position and velocity need to be known together with the time of flight. A universal formulation of Kepler's problem was implemented in GALOMUSIT that is the same for each type of conic section. The end of the Kepler arc is the location where the DSM is performed. The output parameters of the Kepler problem are the position and velocity at the end of the Kepler arc. The second part of the leg is then analyzed using Lambert targeting, which makes sure that the spacecraft encounters the next planet. The discontinuity in the velocity at the end of the Kepler arc and at the start of the Lambert arc is the DSM.

Adding DSMs to the trajectory introduces many additional variables besides the encounter epochs. If a DSM is added to the first leg of the trajectory, 4 variables are added to the problem. A DSM on a leg after an unpowered swingby introduces three new variables. All of the DSM related variables are generated randomly from a user defined search space. Finally, a new subroutine had to be created in GALOMUSIT to analyze unpowered swingbys. The unpowered swingby with subsequent DSM has replaced the powered swingby in this case.

The adaptations to GALOMUSIT are benchmarked and it is concluded that the implementation of the method to analyze trajectories with DSMs is applied correctly. The total ΔV and the orbits corresponding to the best solutions found in the literature could be reproduced. However, this is not obtained directly, using the complete search space for all variables, but after successive steps where the search space is reduced.

For the EdU transfer (where the symbol 'd' denotes a DSM) the optimization on the complete search space produces a total ΔV that is slightly higher than the total ΔV for the Lambert solution (which is 6.673 km/s). After an analysis of the search space it was found that a large part of the search space could be neglected and after search space reduction a value for the total ΔV was found that is 10 m/s lower than the best value for the Lambert solution. A grid sampling around the global optimum showed that the total ΔV behaves in a smooth way.

When a DSM is added to a trajectory with a swingby, the behavior of the total ΔV changes from being smooth to being quite irregular. After an analysis of the search space the results can be improved when the search space has been reduced or certain variables have been given a fixed value.

Adding a DSM may result in trajectories that have more than one revolution between planetary encounters. When only Lambert targeting was concerned, these multi-revolution transfers were not allowed. In this thesis only single-revolution Lambert arcs were allowed as well, but the addition of a Kepler arc prior to a Lambert arc opens up a new range of trajectories that otherwise would not be possible. A prime example of this can be seen in section 15.3.2, where the total ΔV for an EdVEU (so a DSM on the leg between Earth and Venus) transfer was 1.6 km/s lower than for the EVEU Lambert solution.

It can finally be concluded that GALOMUSIT as it exists now is not powerful and sophisticated enough to find the optimal solution at once when DSMs are added to the trajectory. The search space is too large and the objective function behaves very irregularly. After a first run on the complete search space, the search space itself has to be analyzed to determine if certain parts can be ignored. Right now, this still has to be done by hand, which is tedious work. If this process could be automated it will improve the performance of the program.

Chapter 1

Introduction

Since the dawn of the space age many space missions have been carried out in order to explore the solar system. Our home planet Earth has been the subject for most of these missions, but a significant number of missions have gone beyond Earth for example to the gas giants that lie beyond Mars and the asteroid belt. Two of the four giant planets, Jupiter and Saturn, have been studied in detail by planetary orbiters. The next giant planet in terms of distance to the Sun is Uranus. Only one spacecraft has ever had the privilege to travel to this distant planet, namely Voyager 2. However, Voyager 2 has only been the tip of the iceberg when it comes to uncovering the mysteries of Uranus, its rings and moons. An orbiter mission to Uranus is a logical step in the range of planetary explorers, as it could provide insight in for example the formation process of ice giants and in atmospheric phenomena.

Optimization of the interplanetary trajectory is a major part of the analysis of a mission to Uranus. Many different techniques can be applied to go from Earth to another planet. Of course a direct flight is possible, where one engine burn is applied at a parking orbit around Earth and another burn is performed to get into orbit around the target planet. It is also possible, however, to use the gravity of other planets to change the trajectory in such a way that it could save fuel with respect to the direct interplanetary transfer. It is also possible to perform an engine burn somewhere along the interplanetary orbit. Such a deep space maneuver (DSM) may also improve the total fuel consumption for the mission.

At the Faculty of Aerospace Engineering of Delft University of Technology in The Netherlands a software package called GALOMUSIT is used for the optimization of interplanetary trajectories. Prior to this thesis research it was not yet possible to add these DSMs to the trajectory. The mission to Uranus and the addition of DSMs to the trajectory form the backbone of this thesis. Therefore the following thesis objectives can be formulated:

- I *Develop a method to optimize interplanetary trajectories with deep space maneuvers and integrate this method in the software package GALOMUSIT.*
- II *Apply the developed method to optimize the trajectory for a Uranus orbiter mission.*

The purpose of this report is to provide a complete and detailed overview of the work that has been performed for this MSc thesis research. To that end, the report is set up in a structured way by discussing some general background information, the theory of orbital mechanics and the optimization process before presenting the results and drawing the conclusions and recommendations.

1.1 Document overview

This report is divided into several parts, each of which is dedicated to a specific part of the thesis research. An overview of each of these parts is given below.

First, in chapter 2, an overview of the Uranus mission will be presented together with the time scales and reference systems that will be used throughout this thesis.

Part I

Part I, containing chapters 3, 4 and 5, provides some general background information for the interplanetary mission. Chapter 3 provides details on the planet Uranus, its moons and rings. Also the scientific objectives for a mission to Uranus are formulated and the chapter ends with a proposal for a science orbit that can accomplish these objectives. Chapter 4 gives an overview of four interplanetary missions to the outer parts of the solar system, namely Voyager, Galileo, Cassini-Huygens and New Horizons. These missions provide insight in for example what types of instruments are needed for the Uranus mission. Chapter 5 is focused on the spacecraft itself. The chapter goes into detail about the propulsion system and electrical power generation and a selection of payload instruments will be discussed.

Part II

The second part of this thesis report is focused on orbital mechanics. Chapter 6 introduces the basic principles of orbital mechanics, like the different orbit types. The focus in chapter 7 is on perturbing accelerations and why all of them can be neglected for this thesis research. Chapter 8 goes into detail on the different techniques that are applied with high thrust interplanetary trajectories. These include Lambert targeting and gravity assists. The theory behind DSMs is discussed in chapter 9, where the focus is on the introduction of new variables. The final chapter of part II is chapter 10, in which propagation of an orbit along a Kepler arc is discussed. A universal variable formulation for Kepler's equation will be derived that holds for all types of conic sections.

Part III

Part III of this report is dedicated entirely to Genetic Algorithm (GA) optimization. In chapter 11 the general principles of GAs are outlined, as well as some

more advanced operations within a Genetic Algorithm. Chapter 12 focuses on the software tool that is used in this thesis, GALOMUSIT. The history, development and structure of the program are discussed, as well as the additions and modifications that were made for this thesis research. The results for benchmarking GALOMUSIT can be found in chapter 13.

Part IV

In part IV the results of the trajectory optimization for the mission to Uranus will be presented. First, in chapter 14 the trajectory to Uranus is optimized without the addition of DSMs on the trajectory. Then, in chapter 15, DSMs will be added to trajectories with either 0, 1 or 2 gravity assists. Finally, the conclusions that can be drawn from this research and the recommendations for further research will be presented in chapters 16 and 17.

Mission definition

This chapter is intended to present the most important assumptions that are made for the mission to Uranus and to discuss the time scales and reference systems that are used throughout this thesis.

2.1 Assumptions for the Uranus orbiter mission

In this section some of the most important assumptions that are made for this thesis research are outlined. These assumptions are made to set some boundaries on the trajectory analysis for the Uranus mission.

Mission characteristics

It is assumed that the trajectory analysis starts from a parking orbit around Earth. The launch trajectory and insertion of the spacecraft into the parking orbit is not considered. The parking orbit that will be used is a Geostationary Transfer Orbit (GTO). In the remainder of this thesis, if the launch date is mentioned, it means the date at which an engine burn will be performed at pericenter in the GTO.

From the literature study prior to this thesis research it was determined that the launch should occur between 1 January 2015 and 1 January 2025. The latest possible date to arrive at Uranus was determined as 1 January 2035 [Molenaar, 2007]. The spacecraft will be put into orbit around Uranus, so observations can be made of the planet, its rings and moons.

High thrust trajectories

In this thesis only high thrust trajectories will be used. So each engine burn is considered as an impulsive shot, where the velocity changes instantaneously, but the position stays the same. The orbits that are flown are pure Kepler orbits.

No aerogravity assists

The planets can be used to change the velocity and direction of the spacecraft. These gravity assists can be either unpowered or powered, where an engine burn is performed at the pericenter of the swingby. It is also possible to fly through the atmosphere of a planet. Although the possibility exists in the software package GALOMUSIT to perform aerogravity assists, they will not be used in this thesis.

Single-objective optimization

With GALOMUSIT it is possible to perform either single-objective optimization or multi-objective optimization. The former optimizes interplanetary trajectories with respect to the total amount of ΔV , whereas the latter simultaneously optimizes the total ΔV and the time of flight, resulting in a so-called absolute Pareto front. For this thesis use will be made of single-objective optimization.

2.2 Time and reference systems

This particular section is dedicated to the time scales and reference systems that are used throughout this thesis research.

2.2.1 Julian epochs

Next to the standard calendar dates used in everyday life, Julian epochs are also used in this thesis. The Julian Date (JD) is defined as the number of days since noon on 1 January 4713 BC, including the fraction of the day. It provides, for all practical purposes, a positive and continuous time scale. The counting starts at noon out of historical perspective. At present, the JD numbers are quite high, so that is why a Modified Julian Date (MJD) has been introduced [*Montenbruck and Gill, 2005*]:

$$MJD = JD - 2400000.5 \quad (2.1)$$

In this expression Julian Date 2400000.5 corresponds to midnight on 17 November 1858, which therefore is the zero point for the MJD.

The positions of the planets and other celestial bodies at any instant in time are provided by NASA's Jet Propulsion Laboratory (JPL). The JPL provides the so-called Development Ephemerides (DE) publicly. They are the standard for high-precision planetary and lunar coordinates. Currently the DE200 and DE405 are most widely adopted and in this thesis the DE200 ephemeris will be used. The JPL ephemeris covers the period from 1600 to 2170. The DE200 series uses the dynamical equator and equinox of J2000. The J2000 epoch is precisely Julian Date 2451545.0 (or 1 January 2000 at noon) [*Montenbruck and Gill, 2005*]. So the days that have passed since the J2000 epoch are:

$$MJD_{2000} = JD - 2451545.0 = MJD - 51544.5 \quad (2.2)$$

2.2.2 Heliocentric reference frame

The orbit of the Earth around the Sun defines the so-called ecliptic plane. It is convenient use this plane as a reference plane, because all planets in the solar system have relatively small inclinations with respect to the ecliptic. The ecliptic plane is inclined to Earth's equatorial plane by an angle of $i_{ecl} = 23.44^\circ$.

The most commonly used reference frame to describe the motion of the planets is the inertial, heliocentric, ecliptic reference frame, see also figure 2.1.

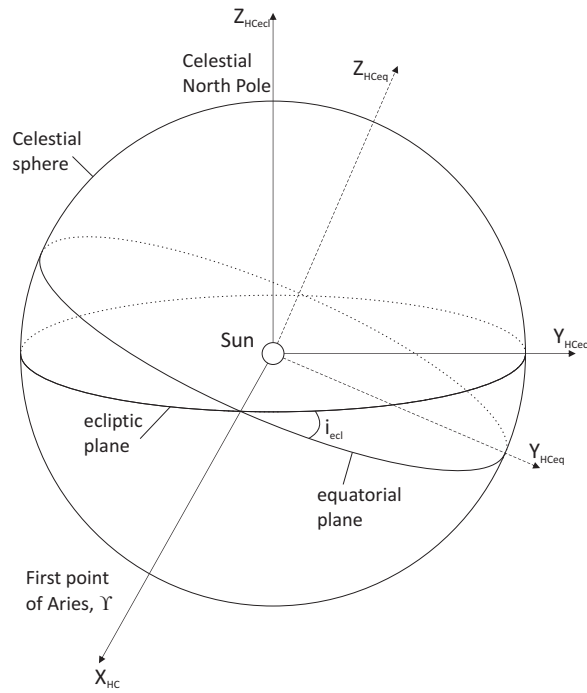


Figure 2.1 Inertial, heliocentric, ecliptic and equatorial reference frames. The X-axis is the same for both reference frames.

The $X_{HC_{ecl}}$ -axis points in the direction of the vernal equinox or First Point of Aries. The $Z_{HC_{ecl}}$ -axis points to the Celestial North Pole and the $Y_{HC_{ecl}}$ completes the right-handed orthogonal frame. The JPL DE200 planetary ephemeris that is used in this thesis provides the position and velocity of a celestial body in the inertial, heliocentric, equatorial reference frame. The $X_{HC_{eq}}$ -axis coincides with the one for the inertial, heliocentric, ecliptic reference frame. The $Z_{HC_{eq}}$ -axis is along Earth's rotation axis and the $Y_{HC_{eq}}$ -axis completes the right-handed orthogonal frame. To transform coordinates from the equatorial frame to the ecliptic frame the following transformation is needed:

$$\tilde{r}_{HC_{ecl}} = \begin{bmatrix} 1 & 0 & 0 \\ 0 & \cos i_{ecl} & \sin i_{ecl} \\ 0 & -\sin i_{ecl} & \cos i_{ecl} \end{bmatrix} \tilde{r}_{HC_{eq}} \quad (2.3)$$

Part I: General Information

Uranus and its surroundings

Uranus is the second most distant planet from the Sun, and up until now only one spacecraft has ever been there, Voyager 2 (see also section 4.1). During its encounter with Uranus, Voyager 2 made the photograph shown in figure 3.1.



Figure 3.1 A photograph of Uranus taken by the Voyager 2 spacecraft during its encounter in January 1986 [NASA/Voyager, 2009].

Looking at figure 3.1, it is no surprise that Uranus was considered by many as a very bland and boring planet. Therefore no other spacecraft has gone to Uranus since Voyager 2 and so far there are no missions planned in the future [NASA/JPL, 2009].

This chapter will show what is known up until now about the planetary system of Uranus, and what questions might be answered when a spacecraft would be sent there. There is more to Uranus than what meets the eye.

3.1 The planet Uranus

Uranus was discovered in 1781 by William Herschel (1738-1822) [NASA/JPL, 2009]. It was the first planet that was discovered with the use of a telescope.

Uranus had been sighted many times before, but it was not recognized as a planet. Before Uranus was recognized as a planet only Mercury, Venus, Earth, Mars, Jupiter and Saturn were known. The discovery of Uranus expanded the boundaries of the solar system significantly.

3.1.1 The giant planets

The four planets closest to the Sun (Mercury, Venus, Earth and Mars) are called the terrestrial planets [De Pater and Lissauer, 2007], see also figure 3.2.

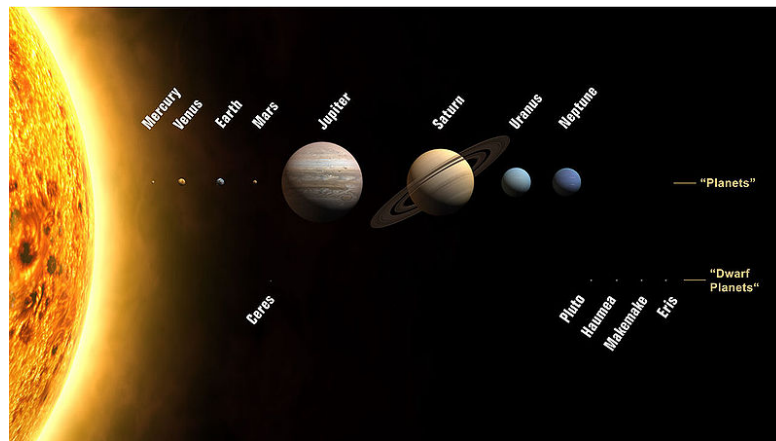


Figure 3.2 The solar system, after [Wikipedia, 2009].

In terms of distance to the Sun these planets are followed by the asteroid belt and the four giant planets. The giant planets are Jupiter, Saturn, Uranus and Neptune. Jupiter is by far the most massive planet in the solar system, with a mass that is more than twice that of all other planets combined. Uranus is the least massive of the giant planets.

Because of notable differences between the four giant planets, they can be further subdivided into the gas giants (Jupiter and Saturn) and ice giants (Uranus and Neptune). The gas giants consist predominantly of hydrogen (H_2) and helium (He). Uranus and Neptune, however, have a completely different internal composition (see also section 3.1.3) [De Pater and Lissauer, 2007].

3.1.2 Planet data

In table 3.1 the most important bulk and orbital parameters of Uranus are presented.

With its mass of $86.832 \cdot 10^{24}$ kg Uranus is more than 14 times as massive as Earth. There is quite a difference between the equatorial and polar radius, causing the flattening to be almost 7 times as high as here on Earth. Since Uranus is an ice giant, its mean density is much lower (4.35 times) than the mean density

Bulk parameters

Mass ($\cdot 10^{24}$ kg)	86.832
Equatorial radius (1 bar level) (km)	25,559
Polar radius (1 bar level) (km)	24,973
Flattening (-)	0.02293
Mean density (g/cm^3)	1.270
Gravitational parameter μ ($\cdot 10^6$ km^3/s^2)	5.794
Solar irradiance (W/m^2)	3.71

Orbital parameters

Semi-major axis ($\cdot 10^9$ km)	2.87246
Sidereal orbit period (days/years)	30,685.4 / 84.01
Inclination ($^\circ$)	0.772
Eccentricity (-)	0.0457
Obliquity ($^\circ$)	97.77
Sidereal rotation period (hrs)	17.24

Table 3.1 Bulk and orbital parameters of Uranus [NASA/GSFC, 2007].

of Earth, a terrestrial planet.

Uranus is located 19.2 times further away from the Sun as Earth. The orbit of Uranus about the Sun is just out of the ecliptic plane, with an inclination with respect to the ecliptic of 0.772° . The orbit is nearly circular, but with an eccentricity of 0.0457 there is still quite some difference from being a perfect circle.

3.1.3 Planetary interior

The exact composition of ice giants Uranus and Neptune is not precisely known up to this point. It could consist for the most part of ices, or of a mixture of rocky materials, hydrogen and helium, or some combination in between. The best models to date for Uranus indicate a small rocky core, a large, icy, ionic ocean and a small atmosphere [De Pater and Lissauer, 2007]. In these models the core has a radius of roughly 4500 km, the thickness of the liquid icy ocean is about 16,000 km and the hydrogen and helium dominated atmosphere is about 5000 km thick [Faure and Mensing, 2007]. Figure 3.3 shows a schematic of this best known model of the interior structure of Uranus.

3.1.4 Configuration

The rotation axis of Uranus is nearly aligned with its orbital plane with an obliquity of 97.77° (so this is the angle the equatorial plane makes with respect to the orbital plane) [NASA/GSFC, 2007]. This is a feature not seen anywhere else in the solar system. The cause for this extreme axial tilt is probably a collision with an object of about the size of the Earth while Uranus was still forming. The disk of gas and dust particles that had orbited Uranus prior to the impact realigned itself with the equatorial plane after its rotation axis had been tipped over by the impact.

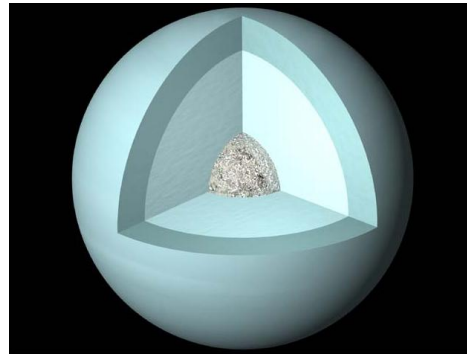


Figure 3.3 Best model of the interior structure of Uranus [Hamilton, 2001]. Grey represents the core of the planet, light blue-green represents the icy, ionic ocean and the atmosphere is represented by dark blue-green.

3.1.5 Atmosphere and meteorology

The interior of Uranus is topped off with an atmosphere dominated by H_2 and He. Uranus also contains a somewhat smaller amount of methane (CH_4). The methane in the upper atmosphere absorbs red light, giving Uranus its characteristic blue-green color. This composition is totally different than for example the atmosphere of Earth, one of the terrestrial planets much closer to the Sun. The Earth's atmosphere consists mostly of nitrogen (N_2) and oxygen (O_2). The atmospheres of Mars and Venus consist mainly of carbon dioxide (CO_2), whereas Mercury only has an extremely tenuous atmosphere [Beebe, 2004].

Because of its unusual orientation, the seasons on Uranus are the most extreme ones in the solar system. During Uranus' orbit around the Sun, the poles bask in sunlight or dwell in total darkness for more than 40 years. During the time of the Voyager 2 flyby in 1986 the north pole of Uranus was pointing in the direction of the Sun, and the atmosphere showed little sign of activity (see figure 3.1) [Hammel and Klein, 2003].

During the last few years, however, the atmosphere of Uranus is showing an increase in activity. A dark spot has been sighted in August 2006 by the Hubble Space Telescope [Sromovsky et al., 2005], which is very rare on Uranus, but on Neptune it is common. The dark spot on Uranus was actually a vortex of about two-thirds the size of the United States. This dark spot may have been an indication that the atmosphere of Uranus was changing as it was approaching equinox in 2007 [Devitt, 2008].

At the Uranus equinox the Sun was shining directly over the planet's equator. Figure 3.4 shows images of Uranus before and during the Uranus equinox.

There are other indications that the atmosphere of Uranus has been increasing in activity. Voyager 2 detected no more than 10 distinct cloud features on Uranus during its encounter. In 2004 however, over 30 features were visible and could be

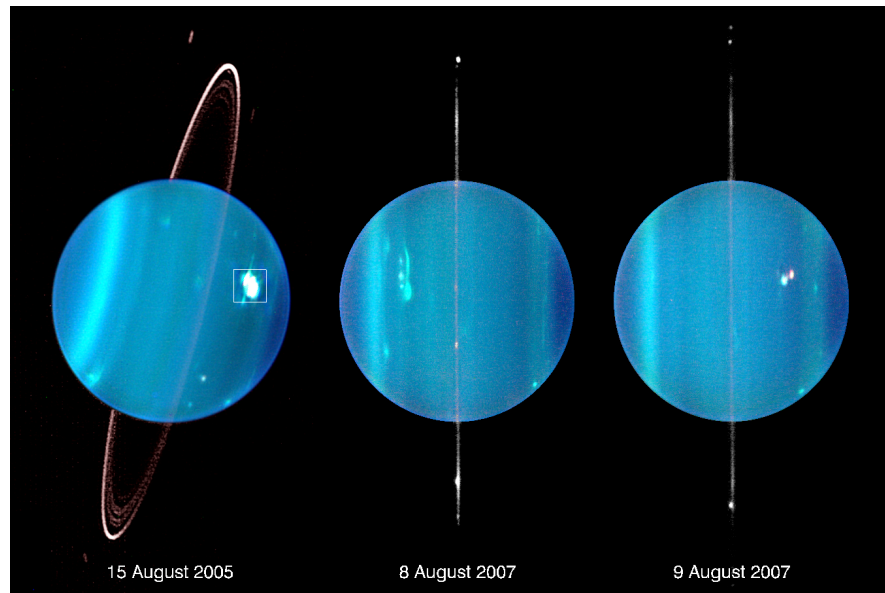


Figure 3.4 Images of Uranus taken at near infra-red wavelengths with the Keck telescope. The left image was taken before equinox, in 2005. The middle and right image show Uranus during equinox in 2007 [Devitt, 2008]. The planet's south pole is to the left in each of the three pictures.

tracked over time. Furthermore, there were many more clouds that appeared and then later on disappeared again on very short time scales [Lakdawalla, 2004].

One cloud feature on Uranus is of special interest, the so-called "Great Spot at 37°S" (GS-37S in short). This particular cloud appeared to persist from 2000 to 2004, in which period regular observations were made using the Keck telescope. This cloud also matched in shape and position with a cloud spotted by the Hubble Space Telescope in 1996 and there is evidence that the cloud was also spotted by Voyager 2 [Lakdawalla, 2004]. Figure 3.5 shows images of both hemispheres of Uranus taken with the Keck Telescope on 11 and 12 July 2004.

3.1.6 Magnetic field

Planetary magnetic fields are generated by complex fluid motion in parts of the planet's interior that are electronically conductive. Both Uranus and Neptune have a different type of magnetic field than Earth, Jupiter and Saturn. The last three planets have axi-symmetric dipole fields, but Uranus and Neptune do not. Determination of these different types of magnetic fields is important for the understanding of the planetary interiors [Stanley and Bloxham, 2004].

The magnetic field of Uranus is tilted 58.6° with respect to its rotational axis. Next to that, the magnetic center is also offset from the center of the planet by about one third of Uranus' radius [De Pater and Lissauer, 2007]. This configuration is shown in figure 3.6.

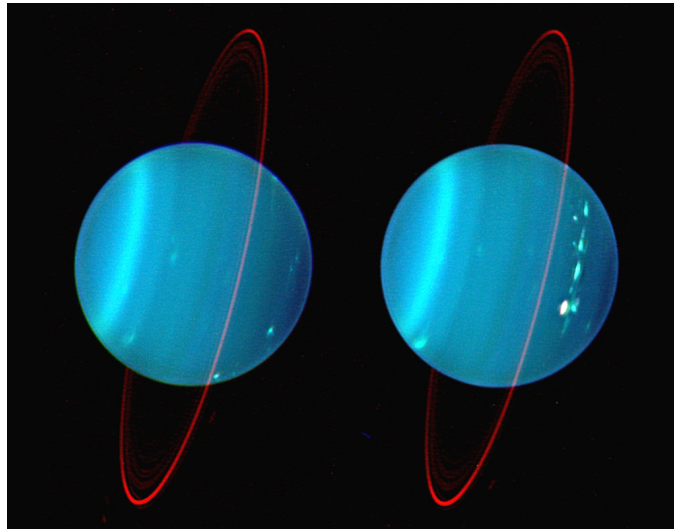


Figure 3.5 The two hemispheres of Uranus showing a large banded wind structure in the northern hemisphere [Devitt, 2004]. the GS-37S storm can be seen in the right image in the lower left corner (it is the faint feature). The images are compositions of pictures taken at different near-infrared wavelengths. Uranus's south pole points to the left in both images.

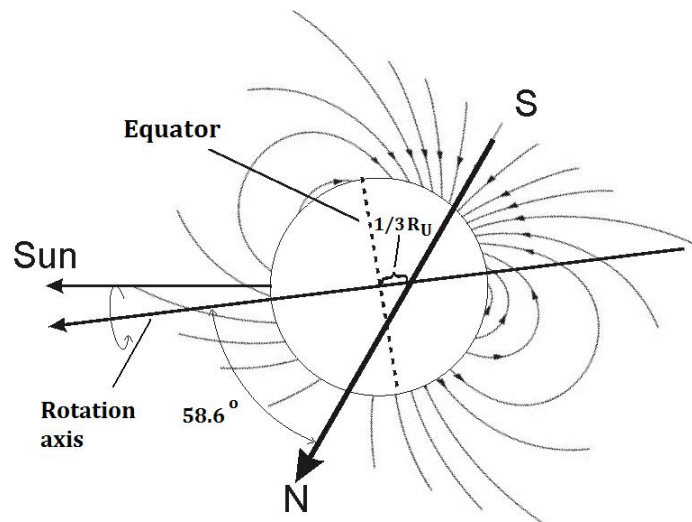


Figure 3.6 The magnetic field configuration of Uranus, adapted from [Wikipedia, 2009].

Uranus has an internal magnetic field, implying that the interior must be electrically conductive and convective. The pressure in the planet's interior is too low, however, for metallic hydrogen to form. The conductivity has to come from somewhere else. On Jupiter this is not the case and the interior pressure allows for forming metallic hydrogen. Uranus' icy mantles are probably hot, dense, liquid ionic 'oceans' of water with some methane, ammonia, nitrogen and hydrogen sulfide, where the conductivity is high enough to set up an electromagnetic current system that can generate the observed magnetic fields [De Pater and Lissauer, 2007].

3.2 The ring system of Uranus

Up until now there are 13 known rings around Uranus [NASA/JPL, 2009]. The first nine rings were discovered in 1977. They are narrow and optically thick, in the range of 41,000 km - 52,000 km from Uranus' center. The rings are identified by numbers and Greek alphabet letters. From the inside out they are called 6, 5, 4, α , β , η , γ , δ , and ε .

Most of the rings are 1 to 10 km wide, nearly circular (eccentricity of the order 10^{-3}) and they lie approximately in the planet's equatorial plane (inclination of less than one tenth of a degree). The outermost ring, the ε -ring, is the widest and most eccentric. Its eccentricity is $8 \cdot 10^{-3}$ and it is 20 km wide in its pericenter and 96 km wide in its apocenter. Particles are in the range 1 cm to 10 m or somewhat larger. They are extremely dark, probably consisting of radiation darkened ice. This consists of complex hydrocarbons embedded in ice [De Pater and Lissauer, 2007].

Voyager 2 discovered two new rings, 1986 U2R and the λ -ring. The first one is located about 1500 km below the 6-ring making it the ring closest to Uranus. The λ -ring is located in between rings δ and ε . These two rings brought the total number of known rings to 11 [Faure and Mensing, 2007]. In December 2005, the Hubble Space Telescope photographed two previously unknown rings. Located about twice as far away from the planet as the other known rings, the new rings are called the second or outer ring system of Uranus. So until now, 13 rings are known to exist [HubbleSite, 2005].

3.3 The moons of Uranus

Uranus has 27 known moons, whose names come forward from characters in plays by William Shakespeare (1564-1616) and poems written by Alexander Pope (1688-1744) [NOAA, 2007]. Uranus is the only planet where the moons don't possess names that come from ancient mythology. Of the 27 moons, there are five main ones. These were the only ones known before Voyager 2 made its flyby at Uranus in 1986 [NASA/JPL, 2009]. Table 3.2 indicates the most important bulk and orbital parameters. The inclination that is shown here is defined with respect to the equatorial plane of Uranus.

Miranda

One of the most peculiar objects in the solar system is the moon Miranda, see figure 3.7.

Miranda is the closest to Uranus of the five main moons. It has a part which is heavily cratered, which would be expected for a small and cold moon. However,

Bulk parameters

<i>Moon</i>	m (10^{20} kg)	R (km)	ρ (g/cm^3)	VGA* (-)
Miranda	0.66	240 x 234.2 x 232.9	1.200	0.27
Ariel	13.5	581.1 x 577.9 x 577.7	1.670	0.35
Umbriel	11.7	584.7	1.400	0.19
Titania	35.2	788.9	1.710	0.28
Oberon	30.1	761.4	1.630	0.25

Orbital parameters

<i>Moon</i>	a (10^3 km)	T (days)	i ($^\circ$)	e (-)
Miranda	129.39	1.413	4.22	0.0027
Ariel	191.02	2.520	0.31	0.0034
Umbriel	266.30	4.144	0.36	0.0050
Titania	435.91	8.706	0.14	0.0022
Oberon	583.52	13.463	0.10	0.0008

Table 3.2 Bulk and orbital parameters of the five main uranian moons [NASA/GSFC, 2007]. * Visual Geometric Albedo



Figure 3.7 The odd surface of Miranda [NASA/JPL, 2009].

there are also three parts of its surface that don't have many craters, but have numerous bands, ridges and steep cliffs. These parts are called coronas and they are named after places mentioned in Shakespeare's plays (Arden, Inverness and Elsinor) [Faure and Mensing, 2007]. What has caused Miranda to have such a unique surface is a mystery. There are a number of hypotheses, the first one being that Miranda has been shattered, perhaps up to five times, during its formation. Another possible explanation involves the sinking of material in regions where the heavy core material reaccreted on the outside and subsequently sank to the center.

Ariel

The four other main moons are shown in figures 3.8 and 3.9. The second main moon in terms of distance from Uranus is its brightest one, Ariel. It has a very old heavily cratered surface, but on its northern hemisphere there are a number of indications of resurfacing. It contains intersecting sets of ridges and grooves as well as several major rift valleys with steep sides and flat floors. So in its youth Ariel has been tectonically active [NASA/JPL, 2009].

Umbriel

Umbriel is the darkest of the main moons of Uranus and one of the darkest moons in the solar system. It is heavily cratered, indicating that the moon is old. There is little or no evidence that there is tectonic activity on Umbriel. The picture of Umbriel shows a bright ring at the top, which is probably the bottom of a large crater [NASA/JPL, 2009].

Titania

Titania is the largest satellite of Uranus. The surface of Titania is heavily cratered. However, there are some small areas that have smoother surface material implying local resurfacing. There are several large faults cutting through Titania's surface, similar to the ones seen on Ariel [NASA/JPL, 2009].

Oberon

The icy surface of Oberon is characterized by many craters. There is little evidence for tectonic activity, but there are several high-contrast albedo features and signs of faulting [NASA/JPL, 2009].

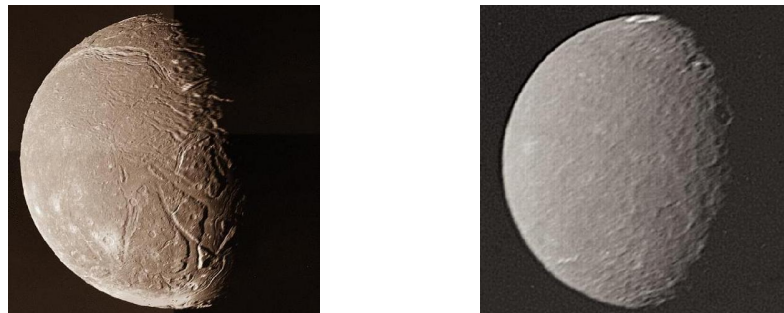


Figure 3.8 Ariel (left) and Umbriel (right) [NASA/JPL, 2009].



Figure 3.9 Titania (left) and Oberon (right) [NASA/JPL, 2009].

Other moons

All other 22 moons are smaller in size than the five main ones. The smallest of them have radii as small as 6-8 km. They are also very dark, so spotting them

with remote observations is quite difficult. The moons that were discovered by Voyager 2 are probably half rocky material and half water ice. The composition of the other moons remains unknown up to this point, but it is likely that they are asteroids that were captured in the gravity field of Uranus. For more information on the other moons, see [NASA/JPL, 2009].

3.4 Possible scientific objectives for a mission to Uranus

It has become clear throughout this chapter that Uranus is more than just a bland blue-green planet. When a spacecraft would be sent to Uranus' planetary system, there are a number of objectives that such a mission could complete.

- Study the composition of the atmosphere of Uranus.
- Study the dynamics of the atmosphere of Uranus:
 - Determine the composition of cloud features present in the atmosphere.
 - Study the winds on Uranus. What are the velocities and where are they located on the planet? How deep within the atmosphere do they occur?
 - Determine how heat is redistributed within the atmosphere.
 - Study how the atmosphere reacts to changing lighting conditions (day/night variations).
- Measure the magnetosphere of Uranus and determine whether it shows any dynamical activity.
- Determine the magnetic field and help explain why it is so asymmetrical.
- Determine the interior structure of Uranus.
- Determine whether there are any new moons or rings to be discovered.
- Study the main moons. Determine whether any of these moons possesses a magnetic field. What is the interior structure of these moons? Make detailed photographs of the surface of these moons.
- Study the dynamics and composition of the rings of Uranus.

3.5 Science orbit

The final orbit around Uranus has to be determined in such a way that it can fulfill the intended scientific objectives. For example, in order to measure a significant part of the magnetosphere the spacecraft will have to fly close to and far away from Uranus. Furthermore, flying close to Uranus provides the possibility of making highly detailed images in different wavelengths of Uranus' atmosphere. These are just two reasons why the final orbit around Uranus should be highly elliptic, with a close pericenter radius and a large apocenter radius.

The orbit around Uranus has to be chosen such that global coverage is achieved, meaning that all longitudes and latitudes of the planet are covered by the spacecraft. This is vital for studying the dynamics of the atmosphere and for

determining the interior structure of Uranus. In order to achieve that, the orbit has to be polar. Uranus itself will rotate around its rotational axis perpendicular to the spacecraft's orbit in that case.

One of the most critical conditions for this polar orbit is that it has to avoid intersecting with one of the many rings that surround Uranus. If particles in these rings impact with the spacecraft, it is very likely that it will result in a mission failure. Using this as a guideline, a preliminary value for the pericenter altitude h_p has been set to 2500 km, which is approximately 10% of the planet's equatorial radius (which is 25,559 km). Because the orbit needs to be highly elliptical, a preliminary value for the eccentricity e has been set to 0.90. The apocenter radius can then be determined as follows (in chapter 6 all upcoming calculations will be discussed in detail):

$$r_a = \frac{r_p(1+e)}{(1-e)} = \frac{(R_U + h_p)(1+e)}{(1-e)} = \frac{28059(1+0.90)}{1-0.90} = 533121 \text{ km} \quad (3.1)$$

The semi-major axis a of the orbit then follows from the following equation:

$$a = \frac{1}{2}(r_p + r_a) = \frac{1}{2}(28059 + 533121) = 280590 \text{ km} \quad (3.2)$$

Using the semi-major axis, the time needed to complete a full revolution in the orbit, T , is determined as follows:

$$T = 2\pi\sqrt{\frac{a^3}{\mu_U}} = 2\pi\sqrt{\frac{(280590)^3}{5.794 \cdot 10^6}} = 387971 \text{ s} = 4.49 \text{ days} \quad (3.3)$$

This orbital period can be related to the rotational period of Uranus, using table 3.1:

$$\frac{T}{T_{rotU}} = \frac{4.49}{\frac{17.24}{24}} = 6.25 \quad (3.4)$$

So in the time the spacecraft needs to complete one revolution around Uranus, Uranus itself will have rotated over six times around its rotational axis.

Figure 3.10 shows the example science orbit. The orbit is shown in a Uranus centered pseudo-inertial reference frame. The ring system of Uranus is indicated in red [NASA/JPL, 2009]. For the sake of simplicity they are drawn as circles in the equatorial plane, which is not all that far from reality (see section 3.2).

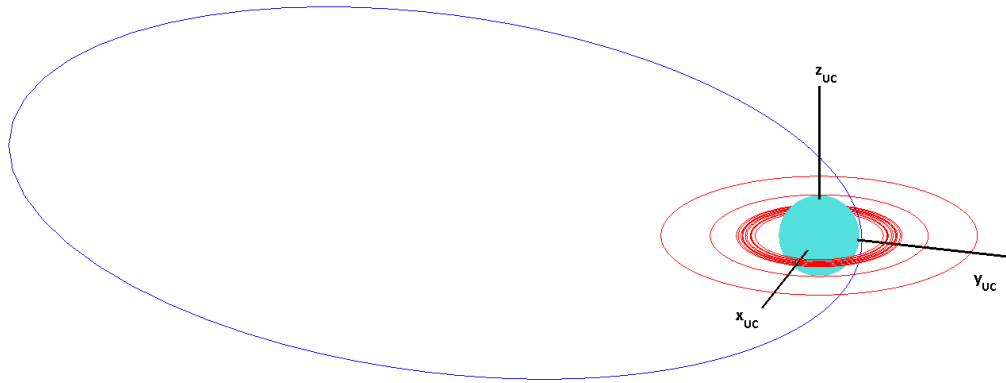


Figure 3.10 Example configuration of the highly elliptic polar orbit within a Uranus centered pseudo-inertial reference frame. The orbit that is shown here lies in the $y_{uc}z_{uc}$ -plane (the index 'UC' indicates Uranus centered).

From this figure it can be concluded that for the chosen science orbit with close pericenter and distant apocenter, the rings should not pose any problems for the mission.

It should be stressed that the orbit chosen for this mission is only a preliminary one. It was stated in chapter 2 that for this thesis research the subject is the optimization of the interplanetary trajectory towards Uranus. The motion of the spacecraft once it is in orbit around Uranus will not be addressed in this report. Therefore subjects like the orientation of the orbit with respect to the Sun, atmospheric effects on the orbit and the effect that Uranus' flattening has on the progression of the orbit will not be covered in this report.

Previous missions to the outer planets

Pioneer 10 was the first spacecraft that traveled through the asteroid belt to reach the outer parts of the solar system. It was also the first spacecraft to use a planetary gravity assist, at Jupiter on 3 December 1973. Pioneer 11 was the second spacecraft to reach the giant planets. It made a flyby at Jupiter on 2 December 1974 and then traveled further to become the first spacecraft to reach Saturn, on 1 September 1979 [NASA/JPL, 2009].

This chapter is intended to give an overview of several interplanetary missions, so that they can give insight into how a mission to Uranus could be performed. The only previous visit to Uranus is described in section 4.1. Missions to two other gas giants, Jupiter and Saturn, will be discussed in sections 4.2 and 4.3. A mission to Pluto which is currently still on its way there, New Horizons, will be addressed in section 4.4. The possible implications and use of these missions will be discussed finally in section 4.5.

4.1 Previous mission to Uranus: Voyager 2

As mentioned in chapter 3, Uranus is located at a very large distance from the Sun (more than 19 times as far as the Earth) and up to now, only one spacecraft has ever traveled to this planet. In January 1986 Voyager 2 made a flyby at Uranus [NASA/JPL, 2009].

4.1.1 Mission overview

Launched in 1977 by Titan 3E-Centaur rockets, Voyager 1 and 2 had as their primary objectives to explore Jupiter, Saturn and their respective moons and ring systems. The spacecraft made many important observations and discoveries there. After completion of the mission objectives (the original duration of both Voyager missions was five years), the mission was extended. Voyager 1 flew out of the ecliptic plane and is now leaving the solar system. After its visit to Saturn, Voyager 2 was first sent to Uranus and later it flew onwards to Neptune. At the Uranus flyby, Voyager 2 gathered many data on its planetary system and made a

large amount of pictures. In August 1989 Voyager 2 made a flyby at Neptune and now it is heading out of the solar system below the ecliptic plane [NASA/Voyager, 2009].

4.1.2 Spacecraft overview

A picture of the Voyager spacecraft is shown in figure 4.1 (Voyager 1 and 2 are identical).



Figure 4.1 The Voyager spacecraft [NASA/Voyager, 2009].

The main characteristics of the spacecraft itself are given below [NASA/Voyager, 2009].

- **Size:** 3.7 m high gain antenna, Magnetometers extend to nearly 13 m.
- **Mass:** At launch 2100 kg, during the mission 825 kg, payload mass 105 kg.
- **Power:** Three radioisotope thermoelectric generators with power level of 315 W (2003).
- **Propulsion:** One large solid-propellant motor and 24 small hydrazine thrusters [Schatz et al., 1979] (there is no information available on thrust levels and specific impulse).
- **Science instruments:** Dual cameras, infrared spectrometer and radiometer, ultraviolet spectrometer, photopolarimeter, plasma detector, low-energy charged particle detector, cosmic ray detector, magnetometer, planetary radio astronomy, plasma wave detector.
- **Cost:** The total cost of the Voyager program from May 1972 through the Neptune encounter in 1989 (including launch vehicles, nuclear-power-source RTGs, and DSN tracking support) is \$865 million.

Next to the scientific payload both Voyager spacecraft also carried a gold-plated copper disk with them. These have images and sounds on them to show what our world looks like, if the spacecraft would ever be found by extraterrestrials.

4.1.3 Trajectory

The interplanetary journey of both spacecraft is shown in figure 4.2. The figure shows the dates of the gravity assists and their respective orbits out of the solar system.

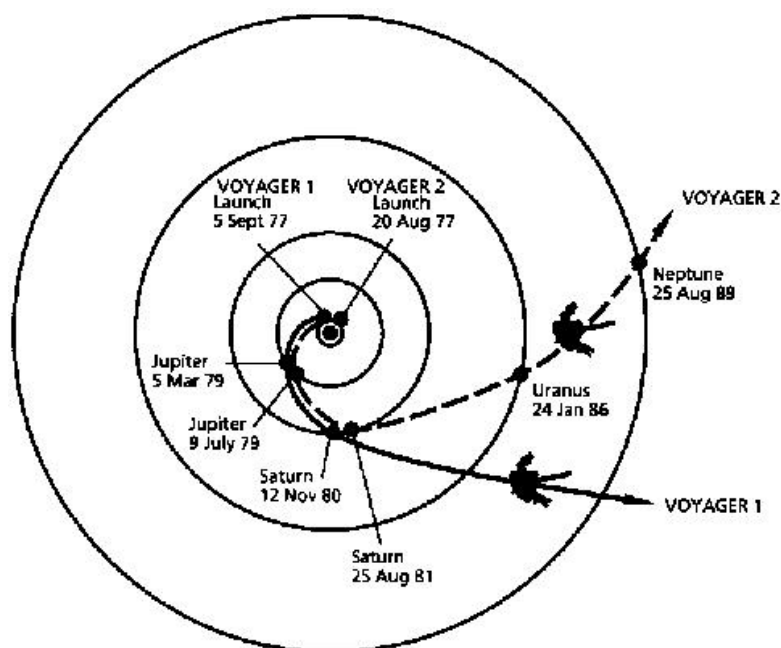


Figure 4.2 The journey of the Voyager spacecraft [NASA/Voyager, 2009].

4.2 Jupiter mission: Galileo

The NASA Galileo spacecraft was launched on 18 October 1989. The primary focus of this mission was to investigate the Jovian system and send a probe into the atmosphere of the solar system's most massive planet [NASA/Galileo, 2007].

4.2.1 Mission overview

After its deployment from the Space Shuttle Atlantis, the Galileo orbiter and probe traveled together to Jupiter and in July 1995 the probe was detached from the orbiter. Five months later the probe entered Jupiter's atmosphere with a stunning velocity of nearly 48 km/s (over 170,000 km/h). It slowed down, released its parachute and dropped its heat shield. From that moment on, the probe had a 58 minute journey through the atmosphere of Jupiter. It collected data and sent it to the orbiter, eventually melting and vaporizing in the extreme heat of the Jovian atmosphere [NASA/Galileo, 2007].

Next, the orbiter was inserted into orbit around Jupiter, starting its primary mission on 7 December 1995. Its objective was to study the Jovian system for



Figure 4.3 A picture of Jupiter taken in 2000 by the Galileo spacecraft [NASA/JPL, 2009].

two years. After its primary objectives were completed on 7 December 1997, the mission was extended since Galileo was capable of more. Galileo went on to make several very close flybys of the moons Europa and Io. The spacecraft was decommissioned on 21 September 2003, disintegrating in Jupiter's atmosphere [NASA/Galileo, 2007].

4.2.2 Spacecraft overview

As mentioned earlier, the Galileo spacecraft consisted of a Jovian orbiter and a probe that was sent in its atmosphere. The general layout of the spacecraft is depicted in figure 4.4.

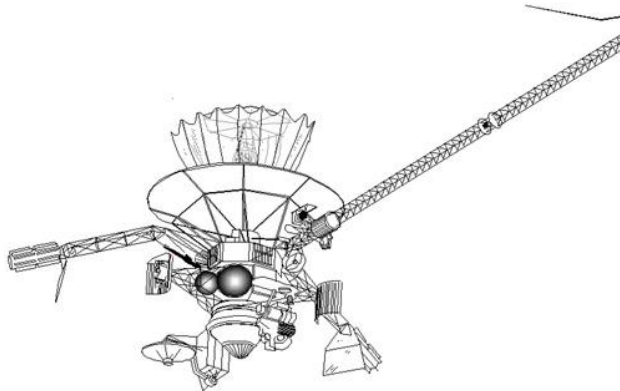


Figure 4.4 Layout of the Galileo spacecraft [NASA/Galileo, 2007].

The most important characteristics of the spacecraft are listed below [NASA/Galileo, 2007].

- **Orbiter:**

- **Size:** 5.3 m high, magnetometer boom extends 11 m to one side.
- **Mass:** 2,223 kg, including 118 kg of science instruments and 925 kg of propellant.
- **Power:** 570 W at launch from radioisotope thermoelectric generators.
- **Propulsion:** Bipropellant system with a single 400 N bipropellant engine ($I_{sp} = 303$ s) and twelve 10 N thrusters (the fuel is MMH and the oxidizer is N_2O_4) [EADS, 2009].
- **Science instruments:** Solid-state imaging camera, near-infrared mapping spectrometer, ultraviolet spectrometer, photopolarimeter radiometer, magnetometer, energetic particles detector, plasma investigation, plasma wave subsystem, dust detector, heavy ion counter.

- **Atmospheric probe:**

- **Size:** 127 cm diameter, 91 cm high.
- **Mass:** 339 kg, of which 33.4 kg science instruments.
- **Science instruments:** Atmospheric structure instrument, neutral mass spectrometer, nephelometer, lightning and radio emissions detector/energetic particles instrument, helium abundance detector, net flux radiometer.

- **Program:**

- **Cost:** Total from start of planning through end of mission is \$1.39 billion. International contribution estimated at an additional \$110 million.

4.2.3 Trajectory

The booster rocket on board the spacecraft was not powerful enough to send it directly to Jupiter. In order to get to Jupiter several gravity assists (see section 8.4 for more details) were performed. The route that was taken became known as the 'Venus Earth Earth Gravity Assist' or VEEGA. So using the gravitational attraction of first Venus and then twice of Earth, the spacecraft gained enough momentum to reach Jupiter. On its way to Jupiter, in 1994, Galileo was in perfect position to watch the impact of comet Shoemaker-Levy 9 on Jupiter. The interplanetary trajectory is shown in figure 4.5.

The elliptic orbits it performed around Jupiter allowed for close flybys of several of its moons and for monitoring different parts of its extensive magnetosphere. After the mission was extended, the first focus was on Jupiter's moon Europa. The additional observations during the Europa flybys supported the idea that an ocean of water currently exists below its surface. After the Europa flybys, the focus shifted to Io, the innermost moon of Jupiter. The radiation environment there is extremely intense and dangerous to spacecraft components, so these orbits were saved for last.

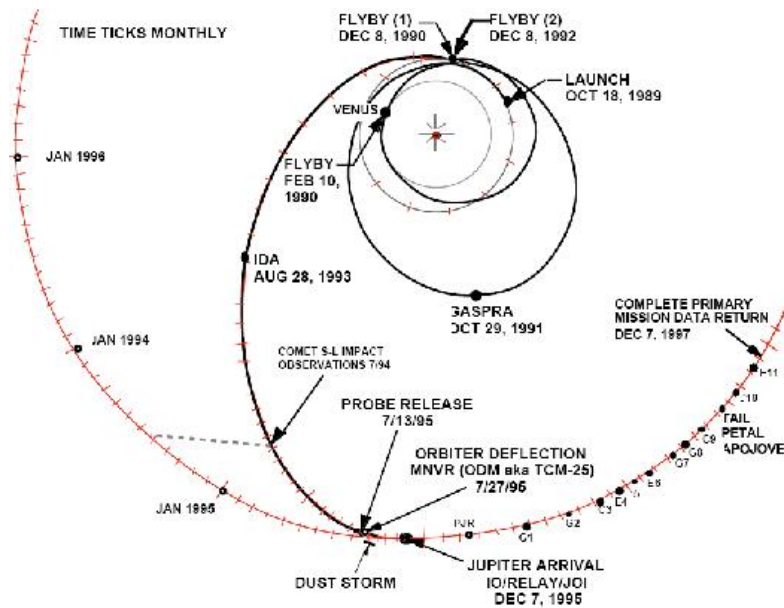


Figure 4.5 Galileo's interplanetary trajectory to Jupiter [NASA/Galileo, 2007].

4.3 Saturn mission: Cassini-Huygens

Cassini-Huygens is the mission to investigate the rings and moons of Saturn and to send a probe into the atmosphere of Saturn's moon Titan and land on its surface. It is a joint three space agency mission, launched on 15 October 1997 by Titan IV-B/Centaur launcher. The Cassini orbiter was developed by NASA's Jet Propulsion Laboratory (JPL), the European Space Agency was responsible for the Huygens probe and the Italian Space Agency provided the high gain antenna. The information in this section has been obtained from [NASA/Cassini, 2009].

4.3.1 Mission overview

Saturn was the next obvious target after the success of the Galileo mission to Jupiter. For many centuries people have been fascinated by this planet with its distinct ring system (see figure 4.6). The list of scientific objectives for the Saturnian system was very extensive for the planet itself, its moons (and for this mission Titan in particular), its rings and its magnetosphere [NASA/Cassini, 2009].

The primary mission of the Cassini orbiter was to make observations of Saturn's planetary system for a period of four years. During this period Cassini made over 70 orbits around Saturn and its moons. The primary mission ended in June of 2008, but the spacecraft was still capable of continuing the mission. The Cassini mission was therefore extended and renamed the Cassini Equinox mission [NASA/Cassini, 2009].

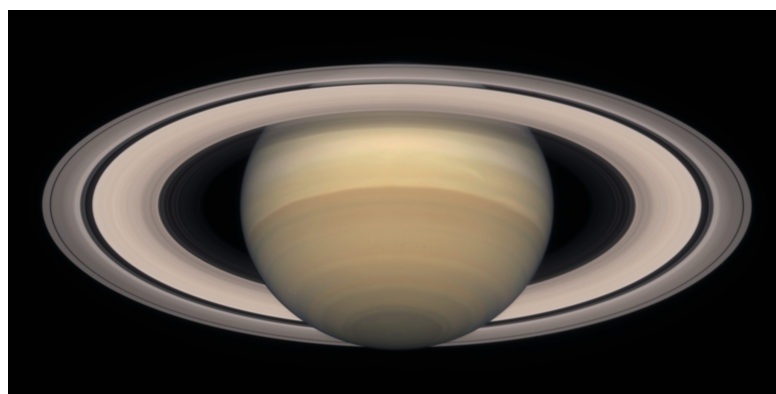


Figure 4.6 A picture of Saturn taken on 9 February 2004 taken by the Cassini spacecraft [NASA/JPL, 2009].

The Cassini Equinox mission for now is set to end in September 2010. In August of 2009 the Sun will shine directly over Saturn's equator, hence the name Equinox. After the Saturn equinox the Sun will start to shine on the planet's northern hemisphere and the north face of its rings. The Cassini orbiter will observe the seasonal changes on the planet, its rings and moons, which were illuminated from the south during the primary mission [NASA/Cassini, 2009].

4.3.2 Spacecraft overview

Figure 4.7 shows the general lay-out of the Cassini-Huygens spacecraft.

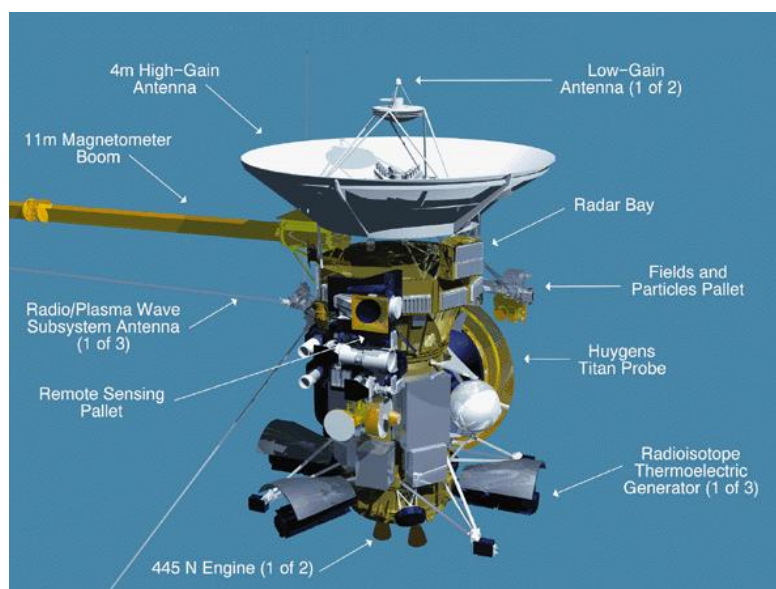


Figure 4.7 The Cassini-Huygens spacecraft [NASA/Cassini, 2009].

The most important specifications and characteristics of the Cassini orbiter and the Huygens probe are given below [NASA/Cassini, 2009].

- **Orbiter:**

- **Size:** 6.7 m high, 4 m wide.
- **Mass:** 5,712 kg with fuel, Huygens probe, adapter, etc. 2,125 kg unfueled orbiter alone, payload mass 279 kg.
- **Power:** 885 W (633 W at end of mission) from radioisotope thermoelectric generators.
- **Propulsion:** Two 445 N bipropellant engines ($I_{sp} = 308$ s) of which one is a backup (the fuel is MMH and the oxidizer is N_2O_4), and sixteen 1 N monopropellant hydrazine thrusters [MAPSView, 2006].
- **Science instruments:** Composite infrared spectrometer, imaging system, ultraviolet imaging spectrograph, visual and infrared mapping spectrometer, imaging radar, radio science, plasma spectrometer, cosmic dust analyzer, ion and neutral mass spectrometer, magnetometer, magnetospheric imaging instrument, radio and plasma wave science.

- **Huygens probe:**

- **Size:** 2.7 m in diameter.
- **Mass:** 320 kg, of which 49 kg science instruments.
- **Science instruments:** Aerosol collector pyrolyser, descent imager and spectral radiometer, Doppler wind experiment, gas chromatograph and mass spectrometer, atmospheric structure instrument, surface science package.

- **Program:**

- **Cost:** \$1.422 billion pre-launch development; \$710 million mission operations; \$54 million tracking; \$422 million launch vehicle; \$500 million ESA; \$160 million ASI; total about \$3.27 billion, of which U.S. contribution is \$2.6 billion and European partners' contribution \$660 million.

4.3.3 Trajectory

After separation from the launch vehicle, the Cassini orbiter together with the Huygens probe traveled for seven years before reaching Saturn. On its way it performed four gravity assist maneuvers. First the spacecraft made two flybys at Venus, then it had a flyby at Earth and it was sent to Saturn after it had gained momentum at a Jupiter swingby. The trajectory, known as the Venus Venus Earth Jupiter Gravity Assist (or VVEJGA) is depicted in figure 4.8.

In July 2004 the spacecraft went into orbit around Saturn. A few months later, in December of 2004, the Huygens probe was released from Cassini and began its journey to Titan. It coasted for 20 days, after which the probe descended into Titan's thick atmosphere on 14 January 2005. It landed two and a half hours later on Titan's surface with the aid of parachutes.

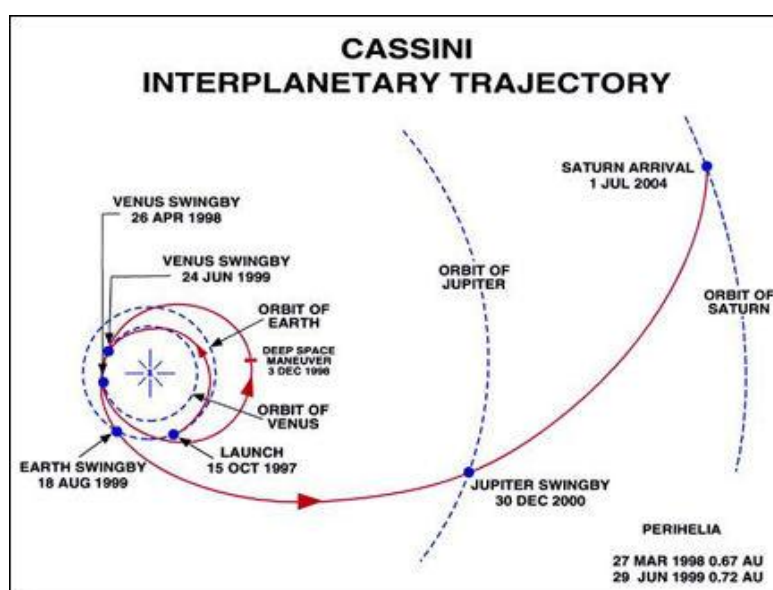


Figure 4.8 The trajectory of the Cassini-Huygens spacecraft [NASA/Cassini, 2009].

4.4 Pluto Mission: New Horizons

In August of 2006 it was decided by the International Astronomical Union that Pluto was no longer considered a planet, but instead it was assigned the status of dwarf planet [ScienceDaily, 2006]. At that time NASA's New Horizons spacecraft to Pluto and its moon Charon (and perhaps later on the Kuiper Belt) was already on its way.

4.4.1 Mission overview

The New Horizons spacecraft was launched on 19 January 2006 by an Atlas V 551 rocket (Lockheed Martin) which was aided by a Star 48-B third stage (Boeing) to increase the heliocentric velocity with an additional 4 km/s, sending the spacecraft into a solar escape trajectory. It was the first ever Atlas V launch with an external third stage. The New Horizons launch was also the first time that five solid rocket boosters were added to the main engine, where three was the previous maximum [NASA/JHU-APL, 2006].

In February 2007 the spacecraft made its only planetary swingby, at Jupiter. At present, the New Horizons spacecraft is in between the orbits of Saturn and Uranus and is expected to pass the orbit of the latter in March 2011 (see also figure 4.10) [NASA/JHU-APL, 2009].

After a period of 'hibernation' the spacecraft will conduct a study of the Pluto system for five months. The surface of Pluto and Charon will be studied in terms of composition, geomorphology and global geology. Pluto's atmospheric composition and structure will also be studied carefully. New Horizons will not go into orbit around Pluto, but it will make a flyby and if the spacecraft is still healthy after

completing the main mission, it will fly on into the Kuiper Belt [NASA/JHU-APL, 2009].

4.4.2 Spacecraft overview

A picture of the New Horizons spacecraft is shown in figure 4.9.

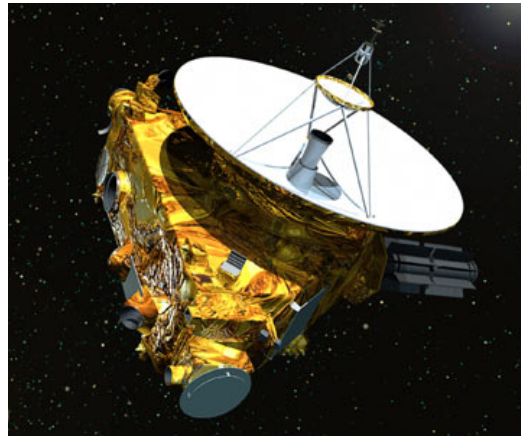


Figure 4.9 The New Horizons spacecraft [NASA/JPL, 2009].

The most important characteristics of the New Horizons spacecraft are listed below [NASA/JHU-APL, 2006].

- **Size:** 0.7 m high, 2.1 m long and 2.7 m wide.
- **Mass:** The mass of the probe is 478 kg, of which 77 kg propellant and 30 kg science instruments.
- **Power:** 240 W at start of mission, provided by a radioisotope thermoelectric generator. Power decrease is about 3.5 W each year.
- **Propulsion:** There are four 4.4 N thrusters used for course corrections and twelve 0.8 N smaller thrusters for attitude control (there is no information available on the specific impulse of the thrusters).
- **Science instruments:** Ultraviolet imaging spectrometer, visible and infrared camera, long-range telescopic camera, particle spectrometers, a detector to measure masses of space-dust particles, two copies of a radio science experiment to examine atmospheric structure, surface thermal properties and mass.
- **Cost:** Approximately \$700 million (including spacecraft and instrument development, launch vehicle, mission operations, data analysis, and education/public outreach) over the period 2001-2016.

4.4.3 Trajectory

The interplanetary trajectory of New Horizons and its position in the solar system on 20 May 2009 is shown in figure 4.10.

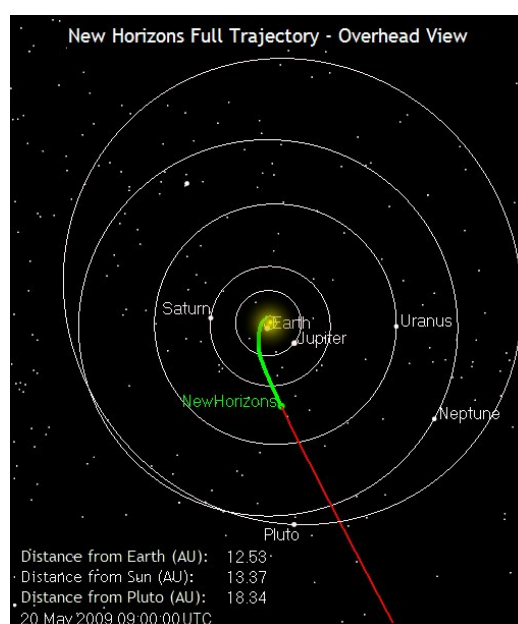


Figure 4.10 The New Horizons interplanetary trajectory. The green part has been covered already by New Horizons (as of 20 May 2009) and the red part is the trajectory that has not been covered yet [NASA/JHU-APL, 2009].

The New Horizons spacecraft approached Jupiter after 13 months (Galileo and Cassini took 6 and 4 years respectively) with a velocity of 21 km/s relative to Jupiter. Flying by Jupiter at a distance of 2.27 million kilometers, New Horizons gained an extra 4 km/s on its way to Pluto [NASA/JHU-APL, 2006].

In order to accomplish the mission's scientific objectives the spacecraft will have to fly through a very narrow circle of about 300 km in diameter near Pluto, so precise orbit determination and control is vital.

4.5 Implications for a mission to Uranus

The missions described in this chapter provide some insight in what a mission to the planetary system of Uranus may look like. They are high-thrust missions and use gravity assists to change the velocity vector in terms of magnitude and direction. These concepts will be outlined further in chapter 8.

What stands out in terms of the gravity assists, is that the spacecraft that go beyond the asteroid belt don't use Mercury as a flyby planet and also Mars is not used. Earth and Venus are the primary gravity assist planets to reach Jupiter in the terrestrial planet system. All missions considered in this chapter have gone beyond Jupiter and they all performed a gravity assist there. This is because Jupiter is an excellent planet for performing gravity assists. Why all of this is the case will be explained in more detail in section 8.4.2.

In the thesis work of Ramon Schlijper, a former student at Delft University of Technology, a comparison has been made of the payload to dry mass ratio for several interplanetary spacecraft [Schlijper, 2003]. It was found that on average the payload mass was 11% of the spacecraft dry mass with an error margin of 3%. The missions described here are in accordance with this number, see table 4.1. The payload mass fraction of New Horizons is slightly below the lower bound at 7.5%, and for the Galileo probe it is slightly higher, 15.3%.

Mission	$\frac{m_{payload}}{m_{dry}}$ (%)
Voyager 1/2	12.7
Galileo (orbiter)	9.1
Galileo (probe)	9.9
Cassini (orbiter)	13.1
Huygens probe	15.3
New Horizons	7.5

Table 4.1 Percentage of the payload mass with respect to the dry mass for the interplanetary spacecraft considered in this chapter.

Several types of instruments are placed on each of the spacecraft that has been considered in this chapter.

- Spectrometers for different wavelengths (from ultraviolet to the near infrared). They are used to learn more about the composition of atmospheres, surfaces and rings.
- Magnetometers are used to measure the strength and the direction of the planet's magnetic field.
- Plasma detectors are used to measure the density, composition, distribution, velocity and temperature of plasmas (low density gases where some of the particles are ionized) in a magnetosphere.
- Imaging devices for different wavelengths, so that (parts of) the planet, its rings or moons are photographed.
- Radio science experiments in order to measure atmospheric temperature and pressure.

In section 5.3 the instruments that will form the baseline for the spacecraft heading to the planetary system of Uranus are discussed, including a first estimate of their mass and required power.

Characteristics of the Uranus orbiter spacecraft

In the previous chapters the characteristics for a mission to Uranus have been outlined and previous missions to the outer planets have been discussed. In this chapter a closer look is taken into the propulsion system that is required for the high thrust mission to Uranus, the means to generate electrical power on board the spacecraft as well as a preliminary selection of payload instruments. It has to be stressed that it is not the intention to make a detailed design of the spacecraft, but just to characterize the different options.

For this thesis work, the spacecraft is assumed to start from a GTO. Therefore there will be no discussion on launch vehicles. Details on different launch vehicles, their performance and costs can be found in the literature study that was performed prior to this thesis [Molenaar, 2007].

This chapter is structured as follows. Section 5.1 will cover the different types of propellant needed for high thrust propulsion systems, as well as some engine characteristics, like the thrust force F and specific impulse I_{sp} . Then, in section 5.2, the focus will be on generating electrical power on board of the spacecraft. In section 5.3 a preliminary selection of scientific payload instruments will be given. Finally, the chapter is concluded by a short summary and a preliminary choice for the propulsion system, power generation and payload instruments.

5.1 Chemical propulsion systems

The most commonly used propulsion method in space applications is chemical propulsion. The energy that is needed to achieve velocity increments is stored in the propellant itself. This immediately poses the restriction that no more energy can be extracted than what is contained within the propellant. In order to reach the outer planets gravity assists are commonly used to add energy to the spacecraft.

5.1.1 Propellant types

Three main types of propellants can be distinguished: liquid propellants, solid propellants and hybrid propellants (as can be expected this is a combination of the former two) [Larson and Wertz, 1999]. Typically, when solid fuel is ignited, it will keep on burning until the propellant is all burnt up. Hybrid rockets have some very attractive features, like throttling capability, but they have not been used much. Therefore, liquid propellant is the preferred option when using chemical propulsion.

The exhaust velocities of liquid propellant rocket engines are limited to about 4.5 km/s resulting in specific impulses that do not exceed 450 s [Turner, 2005]. Thrust levels for liquid propellant rocket engines vary from a few N for attitude control to several MN for launchers.

For liquid propellant rockets there is a distinction between mono-propellant and bi-propellant rockets. A mono-propellant is a liquid containing both the fuel and the oxidizing agents (either in one molecule or as a mixture) [Zandbergen, 2004]. The thrust F and specific impulse I_{sp} that liquid mono-propellant systems can achieve are too low to be of practical use for a mission to Uranus, which will require significant ΔV maneuvers [Larson and Wertz, 1999]. With a bi-propellant system the fuel and oxidizer are separate substances stored in separate tanks [Zandbergen, 2004]. Bi-propellant systems achieve a higher performance, making them suitable for using in orbit maneuvers requiring a large ΔV .

5.1.2 Characteristics

The change in momentum is equal to the force acting on the body over a certain time t_a :

$$\int_0^{t_a} \bar{F} \cdot dt = \int d(M \cdot \bar{V}) \quad (5.1)$$

Considering that a rocket does not have a constant mass, after some steps one arrives at the famous rocket equation derived by Konstantin Tsiolkowski (1857-1935):

$$\Delta V = w \ln \frac{m_0}{m_f} \quad (5.2)$$

It describes the total velocity increment ΔV as a function of the effective exhaust velocity w , the rocket's start mass m_0 and the empty mass m_f . It was assumed that the burn time of the rocket is short enough to consider it as an impulsive shot and furthermore there are no external forces acting on the rocket.

The thrust F and specific impulse I_{sp} in vacuum, two key parameters of a rocket engine, are defined as follows [Zandbergen, 2004]:

$$F = \dot{m}w \quad (5.3)$$

$$I_{sp} = \frac{w}{g_0} \quad (5.4)$$

In the thrust equation the mass flow is denoted by \dot{m} and the gravitational acceleration at sea level is denoted by g_0 . It can be seen from the expressions for F , I_{sp} that a high exhaust velocity leads to a high thrust force and a high specific impulse. Also, when considering equation 5.2, it can be deduced that the higher exhaust velocity, the higher the ΔV that can be achieved for the same ratio $\frac{m_0}{m_f}$.

5.2 Generating electrical power

The payload instruments and the bus systems on board the spacecraft have to be supplied with electrical power for them to work. There are a number of ways through which electrical power can be generated on board of a spacecraft. Three possibilities are discussed here:

- Solar electric power by using solar cells.
- Radioisotope thermoelectric power by using radioisotope thermoelectric generators (RTGs).
- Nuclear electric power by using a nuclear fission reactor.

Solar electric power

The main advantages of using solar cells is that solar energy is readily available in space and the technology has been proven on many missions in the past. However, there are quite some drawbacks when using solar cells [Turner, 2005]. First of all, there is a maximum efficiency of about 26% that can be obtained with current solar cell technology [Larson and Wertz, 1999].

Secondly, as the spacecraft moves away from the Sun, the solar irradiance decreases by the square of the distance (see also section 7.4). So the amount of power that can be extracted from solar energy decreases as well. The decrease is not by the square of the distance but slightly less (to the power 1.5), because the efficiency of the solar cells increases with decreasing temperature [Fortescue and Stark, 1995]. Therefore it seems unrealistic for outer planet spacecraft to use this type of power generation, keeping in mind the power demands of the payload and support systems. Solar cells are also sensitive to radiation damage, so there is always some degree of degradation. Solar arrays therefore have to be overdimensioned, adding to the mass of the spacecraft [Turner, 2005].

It can be concluded that using solar cells to generate electrical power is not a feasible option for a mission to Uranus.

Radioisotope thermoelectric power

RTGs have been used on all outer planet missions so far. The lack of solar energy induced the need for other means of generating electrical power. An RTG uses the heat that is produced in the radioactive decay of a particular element. The most widely adopted isotope for this is Plutonium-238, which has a half-life of 80 years [Turner, 2005].

The thermoelectric generators convert the heat into electrical energy, but the efficiency of this process is no more than 6%. The mass-to-power ratio is very high for current RTGs, but they currently are the only means to generate electrical power in the outer solar system [Turner, 2005]. This is also confirmed by observing that all outer planet missions discussed in chapter 4 had one or more RTGs on board.

Current developments in RTGs have led to the use of mechanical generators to convert the heat of the radioactive decay into electrical power (Stirling Radioisotope Generators). The increase in efficiency that can be obtained is significant (fivefold to sevenfold). This technology is not yet ready to be implemented in space missions, but it is predicted that it will become the standard for RTG use in space [NASA/GRC, 2005].

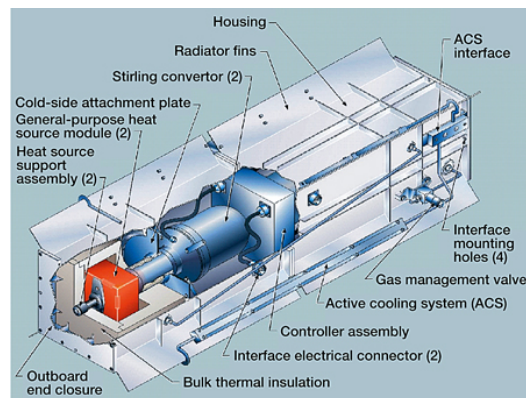


Figure 5.1 Stirling Radioisotope Generator [NASA/GRC, 2005].

Nuclear electric power

The energy that is released with nuclear fission of for example uranium is about 70 times as high as the energy released with the radioactive decay of plutonium. The power output for uranium fission is controllable, whereas for radioactive plutonium decay it is not. Furthermore uranium is very cheap compared to plutonium. So these are all things that work in favor of uranium fission. There are, however, major drawbacks to the use of nuclear fission reactors. The major

drawback is safety related. It is important to make sure that there are no human and environmental risks involved, and even then public opinion might be strongly against it. It should be noted, however, that the reactor core can be launched in an inert state and be turned on when it is in orbit. So the material would not be radioactive until the reactor has been operated [Turner, 2005]. The second drawback of using nuclear fission reactors is their large mass (radiative shielding and thermal control are the major contributors) [Kemble, 2006].

5.3 Payload science instruments

It is not the intention to make a complete spacecraft design, since the focus is on the spacecraft trajectory. Only the scientific instruments, that most likely will be present on the spacecraft, will be discussed.

In section 4.5 a number of types of instruments were listed that were present on other missions to the outer planets. The focus in this section will be on instruments that can be applied for a mission to the planetary system of Uranus, such that the scientific objectives discussed in section 3.4 can be fulfilled. Recently developed and (perhaps in the near future) deployed instruments will serve as a baseline.

Plasma detector

Messenger, NASA's mission to Mercury (launched on 3 August 2004), has an instrument on board that consists of an energetic particle spectrometer and a fast imaging plasma spectrometer. This instrument called EPPS (Energetic Particle and Plasma Spectrometer) will measure energetic ions, electrons and thermal plasmas. The data that are collected will provide insight into the structure and the dynamics of the magnetosphere [Gold, 2001]. Since this is also one of the scientific objectives for a mission to Uranus, it makes sense to use this instrument as a baseline. It has a mass of 2.25 kg and an input power of 2.0 W.

Spectrometer and solar occultation instrument

On 9 November 2005 the Venus Express satellite was launched, ESA's first satellite to Venus. One of the instruments on board is the SPICAV (SPectroscopy for Investigation of Characteristics of the Atmosphere of Venus). This instrument has different channels for observing UV wavelengths, IR wavelengths and a channel to observe the Sun at longer IR wavelengths (SOIR, or Solar Occultation at InfraRed). The mass of this instrument is 13.9 kg and it has a maximum input power of 51.4 W [Bertaux, 2007].

The principle behind solar occultation is that the Sun is viewed through the atmosphere, so the sunlight travels through a large atmospheric path when compared to other means of remote atmospheric sensing. The measured spectra can indicate what isotopes and other minor species at different altitudes [Bertaux, 2007].

Imaging device

On board Venus Express the Venus Monitoring Camera (VMC) is mounted. One of the scientific objectives of Venus Express, as well as for this mission to Uranus, is to study the dynamics of the Venus atmosphere. Therefore it makes sense to use this instrument as a baseline. It has an input power of about 4 W and a mass of 1.1 kg.

Gravimeter

At the end of 2011 the second NASA New Frontiers mission (New Horizons was the first) will commence with the launch of the Juno spacecraft. It will use solar electric propulsion to go into a polar orbit around Jupiter with a close perijove. One of the payload instruments that will be used is the Gravity Science Experiment (GSE). This instrument will make detailed measurements of the complete gravity field of Jupiter so that its interior structure can be determined. Its mass is incorporated with the telecommunications subsystem and therefore it will not contribute as such to the payload mass and input power [Dodge and Boyles, 2007].

This instrument is particularly attractive because a polar orbit around Uranus is a desired science orbit. Next to this, the interior structure of Uranus is unknown up to this point, so it makes sense to use it. Furthermore, the instrument might be used to make measurements of the interior structure of the planet's main moons.

Radiometer

In order to probe the deep atmosphere of Uranus an instrument is required that measures the planet's thermal emissions at different wavelengths. This can be done by incorporating multiple radiometers, each one measuring at a different wavelength, typically in the order of 1 to 50 cm. The MicroWave Radiometer that will be used in the earlier mentioned Juno mission will serve as a baseline, measuring at six different wavelengths. It has a mass of 42.13 kg and an input power of 32.6 W [Dodge and Boyles, 2007].

Magnetometer

The magnetometer that will be used as a baseline for the Uranus polar orbiter mission is the Flux Gate Magnetometer that will be used in the Juno mission. It has a mass of 15.25 kg and a maximum power input of 12.5 W [Dodge and Boyles, 2007].

5.4 Preliminary layout of the spacecraft

A number of options have been considered and discussed for the spacecraft propulsion system, power generation and the payload instruments. This section will present an overview of the feasible options for the Uranus mission.

Chemical propulsion

Solid and hybrid propellant rocket engines have been excluded from the propulsion system trade-off, as discussed earlier in section 5.1.1. Only liquid rocket engines are considered. Mono-propellant liquid rocket engines are simple, reliable and cheap, but have low performance. Bi-propellant liquid rocket engines have high performance, but the system is more complicated. Both Galileo and Cassini used a bi-propellant propulsion system for their main engines. The fuel used was MMH and the oxidizer was N_2O_4 . Because of its better performance and because it has been used in missions to Jupiter and Saturn, a bi-propellant propulsion system is preferred over a mono-propellant system.

Electrical power generation

In terms of power supply systems, solar cells are not feasible in the outer planet regions, but perhaps a hybrid solution can be obtained. First, in the inner part of the solar system, solar panels are used for electric power generation. Then the solar panels are jettisoned somewhere along the trajectory. Another power source, for example one or more SRGs (Stirling Radioisotope Generators) can then be used. Such a hybrid system will add complexity to the propulsion system though, which is undesirable and will therefore not be used for this mission.

Nuclear fission reactors have many benefits for long duration, high power missions. It is questionable, however, whether nuclear fission reactors will become operational for space missions in the near future. Next to this, the public opinion towards nuclear fission reactors might enforce the use of other power generators because of safety and environmental issues. Therefore, it will not be considered as a power generation option for this mission to Uranus.

Radioisotope thermoelectric generators are the only current means of power generation in the outer parts of the solar system. The new SRGs will provide significant mass and performance benefits over conventional RTGs [NASA/GRC, 2005]. The power levels generated are in the range 100-200 W.

Payload instruments

Table 5.1 gives an overview of all payload instruments in terms of their mass and input power.

Instrument	Mass (kg)	Input power (W)
Plasma detector	2.25	2.0
Spectrometer/S.O.I.*	13.90	51.4
Imaging device	1.10	4.0
Radiometer	42.13	32.6
Magnetometer	15.25	12.5
Total	74.63	102.5

Table 5.1 Preliminary selection of payload instruments that can be used for a Uranus orbiter mission (* Solar Occultation Instrument)

In section 4.5 it was mentioned that the payload mass is approximately 11% of the spacecraft's dry mass. Based on the total payload mass in table 5.1, the spacecraft's dry mass will be 678.45 kg. It should be noted that in the remainder of this thesis research no further attention will be paid to the spacecraft itself. The focus will be entirely on the trajectory that will be flown. Since the analysis of the trajectory will only involve analytical techniques, as will become clear throughout part II, the spacecraft mass will not be an issue.

Part II: Orbital Mechanics

Principles of orbital mechanics

In order to determine the trajectory to Uranus, the underlying principles of orbital mechanics have to be fully understood. This chapter gives an overview of these principles, starting from the general case of the many-body problem in section 6.1. The two-body problem is derived from the many-body problem and it is discussed in section 6.2.

6.1 The many-body problem

All objects exert forces on each other. Isaac Newton (1643-1727) was the first to make formulation of the resulting system of equations of motion [Wakker, 2002].

6.1.1 Newton's laws of motion and gravitational law

In his world famous work *Philosophiae Naturalis Principia Mathematica* (published in 1687) Newton formulated three laws of motion and a gravitational law [Wakker, 2002]:

- Newton's first law states that every point mass continues in its state of uniform motion in a straight line or remains at rest with respect to an inertial reference frame, unless it is compelled to change that state by forces acting upon it.
- Newton's second law states that for a point mass, the time derivative of linear momentum with respect to an inertial reference frame is equal to the resulting force of all forces that act on that body. When put into an equation, this yields (for a body with constant mass):

$$\vec{F} = m \frac{d\vec{V}}{dt} = m \frac{d^2\vec{r}}{dt^2} \quad (6.1)$$

- Newton's third law states that if two point masses exert forces on each other, these forces are equal in magnitude and opposite in direction (action = reaction).
- Newton's gravitational law states that two particles attract each other with a force, acting along the line joining them, proportional to their masses, mass m_1

and m_2 respectively, and inversely proportional to the square of the distance r between them.

$$\bar{F} = G \frac{m_1 m_2 \bar{r}}{r^2 r} \quad (6.2)$$

In this equation G is the universal gravitational constant ($G = 6.668 \cdot 10^{-11} \text{ Nm}^2/\text{kg}^2$), and \bar{r} is the vector pointing from body 1 to body 2 (see also figure 6.1).

An inertial reference frame is a frame with respect to which a point mass is in rectilinear motion, or is in rest when no force is exerted on it. The many-body problem is formulated when Newton's second law and his gravitational law are equated [Wakker, 2002].

6.1.2 A system of n bodies

In a system of n bodies, body i has mass m_i and coordinates x_i , y_i and z_i with respect to an inertial reference frame. The other bodies in the system are denoted with mass m_j , and coordinates x_j , y_j and z_j . This is shown in figure 6.1.

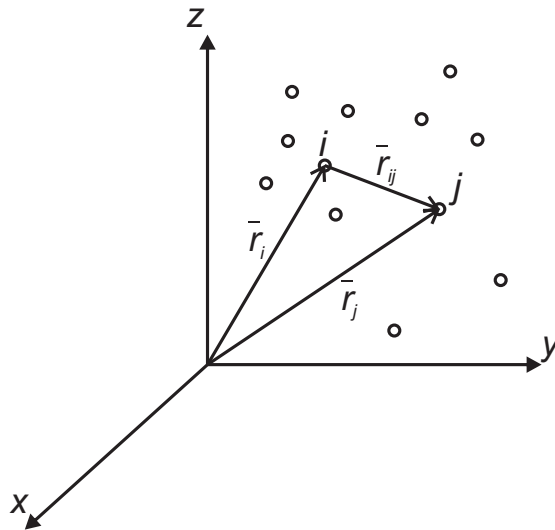


Figure 6.1 A system of n bodies, after [Wakker, 2002].

In this figure:

$$\bar{r}_{ij} = \bar{r}_j - \bar{r}_i \quad (6.3)$$

$$r_{ij} = |\bar{r}_{ij}| = \sqrt{(x_j - x_i)^2 + (y_j - y_i)^2 + (z_j - z_i)^2} \quad (6.4)$$

When Newton's second law and Newton's gravity law are combined, then it holds for body i :

$$m_i \frac{d^2 \bar{r}_i}{dt^2} = \sum_{j=1}^* G \frac{m_i m_j}{r_{ij}^3} \bar{r}_{ij} \quad (6.5)$$

The summation goes from $j = 1$ to $j = n$, but excluding $j = i$ (this is indicated by the $*$). There are n bodies, but $3n$ equations of motion, a system that can not be solved analytically in general. For this equation it is assumed that there are no other bodies outside the n -body system and that there are only mutual attraction forces between the bodies. The motion of body i is described with respect to an inertial reference frame. In reality one can not take all universal matter into account, so that is why the concept of a pseudo-inertial reference frame is introduced, in which the accelerations and rotations of this frame are neglected intentionally.

6.1.3 Motion of a body with respect to another body

For most practical purposes the motion of a body with respect to other bodies is of prime interest. For a body i that moves about a body k the following expression for the acceleration of body i can be derived [Wakker, 2002]:

$$\ddot{\bar{r}}_i = -G \frac{m_i + m_k}{r_i^3} \bar{r}_i + G \sum_{j=1}^* m_j \left(\frac{\bar{r}_j - \bar{r}_i}{r_{ij}^3} - \frac{\bar{r}_j}{r_j^3} \right) \quad (6.6)$$

This equation describes the motion of body i with respect to a non-rotating reference frame with body k as its origin, under the influence of all attracting forces between i , j and k . The second term on the right hand side of equation 6.6 describes the disturbing acceleration. It can be derived that there exists a maximum for the ratio between the acceleration caused by a disturbing body (index ' d ') and the acceleration of the main body (index ' m ') [Wakker, 2002]:

$$\left(\frac{a_d}{a_m} \right)_{max} = 2 \frac{m_d}{m_m} \left(\frac{r_s}{r_d} \right)^3 \quad (6.7)$$

In this equation m_d is the mass of the disturbing body, m_m is the mass of the central body, r_s is the distance of the spacecraft to the center of the central body and r_d is the distance from the central body to the disturbing body. In chapter 7 this ratio will be calculated for two cases, namely a 185 km altitude circular parking orbit around Earth and an orbit around Uranus at 1.1 times its planetary radius.

6.2 The two-body problem

When the disturbing bodies j are neglected, only the motion of body i about body k remains. Equation 6.6 then reduces to:

$$\ddot{\vec{r}}_i = -G \frac{m_i + m_k}{r_i^3} \vec{r}_i \quad (6.8)$$

The gravitational parameter $\mu = G(m_i + m_k)$ can now be introduced. Since $m_i \ll m_k$ in most practical cases, μ becomes a function of the mass of the central body only ($\mu = Gm_k$). Removing the index i then yields:

$$\ddot{\vec{r}} = -\frac{\mu}{r^3} \vec{r} \quad (6.9)$$

Several operations can be used on the above equation, yielding expressions for the conservation of total energy \mathcal{E} per unit mass of m_i , conservation of angular momentum and the radial distance r [Wakker, 2002]:

$$\frac{1}{2}V^2 - \frac{\mu}{r} = -\frac{\mu}{2a} = \text{constant} = \mathcal{E} \quad (6.10)$$

$$\vec{H} = \vec{r} \times \vec{V} = \text{constant} \quad (6.11)$$

$$r = \frac{H^2/\mu}{1 + c_3 \cos(\varphi - \omega)} \quad (6.12)$$

Equation 6.10 shows that there is conservation of total energy per unit mass of body i and equation 6.11 shows conservation of angular momentum. Close inspection of equation 6.12 reveals that this expression is similar to that of a conic section in polar coordinates. H is the magnitude of the angular momentum, φ is the angle measured from some reference direction and c_3 and ω are integration constants.

6.2.1 Conic sections

The equation for a conic section in polar coordinates is [Wakker, 2002]:

$$r = \frac{p}{1 + e \cos \theta} \quad (6.13)$$

Indeed this expression is similar to equation 6.12, and so the following expressions may be derived from a comparison between the two:

$$\frac{H^2}{\mu} = p \quad (6.14)$$

$$c_3 = e \quad (6.15)$$

$$\varphi - \omega = \theta \quad (6.16)$$

The parameter p determines the size of conic section and ω determines the orientation. The value of the eccentricity e determines the shape of the orbit:

- $e = 0$: the orbit is circular. In practice, there are many nearly circular orbits, but perfectly circular is not possible.
- $0 < e < 1$: the orbit is an ellipse. This type of orbit will be further outlined in section 6.2.2.
- $e = 1$: the orbit is a parabola. As with the circle, the parabola does not occur in reality.
- $e > 1$: the orbit is a hyperbola. The hyperbolic orbit will be outlined in section 6.2.3.

The parameter θ is the angle in the orbital plane, measured from the point where r is minimal, also called the pericenter (see also figures 6.2 and 6.3).

6.2.2 Elliptical orbits

The basic configuration of an elliptical orbit is depicted in figure 6.2.

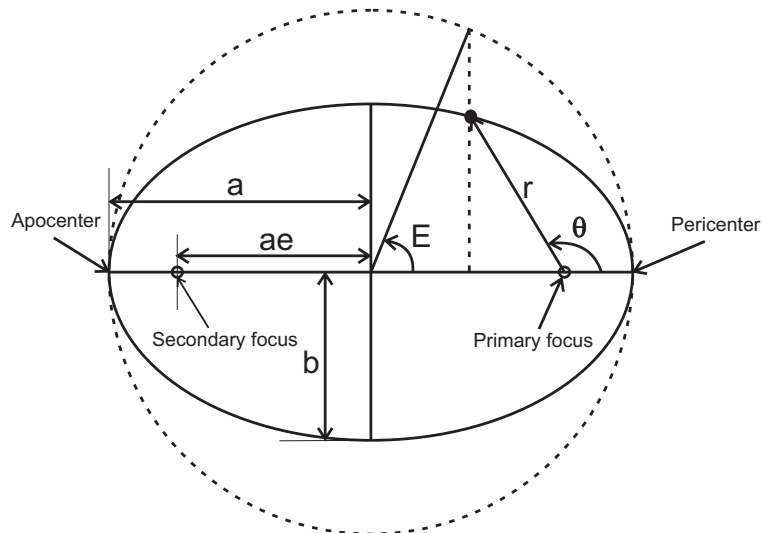


Figure 6.2 Configuration of an elliptical orbit, after [Wakker, 2002]. The central body is located in the primary focus of the ellipse. The dashed circle is an auxiliary circle with radius a , used for determining the eccentric anomaly E .

The distance r between the body of interest and the central body was given by equation 6.13. For an elliptical orbit it holds for the semi-latus rectum p that $p = a(1 - e^2)$, where a is the semi-major axis. The semi-major axis of the ellipse and the eccentricity of the ellipse are completely defined if the pericenter distance r_p and apocenter distance r_a are known. These are the minimum and maximum distance with respect to the central body [Wakker, 2002].

$$a = \frac{1}{2}(r_a + r_p) \quad (6.17)$$

$$e = \frac{r_a - r_p}{r_a + r_p} \quad (6.18)$$

For the pericenter distance it holds that the true anomaly θ is equal to zero. Substitution into equation 6.13, together with the expression for p yields:

$$r_p = \frac{a(1 - e^2)}{1 + e} = a(1 - e) \quad (6.19)$$

The same principle holds for the apocenter distance, where the true anomaly is 180° .

$$r_a = \frac{a(1 - e^2)}{1 - e} = a(1 + e) \quad (6.20)$$

For the velocity in the orbit the vis-viva equation can be applied:

$$V = \sqrt{\mu \left(\frac{2}{r} - \frac{1}{a} \right)} \quad (6.21)$$

The velocity in the pericenter and in the apocenter can be determined now by substituting the expressions for r_p and r_a into equation 6.21. After some steps this yields:

$$V_p = V_{cp} \sqrt{1 + e} \quad (6.22)$$

$$V_a = V_{ca} \sqrt{1 - e} \quad (6.23)$$

In these last two equations a new quantity has been introduced, the local circular velocity. It is the velocity that the body of interest would have in a circular orbit at the same distance from the central body. It is defined as follows:

$$V_c = \sqrt{\frac{\mu}{r}} \quad (6.24)$$

The orbital period in an elliptical orbit is described in Kepler's third law, which states that the ratio between the third power of the semi-major axis and the square of the orbital period is constant.

$$\frac{a^3}{T^2} = \frac{\mu}{4\pi^2} = \text{constant} \quad (6.25)$$

Rewriting Kepler's third law for the orbital period yields:

$$T = 2\pi \sqrt{\frac{a^3}{\mu}} \quad (6.26)$$

In order to escape from the gravity field of the attracting body, the so-called escape velocity must be reached. After some steps it can be derived that one can write for the escape velocity V_{esc} [Wakker, 2002]:

$$V_{esc} = \sqrt{\frac{2\mu}{r}} = \sqrt{2}V_c \quad (6.27)$$

Figure 6.2 shows two angles, namely the true anomaly θ and the eccentric anomaly E . The eccentric anomaly is a parameter that is needed in chapter 10 when Kepler's equation will be discussed. The distance r can be related to the eccentric anomaly E as follows:

$$r = a(1 - e \cos E) \quad (6.28)$$

This relationship will be needed in chapter 10, as well as the following relationship which relates θ to E [Wakker, 2002]:

$$\tan \frac{\theta}{2} = \sqrt{\frac{1+e}{1-e}} \tan \frac{E}{2} \quad (6.29)$$

6.2.3 Hyperbolic orbits

The basic configuration of a hyperbolic orbit is depicted in figure 6.3.

For a hyperbolic orbit $e > 1$, so then $1 - e^2 < 0$. In order for r in equation 6.13 to be positive, the semi-latus rectum $p = a(1 - e^2)$ has to be positive. This

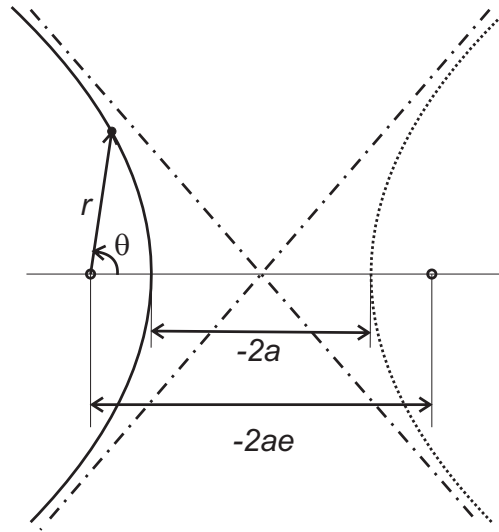


Figure 6.3 Configuration of a hyperbolic orbit, after [Wakker, 2002].

means that the semi-major axis in a hyperbolic orbit has a negative value.

A general hyperbola has two different branches, whose asymptotes go through a central point along the horizontal. The two branches of the hyperbola are mirror images of each other with respect to a line perpendicular to the horizontal going through the central point. Only one of the two branches is of physical interest, since one branch represents a repulsive central force, but this is of course not the case in celestial mechanics. In figure 6.3 the physically interesting branch is indicated by the solid line. The other branch is indicated by a dotted line.

The maximum velocity in the hyperbolic orbit is reached in the pericenter, for which the following relationship can be derived [Wakker, 2002]:

$$V_p = \sqrt{\frac{\mu}{-a} \left(\frac{e+1}{e-1} \right)} = V_{cp} \sqrt{e+1} \quad (6.30)$$

From equation 6.21, it can be seen that the minimum velocity is reached at $r = \infty$:

$$V_\infty^2 = -\frac{\mu}{a} \quad (6.31)$$

Substitution of equations 6.31 and 6.27 into equation 6.21 gives the following relationship:

$$V^2 = V_{esc}^2 + V_\infty^2 \quad (6.32)$$

So on every point in the hyperbolic orbit, the instantaneous velocity is determined by the local escape velocity and the velocity at infinity, the hyperbolic excess velocity.

In section 6.2.2 the concept of eccentric anomaly was introduced. For hyperbolic orbits a similar parameter called the hyperbolic anomaly (indicated by F) can be defined [Wakker, 2002]:

$$r = a(1 - e \cosh F) \quad (6.33)$$

For an elliptical orbit the eccentric anomaly E could be interpreted directly as an angle indicating the position of a body in an elliptical orbit around a central body. For the hyperbolic anomaly F this can not be done. F is not an actual angle, which can be deduced from the fact that, since $1 \leq \cosh F < \infty$, F varies from $-\infty$ to $+\infty$. It can be interpreted as a ratio of areas [Wakker, 2002].

As was the case for elliptical orbits, a relationship can be derived between the true anomaly θ and in this case the hyperbolic anomaly F (see [Wakker, 2002]):

$$\tan \frac{\theta}{2} = \sqrt{\frac{e+1}{e-1}} \tanh \frac{F}{2} \quad (6.34)$$

Equations 6.33 and 6.34 are needed later on in chapter 10.

6.2.4 Sphere of influence

The sphere of influence is a concept that is used to determine which is the central body during the different stages of an interplanetary trajectory. In order to understand the concept of the sphere of influence, figure 6.4 can be used.

The motion of body P_2 is described with respect to bodies P_1 , where body P_3 is a disturbing body. The masses of these bodies are denoted by m_1 , m_2 and m_3 respectively. An expression for the radius of the sphere of influence has been derived in [Battin, 1999], using the assumption that $m_2 \ll m_1, m_3$ and that $r_{12} \ll r_{13}$.

$$R_{SoI} = r_{13} \left(\frac{m_1}{m_3} \right)^{2/5} \quad (6.35)$$

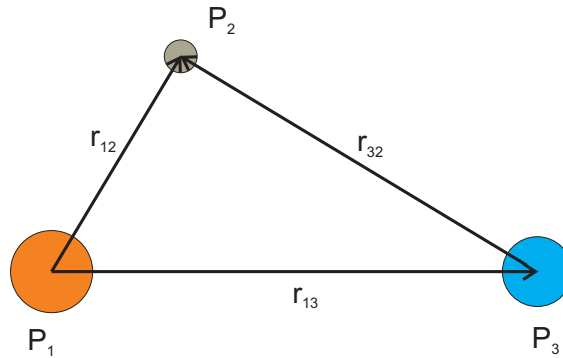


Figure 6.4 Positions of bodies P_1 , P_2 and P_3 relative to each other, after [Battin, 1999].

In this expression R_{SoI} is the radius of the sphere of influence. On the boundary of this sphere the ratio of disturbance accelerations of P_3 with respect to the accelerations of the primary body P_1 are the same. The sphere of influence then describes a sphere about body P_1 with respect to body P_3 . Inside this sphere the gravitational acceleration of P_1 is dominant over the acceleration of P_3 . Therefore the motion of P_2 is determined relative to P_1 inside the sphere of influence, and the motion is described with respect to P_3 when P_2 is outside the sphere of influence.

Table 6.1 shows the radius of the sphere of influence for each planet in the solar system. The planets are P_1 in the earlier notation and the Sun is body P_3 .

<i>Planet</i>	R_{SoI} (km)	% of r_{pl}
Mercury	112,630	0.19
Venus	616,247	0.57
Earth	923,566	0.62
Mars	574,413	0.25
Jupiter	48,168,633	6.19
Saturn	54,495,221	3.82
Uranus	51,732,568	1.80
Neptune	86,731,536	1.93

Table 6.1 Radii of the spheres of influence of all planets in the solar system, after [Battin, 1999]. The last column indicates the percentage that R_{SoI} constitutes of each planet's mean distance to the Sun r_{pl} .

On an interplanetary scale the radii of the spheres of influence are very small, as can be seen in table 6.1. When it comes to interplanetary motion (for details see chapter 8), the trajectory of the spacecraft can be approximated by a sequence of two-body problems [Battin, 1999]. For example, a spacecraft starting from a parking orbit around Earth and going directly to a parking orbit around another body (like Uranus), will move along three distinct conic sections. The first part of the trajectory, escaping into a heliocentric orbit, is described by a hyperbola centered at Earth. The second part of the trajectory is described by a conic section with the Sun acting as the attracting body. Finally,

the third part of the trajectory is described by a Uranus centered hyperbola, after which the spacecraft is put into orbit around Uranus. For each part of the trajectory, it is assumed that only one center of attraction is active at the time.

During a gravity assist (see section 8.4) or approach to a target planet, the period of time in which the gravity of the planet is the dominant force is very small compared to the total mission time. Therefore, during the encounter with the planet, the solar gravity can be ignored to first approximation. It can then be assumed that the state of the spacecraft changes instantaneously [*Battin*, 1999].

Orbit perturbations

To derive the equations for pure Kepler orbits it was assumed that the mass distribution of the planets was radially symmetric and that no disturbing forces were acting on the body [Wakker, 2002]. In reality, however, there are numerous forces acting on the body, deviating it from the pure Kepler orbit. This chapter will address the most important disturbing forces and give an indication of their magnitudes:

- Radially non-symmetric mass distribution
- Aerodynamic forces
- Attraction forces from other bodies
- Solar radiation pressure
- Electromagnetic forces

7.1 Radially non-symmetric mass distribution

The gravitational potential of a body with an arbitrary mass distribution (point outside the body) is [Wakker, 2002]:

$$U = -\frac{\mu}{r} \left[1 - \sum_{n=2}^{\infty} J_n \left(\frac{R}{r} \right)^n P_n(\sin \delta) - \sum_{n=2}^{\infty} \sum_{m=1}^{\infty} J_n^m \left(\frac{R}{r} \right)^n P_n^m(\sin \delta) \{ \cos m(\lambda - \lambda_{n,m}) \} \right] \quad (7.1)$$

This equation is based on spherical coordinates (with respect to a geocentric rotating reference frame), where r is the distance to the planet's center, δ is the geocentric latitude (positive from the equator going North) and λ is the geographic longitude (measured positive to the East from a reference meridian). The central body's average equatorial radius is denoted by R . The body's gravity field has several constants, given by J_n , J_n^m and $\lambda_{n,m}$. The last unknown terms in

this elaborate expression are $P_n(\sin \delta)$ and $P_n^m(\sin \delta)$. the first one is a Legendre polynomial and the second one is an added first order Legendre function. For the Legendre polynomial one can write [Wakker, 2002]:

$$P_n(x) = \frac{1}{(-2)^n n!} \frac{d^n}{dx^n} (1 - x^2)^n \quad (7.2)$$

The argument x of the Legendre polynomial is equal to $\sin \delta$ in equation 7.1. The added first order Legendre function is given by [Wakker, 2002]:

$$P_n^m(x) = (1 - x^2)^{m/2} \frac{d^m P_n(x)}{dx^m} \quad (7.3)$$

The first term of equation 7.1 is the potential for a body that has a radially symmetric mass distribution. The second term expresses the influence of a deviating mass distribution in the North-South direction, also called zonal harmonics. The third term, finally, gives the influence of a deviating mass distribution in both North-South and East-West direction (tesseral and sectoral harmonics respectively).

For the Earth, the J-coefficient with the largest value is J_2 ($J_2 = 1.083 \cdot 10^{-3}$). The other J-coefficients are all of the order 10^{-6} or less, a factor of at least 10^3 smaller. As a first order approximation of the perturbing acceleration due to the fact that the Earth's mass distribution is not radially symmetric, only the J_2 term is taken into account. It can then be derived that for the maximum acceleration in radial and latitudinal direction one can write [Wakker, 2002]:

$$|a_r|_{max} = 3\mu J_2 \frac{R^2}{r^4} \quad (7.4)$$

$$|a_\delta|_{max} = \frac{3}{2}\mu J_2 \frac{R^2}{r^4} \quad (7.5)$$

This implies, for a parking orbit around the Earth at an altitude of 185 km, that the maximum perturbing accelerations are $|a_r|_{max} = 2.63 \cdot 10^{-2} \text{ m/s}^2$. The maximum acceleration in latitudinal direction is two times smaller. The magnitude acceleration due to the main term of Earth's gravitational potential a_{main_E} at an altitude of 185 km is given as follows [Wakker, 2002]:

$$|a_{main_E}| = \frac{\mu_E}{r^2} = 9.25 \text{ m/s}^2 \quad (7.6)$$

So the maximum radial perturbing acceleration for a spacecraft at 185 km altitude around Earth due to the J_2 term is 0.28 % of the main acceleration.

The J_2 -term of the gravity field of Uranus is $3.34343 \cdot 10^{-3}$, so more than three times larger than the one of Earth [NASA/GSFC, 2007]. The next largest term in the list of J-coefficients in the Uranian gravity field model is the J_4 -term, whose absolute value is more than 100 times smaller than J_2 . At a distance of 1.1 times the planetary radius of Uranus the maximum perturbing acceleration in radial direction due to J_2 is $1.82 \cdot 10^{-2} \text{ m/s}^2$. In a similar way as for Earth, the acceleration due to the main term for Uranus can be calculated. This comes down to 7.33 m/s^2 at 1.1 times the radius of Uranus, which means that the maximum radial acceleration due to J_2 is 0.25 % of the local main gravitational acceleration.

7.2 Aerodynamic forces

The acceleration due to aerodynamic forces acting on a spacecraft is given by [Wakker, 2002]:

$$\bar{a}_{d_{aero}} = -C_D \frac{1}{2} \rho \frac{S}{m} |\bar{V}| \bar{V} \quad (7.7)$$

In this expression ρ is the local atmospheric density (in kg/m^3), S is a reference surface area of the spacecraft (in m^2), m is the mass of the spacecraft (in kg), C_D is the drag coefficient related to the surface area and \bar{V} is the velocity vector with respect to the (rotating) atmosphere in m/s.

As a calculation example, the satellite for the current Uranus orbiter mission is taken at an orbital altitude of 185 km. The maximum atmospheric density at that altitude is $7.201 \cdot 10^{-10} \text{ kg/m}^3$ [Larson and Wertz, 1999]. A drag coefficient of 2.2 is assumed, which is a typical number for spacecraft [Wakker, 2002]. The spacecraft's dry mass will be used, which is 678.45 kg. As a reference surface area, the area of the Voyager high gain antenna is taken. This because the mass of the spacecraft is lower than the mass of the Voyager spacecraft and therefore the spacecraft is assumed to be smaller than Voyager. The high gain antenna can then serve as a reference surface area of 10.75 m^2 and the orbital velocity at 185 km is 7.79 km/s. The disturbance acceleration then becomes:

$$|a_{d_{aero}}| = \frac{1}{2} \frac{C_D S}{m} \rho V^2 = 7.62 \cdot 10^{-4} \text{ m/s}^2 \quad (7.8)$$

This disturbance has a magnitude that is $8.17 \cdot 10^{-5}$ times the local main gravitational acceleration.

7.3 Attraction forces from other bodies

In section 6.1.3 the maximum acceleration caused by the attraction of a disturbing body was given by:

$$\left(\frac{a_d}{a_m}\right)_{max} = 2 \frac{m_d}{m_m} \left(\frac{r_s}{r_d}\right)^3 \quad (7.9)$$

To examine the order of magnitude of this ratio, a spacecraft is considered in a 185 km circular parking orbit around Earth and a spacecraft in circular orbit around Uranus at 1.1 times its radius. Table 7.1 shows the maximum relative disturbing acceleration for both orbits.

<i>Disturbing body</i>	$\left(\frac{a_d}{a_m}\right)$ <i>at Earth</i>	$\left(\frac{a_d}{a_m}\right)$ <i>at Uranus</i>
Sun	$5.63 \cdot 10^{-8}$	$4.30 \cdot 10^{-11}$
Mercury	$4.06 \cdot 10^{-14}$	$7.58 \cdot 10^{-18}$
Venus	$6.55 \cdot 10^{-12}$	$1.19 \cdot 10^{-16}$
Earth	-	$1.50 \cdot 10^{-16}$
Mars	$1.26 \cdot 10^{-13}$	$1.76 \cdot 10^{-17}$
Jupiter	$7.15 \cdot 10^{-13}$	$1.05 \cdot 10^{-13}$
Saturn	$2.62 \cdot 10^{-14}$	$1.00 \cdot 10^{-13}$
Uranus	$4.07 \cdot 10^{-16}$	-
Neptune	$1.18 \cdot 10^{-16}$	$1.22 \cdot 10^{-14}$

Table 7.1 Maximum acceleration caused by a disturbing body with respect to the acceleration of the main body for the Earth and Uranus reference orbits.

It can be seen from this table that the Sun has the largest relative disturbance acceleration for both a spacecraft in orbit around Earth and around Uranus. However, the magnitude of this disturbance acceleration compared to the acceleration of the central body (either Earth or Uranus) is very small. This means that for a spacecraft in a low orbit around a central body, the disturbance acceleration caused by the other planets can be neglected. The question that now arises is whether this holds for moons orbiting that same planet, and for a heliocentric interplanetary trajectory with gravity assists.

The assumption that was made to arrive at the maximum relative disturbance acceleration was that $r_s \ll r_d$. For moons orbiting the same planet as the spacecraft, this assumption is not true. Then the following equation has to be used for calculating the disturbance acceleration [Wakker, 2002]:

$$a_d = Gm_d \left(\frac{\bar{r}_{sd}}{r_{sd}^3} - \frac{\bar{r}_d}{r_d^3} \right) \quad (7.10)$$

In this equation, r_{sd} is the distance from the spacecraft to the disturbing body. Table 7.2 shows the perturbing acceleration caused by the Moon for a satellite in the circular orbit used earlier, as well as the perturbing acceleration caused by Uranus' main moons on a satellite in the reference orbit around Uranus.

<i>Disturbing moon</i>	a_d (m/s ²)	$\frac{a_d}{a_m}$
Moon (E)	$1.16 \cdot 10^{-6}$	$1.25 \cdot 10^{-7}$
Miranda (U)	$1.14 \cdot 10^{-10}$	$1.56 \cdot 10^{-11}$
Ariel (U)	$7.26 \cdot 10^{-10}$	$9.90 \cdot 10^{-11}$
Umbriel (U)	$2.32 \cdot 10^{-10}$	$3.17 \cdot 10^{-11}$
Titania (U)	$1.59 \cdot 10^{-10}$	$2.17 \cdot 10^{-11}$
Oberon (U)	$5.68 \cdot 10^{-11}$	$7.75 \cdot 10^{-12}$

Table 7.2 Disturbing accelerations caused by the Moon on a satellite orbiting the Earth (E) and of the five main moons of Uranus (U) on a satellite orbiting this planet.

From this table it can be seen that the five main Uranian moons disturb the satellite's orbit around Uranus several orders of magnitude less than the Moon does for a spacecraft in orbit around Earth. The main acceleration of the Earth as a central body for a spacecraft in a 185 km circular orbit is 9.25 m/s² and for the reference Uranus orbit the main acceleration is 7.33 m/s².

On the heliocentric part of the interplanetary journey, the Sun is the central body. It is very likely that a spacecraft on its way to Uranus will make a gravity assist at a certain planet. When the spacecraft gets closer to a planet, the disturbing acceleration of that planet increases, until the moment (at the radius of the sphere of influence) where the gravity of the planet prevails and it becomes the central body. The attraction force of other bodies (also moons) is therefore very important and has to be taken into account with gravity assists.

7.4 Solar radiation pressure

Photons coming from the Sun can hit the spacecraft, causing a perturbation from a pure Kepler orbit. This is called solar radiation pressure and for the acceleration that it causes one can write [Wakker, 2002]:

$$a_{d_{solar}} = \frac{Q}{mc} S(1 + RC) \cos^2 \eta \quad (7.11)$$

In this expression Q is the power density of the incoming solar radiation in W/m², m is the mass of the satellite in kg, c is the speed of light ($c = 2.9979 \cdot 10^8$ m/s), S is again the reference surface area of the satellite in m², RC is the reflection coefficient ($0 < RC < 1$), and η is the angle of incidence of the incoming sunlight.

The intensity of the incoming sunlight (also called solar irradiance Q_{ir}) at the orbit of Uranus is 3.71 W/m². On Earth the solar irradiance is 1367.6 W/m². At a distance r from the Sun, the irradiance is proportional to $1/r^2$, which explains the large difference between Earth and Uranus (Uranus being located much farther away from the Sun). Next to the solar irradiance the planets themselves also reflect and emit radiation (albedo radiation Q_{al} and thermal

radiation Q_{th} respectively). The amount of albedo radiation is determined by the planet's reflection coefficient and the thermal radiation is based on the effective temperature T_{eff} of the planet. This is the temperature that a black body would have that emits the same amount of energy as the body does when it does not behave like a perfect black body [De Pater and Lissauer, 2007].

$$Q_{al} = (RC)_{pl}(Q_{ir})_{pl} \quad (7.12)$$

$$Q_{th} = \sigma T_{eff}^4 \quad (7.13)$$

The reflection coefficient of the planet is also referred to as the planet's Bond albedo. The parameter σ is the constant of Stefan-Boltzmann ($\sigma = 5.67 \cdot 10^{-8} \text{ W}/(\text{m}^2\text{K}^4)$). For all planets in the solar system the irradiance, the albedo radiation and the thermal radiation are shown in table 7.3.

<i>Planet</i>	<i>BA*</i>	<i>T_{eff} (K)</i>	<i>Q_{ir} (W/m²)</i>	<i>Q_{al} (W/m²)</i>	<i>Q_{th} (W/m²)</i>
Mercury	0.119	442.5	9126.6	1086.1	2173.9
Venus	0.750	231.7	2613.9	1960.4	163.4
Earth	0.306	254.3	1367.6	418.5	237.1
Mars	0.250	210.1	589.2	147.3	110.5
Jupiter	0.343	110.0	50.5	17.32	8.30
Saturn	0.342	81.1	14.9	5.10	2.45
Uranus	0.300	58.2	3.71	1.11	0.65
Neptune	0.290	46.6	1.51	0.44	0.27

Table 7.3 Irradiation, albedo radiation and thermal radiation for all planets [NASA/GSFC, 2007].
*Bond Albedo

The highest disturbance acceleration is attained at Mercury, since it is located closest to the Sun. As a worst case scenario for a spacecraft like Voyager the disturbance acceleration due to solar radiation pressure is $1.13 \cdot 10^{-6} \text{ m/s}^2$. This is 0.28% of the local acceleration due to the Sun's gravity. This value has been obtained by assuming the power density Q as the sum of the three tabulated values, a maximum mass of 2100 kg, the surface area $S = 3.7 \cdot 13 = 48.1 \text{ m}^2$, the reflection coefficient equal to 0.119 and normal incidence on the spacecraft, so $\eta = 0$.

7.5 Electromagnetic forces

Not all planets in the solar system have magnetic fields. Venus and Mars have no magnetic field at all and the magnetic field strength of Mercury is about 167 times weaker than the one of Earth [NASA/GSFC, 2007]. The giant planets all have magnetic fields that are much stronger than Earth's magnetic field. For example, the magnetic field strength (the dipole moment) of Uranus is 47.9 times as large [Faure and Mensing, 2007].

A spacecraft can be considered as a charged particle when moving through a magnetic field. It will then experience a force called the Lorentz force. The

magnitude of the Lorentz force depends on the electric charge q , the velocity V with which the spacecraft moves through the magnetic field, and on the strength of the magnetic field [Noomen, 2003].

$$\bar{F}_L = q\bar{V} \times \bar{B} \quad (7.14)$$

The electric charge is calculated when the voltage U is multiplied with the capacitance C :

$$q = UC \quad (7.15)$$

When a spherical satellite is assumed, the capacitance can be written as a function of the spacecraft radius R_s only [Wakker, 2002]:

$$C = 1.1 \cdot 10^{-10} R_s \quad (7.16)$$

When the magnetic field of a planet is modeled by a dipole (two 'poles' that may be considered as a source and a sink of magnetic energy), the strength of the magnetic field may be written as [Noomen, 2003]:

$$B = H_0 \left(\frac{R}{r} \right)^3 \sqrt{1 + 3 \sin^2 \Phi} \quad (7.17)$$

In this equation H_0 is the magnetic field strength at the magnetic equator of the planet, and Φ is the latitude measured from the magnetic axis. The above equation implies that the magnetic field strength is twice as large at the magnetic poles ($\Phi = \pm 90^\circ$) than at the magnetic equator ($\Phi = 0^\circ$).

In order to find out the magnitude of the disturbance caused by the magnetic field, again the two earlier used reference orbits around Earth and Uranus are considered. Now the orbit planes are assumed to be aligned with the magnetic poles, yielding a worst case scenario for that particular orbit. The disturbance acceleration is then calculated as follows:

$$a_{del} = \frac{F_L}{m_s} \quad (7.18)$$

As a reference satellite, the Voyager spacecraft is taken (it will be assumed spherical), with a mass m_s of 825 kg and a radius R_s of 3.7 m. The voltage is taken as -50 V [Wakker, 2002]. Table 7.4 shows the values of the disturbance acceleration for the two previously considered reference orbits.

<i>Planet</i>	a_d (m/s^2)	$\frac{a_d}{a_m}$
Earth	$1.09 \cdot 10^{-11}$	$1.18 \cdot 10^{-12}$
Uranus	$1.23 \cdot 10^{-14}$	$1.68 \cdot 10^{-15}$

Table 7.4 Magnetic field disturbing acceleration for reference orbits around Earth (at 185 km altitude) and Uranus (at a $1.1 R_U$ orbit) assuming a dipole field. The reference orbits are aligned with a magnetic latitude of 90° .

7.6 Implications

From the discussion in section 6.2.4 on the sphere of influence it was deduced that the encounter times at the planets are very small compared to the total mission time and that the radius of the sphere of influence was small on an interplanetary scale. The disturbing accelerations that have been calculated throughout this chapter are all small compared to the main gravitational acceleration of the central body (not even 1% of the magnitude). Therefore, to a first-order approximation of interplanetary trajectories all disturbing forces can be neglected. Analyzing interplanetary trajectories can then be done using analytical methods. This is very useful since there is no need for numerical integration of the equations of motion, saving computation time. It should be stressed that for precision orbital analysis numerical integration is required. In this thesis, however, this will not be the case and only analytical methods will be used.

High thrust interplanetary trajectories

In chapter 6 the basic principles of orbital mechanics have been discussed. In this chapter these principles will be applied to high thrust interplanetary missions using chemical propulsion. With these high thrust missions it is assumed that the impulsive maneuver (engine burn) is applied in such a short amount of time that the velocity of the spacecraft changes instantaneously, while the spacecraft's position remains the same as before the maneuver.

In section 8.1 the basic two-dimensional interplanetary transfer is discussed. However, interplanetary trajectories are three-dimensional in reality, so the implications of that are discussed as well. In section 8.2 the technique to determine the spacecraft orbit based on planetary positions and flight time is presented. The calculations needed to obtain the required impulsive maneuvers at launch and capture are discussed in section 8.3. Patching subsequent interplanetary legs together can be done using gravity assists, the details of which are treated in sections 8.4 and 8.5.

8.1 Two-dimensional interplanetary trajectories

An interplanetary trajectory from planet P_1 to planet P_2 can be subdivided into three main parts, as already mentioned in section 6.2.4. First of all the spacecraft trajectory within the sphere of influence of Earth has to be assessed. The trajectory is considered as a geocentric hyperbola. After leaving Earth's sphere of influence the trajectory is a heliocentric conic section, since the motion is now described with respect to the Sun. Upon arrival in the target planet's sphere of influence, the motion will be described as a hyperbola centered at the target planet. This method is known as patched conics.

To start the interplanetary trajectory analysis, the motion is assumed to be two-dimensional. A number of assumptions is made. The first one is that the planets all orbit the Sun in circular orbits. In reality, the orbits of the planets have small eccentricities, making them nearly circular. The second assumption is that all the planets move in the ecliptic plane, so the inclinations are assumed to

be zero. These assumptions will of course induce errors. Some remarks about the differences between two-dimensional motion and the reality of three-dimensional motion can be found in section 8.1.2. The geometry of a two-dimensional interplanetary trajectory is shown in figure 8.1.

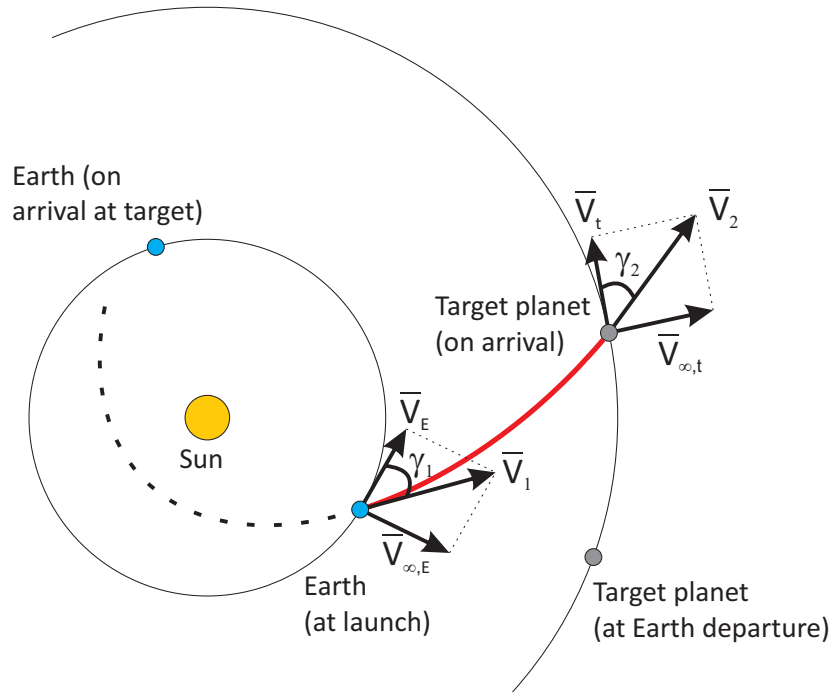


Figure 8.1 Geometry of a two-dimensional interplanetary trajectory from Earth to another target planet, after [Cornelisse *et al.*, 1979].

For the current analysis it is assumed that the journey starts from a circular parking orbit around Earth. As already mentioned, the burning time for high thrust propulsion systems is short, so the impulsive shot concept may be used. After an impulsive shot the velocity changes instantly, but the position remains unaltered. Each maneuver will be performed with only one firing of the engine.

It can be shown that it is most advantageous to apply the impulsive shot tangentially to the parking orbit, at a location where the orbital velocity is at a maximum [Cornelisse *et al.*, 1979]. For a circular parking orbit around the Earth, the velocity right after the impulsive shot V_0 is:

$$V_0 = V_{c_0} + \Delta V_0 \quad (8.1)$$

The velocity in the parking orbit is given by V_{c_0} and the impulsive shot is denoted by ΔV_0 . The velocity in a hyperbolic trajectory can be obtained with equation 6.32. Then the required impulsive shot is:

$$\Delta V_0 = V_0 - V_{c_0} = \sqrt{\frac{2\mu_E}{r_0} + V_{\infty E}^2} - \sqrt{\frac{\mu_E}{r_0}} \quad (8.2)$$

Here r_0 is the radius of the circular parking orbit (and the perigee distance of the escape trajectory), μ_E the gravitational parameter of Earth. The magnitude of the impulsive shot needed to decelerate the spacecraft so that it can go into orbit around the target planet is obtained analogously:

$$\Delta V_3 = \sqrt{\frac{2\mu_t}{r_3} + V_{\infty t}^2} - \sqrt{\frac{\mu_t}{r_3}} \quad (8.3)$$

The target planet's gravitational parameter is given by μ_t , r_3 is the pericenter distance of the hyperbolic trajectory about the planet and V_{par_3} is the velocity of the spacecraft in orbit about the planet.

8.1.1 Example: Hohmann transfer to Uranus

It can be shown that the interplanetary trajectory that requires the least amount of propellant is the so-called Hohmann transfer orbit. This is a heliocentric ellipse that is tangential to both Earth's orbit and Uranus' orbit, so then it holds that $\gamma_1 = \gamma_2 = 0$. The assumptions made are that both Earth and Uranus move in circular co-planar orbits around the Sun. The altitude of the parking orbit is taken as 185 km and the radius of the orbit around Uranus is taken as $1.1 R_U$. The complete derivation of the results is shown in appendix A.

The magnitude of the impulsive shot in the parking orbit around the Earth is:

$$\Delta V_0 = 7.98 \text{ km/s} \quad (8.4)$$

The next impulsive shot is needed to decelerate the spacecraft and go into orbit around Uranus. Its magnitude is:

$$\Delta V_3 = 6.49 \text{ km/s} \quad (8.5)$$

The transfer time for the Hohmann transfer orbit is half the orbital period of an ellipse with semi-major axis a_H . This comes down to:

$$T_H = \frac{1}{2} \cdot 2\pi \sqrt{\frac{a_H^3}{\mu_S}} = 5.04 \cdot 10^8 \text{ s} = 15.97 \text{ yr} \quad (8.6)$$

The planets all move in orbits with different angular velocities, so the configuration of the planets in the solar system changes constantly. After a certain amount of time, the so-called synodic period, the relative positions of the Sun, Earth and another planet are the same again. So a certain trajectory would have the same geometry after this specific amount of time. An expression for the synodic period T_{syn} has been derived in [Cornelisse et al., 1979]:

$$\frac{1}{T_{syn}} = \left| \frac{1}{T_E} - \frac{1}{T_t} \right| \quad (8.7)$$

Here, T_E is the orbital period of Earth and T_t is the orbital period of the target planet. For the planets beyond Jupiter $T_E \ll T_t$, so then $T_{syn} \approx 1$ yr.

8.1.2 Three-dimensional interplanetary trajectories

The assumptions made for the interplanetary trajectory were that the planetary orbits were circular and they were all coplanar in the ecliptic plane. In reality, this is not the case and the planets orbit the Sun in slightly elliptic and inclined orbits. This will have important consequences on the energy requirements and transfer time.

As an example a minimum ΔV transfer from Earth to Uranus is analyzed using the software package GALOMUSIT. The parking orbit around Earth was chosen circular with an altitude of 185 km and the final orbit around Uranus was chosen circular with an altitude of 2555.9 km (which is 1.1 R_U). The launch window in which the optimizer in GALOMUSIT was searching spanned from 1 January 2015 up to and including 1 January 2025. The spacecraft had to arrive before 1 January 2035. The resulting orbit is shown in figure 8.2.

For this best orbit the launch date is 15 June 2015 and the arrival date is 13 November 2030. The total ΔV that is required for this trajectory is 14.566 km/s (8.094 km/s for launch and 6.472 km/s for capture). This total ΔV is 10 m/s higher than for the two-dimensional Hohmann transfer. The transfer time for the three-dimensional minimum ΔV transfer is 7 months shorter than the transfer time for the two-dimensional Hohmann transfer.

This example illustrates that there can be significant differences between two-dimensional and three-dimensional orbits. Therefore the analysis of interplanetary trajectories will from now on be solely focused on three-dimensional trajectories.

8.2 Lambert's problem

The analysis up to this point has not taken into account yet whether the target planet will actually be there when the spacecraft arrives at the planet's orbit. This problem is known as Lambert's problem, where given an initial and final

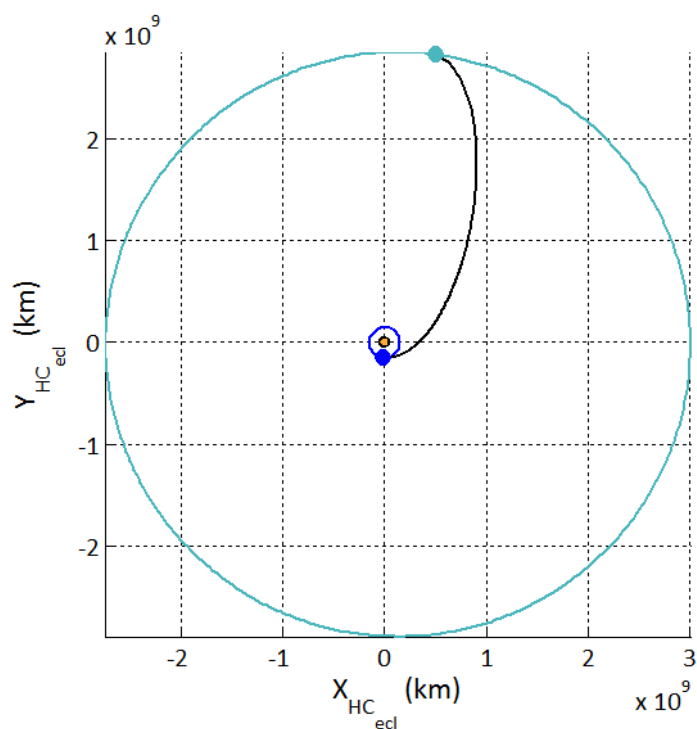


Figure 8.2 Orbit corresponding to the minimum ΔV transfer between a circular orbit around Earth ($h = 185$ km) and a circular orbit around Uranus ($h = 2555.9$ km). This result was obtained using GALOMUSIT.

position, together with the flight time, the connecting orbit is determined.

The general configuration of Lambert's problem is shown in figure 8.3. The central body for the orbit connecting bodies P_1 and P_2 is C . The positions of P_1 and P_2 are indicated by the magnitudes of the position vectors \bar{r}_1 and \bar{r}_2 . The time needed to travel along the orbit from P_1 to P_2 is given by Δt .

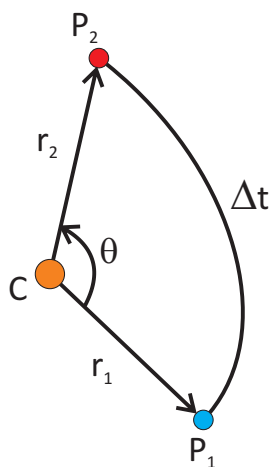


Figure 8.3 Configuration of Lambert's problem, adapted from [Gooding, 1990].

Taking a closer look at figure 8.3, two solutions for the Lambert problem exist. The first one, also indicated in figure 8.3, subtends an angle θ , whereas the second solution subtends an angle of $2\pi - \theta$. Using the fact that the common direction of motion in the solar system is counterclockwise, only θ is left as the solution.

The fact that θ is the solution for the transversed angle along the Lambert arc does not mean that θ has to be within 0 and 2π . Multi-revolution Lambert arcs are also possible solutions to the problem. However, as mentioned in chapter 2, multi-revolution Lambert arcs are not considered in this thesis.

The analysis of Lambert's problem starts with Kepler's equation for a transfer from P_1 to P_2 (see chapter 10 for details regarding Kepler's equation) [Wakker, 2002]:

$$t_2 - t_1 = \Delta t = \sqrt{\frac{a^3}{\mu}} (E_2 - E_1 - e(\sin E_2 - \sin E_1)) \quad (8.8)$$

For Lambert's problem, there is no direct solution, so an iteration procedure should be applied. Furthermore, the equation for Δt has to be rewritten in terms of the known parameters r_1 , r_2 and θ . The only unknown in the problem should then be the iteration parameter. Gooding [1990] uses the semi-major axis a of the transfer orbit as the iteration parameter. Instead of using a directly, it is first made non-dimensional by means of the following transformation [Gooding, 1990]:

$$x^2 = 1 - \frac{s}{2a} \quad (8.9)$$

In this equation s is the semi-parameter of the triangle CP_1P_2 . It is defined in the following way [Gooding, 1990]:

$$s = \frac{r_1 + r_2 + c}{2} \quad (8.10)$$

The chord c is the length of side P_1P_2 in the triangle. Different values for x correspond to different types of orbits. If $|x| < 1$, then the orbit is elliptical, whereas $x = 1$ corresponds to a parabolic orbit and $x > 1$ to a hyperbolic orbit. Values of $x \leq -1$ are assumed not to arise, since they indicate a negative value for the time of flight Δt [Gooding, 1990].

Next to the semi-major axis a , also Δt is made non-dimensional. This is done as follows [Gooding, 1990]:

$$T = \sqrt{\frac{8\mu}{s^3}} \Delta t \quad (8.11)$$

After an extensive derivation, which will not be repeated here, equations 8.8, 8.9 and 8.11 can be combined into the following expression for T :

$$T = \frac{2 \left(x - qz - \frac{d}{y} \right)}{E_{Lam}} \quad (8.12)$$

Equation 8.12 introduces several new parameters. The parameters q , E_{Lam} , y , z and d are defined as follows:

$$q = \frac{\sqrt{r_1 r_2}}{s} \cos \frac{\theta}{2} \quad (8.13)$$

$$E_{Lam} = x^2 - 1 \quad (8.14)$$

$$y = \sqrt{|E_{Lam}|} \quad (8.15)$$

$$z = \sqrt{1 - q^2 + q^2 x^2} \quad (8.16)$$

$$d = \begin{cases} \arctan \left(\frac{f}{g} \right), & \text{if } E_{Lam} < 0 \\ \ln(f + g), & \text{if } E_{Lam} > 0 \end{cases} \quad (8.17)$$

In the expression for d two new variables are introduced, f and g . They are given by the following expressions:

$$f = y(z - q) \quad (8.18)$$

$$g = xz - qE_{Lam} \quad (8.19)$$

In order to see which kinds of solutions can be found, figure 8.4 can be used [Gooding, 1990]. It shows the T plotted against x for certain values of the parameter q , as well as for the number of full revolutions m . In this thesis work multi-revolution Lambert solutions are not considered. Possible solutions are indicated by the white area, whereas solutions that are not feasible are indicated by the gray area.

In order to come up with a solution to Lambert's problem, an iteration process is needed. Gooding [1990] uses a Halley iteration procedure. This is essentially a basic Newton-Raphson procedure, extended to give third-order convergence. The Halley iteration process can be stated as follows [MathWorld, 2009a]:

$$x_{n+1} = x_n - \frac{f(x_n)f'(x_n)}{2(f'(x_n))^2 - f(x_n)f''(x_n)} \quad (8.20)$$

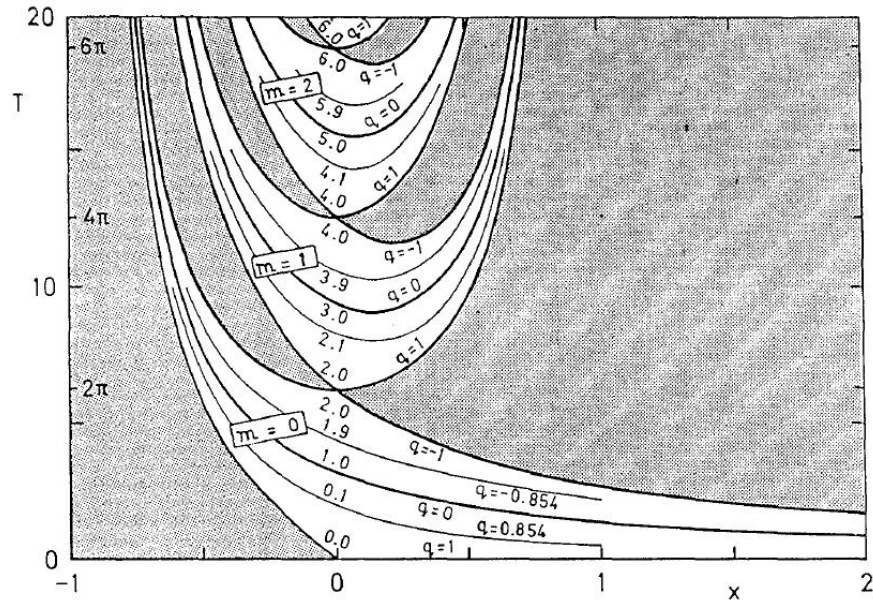


Figure 8.4 Plot of T vs. x for certain values of q and m [Gooding, 1990]. The number of full revolutions is indicated by m (in this thesis, only single-revolution Lambert arcs are considered, so $m = 0$).

In this procedure $f(x_n)$ is given by:

$$f(x_n) = T - \frac{2 \left(x_n - q_n z_n - \frac{d_n}{y_n} \right)}{E_{Lam_n}} \quad (8.21)$$

The first and second derivative of f with respect to x are represented by f' and f'' in equation 8.20. For the iteration process to function well, an appropriate starting value x_0 is required. Gooding [1990] uses the following starting values, which depend on the sign of x :

$$x_0 = \begin{cases} \frac{T_{x=0}(T_{x=0}-T)}{4T}, & \text{if } x > 0 \\ -\frac{T-T_{x=0}}{T-T_{x=0}+4}, & \text{if } x < 0 \end{cases} \quad (8.22)$$

The value for T when x is equal to zero is indicated by $T_{x=0}$. Whether x is positive or negative depends on $T_{x=0}$. If $T_{x=0} - T$ is negative, then x is negative and if $T_{x=0} - T$ is positive then x is also positive. It was found by Gooding [1990] that, for single-revolution Lambert arcs, the Halley iteration method with the above starting values always converges to within 13 digits in three iteration steps. The number of iterations has therefore been fixed at three.

After the Halley procedure has converged, a value for x , and thus for the semi-major axis a of the transfer arc, has been obtained. The next step is to compute the velocity components in radial and transverse direction at P_1 and P_2 . For these

components at the start and end of the Lambert arc, the following expressions hold [Gooding, 1990]:

$$V_{R_1} = \gamma \frac{(qz - x) - \rho(qz + x)}{r_1} \quad (8.23)$$

$$V_{T_1} = \gamma \frac{\sigma(z + qx)}{r_1} \quad (8.24)$$

$$V_{R_2} = -\gamma \frac{(qz - x) - \rho(qz + x)}{r_2} \quad (8.25)$$

$$V_{T_2} = \gamma \frac{\sigma(z + qx)}{r_2} \quad (8.26)$$

In these equations some auxiliary variables have been used:

$$\gamma = \sqrt{\frac{\mu s}{2}} \quad (8.27)$$

$$\rho = \frac{r_1 - r_2}{c} \quad (8.28)$$

$$\sigma = 2\sqrt{\frac{r_1 r_2}{c^2}} \sin \frac{\theta}{2} \quad (8.29)$$

The velocity components V_{R_1} , V_{T_1} , V_{R_2} and V_{T_2} are defined in the plane spanned by the triangle CP_1P_2 . The state of the spacecraft, and its trajectory is determined in an inertial, heliocentric reference frame (either ecliptic or equatorial). Therefore, the tangential and radial components in the plane spanned by CP_1P_2 have to be converted into this inertial, heliocentric reference frame.

The conversion is done as follows, starting with the position vectors of P_1 and P_2 :

$$\bar{r}_1 = \begin{pmatrix} x_1 \\ y_1 \\ z_1 \end{pmatrix} \quad \bar{r}_2 = \begin{pmatrix} x_2 \\ y_2 \\ z_2 \end{pmatrix}$$

The longitude of P_1 and P_2 (λ_1 and λ_2 respectively) can be found using the following expressions:

$$\lambda_1 = \arctan 2(y_1, x_1) \quad (8.30)$$

$$\lambda_2 = \arctan 2(y_2, x_2) \quad (8.31)$$

The latitude of P_1 and P_2 (δ_1 and δ_2 respectively) can be found as follows:

$$\delta_1 = \arctan 2 \left(z_1, \sqrt{x_1^2 + y_1^2} \right) \quad (8.32)$$

$$\delta_2 = \arctan 2 \left(z_2, \sqrt{x_2^2 + y_2^2} \right) \quad (8.33)$$

The radial velocity components V_{R_1} and V_{R_2} can now be converted to the inertial, heliocentric reference frame as follows:

$$\bar{V}_{R_{In,HC_1}} = V_{R_1} \begin{pmatrix} \cos \delta_1 \cos \lambda_1 \\ \cos \delta_1 \sin \lambda_1 \\ \sin \delta_1 \end{pmatrix} \quad (8.34)$$

$$\bar{V}_{R_{In,HC_2}} = V_{R_2} \begin{pmatrix} \cos \delta_2 \cos \lambda_2 \\ \cos \delta_2 \sin \lambda_2 \\ \sin \delta_2 \end{pmatrix} \quad (8.35)$$

The tangential velocity components V_{T_1} and V_{T_2} can be converted to the inertial, heliocentric reference frame in the following way:

$$\bar{V}_{T_{In,HC_1}} = V_{T_1} \left(\frac{\bar{r}_1 \times \bar{r}_2}{|\bar{r}_1 \times \bar{r}_2|} \times \frac{\bar{r}_1}{|\bar{r}_1|} \right) \quad (8.36)$$

$$\bar{V}_{T_{In,HC_2}} = V_{T_2} \left(\frac{\bar{r}_1 \times \bar{r}_2}{|\bar{r}_1 \times \bar{r}_2|} \times \frac{\bar{r}_2}{|\bar{r}_2|} \right) \quad (8.37)$$

Then finally the velocity vectors of P_1 and P_2 in the inertial, heliocentric reference frame can be calculated simply by adding the converted radial and tangential velocity components:

$$V_{1In,HC} = \bar{V}_{R_{In,HC_1}} + \bar{V}_{T_{In,HC_1}} \quad (8.38)$$

$$V_{2In,HC} = \bar{V}_{R_{In,HC_2}} + \bar{V}_{T_{In,HC_2}} \quad (8.39)$$

8.3 Calculating the ΔV needed for launch and capture

From the solution of Lambert's problem, as described in section 8.2, the required heliocentric velocity vectors at the start and at the end of a Lambert arc are determined. The required heliocentric velocity at the start of the first interplanetary leg is used to determine the ΔV needed to inject a spacecraft from a parking orbit around the initial body into the interplanetary leg. In

the same way, the heliocentric velocity at the end of the final leg is used to determine the ΔV needed to inject the spacecraft into orbit around the target planet.

It is assumed that the engine burn is performed at the pericenter of the parking orbit. This is done to take advantage of the fact that the velocity in pericenter is already at its highest value within the orbit. In order to calculate the ΔV needed at launch or at capture, the characteristics of the parking orbits need to be known. The parking orbit is defined when the pericenter radius r_p and the eccentricity e are known.

When the spacecraft is in a parking orbit around the launch body, its velocity in pericenter V_{pL} is given by equation 6.22, which is repeated here for convenience:

$$V_{pL} = V_{c_{pL}} \sqrt{1 + e_L} = \sqrt{\frac{\mu_L}{r_{pL}}} \sqrt{1 + e_L} \quad (8.40)$$

The subscript 'L' indicates that it concerns the launch body. The local circular velocity at pericenter is given by $V_{c_{pL}}$.

Now that the initial velocity is known, the required velocity at the start of the hyperbolic escape trajectory has to be determined. The velocity in a hyperbolic orbit can be determined using equation 6.32. When the equation is applied to the pericenter of the parking orbit around the launch body, this leads to:

$$V_{pLhyp}^2 = V_{esc}^2 + V_\infty^2 \quad (8.41)$$

The local escape velocity V_{esc} at the pericenter of the parking orbit around the launch body is calculated using equation 6.27:

$$V_{esc} = \sqrt{\frac{2\mu_L}{r_{pL}}} = \sqrt{2}V_c \quad (8.42)$$

The hyperbolic excess velocity V_∞ of the hyperbolic escape orbit can be determined using the required heliocentric velocity at the start of the interplanetary leg, \bar{V}_{HCL} . This velocity is determined by Lambert's problem, as outlined in section 8.2. The launch body's heliocentric velocity \bar{V}_{plL} has to be known as well. Then one can write for V_∞ :

$$V_\infty = |\bar{V}_{HCL} - \bar{V}_{plL}| \quad (8.43)$$

Now the required ΔV needed at pericenter of the parking orbit around the launch body can be determined:

$$\Delta V_L = V_{pL_{hyp}} - V_{pL} = \sqrt{\frac{2\mu_L}{r_{pL}} + V_{\infty L}^2} - \sqrt{\frac{\mu_L}{r_{pL}} \sqrt{1 + e_L}} \quad (8.44)$$

For the ΔV capture maneuver needed to insert the spacecraft into a parking orbit around the target planet the same procedure can be applied as was done for ΔV_L . The pericenter radius and eccentricity for the capture orbit, r_{pC} and e_C respectively, need to be known. The same holds for the target planet's heliocentric velocity V_{plC} and the required heliocentric velocity at the end of the interplanetary leg towards the target planet, \bar{V}_{HC_C} . The capture ΔV can then be written as:

$$\Delta V_C = V_{pC_{hyp}} - V_{pC} = \sqrt{\frac{2\mu_C}{r_{pC}} + V_{\infty C}^2} - \sqrt{\frac{\mu_C}{r_{pC}} \sqrt{1 + e_C}} \quad (8.45)$$

8.4 Unpowered gravity assists

In order to keep the spacecraft mass low and to keep the flight time in the interplanetary trajectory low, the concept of the planetary gravity assist can be used. The magnitude and direction of the spacecraft's velocity can be changed by flying through the gravitational field of a planet or a planetary moon.

8.4.1 Principle of gravity assists

During a gravity assist momentum is exchanged between the spacecraft and the target planet. Using conservation of linear momentum one can write [Allen, 2003]:

$$m_s(\bar{V}_{in} - \bar{V}_{out}) = -m_{pl}(\bar{V}_{pl_{in}} - \bar{V}_{pl_{out}}) \quad (8.46)$$

The mass of the satellite is denoted by m_s , the satellite's velocity is given by \bar{V} , the target planet's mass is m_{pl} and its velocity is \bar{V}_{pl} . The subscripts 'in' and 'out' indicate the initial and final or outgoing velocity respectively. The mass of the spacecraft is much smaller than the mass of the target planet (order 1000 kg versus order 10^{25} kg). For spacecraft velocities in the range of several km/s the planet's velocity remains effectively unchanged. A schematic of an unpowered gravity assist is shown in figure 8.5.

Within the planet's sphere of influence, the gravity assist trajectory is a hyperbola, with the target planet in its pericenter. The projection of the planet's heliocentric velocity vector into the plane of the planetocentric hyperbola is \bar{V}_{planet} . The hyperbolic excess velocity of the spacecraft with respect to the target planet is $\bar{V}_{\infty in}$. Its magnitude does not change during the gravity assist, but its

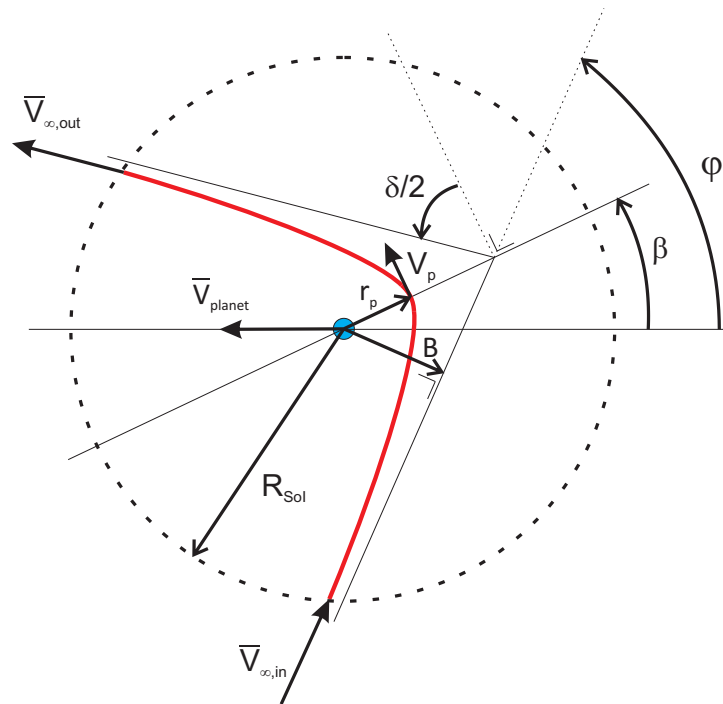


Figure 8.5 Geometry of a planetocentric hyperbola, after [Cornelisse et al., 1979].

orientation will be changed. All the velocity vectors can be put into a vector diagram, as shown in figure 8.6.

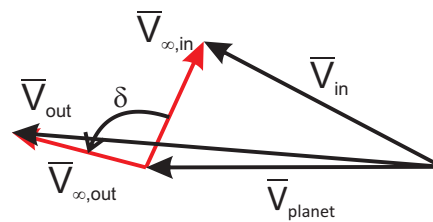


Figure 8.6 Gravity assist vector diagram, after [Strange and Longuski, 2002].

The final heliocentric velocity of the spacecraft is determined by vectorially adding the hyperbolic excess velocity vector and the target planet’s velocity vector:

$$\vec{V}_{out} = \vec{V}_{\infty out} + \vec{V}_{planet} \tag{8.47}$$

8.4.2 Heliocentric energy increase

From the conservation of angular momentum one can write (the parameters are from figure 8.5):

$$BV_{\infty in} = r_p V_p \tag{8.48}$$

The impact parameter B is defined as the perpendicular distance from the pericenter to the incoming asymptote of the hyperbola. For r_p the following equation can be derived [Cornelisse et al., 1979]:

$$r_p = -\frac{\mu_{pl}}{V_{\infty in}^2} + \sqrt{\frac{\mu_{pl}^2}{V_{\infty in}^4} + B^2} \quad (8.49)$$

The eccentricity of the hyperbolic trajectory is related to half of the deflection angle δ as follows:

$$\cos\left(\frac{\pi}{2} + \frac{\delta}{2}\right) = -\frac{1}{e} \quad (8.50)$$

The asymptotic deflection angle δ can be calculated as follows:

$$\sin\frac{\delta}{2} = \frac{1}{1 + \frac{r_p V_{\infty in}^2}{\mu_{pl}}} = \frac{1}{\sqrt{1 + \frac{B^2 V_{\infty in}^4}{\mu_{pl}^2}}} \quad (8.51)$$

The angle β (see figure 8.5) is obtained with the following relationship:

$$\beta = \varphi + \frac{\delta}{2} - \frac{\pi}{2} \quad (8.52)$$

When r_p is smaller than the radius of the target planet R_{pl} , the spacecraft will impact on the planet's surface. The condition for impact is given by (see equation 8.49):

$$\sqrt{1 + \frac{B^2 V_{\infty in}^4}{\mu_{pl}^2}} \leq \frac{V_{\infty in}^2 R_{pl}}{\mu_{pl}} + 1 \quad (8.53)$$

Using the expression for the local escape velocity at the surface of the target planet, this expression can be rewritten for B :

$$B \leq R \sqrt{1 + \frac{V_{esc_{surface}}^2}{V_{\infty in}^2}} \quad (8.54)$$

The right-hand side of the above equation determines the so-called capture radius r_{cap} for each value of $V_{\infty in}$. When the incoming asymptote of the hyperbola

crosses a sphere with radius r_{cap} around the planet, the spacecraft will impact on the planet's surface.

The dimensions of the planet's sphere of influence can be neglected on interplanetary scale. Then the change of heliocentric energy per unit mass can be written as follows:

$$\Delta\mathcal{E} = \frac{1}{2} (V_{out}^2 - V_{in}^2) = \frac{1}{2} (\bar{V}_{out} + \bar{V}_{in}) \cdot (\bar{V}_{out} - \bar{V}_{in}) \quad (8.55)$$

In this equation \bar{V}_{in} is the heliocentric velocity of the spacecraft as it enters the sphere of influence and \bar{V}_{out} is the spacecraft's heliocentric velocity when it leaves the planet's sphere of influence. Using $\bar{V}_{in} = \bar{V}_{planet} + \bar{V}_{\infty in}$ and $\bar{V}_{out} = \bar{V}_{planet} + \bar{V}_{\infty out}$, the above equation can be rewritten:

$$\Delta\mathcal{E} = \bar{V}_{planet} \cdot (\bar{V}_{\infty out} - \bar{V}_{\infty in}) \quad (8.56)$$

With the vector diagram of figure 8.6 this comes down to:

$$\Delta\mathcal{E} = 2V_{planet}V_{\infty in} \sin \frac{\delta}{2} \cos \beta \quad (8.57)$$

When equations 8.51 and 8.57 are combined, it yields an expression for the total increase in heliocentric energy per unit mass that is dependent on $V_{\infty in}$, B and β :

$$\Delta\mathcal{E} = \frac{2V_{planet}V_{\infty in} \cos \beta}{\sqrt{1 + \frac{B^2 V_{\infty in}^4}{\mu_{pl}^2}}} \quad (8.58)$$

This equation will attain a maximum if $\beta = 0$ and when B takes on its minimum value. This maximum is given by:

$$\Delta\mathcal{E}_{max} = \frac{2V_{planet}V_{\infty in}}{1 + \frac{R_{pl}V_{\infty in}^2}{\mu_{pl}}} \quad (8.59)$$

From this expression it can be seen that the maximum change in energy is large for massive planets (so a large gravitational parameter μ_{pl}), planets with high orbital velocity and small radius. From chapter 4 it was concluded that for trajectories to the giant planets, gravity assists at Venus and Earth are common and going beyond Jupiter commonly requires a gravity assist at Jupiter. Figure 8.7 shows a plot of the maximum energy increase as a function of the hyperbolic

excess velocity for all planets.

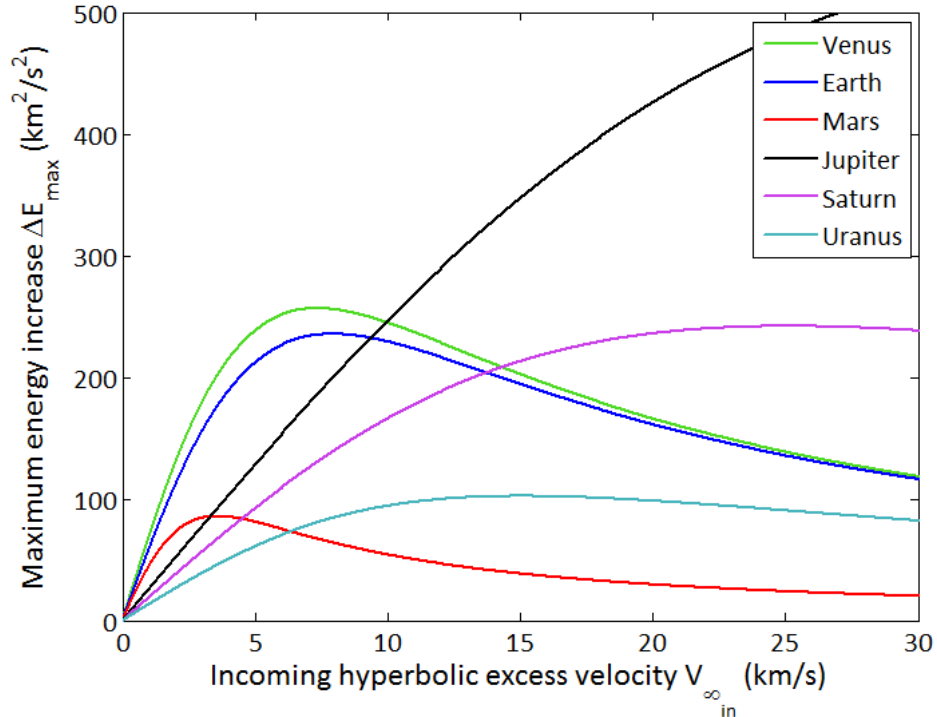


Figure 8.7 Maximum energy increase $\Delta\mathcal{E}_{max}$ during a gravity assist as a function of the incoming hyperbolic excess velocity $V_{\infty in}$.

This figure confirms the earlier made observation. A gravity assist at Jupiter increases the total heliocentric energy of the spacecraft significantly for large values of $V_{\infty in}$. High values of $V_{\infty in}$ could be obtained when performing a gravity assist at Venus or Earth. Both are very well capable of increasing the total heliocentric energy for lower values of $V_{\infty in}$.

8.5 Powered gravity assists

When Lambert targeting is used in designing interplanetary trajectories, the heliocentric velocities at the start and end of each leg are known. It is, however, not necessarily the case that the legs can be joined together with only an unpowered swingby. The required incoming and outgoing hyperbolic excess velocity at the swingby planet can be different or the required swingby angle at the planet is larger than the maximum attainable swingby angle. Therefore some patch is needed to join the two legs of the interplanetary trajectory.

Figure 8.8 shows the geometry of a swingby where the incoming and outgoing hyperbolic velocities are different.

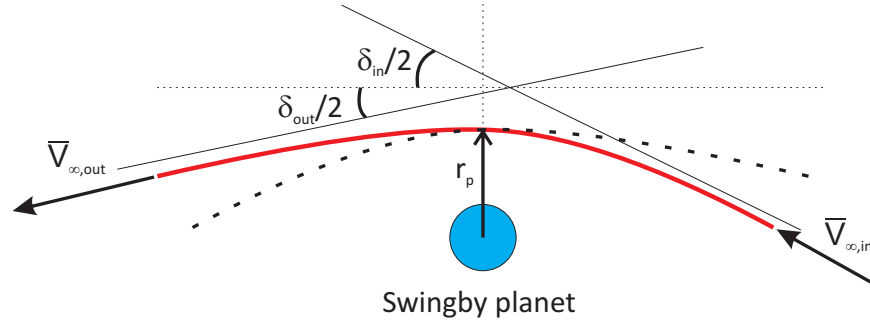


Figure 8.8 Configuration of a powered gravity assist. The ΔV maneuver is performed at the pericenter of the hyperbolic trajectory.

The required bending angle associated with these two hyperbolic excess velocities is composed of two components, one for $V_{\infty in}$ and one for $V_{\infty out}$. This required bending angle δ_{req} is calculated as follows:

$$\delta_{req} = \arccos \left(\frac{\bar{V}_{\infty in} \cdot \bar{V}_{\infty out}}{|\bar{V}_{\infty in}| |\bar{V}_{\infty out}|} \right) \quad (8.60)$$

In order to achieve δ_{req} , the pericenter radius has to be determined accordingly. Using equation 8.51 and the swingby geometry as shown in figure 8.8, δ_{req} can be written as a function of the pericenter radius as follows:

$$\delta_{req} = \frac{\delta_{in}}{2} + \frac{\delta_{out}}{2} = \arcsin \left(\frac{1}{1 + \frac{r_p V_{\infty in}^2}{\mu_{pl}}} \right) + \arcsin \left(\frac{1}{1 + \frac{r_p V_{\infty out}^2}{\mu_{pl}}} \right) \quad (8.61)$$

To solve for the pericenter radius r_p is not straightforward and an iteration procedure is required. Instead of using r_p directly, the eccentricity e is used as an iteration parameter. The pericenter radius has to be the same for both the incoming and outgoing part of the swingby.

$$r_p = a_{in}(1 - e_{in}) = a_{out}(1 - e_{out}) \quad (8.62)$$

The semi-major axes of the incoming and outgoing leg are given by a_{in} and a_{out} respectively. Using equations 6.21 and 6.31, equation 8.61 can be rewritten in terms of the eccentricities e_{in} and e_{out} :

$$\delta_{req} = \arcsin \left(\frac{1}{e_{in}} \right) + \arcsin \left(\frac{1}{e_{out}} \right) \quad (8.63)$$

In order to leave only one unknown parameter in this expression, the eccentricity of the outgoing leg e_{out} is written in terms of e_{in} , yielding the following expression:

$$\delta_{req} = \arcsin\left(\frac{1}{e_{in}}\right) + \arcsin\left(\frac{1}{1 - \frac{a_{in}}{a_{out}}(1 - e_{in})}\right) \quad (8.64)$$

Since a_{in} and a_{out} are determined from equation 6.31, e_{in} is the only unknown parameter. It can be solved through an iterative procedure like Newton-Raphson [MathWorld, 2009b]:

$$e_{in_{j+1}} = e_{in_j} - \frac{f(e_{in_j})}{f'(e_{in_j})} \quad (8.65)$$

In this iterative procedure the function $f(e_{in_j})$ is given by:

$$f(e_{in_j}) = \arcsin\left(\frac{1}{e_{in_j}}\right) + \arcsin\left(\frac{1}{e_{out_j}}\right) - \delta_{req} \quad (8.66)$$

The derivative of $f(e_{in_j})$ with respect to e_{in_j} is denoted by $f'(e_{in_j})$. In order for the iteration procedure to work well, a suitable initial value e_{in_0} has to be used. Since swingbys involve hyperbolic orbits only, e_{in_0} should be larger than 1. There is no real other restriction on the choice for e_{in_0} , so a bit of an arbitrary value of 1.01 is used.

When a converged value for e_{in} has been found, e_{out} is easily determined. The velocity in the pericenter for the incoming and outgoing hyperbola are then determined using the following equations:

$$V_{pin} = V_{\infty in} \sqrt{\frac{e_{in} + 1}{e_{in} - 1}} \quad (8.67)$$

$$V_{pout} = V_{\infty out} \sqrt{\frac{e_{out} + 1}{e_{out} - 1}} \quad (8.68)$$

The ΔV needed at the pericenter of the swingby to patch the incoming and outgoing hyperbolic leg together can be calculated as follows:

$$\Delta V_{SB\infty} = |V_{pout} - V_{pin}| \quad (8.69)$$

If the required bending angle δ_{req} is smaller than the maximum attainable bending angle, the pericenter engine burn to patch the incoming and outgoing

hyperbolic legs is sufficient. If the required bending angle is still larger than the maximum attainable bending angle another engine burn maneuver is needed. The hyperbolic excess velocity vector needs to be rotated over an angle $\Delta\delta = \delta_{req} - \delta_{max}$. The corresponding ΔV that is needed is given by the following expression [Wertz, 2001]:

$$\Delta V_{SB_\delta} = 2V_\infty \sin\left(\frac{\Delta\delta}{2}\right) \quad (8.70)$$

This maneuver can be applied anywhere on the hyperbolic trajectory. It is, however, advantageous to apply ΔV_{SB_δ} when V_∞ is minimal. This can be either somewhere on the incoming leg or somewhere on the outgoing leg, depending whether or not $V_{\infty_{in}} < V_{\infty_{out}}$ or not.

Deep Space Maneuvers

One of the main objectives of this thesis is to develop a method to optimize interplanetary trajectories with DSMs, as mentioned in chapter 2. The previous chapters have introduced all necessary background information on orbital mechanics. In this chapter the focus will be on characterizing trajectories with DSMs.

The basic principles of DSMs are discussed in section 9.1. The way in which these trajectories with DSMs can be modeled is covered in section 9.2.

9.1 Basic principles of deep space maneuvers

The importance of DSMs becomes clear when considering a transfer from planet P_1 to planet P_2 [Vasile and De Pascale, 2006]. First the two-impulse transfer is considered. This transfer can be modeled as a function of the departure epoch t_0 and the transfer time T . The arrival epoch t_1 is given by:

$$t_1 = t_0 + T \quad (9.1)$$

The two required heliocentric velocities at the start and at the end of the leg are calculated using Lambert's problem from body P_1 to body P_2 for a time of flight T (see section 8.2). The ΔV impulsive maneuvers needed at launch and capture are then calculated using the procedure of section 8.3. So the two-impulse transfer problem is completely defined when t_0 and t_1 are known, since the positions and the time of flight are known. In terms of minimizing the required total ΔV for such a trajectory, the objective function f_{2-Imp} that has to be minimized is:

$$f_{2-Imp} = \Delta V_1 + \Delta V_2 \quad (9.2)$$

The two-impulse transfer problem can be extended to a three-impulse transfer by adding a DSM somewhere between P_1 and P_2 , at a point M , see figure 9.1.

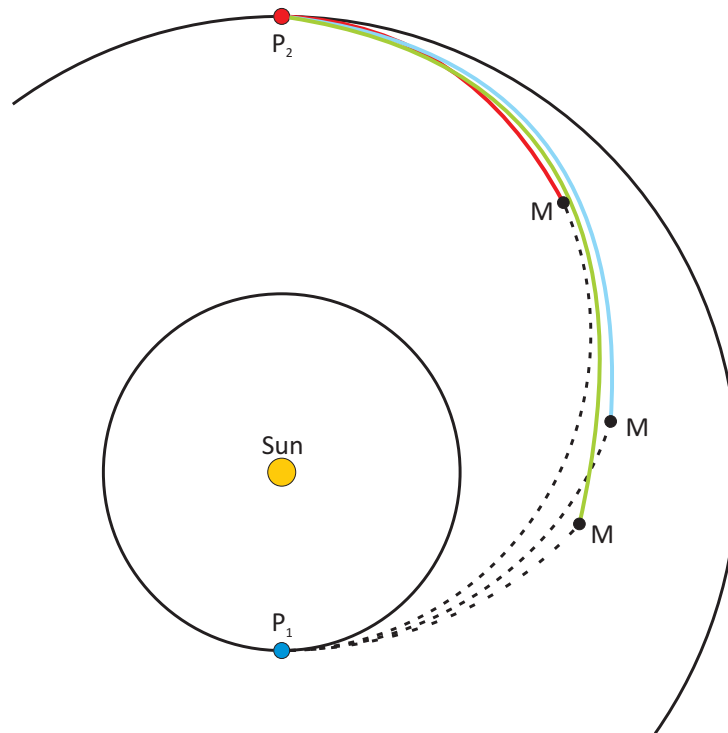


Figure 9.1 Possible layouts of a 3-impulse trajectory, after [Vasile and De Pascale, 2006]. One impulse is needed at launch, a second impulse, the DSM, is required somewhere along the trajectory at point M and a third impulse is needed at arrival.

The DSM is considered an impulsive shot, like the impulsive maneuvers at launch and capture. The epoch of the application of the DSM is the launch epoch t_0 added by a fraction of the total time of flight in between P_1 and P_2 . This is denoted by [Vasile and De Pascale, 2006]:

$$t_{DSM} = t_0 + T_{DSM} = t_0 + \eta T \quad (9.3)$$

In this equation $0 < \eta < 1$ and the total time of flight T is a known parameter. The magnitude of the DSM is denoted by ΔV_{DSM} . As can be seen in figure 9.1, the addition of a DSM between P_1 and P_2 opens up a range of possible trajectories that can't be flown using a direct transfer. The objective function f_{3-Imp} for the three-impulse transfer becomes [Vasile and De Pascale, 2006]:

$$f_{3-Imp} = \Delta V_1 + \Delta V_{DSM} + \Delta V_2 \quad (9.4)$$

The three-impulse transfer has more variables than the two-impulse transfer. Next to the launch and arrival epochs, also the fraction of the time of flight at which the DSM is applied is a variable. Furthermore, the arc after Earth departure up until the moment of application of the DSM can be a variable (see the dashed arcs

in figure 9.1). The variable arc after Earth departure will introduce 3 additional variables, which will be shown in section 9.2. Solving a Lambert problem from the DSM to the target planet then ensures that the target planet will be reached.

9.2 Trajectory model

In order to outline the trajectory model when DSMs are considered, an example interplanetary trajectory is used. In this example the launch planet is Earth, the target planet is Jupiter and there is an unpowered swingby at Mars. On each leg of the trajectory a DSM is present. A DSM is denoted by 'd' in a planetary swingby sequence, therefore the trajectory is also described as EdMdJ. This configuration is shown in figure 9.2.

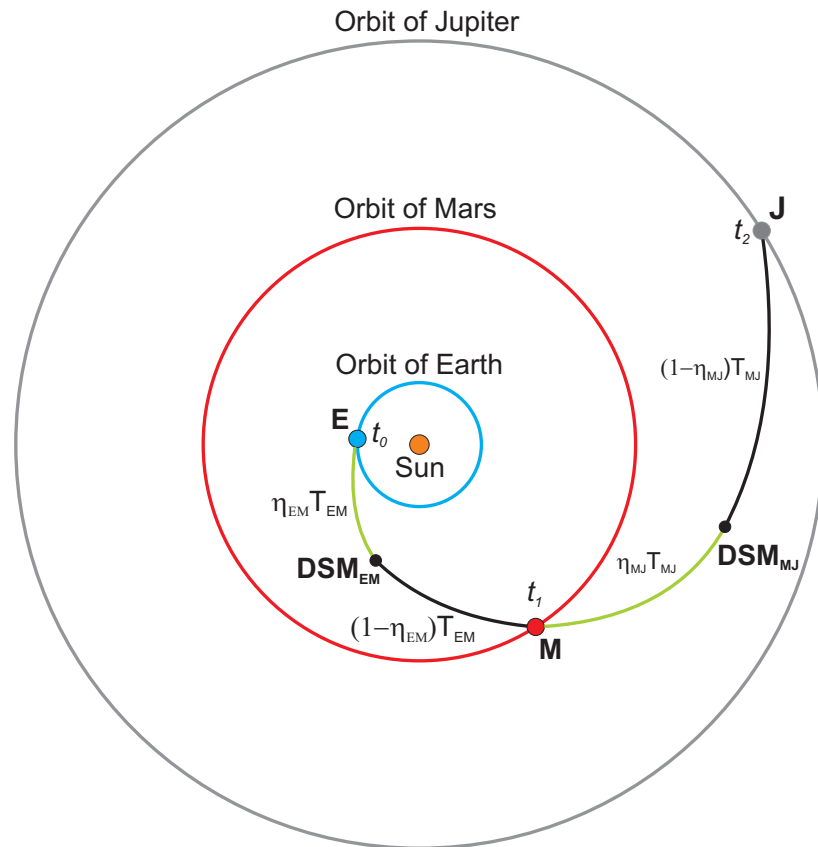


Figure 9.2 Geometry of an interplanetary trajectory from Earth to Jupiter with an unpowered gravity assist at Mars. A DSM is present on each leg of the trajectory.

If this sequence of planets would be analyzed using only Lambert targeting, the problem would be completely defined by the encounter epochs t_0 , t_1 and t_2 and it would be denoted by EMJ. If the total ΔV for such a mission would be minimized,

the decision vector (a vector containing all variables to the optimization problem) would then look as follows:

$$\bar{x}_{Lam} = [t_0, t_1, t_2] \quad (9.5)$$

It can be seen in figure 9.2 that introducing two deep space maneuvers, DSM_{EM} and DSM_{MJ} , already adds two additional variables to the problem. Both DSMs can be applied on any point along along the respective interplanetary legs.

The DSMs are applied at the end of the green arcs in figure 9.2. These particular arcs are analyzed using Kepler propagation and not Lambert targeting. A thorough analysis of propagating a spacecraft trajectory along a Kepler arc can be found in chapter 10. Two things are important at this stage of the analysis:

- The initial position \bar{r}_0 and initial velocity \bar{V}_0 need to be known as well as the time of flight that will be flown along the Kepler arc.
- The position \bar{r} and velocity \bar{V} at the end of the Kepler arc are determined using Kepler propagation.

This problem is different from Lambert targeting, where the initial and final positions are all known, as well as the time of flight. The corresponding orbit is then determined by patching the legs together at the planetary encounters. In this case, however, there is an intermediate maneuver, but it is not clear what the velocity at the start of a leg actually is.

In the current EdMdJ example, if the arc after Earth departure is considered, the heliocentric velocity \bar{V}_L at the start of the leg is given by:

$$\bar{V}_L = \bar{V}_{pL} + \bar{V}_{\infty L} \quad (9.6)$$

The planet's heliocentric velocity \bar{V}_{pL} is known at each instant in time through planetary ephemeris. The hyperbolic excess velocity vector is an unknown parameter at this point and thus needs to be generated randomly. This is described in detail in section 9.2.1.

The same problem holds at a planetary swingby. The heliocentric velocity at the end of the Lambert arc going from the DSM to the swingby planet is known. Therefore the incoming hyperbolic excess velocity at the swingby is also known using equation 8.43. The required heliocentric velocity at the end of the swingby in this case is not known, because the direction of the outgoing hyperbolic excess velocity is not specified. After the swingby a Kepler arc will follow, because a DSM is present on the leg between Mars and Jupiter. The outgoing hyperbolic excess

velocity has to be determined somehow. If the swingby is forced to be unpowered, then $\bar{V}_{\infty_{in}}$ can be given a random rotation. After that rotation, $\bar{V}_{\infty_{out}}$ is known and therefore also the heliocentric velocity right after the swingby. The details about this vector rotation are found in section 9.2.2.

9.2.1 Randomly generating \bar{V}_{∞_L}

When a DSM is present on the leg after Earth departure, \bar{V}_{∞_L} has to be generated randomly as mentioned earlier. The magnitude of the outgoing hyperbolic excess velocity, $|\bar{V}_{\infty_L}|$, and its direction are needed to determine \bar{V}_{∞_L} . Two variables are needed to determine the direction of \bar{V}_{∞} , namely θ and φ . They are defined as follows (see also figure 9.3) [Vinko et al., 2007]:

$$\begin{aligned}\theta &= \theta_{min} + u(\theta_{max} - \theta_{min}) \\ \varphi &= \varphi_{min} + v(\varphi_{max} - \varphi_{min}) \\ \bar{V}_{\infty_L} &= |\bar{V}_{\infty_L}| [\cos \varphi \cos \theta \bar{i} + \cos \varphi \sin \theta \bar{j} + \sin \varphi \bar{k}]\end{aligned}\tag{9.7}$$

In the above expressions $u, v \in [0, 1]$. If the search space for θ and φ is used, then $\theta \in [0, 2\pi]$ and $\varphi \in [-\frac{\pi}{2}, +\frac{\pi}{2}]$.

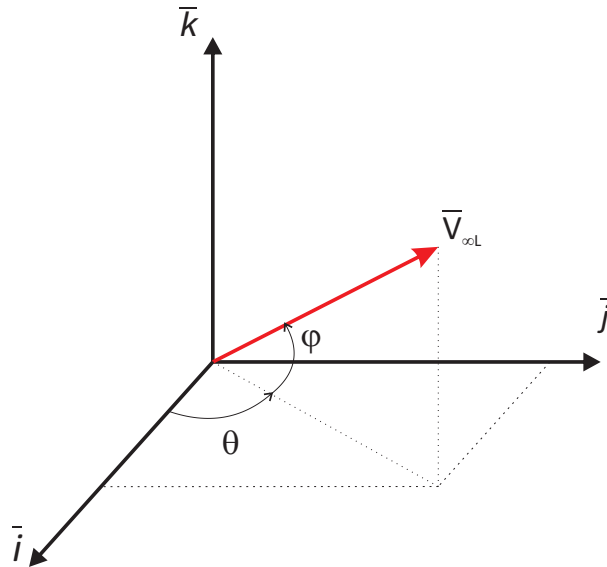


Figure 9.3 Frame $\bar{i}\bar{j}\bar{k}$ used for defining \bar{V}_{∞_L} , as defined in [Vinko et al., 2007].

The magnitude of the hyperbolic excess velocity vector is chosen randomly as well from a predefined search domain, so $|\bar{V}_{\infty_L}| \in [|\bar{V}_{\infty_{Lmin}}|, |\bar{V}_{\infty_{Lmax}}|]$. The coordinate frame $\bar{i}\bar{j}\bar{k}$ is defined as follows [Vinko et al., 2007]:

$$\bar{i} = \frac{\bar{V}_{pl_L}(t_0)}{|\bar{V}_{pl_L}(t_0)|}$$

$$\bar{k} = \frac{\bar{r}_{pl_L}(t_0) \times \bar{V}_{pl_L}(t_0)}{|\bar{r}_{pl_L}(t_0) \times \bar{V}_{pl_L}(t_0)|}$$

$$\bar{j} = \bar{k} \times \bar{i}$$

The heliocentric velocity and position vector of the departure planet are given by $\bar{V}_{pl_L}(t_0)$ and $\bar{r}_{pl_L}(t_0)$.

After the first four parameters are known (t_0 , $|\bar{V}_{\infty_L}|$, θ and φ), the trajectory after Earth departure can be propagated along a Kepler orbit (see chapter 10) [Vinko et al., 2007]. The trajectory is propagated for a time $\eta_{EM}T_{EM}$, where T_{EM} is the total time of flight between Earth and the gravity assist at Mars, and η_{EM} is the fraction of that total flight time that has passed until performing the DSM [Vinko et al., 2007]. Since the position of the DSM is known, a Lambert problem can be solved to ensure that the spacecraft position matches the position of the next planet in the remaining time $(1-\eta_{EM})T_{EM}$.

With respect to the complete Lambert trajectory EMJ, the number of variables has increased. The decision vector, if there were no DSM in the leg between Mars and Jupiter, would now look as follows:

$$\bar{x}_{EdMJ} = [t_0, t_1, t_2, |\bar{V}_{\infty_L}|, \theta, \varphi, \eta_{EM}] \quad (9.8)$$

The index 'EdMJ' is added to clarify that this would be the decision vector if there were a DSM in between Earth and Mars only. The swingby at Mars could possibly be powered, since two Lambert arcs are patched together in that case. However, there actually is a DSM in between Mars and Jupiter, which will add new variables to the problem. The swingby at Mars is therefore forced to be unpowered.

9.2.2 Random rotation of $\bar{V}_{\infty_{in}}$ at an unpowered swingby

The geometry of the unpowered gravity assist has to be taken into account now. In essence, the powered swingby that was used when patching two Lambert arcs together has been replaced by an unpowered swingby followed by a DSM. The swingby geometry is defined by the pericenter radius r_p and the plane change angle ζ [Vinko et al., 2007]. The pericenter radius is needed to determine the swingby angle δ .

With a gravity assist, the incoming hyperbolic excess velocity vector $\bar{V}_{\infty_{in}}$ is rotated over an angle δ , while its magnitude remains constant. $\bar{V}_{\infty_{in}}$ is obtained by vectorially subtracting the planet's heliocentric velocity vector from the spacecraft's heliocentric velocity vector at the end of the incoming Lambert arc $\bar{V}_{HCSB_{in}}$:

$$\bar{V}_{\infty_{in}} = \bar{V}_{HCSB_{in}} - \bar{V}_{pl_{SB}} \quad (9.9)$$

Figure 9.4 shows the configuration of $\vec{V}_{\infty out}$, the outgoing hyperbolic velocity vector. The components along the axes \bar{b}_1 , \bar{b}_2 and \bar{b}_3 are shown in red. The angles δ and ζ are indicated as well.

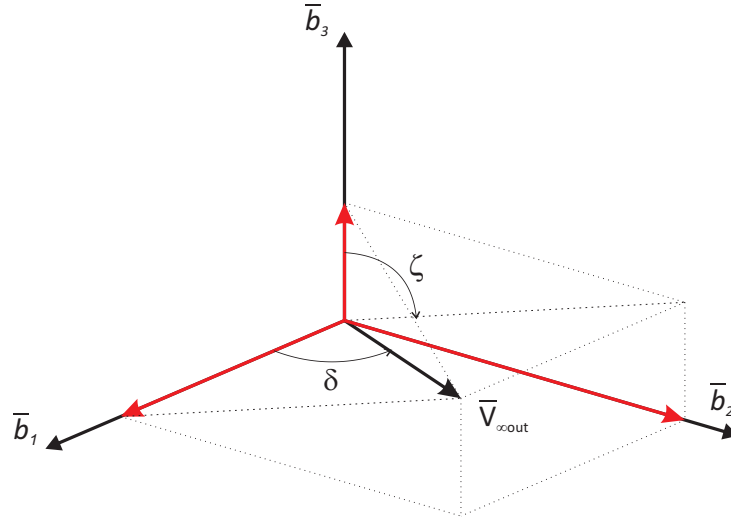


Figure 9.4 Frame $\bar{b}_1\bar{b}_2\bar{b}_3$ used for defining δ and ζ for an unpowered swingby, adapted from [Vinko et al., 2007].

The coordinate frame $\bar{b}_1\bar{b}_2\bar{b}_3$ is defined in the following way [Vinko et al., 2007]:

$$\bar{b}_1 = \frac{\vec{V}_{\infty in}}{|\vec{V}_{\infty in}|}$$

$$\bar{b}_2 = \frac{\bar{b}_1 \times \vec{r}_{pl}}{|\bar{b}_1 \times \vec{r}_{pl}|}$$

$$\bar{b}_3 = \bar{b}_1 \times \bar{b}_2$$

So \bar{b}_1 is aligned with the incoming hyperbolic excess velocity vector. The deflection angle δ is a function of the eccentricity of the planetocentric hyperbola, which itself is a function of the pericenter radius r_p [Vinko et al., 2007]:

$$\delta = 2 \arcsin \left(\frac{1}{e} \right) \quad (9.10)$$

$$e = 1 + \frac{r_p V_{\infty in}^2}{\mu_{pl}} \quad (9.11)$$

The pericenter radius is determined by the planet's radius and the pericenter altitude h_p . The unknown parameter in this case is h_p , which therefore has to be generated randomly within a predefined range of possible values ($h_p \in [h_{pmin}, h_{pmax}]$). Once h_p has been generated, the outgoing hyperbolic excess velocity vector is now defined using the plane change angle ζ (see also figure 9.4):

$$\bar{V}_{\infty out} = |\bar{V}_{\infty in}| [\cos \delta \bar{b}_1 + \sin \delta \sin \zeta \bar{b}_2 + \sin \delta \cos \zeta \bar{b}_3] \quad (9.12)$$

In this vector rotation $|\bar{V}_{\infty in}|$ is used, because its value is known and it is equal to $|\bar{V}_{\infty out}|$ during the unpowered swingby. The plane change angle ζ is an unknown parameter and therefore has to be generated randomly. From figure 9.4 it can be concluded that $\zeta \in [0, 2\pi]$.

With h_p (and thus δ) and ζ known, $\bar{V}_{\infty out}$ is now known. Therefore the heliocentric velocity vector $\bar{V}_{HCSBout}$ can now be obtained by adding the planet's heliocentric velocity vector \bar{V}_{plSB} to $\bar{V}_{\infty out}$:

$$\bar{V}_{HCSBout} = \bar{V}_{\infty out} + \bar{V}_{plSB} \quad (9.13)$$

Now that the initial velocity of the leg between Mars and Jupiter is known, the trajectory can be propagated along a Kepler arc for a time $\eta_{MJ}T_{MJ}$, at which time a DSM is performed. After the DSM the final part of the trajectory is obtained by analyzing a Lambert problem from the DSM to Jupiter.

The decision vector for the complete EdMdJ trajectory can now be written as follows:

$$\bar{x}_{EdMdJ} = [t_0, t_1, t_2, |\bar{V}_{\infty L}|, \theta, \varphi, \eta_{EM}, r_p, \zeta, \eta_{MJ}] \quad (9.14)$$

9.2.3 Consequences on the size of the search space

The addition of DSMs in both legs of the EMJ trajectory has increased the number of variables from 3 (using Lambert arcs only) to 10. The addition of these extra variables increases the size of the search space in the optimization process drastically. For each of the variables a range of values is possible and finding the optimum solution (the minimum total ΔV) becomes more difficult with the addition of each variable.

In general it can be stated that if a DSM is present on the leg after launch at Earth, the number of variables increases by 4. If a DSM is present on any of the subsequent legs in the interplanetary trajectory, the number of variables

increases by 3 for each DSM. As an example, consider a trajectory from Earth to Uranus with five swingbys. If a DSM would then be present in each leg of the trajectory, the number of variables would be 26. The first 7 variables are the encounter epochs at each planet, the next 4 are due to the DSM on the first leg of the trajectory and the final 15 are due to 5 swingbys, each followed by a DSM.

Propagation along a Kepler orbit

It was mentioned in section 9.2 that when a DSM is applied between two planetary encounters on an interplanetary trajectory, the leg will be split up into two distinct parts. The first part, which is analyzed by means of a Kepler problem, starts at the initial planet and ends at the time when the DSM is applied. The second part of the leg, which is analyzed as a Lambert problem (see section 8.2), starts at the time of applying the DSM and ends at the next planetary encounter.

The focus in this chapter is on the propagation of an orbit along a Kepler arc. The chapter is structured in the following way. Kepler's problem for the different types of conic sections is discussed in section 10.1. The solution to Kepler's problem for the different types of conic sections is outlined in section 10.2. Kepler's problem can be written in such a way that its formulation is the same for all conic sections. The derivation, as well as the solution process can be found in section 10.3.

10.1 Introducing the Kepler problem

In chapter 6 the different types of conic sections have been introduced. The focus has been on the characteristics of position and velocity within the particular orbit. It is also possible to derive expressions for the relation between the time of flight and the position within the orbit.

10.1.1 Kepler's equation for elliptical orbits

To start the discussion on Kepler's equation for elliptical orbits, equation 6.28 is repeated here for clarity.

$$r = a(1 - e \cos E) \tag{10.1}$$

When this equation is differentiated with respect to time, this yields:

$$\dot{r} = ae\dot{E} \sin E \tag{10.2}$$

The dot indicates a time derivative. When combining equations 6.13 and 6.14 the following expression for r is obtained:

$$r = \frac{H^2/\mu}{1 + e \cos \theta} \quad (10.3)$$

If this expression is differentiated with respect to time, *Wakker* [2002] shows that this gives:

$$\dot{r} = \frac{\mu}{H} e \sin \theta \quad (10.4)$$

One of the properties of an elliptical orbit (see figure 6.2) is that $\frac{b}{a} = \sqrt{1 - e^2}$. It is then shown in [*Wakker*, 2002] that the following relationship holds:

$$r \sin \theta = a \sqrt{1 - e^2} \sin E \quad (10.5)$$

It is shown by *Wakker* [2002] that the following differential equation in E can now be obtained:

$$\dot{E}(1 - e \cos E) = \sqrt{\frac{\mu}{a^3}} \quad (10.6)$$

When this expression is integrated an expression is obtained relating the eccentric anomaly and time:

$$E - e \sin E = \sqrt{\frac{\mu}{a^3}}(t - \tau) \quad (10.7)$$

In this expression τ is an integration constant, indicating the time of the last pericenter passage. The expression $\sqrt{\frac{\mu}{a^3}}$ is called the mean angular velocity n of the body and the complete right-hand side of this equation is called the mean anomaly M . So equation 10.7 may also be written as [*Wakker*, 2002]:

$$E - e \sin E = n(t - \tau) = M \quad (10.8)$$

This expression is also known as Kepler's equation. This equation holds for elliptical orbits, but similar time of flight equations can be derived for hyperbolic

and parabolic orbits, as will be derived in sections 10.1.2 and 10.1.3.

If the time of flight needs to be calculated between a point defined by its true anomaly θ_0 (not necessarily at the time of last pericenter passage) and some other point along the orbit defined by θ , then the following expression for the time of flight can be derived, based on Kepler's equation [Bate et al., 1971]:

$$t - t_0 = \sqrt{\frac{a^3}{\mu}} [2k\pi + (E - e \sin E) - (E_0 - e \sin E_0)] \quad (10.9)$$

This expression is very general, since also multiple pericenter passages in between θ_0 and θ are considered by it, which is indicated by k , the number of pericenter passages.

10.1.2 Kepler's equation for hyperbolic orbits

Just like for elliptical orbits, an expression can be derived for hyperbolic orbits that relates the time of flight to, in this case, the hyperbolic anomaly F . Starting from the vis-viva equation (equation 6.21), and using the radial and tangential components of the velocity (\dot{r} and $r\dot{\theta}$ respectively), the following expression can be derived [Wakker, 2002]:

$$V^2 = \dot{r}^2 + (r\dot{\theta})^2 = \mu \left(\frac{2}{r} - \frac{1}{a} \right) \quad (10.10)$$

By substituting the equation for the angular momentum, $H = r^2\dot{\theta} = \sqrt{\mu a(1 - e^2)}$, this equation can be rewritten into the following form [Wakker, 2002]:

$$\dot{r}^2 = \left(\frac{\mu}{-a} \right) \left[\frac{a^2(1 - e^2)}{r^2} - \frac{2a}{r} + 1 \right] \quad (10.11)$$

Differentiating equation 6.33 with respect to time gives an expression relating \dot{r} to F and \dot{F} [Wakker, 2002]:

$$\dot{r} = -ae\dot{F} \sinh F \quad (10.12)$$

Substitution of equations 6.33 and 10.12 into equation 10.11 leads to the following differential equation in F after some steps:

$$\dot{F}(1 - e \cosh F) = \pm \sqrt{\frac{\mu}{-a^3}} \quad (10.13)$$

Wakker [2002] argues that \dot{F} is always positive and furthermore, that $e \cosh F > 1$, which means that only the plus-sign in equation 10.13 should be used. Integration of this equation gives:

$$e \sinh F - F = \sqrt{\frac{\mu}{-a^3}}(t - \tau) \quad (10.14)$$

Like for the elliptical case, τ is an integration constant indicating the time of pericenter passage. For the hyperbolic orbit, a mean angular velocity is defined as follows [*Wakker*, 2002]:

$$\bar{n} = \sqrt{\frac{\mu}{-a^3}} \quad (10.15)$$

Also a type of mean anomaly for hyperbolic orbits is defined as [*Wakker*, 2002]:

$$\bar{M} = \bar{n}(t - \tau) \quad (10.16)$$

Equation 10.14 can now be written as [*Wakker*, 2002]:

$$e \sinh F - F = \bar{n}(t - \tau) = \bar{M} \quad (10.17)$$

When comparing this equation with equation 10.8 it shows a clear resemblance with Kepler's equation for elliptical orbits. Therefore from this point on, equation 10.17 will be referred to as Kepler's equation for hyperbolic orbits.

As was the case for elliptical orbits, an expression can be derived from Kepler's equation for hyperbolic orbits that calculates the time of flight based on a , e , θ_0 and θ (or equivalently F_0 and F) [*Bate et al.*, 1971]:

$$t - t_0 = \sqrt{\frac{\mu}{(-a)^3}} [(e \sinh F - F) - (e \sinh F_0 - F_0)] \quad (10.18)$$

10.1.3 Kepler's equation for parabolic orbits

For parabolic orbits the analysis starts with the equation for the angular momentum:

$$H = r^2 \dot{\theta} = \sqrt{\mu p} \quad (10.19)$$

Because the semi-major axis of a parabolic orbit is ∞ , an alternative formulation has to be found. For a parabolic orbit it holds that $e = 1$, so then equation 6.13 can be rewritten as follows [Vallado and McClain, 2007]:

$$r = \frac{p}{1 + e \cos \theta} = \frac{p}{1 + \cos \theta} = \frac{p}{2 \cos^2 \left(\frac{\theta}{2}\right)} \quad (10.20)$$

This expression can be simplified in such a way that a compact expression for r in a parabolic orbit is obtained [Vallado and McClain, 2007]:

$$r = \frac{p}{2} \left(\frac{\cos^2 \left(\frac{\theta}{2}\right) + \sin^2 \left(\frac{\theta}{2}\right)}{\cos^2 \left(\frac{\theta}{2}\right)} \right) = \frac{p}{2} \left(1 + \tan^2 \left(\frac{\theta}{2}\right) \right) \quad (10.21)$$

The resulting equation for r can now be substituted into equation 10.19. After some rewriting the following equation is obtained [Bate et al., 1971]:

$$\sqrt{\mu p} dt = r^2 d\theta = \frac{p^2}{4} \left(1 + \tan^2 \left(\frac{\theta}{2}\right) \right)^2 d\theta \quad (10.22)$$

Equation 10.22 has to be integrated to obtain the time of flight equation for parabolic orbits [Vallado and McClain, 2007]:

$$\int_{t_0}^t 4\sqrt{\frac{\mu}{p^3}} dt = \int_0^\theta \left(1 + 2 \tan^2 \left(\frac{\theta}{2}\right) + \tan^4 \left(\frac{\theta}{2}\right) \right) d\theta \quad (10.23)$$

The solutions to these integrations can be found in standard integral tables, so only the result of the integration (after rearranging) is shown:

$$2\sqrt{\frac{\mu}{p^3}}(t - t_0) = \tan \left(\frac{\theta}{2}\right) + \frac{\tan^3 \left(\frac{\theta}{2}\right)}{3} \quad (10.24)$$

Like for elliptical and the hyperbolic orbits, a mean motion n_p can be defined as well as a parabolic anomaly D [Vallado and McClain, 2007].

$$n_p \equiv 2\sqrt{\frac{\mu}{p^3}} \quad (10.25)$$

$$D \equiv \tan \left(\frac{\theta}{2}\right) \quad (10.26)$$

Substituting n_p and D into equation 10.24 leads to a time of flight equation that is a third order polynomial in D [Vallado and McClain, 2007]:

$$n_p(t - t_0) = D + \frac{D^3}{3} \quad (10.27)$$

The time of flight equation for parabolic orbits can be written in a general way so it includes the initial and final locations of the spacecraft [Vallado and McClain, 2007]:

$$t - t_0 = \frac{1}{2} \sqrt{\frac{p^3}{\mu}} \left[D + \frac{D^3}{3} - \left(D_0 + \frac{D_0^3}{3} \right) \right] \quad (10.28)$$

10.2 Position and velocity at a certain point in time

Using the Kepler time of flight equation, it is straightforward to determine the time of flight if a , e , θ and θ_0 are known. Using equation 6.28 the eccentric anomaly at the start and end point can then be computed and all parameters can be put into equation 10.9, yielding the time of flight. It is, however, not all that straightforward to determine where a body is at a certain moment in time. This prediction problem is also referred to as Kepler's problem and can be stated as follows [Bate et al., 1971]:

Given: \bar{r}_0, \bar{V}_0 and t_0
Find: \bar{r}, \bar{V} at time t

This problem states exactly what is needed when modeling Kepler arcs for trajectories with DSMs. For example, when Earth is the initial launch body, its position and velocity (in the heliocentric inertial equatorial reference frame) are obtained from the JPL DE200 planetary ephemeris for the specific launch date. JPL DE200 is applied in the software package GALOMUSIT, which will be used for the optimization of the interplanetary trajectories (see chapter 12). As mentioned in section 9.2.1, a hyperbolic excess velocity vector \bar{V}_∞ with random magnitude and direction is generated. This vector is then added to the planet's velocity vector. This gives the initial heliocentric velocity vector, which is needed as an input for the Kepler problem.

The total time of flight that the spacecraft moves along the Kepler orbit is obtained from taking a fraction of the total time the spacecraft needs to go from Earth to the subsequent planet. By solving the Kepler problem the position and velocity vector at the end of the Kepler orbit are obtained. Since at this point

in time (when the DSM will be performed) the position is known, as well as the position and time of the next planetary encounter, a Lambert problem can be solved. This will give the necessary velocity at the start and end points of the Lambert arc. The discontinuity in the velocity vectors prior to and right after the DSM represents the magnitude and direction of the DSM.

In the following sections procedures are discussed for the solution of Kepler's problem for all types of conic sections.

10.2.1 Solution of Kepler's problem for elliptical orbits

In order to start solving Kepler's problem, Kepler's equation is rewritten slightly [Wakker, 2002]:

$$f(E, M) = E - e \sin E - M \quad (10.29)$$

For a certain value of M , the following holds:

$$\begin{aligned} f(-\infty, M) &= -\infty \\ f(+\infty, M) &= +\infty \\ \frac{df}{dE} &= 1 - e \cos E > 0 \end{aligned} \quad (10.30)$$

This implies that for every value of M , there is always one single value for E for which it holds that $f(E, M) = 0$, which is the solution of Kepler's problem.

In order to solve for E an iterative approach is required, like the Newton-Raphson procedure as proposed in [Wakker, 2002]. This procedure looks as follows:

$$E_{k+1} = E_k - \frac{f(E_k, M)}{\frac{d}{dE}(f(E_k, M))_{E=E_k}} = E_k - \frac{E_k - e \sin E_k - M}{1 - e \cos E_k} \quad (10.31)$$

As an initial guess for this iteration procedure $E_0 = M$ can be used [Wakker, 2002].

10.2.2 Solution of Kepler's problem for hyperbolic orbits

Kepler's problem for hyperbolic orbits can be solved using a procedure analogous to the one for elliptical orbits. As a starting point Kepler's equation is rewritten [Wakker, 2002]:

$$f(F, \bar{M}) = e \sinh F - F - \bar{M} \quad (10.32)$$

In order to examine whether $f(F, M)$ has one unique solution for an arbitrary value of \bar{M} , $\sinh F$ is written as a series expansion:

$$\sinh F = F + \frac{F^3}{3!} + \frac{F^5}{5!} + \frac{F^7}{7!} + \dots \quad (10.33)$$

For a certain value of \bar{M} , the following holds:

$$\begin{aligned} f(-\infty, \bar{M}) &= -\infty \\ f(+\infty, \bar{M}) &= +\infty \\ \frac{df}{dF} &= e \cosh F - 1 > 0 \end{aligned} \quad (10.34)$$

This implies that there is one single value for F for which it holds that $f(F, \bar{M}) = 0$, which is the solution of Kepler's problem for hyperbolic orbits [Wakker, 2002].

To solve Kepler's problem for a hyperbolic orbit, a Newton-Raphson iteration procedure can be applied, as was the case for elliptical orbits. In the hyperbolic case, the procedure looks as follows [Wakker, 2002]:

$$F_{k+1} = F_k - \frac{f(F_k, \bar{M})}{\frac{d}{dF} (f(F_k, \bar{M}))_{F=F_k}} = F_k - \frac{e \sinh F_k - F_k - \bar{M}}{e \cosh F_k - 1} \quad (10.35)$$

For the initial guess F_0 , the situation is a bit more complicated than for elliptical orbits. Wakker [2002] shows that the initial guess for the solution of Kepler's problem in a hyperbolic orbit depends on the value of \bar{M} :

- $|\bar{M}| < 6e$: $F_0 = x \sinh y$

$$x = \sqrt{\frac{8(e-1)}{e}}$$

$$y = \frac{1}{3} \operatorname{arcsinh} \left(\frac{3\bar{M}}{x(e-1)} \right)$$

- $\bar{M} > 6e$: $F_0 = \ln \left(\frac{2\bar{M}}{e} \right)$
- $\bar{M} < -6e$: $F_0 = \ln \left(\frac{-2\bar{M}}{e} \right)$

10.2.3 Solution of Kepler's problem for parabolic orbits

With respect to the elliptical and hyperbolic case, the solution of Kepler's equation for parabolic orbits is more straightforward. Equation 10.27 is a third order polynomial in D . Since the time instances t and t_0 are known, the polynomial expression can be solved:

$$f(D, M_{par}) = \frac{1}{3}D^3 + D - M_{par} = 0 \quad (10.36)$$

In the polynomial expression M_{par} is introduced, which is equal to $n_p(t - t_0)$. For every M_{par} , there is one single solution for D [Wakker, 2002]. This is because:

$$\begin{aligned} f(-\infty, M_{par}) &= -\infty \\ f(+\infty, M_{par}) &= +\infty \\ \frac{df}{dD} &= D^2 + 1 > 0 \end{aligned} \quad (10.37)$$

As was the case for elliptical and hyperbolic orbits, the value for D can be obtained using a Newton-Raphson iteration procedure. As an initial guess $D_0 = M_{par}$ can be used.

10.3 Universal variable formulation

The classical formulations for the time of flight involving either the eccentric or hyperbolic anomaly do not work well for near-parabolic orbits [Bate *et al.*, 1971]. Iteration procedures like Newton-Raphson converge very slowly or do not converge at all. Therefore a new formulation for the time of flight equations will be derived in this section that uses a new auxiliary variable that is different from either the eccentric or hyperbolic anomaly [Bate *et al.*, 1971]. The use of this variable will allow for formulation of the time of flight equation that is valid for all types of orbits.

10.3.1 The Sundman transformation

The change in variable is known as the so-called Sundman transformation, after Karl F. Sundman (1873-1949) [Bate *et al.*, 1971]. The derivation of this variable starts with the equations for the total energy and angular momentum of the satellite in the orbit:

$$H = r^2\dot{\theta} = \sqrt{\mu p} \quad (10.38)$$

$$\mathcal{E} = \frac{1}{2}V^2 - \frac{\mu}{r} = \frac{1}{2}(\dot{r}^2 + (r\dot{\theta})^2) - \frac{\mu}{r} = -\frac{\mu}{2a} \quad (10.39)$$

When solving for \dot{r}^2 in equation 10.39 and using $(r\dot{\theta})^2 = \frac{\mu p}{r^2}$ from equation 10.38, the following expression is obtained [Bate et al., 1971]:

$$\dot{r}^2 = -\frac{\mu p}{r^2} + \frac{2\mu}{r} - \frac{\mu}{a} \quad (10.40)$$

The solution of this differential equation is not straightforward, so therefore a new independent universal variable x is introduced through the Sundman transformation [Bate et al., 1971]:

$$\dot{x} = \frac{dx}{dt} = \frac{\sqrt{\mu}}{r} \quad (10.41)$$

When equation 10.40 is divided by the square of equation 10.41 the following relationship is obtained, which has no explicit time derivatives anymore [Bate et al., 1971]:

$$\left(\frac{dr}{dx}\right)^2 = -p + 2r - \frac{r^2}{a} \quad (10.42)$$

Rewriting this expression and separating the variables yields [Bate et al., 1971]:

$$dx = \frac{dr}{\sqrt{-p + 2r - \frac{r^2}{a}}} \quad (10.43)$$

Bate et al. [1971] shows that the integration of this expression results in the following equation for x :

$$x + C = \sqrt{a} \arcsin\left(\frac{\frac{r}{a} - 1}{\sqrt{1 - \frac{p}{a}}}\right) \quad (10.44)$$

In this equation C is a constant of integration. Using $p = a(1 - e^2)$, so $e = \sqrt{1 - \frac{p}{a}}$, the equation for x can be written as [Bate et al., 1971]:

$$x + C = \sqrt{a} \arcsin\left(\frac{\frac{r}{a} - 1}{e}\right) \quad (10.45)$$

Solving this equation for r in terms of x yields:

$$r = a \left(1 + e \sin\left(\frac{x + C}{\sqrt{a}}\right)\right) \quad (10.46)$$

Substitution of equation 10.46 into equation 10.41 results in [Bate et al., 1971]:

$$\sqrt{\mu} dt = a \left(1 + e \sin \left(\frac{x + C}{\sqrt{a}} \right) \right) dx \quad (10.47)$$

Integration of equation 10.47, assuming that $x = 0$ at $t = t_0$, then finally results into an expression for the time of flight [Bate et al., 1971]:

$$\sqrt{\mu}(t - t_0) = ax - ae\sqrt{a} \left(\cos \left(\frac{x + C}{\sqrt{a}} \right) - \cos \left(\frac{C}{\sqrt{a}} \right) \right) \quad (10.48)$$

Now expressions have been derived for r and the time of flight that are a function of the universal variable x . In the following section these expressions will be discussed in more detail and an extension will be made to the Kepler problem using the universal variable formulation.

10.3.2 Kepler's equation using the universal variable formulation

Starting from equation 10.46 and assuming that $x = 0$ at $t = t_0$, the following holds [Bate et al., 1971]:

$$e \sin \frac{C}{\sqrt{a}} = \frac{r_0}{a} - 1 \quad (10.49)$$

In this equation r_0 is the distance to the center of attraction at time t_0 . If equation 10.46 is now differentiated with respect to time, this results in the following expression [Bate et al., 1971]:

$$\dot{r} = \frac{ae}{\sqrt{a}} \cos \left(\frac{x + C}{\sqrt{a}} \right) \frac{\sqrt{\mu}}{r} \quad (10.50)$$

Equation 10.50 can be rewritten as follows [Bate et al., 1971]:

$$\frac{r\dot{r}}{\sqrt{\mu a}} = e \cos \left(\frac{x + C}{\sqrt{a}} \right) \quad (10.51)$$

Using the identity $r\dot{r} = \bar{r} \cdot \dot{\bar{r}} = \bar{r} \cdot \bar{V}$ and the assumption that $x = 0$ at $t = t_0$, equation 10.51 can be reduced to:

$$e \cos \frac{C}{\sqrt{a}} = \frac{\bar{r}_0 \cdot \bar{V}_0}{\sqrt{\mu a}} \quad (10.52)$$

Now equation 10.48 can be rewritten in the following way (using the trigonometric identity for the cosine of a sum¹) [Bate *et al.*, 1971]:

$$\mu(t - t_0) = ax - ae\sqrt{a} \left(\cos \frac{x}{\sqrt{a}} \cos \frac{C}{\sqrt{a}} - \sin \frac{x}{\sqrt{a}} \sin \frac{C}{\sqrt{a}} - \cos \frac{C}{\sqrt{a}} \right) \quad (10.53)$$

Now equations 10.49 and 10.52 can be substituted into equation 10.53, which leads to the following expression for the time of flight [Bate *et al.*, 1971]:

$$\sqrt{\mu}(t - t_0) = a \left(x - \sqrt{a} \sin \frac{x}{\sqrt{a}} \right) + \frac{\bar{r}_0 \cdot \bar{V}_0}{\sqrt{\mu}} a \left(1 - \cos \frac{x}{\sqrt{a}} \right) + r_0 \sqrt{a} \sin \frac{x}{\sqrt{a}} \quad (10.54)$$

Similar to the time of flight equation, the equation for r (equation 10.46) can be rewritten to [Bate *et al.*, 1971]:

$$r = a + ae \left(\sin \frac{x}{\sqrt{a}} \cos \frac{C}{\sqrt{a}} + \cos \frac{x}{\sqrt{a}} \sin \frac{C}{\sqrt{a}} \right) \quad (10.55)$$

If then equations 10.49 and 10.52 are substituted into equation 10.55, the following expression for r is obtained [Bate *et al.*, 1971]:

$$r = a + a \left(\frac{\bar{r}_0 \cdot \bar{V}_0}{\sqrt{\mu a}} \sin \frac{x}{\sqrt{a}} + \left(\frac{r_0}{a} - 1 \right) \cos \frac{x}{\sqrt{a}} \right) \quad (10.56)$$

If a new variable z is introduced ($z = \frac{x^2}{a}$) and substituted into equation 10.54, this yields [Bate *et al.*, 1971]:

$$\sqrt{\mu}(t - t_0) = \frac{x^2}{z} \left(x - \frac{x}{\sqrt{z}} \sin \sqrt{z} \right) + \frac{\bar{r}_0 \cdot \bar{V}_0}{\sqrt{\mu}} \frac{x^2}{z} (1 - \cos \sqrt{z}) + r_0 \frac{x}{\sqrt{z}} \sin \sqrt{z} \quad (10.57)$$

If z is introduced into equation 10.56, it results in the following expression [Bate *et al.*, 1971]:

$$r = \frac{x^2}{z} + \frac{x^2}{z} \left(\frac{\bar{r}_0 \cdot \bar{V}_0}{\sqrt{\mu}} \frac{\sqrt{z}}{x} \sin \sqrt{z} + \cos \sqrt{z} \left(\frac{r_0 z}{x^2} - 1 \right) \right) \quad (10.58)$$

¹ $\cos(a + b) = \cos a \cos b - \sin a \sin b$

It should be noted that if $z = 0$, the orbit is a parabola, if $z > 0$ then the orbit must be an ellipse and if $z < 0$, the orbit must be hyperbolic.

Equations 10.57 and 10.58 share a number of common terms, which becomes clear after some rearranging [Bate *et al.*, 1971]:

$$\sqrt{\mu}(t - t_0) = x^3 \left(\frac{\sqrt{z} - \sin \sqrt{z}}{\sqrt{z^3}} \right) + x^2 \frac{\bar{r}_0 \cdot \bar{V}_0}{\sqrt{\mu}} \left(\frac{1 - \cos \sqrt{z}}{z} \right) + x \frac{r_0 \sin \sqrt{z}}{\sqrt{z}} \quad (10.59)$$

$$r = x^2 \left(\frac{1 - \cos \sqrt{z}}{z} \right) + x \frac{\bar{r}_0 \cdot \bar{V}_0}{\sqrt{\mu}} \left(1 - z \frac{\sqrt{z} - \sin \sqrt{z}}{\sqrt{z^3}} \right) + r_0 \left(1 - z \frac{1 - \cos \sqrt{z}}{z} \right) \quad (10.60)$$

Some auxiliary variables can be defined that are a function of z [Bate *et al.*, 1971]:

$$C = \begin{cases} \frac{1 - \cos \sqrt{z}}{z} \\ \frac{1 - \cosh \sqrt{-z}}{z} \\ \frac{1}{2} \end{cases} \quad (10.61)$$

$$S = \begin{cases} \frac{\sqrt{z} - \sin \sqrt{z}}{\sqrt{z^3}} \\ \frac{\sinh \sqrt{-z} - \sqrt{-z}}{\sqrt{-z^3}} \\ \frac{1}{6} \end{cases} \quad (10.62)$$

For both equation 10.61 and 10.62 the top expression holds for $z > 0$, the middle expression holds for $z < 0$ and the final expression holds for $z = 0$.

After substitution of C and S into equation 10.59 and after some rewriting a relatively compact expression for the time of flight is obtained [Bate *et al.*, 1971]:

$$\sqrt{\mu}(t - t_0) = x^3 S + \frac{\bar{r}_0 \cdot \bar{V}_0}{\sqrt{\mu}} x^2 C + r_0 x (1 - z S) \quad (10.63)$$

This equation is the Kepler equation in universal variable formulation. This expression is the same for all types of conic sections. The same holds for the following expression for r , which is obtained by introducing equations 10.61 and 10.62 into equation 10.60 [Bate *et al.*, 1971]:

$$r = x^2 C + x \frac{\bar{r}_0 \cdot \bar{V}_0}{\sqrt{\mu}} (1 - z S) + r_0 (1 - z C) \quad (10.64)$$

10.3.3 Solving the universal variable form of Kepler's problem

In order to solve Kepler's equation in universal variable formulation for x when t_0 and t are known is done using an iterative procedure. *Der* [1996] uses a so-called Laguerre iteration procedure, which can be described as follows:

$$x_{n+1} = x_n - \frac{5f(x_n)}{f'(x_n) + \frac{f'(x_n)}{|f'(x_n)|} \sqrt{16f'(x_n)^2 - 20f(x_n)f''(x_n)}} \quad (10.65)$$

In the above iteration procedure the functions $f(x)$, $f'(x)$ and $f''(x)$ are defined as follows [*Der*, 1996], [*Bate et al.*, 1971]:

$$f(x) = (1 - \alpha r_0) x^3 S + \frac{\bar{r}_0 \cdot \bar{V}_0}{\sqrt{\mu}} x^2 C + r_0 x - \sqrt{\mu}(t - t_0) \quad (10.66)$$

$$f'(x) = x^2 C (1 - \alpha r_0) + \frac{\bar{r}_0 \cdot \bar{V}_0}{\sqrt{\mu}} x (1 - \alpha x^2 S) + r_0 \quad (10.67)$$

$$f''(x) = \frac{\bar{r}_0 \cdot \bar{V}_0}{\sqrt{\mu}} (1 - \alpha x^2 C) + (1 - \alpha r_0) (1 - \alpha x^2) x \quad (10.68)$$

In the above equations $\alpha = \frac{1}{a}$ has been used. This is because in the calculation of the semi-major axis a using the vis-viva equation (equation 6.21), if the orbit is parabolic, the denominator of this expression would be equal to zero [*Bate et al.*, 1971].

Now that the functions of x needed for the iteration process are known, only the initial value for x has to be set. The initial value for x depends on the type of orbit that is under consideration. *Bate et al.* [1971] and *Der* [1996] suggest the following initial guess for elliptical orbits:

$$x_{0_{ell}} = \frac{\sqrt{\mu}(t - t_0)}{a} = \alpha \sqrt{\mu}(t - t_0) \quad (10.69)$$

When the orbit is a hyperbola, the initial guess proposed by *Bate et al.* [1971] is:

$$x_{0_{hyp}} = \pm \sqrt{-a} \ln \left[\frac{-2\mu(t - t_0)}{a [\bar{r}_0 \cdot \bar{V}_0 \pm \sqrt{-\mu a} (1 - \frac{r_0}{a})]} \right] \quad (10.70)$$

In this equation ' \pm ' means that if $t > t_0$, it will be a plus-sign, whereas if $t < t_0$, then it will be a minus-sign [*Bate et al.*, 1971].

Finally, if the orbit is parabolic, the following initial value $x_{0_{par}}$ can be used [Vallado and McClain, 2007]:

$$x_{0_{par}} = \sqrt{p} \tan\left(\frac{\theta_0}{2}\right) \quad (10.71)$$

Now that the functions and the initial guess are known, the iteration procedure can be performed, yielding a converged value for x in at most five iterations [Der, 1996]. This parameter x has a physical significance, since it can be related to the difference in either the eccentric, parabolic or hyperbolic anomaly at time instances t_0 and t . Bate et al. [1971] shows that for elliptical orbits the x can be expressed as:

$$x = \sqrt{a}(E - E_0) = \sqrt{a}\Delta E \quad (10.72)$$

For hyperbolic orbits a similar expression can be derived [Bate et al., 1971]:

$$x = \sqrt{-a}(F - F_0) = \sqrt{-a}\Delta F \quad (10.73)$$

Finally, Vallado and McClain [2007] shows that for parabolic orbits the following expression holds for x :

$$x = \sqrt{p}(D - D_0) = \sqrt{p}\Delta D \quad (10.74)$$

Now that the anomaly difference is known the position and velocity at time t (\bar{r} and \bar{V}) can be obtained as a function of \bar{r}_0 and \bar{V}_0 in the following way [Bate et al., 1971]:

$$\bar{r} = f\bar{r}_0 + g\bar{V}_0 \quad (10.75)$$

$$\bar{V} = \dot{f}\bar{r}_0 + \dot{g}\bar{V}_0 \quad (10.76)$$

The coefficients f , g , \dot{f} and \dot{g} are called the f and g expressions. These expressions are given by the following equations (the complete derivations can be found in [Bate et al., 1971]):

$$f = 1 - \frac{x^2}{r_0} C \quad (10.77)$$

$$g = (t - t_0) - \frac{x^3}{\sqrt{\mu}} S \quad (10.78)$$

$$\dot{f} = 1 - \frac{x^2}{r} S \quad (10.79)$$

$$\dot{g} = \frac{\sqrt{\mu}}{r_0 r} x (\alpha S - 1) \quad (10.80)$$

The procedure described in this section can be summarized as follows:

- Given \bar{r}_0, \bar{V}_0 at t_0 , determine r_0 and a .
- Given $t - t_0$, solve the Laguerre iteration procedure of equation 10.65 using the appropriate starting value for x (which depends on the type of orbit).
- When a converged value of x has been reached, the f and g expressions can be calculated.
- The position \bar{r} at time t can be calculated using equation 10.75, after which its magnitude r can be calculated easily.
- The velocity \bar{V} at time t can then be calculated using equation 10.76.

Part III: Optimization

Chapter 11

Optimization

This thesis research is focused on optimizing the trajectory for a Uranus orbiter mission. This chapter will focus on the characteristics of the optimization process. First an overview of different classes of optimization methods is given in section 11.1. The simple Genetic Algorithm (GA) is discussed in section 11.2, after which some more advanced genetic operators can be found in section 11.3. The chapter is concluded with a section on random number generators.

11.1 Overview of optimization methods

This section will focus on the main classes of optimization techniques, each of which will be briefly discussed [Goldberg, 1989]:

- Calculus-based methods.
- Enumerative methods.
- Random methods.

Calculus-based

Calculus-based methods can be subdivided into two main classes: direct and indirect methods. Direct methods search for a local optimum by moving along the function and following the gradient. Indirect methods search for a local optimum by setting the gradient of the objective function equal to zero.

Both direct and indirect methods have a local scope. The optimum that is found is not guaranteed to be the global optimum. Next to that, if a local optimum has been found, further improvement can only be found through some restarting function. Furthermore, calculus-based methods require the existence of derivatives, substantially reducing the amount of problems that can be tackled [Goldberg, 1989]. Because of the clear shortcomings, calculus-based methods will not be used for the trajectory optimization process.

Enumerative

Enumerative methods look at the objective function values for each point within a finite search space. The principle behind this method is very simple, but there is a major drawback. Many problems have too large search spaces, making enumerative methods very inefficient.

An advanced enumerative technique is dynamic programming. A complex problem is broken down into a set of problems that are more likely to be solved. Solutions of these intermediate problems form the solution of the original problem. For large problems (such as interplanetary trajectory optimization), dynamic programming is very slow, making them unsuitable for the current analysis.

Random

Random optimization techniques have become increasingly popular over the years, because of the earlier mentioned shortcomings of calculus-based and enumerative methods. Random methods like the Monte Carlo method randomly go through the search space in order to find the optimal solution. For large search spaces this is not efficient, because an enormous amount of samples has to be taken to find the optimal solution, increasing the computation time.

Random searches are different from randomized search techniques, such as simulated annealing and GAs. Here random choice is used as a tool to guide the search to regions of the search space where improvement is likely. Simulated annealing performs with a higher efficiency than Monte Carlo methods, but for large problems it requires long computing times. GAs are based on evolutionary principles applied to a population of solutions, where the principle of 'survival of the fittest' plays a major role. The software package GALOMUSIT is used at the Faculty of Aerospace Engineering of Delft University of Technology in The Netherlands to optimize interplanetary trajectories. This program uses a GA for the optimization process, and therefore GAs will also be used in this thesis research. The way in which GAs work is described in the next sections.

11.2 The simple GA

GAs are based on genetic inheritance and Charles Darwin's (1809-1882) principle of survival of the fittest. A population of potential solutions to the problem will evolve so that a more optimal solution can be found. Analogous processes are encountered in nature many times.

11.2.1 The working principle of a simple GA

Figure 11.1 shows a flowchart that indicates the general structure of a GA.

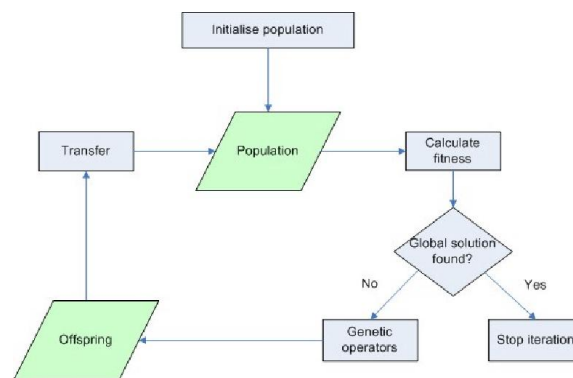


Figure 11.1 Flowchart of a simple GA, after [Noomen, 2006].

The simple GA starts by randomly generating potential solutions to the problem. This process continues until enough potential solutions have been found to fill an entire population of predefined size. For each of these population members it has to be assessed how good it actually is. In other words, for each population member the fitness with respect to a fitness or objective function is evaluated. The population members are also referred to as individuals or decision vectors throughout this thesis. If no global optimal solution to the problem is found, genetic operations are performed on the initial population. This will result in a new population and it is said that a generation has passed (so the GA maintains a population of potential solutions). The new population will be evaluated again with respect to the fitness function. This process will continue until convergence is reached or until some stopping criterion is met. It should be noted that checking for convergence is usually done after a number of generations has already passed, so that the population has already had time to evolve.

11.2.2 Structure of the simple GA

A GA applied to a certain problem should have the following components [Michalewicz, 1996]:

- A genetic representation for potential solutions to the problem at hand.
- A means to create a starting or initial population of potential solutions.
- Some sort of function that evaluates the potential solutions and rates them in terms of 'fitness' to the function.
- Genetic operators that change the composition of children or offspring.
- Generate a new population from the newly created offspring and other genetic operators.

Genetic representation

The simple GA could use binary strings to represent potential solutions to the problem. For example, the decimal number 47 is represented by binary string

101111:

$$101111 = 1 \cdot 2^5 + 0 \cdot 2^4 + 1 \cdot 2^3 + 1 \cdot 2^2 + 1 \cdot 2^1 + 1 \cdot 2^0 = 32 + 0 + 8 + 4 + 2 + 1 = 47 \quad (11.1)$$

If, for example, the problem at hand has two variables, x_1 and x_2 , an individual or string in the population should be composed of two variables. If a binary representation for the string is used, string i in the population could look like this:

$$\bar{x}^i = [01100|11010] \quad (11.2)$$

A series of 10 randomly generated 0's and 1's fills the string. Since the string represents two variables, the value of x_1^i is then represented by the first 5 numbers in the string. The last 5 numbers in the string then represent x_2^i . The numbers can of course represent their decimal value, giving the following values for x_1 and x_2 :

$$\bar{x}^i = [x_1^i \quad x_2^i] = [12 \quad 26] \quad (11.3)$$

Another possibility is that the binary strings are used for scaling the value of a variable within its allowable search space. The value of a variable x_1 represented by a binary string of length q has values in the range $0 < x_1 < 2^q$. The search space for x_1 in general is defined by a lower bound LB and an upper bound UB . The binary string can then be scaled to be in the $[LB, UB]$ domain in the following way [Noomen, 2006]:

$$x_1 = LB + \frac{UB - LB}{2^q} x_{1_{bin}} \quad (11.4)$$

In this expression $x_{1_{bin}}$ is the decimal value of the binary string.

Instead of representing the variables of the optimization problem by means of a binary string, floating point representation can also be used. If a complex problem with many variables has to be tackled requiring high accuracy using a binary representation for the strings, the strings would become extremely large. The GA will then perform poorly [Goldberg, 1989]. This problem can be overcome by representing each variable by a floating point number. Each individual can then be considered a vector of floating point numbers, each of which represents a variable. Each variable has a specific range of possible values and the floating point values should be within the allowable search space.

Initialization of the population

It could already be seen in figure 11.1 that the GA optimization process starts by initializing a population of individuals that are all possible solutions to the problem. In case of binary representation a random sequence of 0's and 1's is generated. The length of the string depends on the number of variables and the number of bits per variable that is used. In the case of floating point representation, random values of each variable within its allowable search space are generated.

An important parameter is the population size N_{pop} , so the number of individuals that are present in the population. The size of the population is of importance because it relates to computation time and being able to find the global optimum. A large population size increases the probability of finding good solutions, but at the cost of the time it needs to complete the optimization. On the other hand, performing the optimization for a small population may be very efficient in terms of computation time, but the probability of finding good solutions decreases.

The complexity of the problem, thus the number of variables and the accuracy required for the solution, is of major influence on the choice of the population size. It is difficult to find potential solutions to complex problems and therefore a larger population is generally more required than for a simple problem. This is at the cost of computation time, but since the probability of finding good individuals increases a larger population size makes sense.

Objective function evaluation

Each individual that is generated is evaluated with respect to an objective function. The objective function depends on the type of optimization problem. For example, in this thesis research the objective is to find the minimum total ΔV for an interplanetary transfer. Therefore, an individual is called 'good' if the total ΔV for the transfer trajectory is small.

Genetic operations

A simple GA has the following genetic operators [Goldberg, 1989]:

- Selection
- Crossover
- Mutation

Selection

During the selection process, individuals from the current population are chosen to generate the next generation of individuals. Basically, selection can be done in a completely random way, where each individual in the current population has the same probability for being selected. Selection can also be based on the fitness of each individual in the current population. The better the fitness of a certain

individual, the higher the probability of it being selected.

This selection process based on fitness can be represented by a so-called roulette wheel, where each slot represents the probability of selection of each individual i (the slot size is proportional to the fitness) [Michalewicz, 1996]. If the sum of the fitness for all individuals in the population of size N is given by F , then the probability of each string to be selected p_{s_i} is given by:

$$p_{s_i} = \frac{f_i}{\sum_{i=1}^N f_i} = \frac{f_i}{F} \quad (11.5)$$

The cumulative probabilities p_{cum} are generated by summing the probabilities of all previous individuals:

$$\begin{aligned} p_{cum_1} &= p_{s_1} \\ p_{cum_2} &= p_{s_2} + p_{cum_1} \\ &\dots \\ p_{cum_N} &= p_{s_N} + p_{cum_{N-1}} \end{aligned}$$

So the cumulative probability of the final string in the population is 1.0. Now a roulette wheel is spun N times generating random numbers in the interval $[0,1]$. If the random number is between the cumulative probability of strings i and $i + 1$, then string $i + 1$ is selected for the new population. The new population will then again be of size N [Michalewicz, 1996].

Crossover

During crossover individuals are paired randomly from the selected individuals. These pairs are often referred to as parents. From the parents two offspring are created in the following way in the case of a binary representation. Suppose that the length of the string is L . Then first a random number k is generated in the range $[1, L-1]$, which will indicate behind which bit position the string is split up. The split up parts behind position k are then interchanged between the parents. In the following example the string length L is 10 and k is chosen randomly as 6.

$$P_1 = 010011|1001$$

$$P_2 = 111001|0110$$

The offspring of these two parent strings will look as follows:

$$O_1 = 010011|0110$$

$$O_2 = 111001|1001$$

This crossover operator could be performed with a probability p_c . So each selected string then has this probability to be a parent string and produce offspring [Goldberg, 1989].

In the case of floating point representation, crossover is done slightly differently. There are still two parents that have to be selected. After selecting the parent one of the positions in the individual is chosen at random, which will be variable where the crossover will take place. Instead of exchanging the values of this variable between the two parents, an average is taken. Consider the following two parent individuals:

$$P_1 = [20.8 \quad 55.9 \quad 2.4]$$

$$P_2 = [11.2 \quad 8.4 \quad 40.7]$$

If the second variable would be selected for the crossover, the single offspring for these two parents would be:

$$O_1 = [20.8 \quad r_c \cdot 55.9 + (1 - r_c) \cdot 8.4 \quad 40.7]$$

The parameter r_c is a random number between 0 and 1 used for averaging the parent values at the crossover variable.

Mutation

The new population created with crossover could face another genetic operator, mutation. Every so often the value of one of the variables within an individual changes. The mutation of the value of the variable occurs with a probability p_m . The value of p_m is usually in the order of magnitude 0.001 [Goldberg, 1989]. Mutation plays a secondary role within the GA. Mutation makes sure that extra variability is added to the population. As an example of mutation, consider the following binary string (the bit that will be mutated is in boldface):

010**0**111001

After mutation the string will look like this:

0101111001

Generating a new population

In the case of the simple GA the newly created individuals completely replace the old population [Goldberg, 1989]. However, there are a number of ways in which this process can be improved. For example, the best individuals in the old population are not preserved, causing the loss of valuable genetic information. In the next section some more advanced genetic operators will be discussed.

11.3 Some advanced genetic operators

In the literature study prior to this thesis research a number of advanced genetic operators were researched. In this thesis, however, not all of them will be used and therefore will not be discussed in this section. For example, a variable population size will not be used. For more information, refer to [Molenaar, 2007].

11.3.1 Elitism

When elitism is applied in a GA, the best individuals in terms of fitness in the old generation are preserved and copied into the new generation. This prevents valuable genetic information from being lost. However, if the fraction of the population that is copied into the new generation is too large, it may cause premature convergence.

11.3.2 Immigration

Immigration is intended to maintain diversity in a population and prevent premature convergence. As is the case in nature, it might be that an individual from outside the initial population comes in and replaces an individual. However, a large population diversity implies extending the computation time.

At random, one or more individuals are generated to replace a part of the existing population of strings. This is done after crossover and mutation, so just prior to going to the next generation. It makes sense to apply this operator to the worst individuals in the population, in order to prevent important genetic material to be lost.

11.3.3 Constraint handling

Optimization problems can be subject to constraints. For an interplanetary transfer, a constraint can be a maximum allowable total ΔV for each individual. Also a maximum time of flight is a commonly used constraint for interplanetary transfers. There are many fancy ways to handle constraints in global optimization problems. In the remainder of this thesis research, if an individual is created that violates the constraints, it will simply 'die' and will not be put into the population. Instead, a new individual will be generated, which will then be tested against the constraints.

11.4 Random number generator

Throughout this chapter it has become clear that GAs depend greatly on drawing random numbers. Random number generators are used to this end. Random number generators use complex algorithms to produce long sequences of numbers that appear to be random. However, these random number generators depend on an initial value, called the seed number. If the same seed number is used in the random generator, the sequence of numbers that it produces will be exactly the same every time.

In the remainder of this thesis research, optimization runs are performed multiple times for the same settings, but each time with a different seed number for the random generator. This is done in order to diminish the influence of randomness, since a certain seed number might produce bad results. If runs are executed multiple times, this effect can be overcome. The seed number will also be indicated throughout this thesis. This is done so that, if necessary, results of a certain run can be recreated exactly.

Chapter 12

GALOMUSIT

The software tool that is used for this thesis research is called GALOMUSIT (Genetic Algorithm Optimization of a MULTiple Swingby Interplanetary Trajectory). This tool, which is written in the FORTRAN 77 programming language, has been developed in recent years by a number of students at the Faculty of Aerospace Engineering at Delft University of Technology.

This chapter is structured in the following way. First of all a historic overview of the program is discussed in section 12.1, after which the general structure is assessed in section 12.2. The capabilities of the original version of GALOMUSIT are discussed, followed by the changes that have been made during this thesis research.

12.1 History and development of GALOMUSIT

The original version of GALOMUSIT has been created by *Schlijper* [2003] for his thesis research on a gravity assist mission to Pluto. *De Jong* [2004] was the next user of GALOMUSIT. He added the possibility of performing aerogravity assists for a mission to Pluto. Later on *Erdogan* [2005] used GALOMUSIT to search for manned Mars mission opportunities. *Melman* [2007] then applied and modified the program for a mission to Neptune. The program was made much more generic and consistent, since at that time only the missions to Pluto and Mars could be used. Many comments were added to the code as well, improving the readability of the program. *Heiligers* [2008] has extended GALOMUSIT to incorporate missions to asteroids and return missions. Furthermore, multi-objective optimization was added, in which the optimization is done with respect to the total ΔV and the time of flight. *Heiligers* [2008], together with *Evertsz* [2008], then included the possibility of performing multiple asteroid rendezvous missions. Finally, *Corradini* [2008] added low-thrust missions, in which the trajectory is modeled by exponential sinusoids.

The result of all these past users is that now a program exists that is capable of optimizing many different interplanetary missions using GAs. Next to the eight planets and the dwarf planet Pluto, also 35 different asteroids and 2 comets can be a potential target in GALOMUSIT. Furthermore, next to high thrust trajectories along Kepler orbits, also low-thrust missions along an exponential sinusoid can be

optimized.

The user of GALOMUSIT is able to define and quantify many variables in the input part of the program, customizing it to the user's specific needs. Choices can vary from the type of parking orbits used to the swingby planets and from the GA settings to the maximum allowable total ΔV that is allowed for each generated individual.

12.2 Original version of GALOMUSIT

GALOMUSIT is built up of several subroutines, each of which has its own specific purpose. It goes into too much detail and it is beyond the scope of this thesis to discuss each subroutine. For that purpose a manual has been created that covers all details of the program [Heiligers *et al.*, 2009]. This manual has been updated to include exponential sinusoidal trajectories and also the additions made for this thesis research have been added to the manual. In this section the main structure of GALOMUSIT will be assessed together with the most important parts of the program.

12.2.1 Program structure

As mentioned earlier, GALOMUSIT can be used to optimize high thrust and low thrust trajectories. With high thrust trajectories (powered) gravity assists or aerogravity assists may be used on the interplanetary trajectory. Low thrust missions and aerogravity assists will not be considered in this thesis. More information on the implementation of these subjects in GALOMUSIT can be found in Heiligers *et al.* [2009].

The main structure of GALOMUSIT for high thrust trajectories prior to this thesis can be represented by the flow diagram in figure 12.1. It can be seen in figure 12.1 that the structure of GALOMUSIT is quite simple. After the user has defined the program settings, an initial population is created. Each generated individual will pass through the problem model, where the total ΔV and time of flight are calculated. The calculations that are performed in the problem model have been extensively discussed in chapter 8. If the individual does not violate any constraints it is allowed in the population, otherwise it dies and a new individual is created. This process continues until the entire initial population is filled with viable individuals.

When the initial population is full, the next step is to assign lifetimes to the individuals if multi-objective optimization is applied. In this thesis research, multi-objective optimization is not used, but in section 12.2.4 the implementation in GALOMUSIT will be addressed briefly. After the assigning of lifetimes (or not, in the case of single-objective optimization), the program checks whether or not convergence has been reached. The user can specify after which generation these checks will be performed, so the population can first have some time to evolve. If convergence has not been reached, a new population is created using genetic

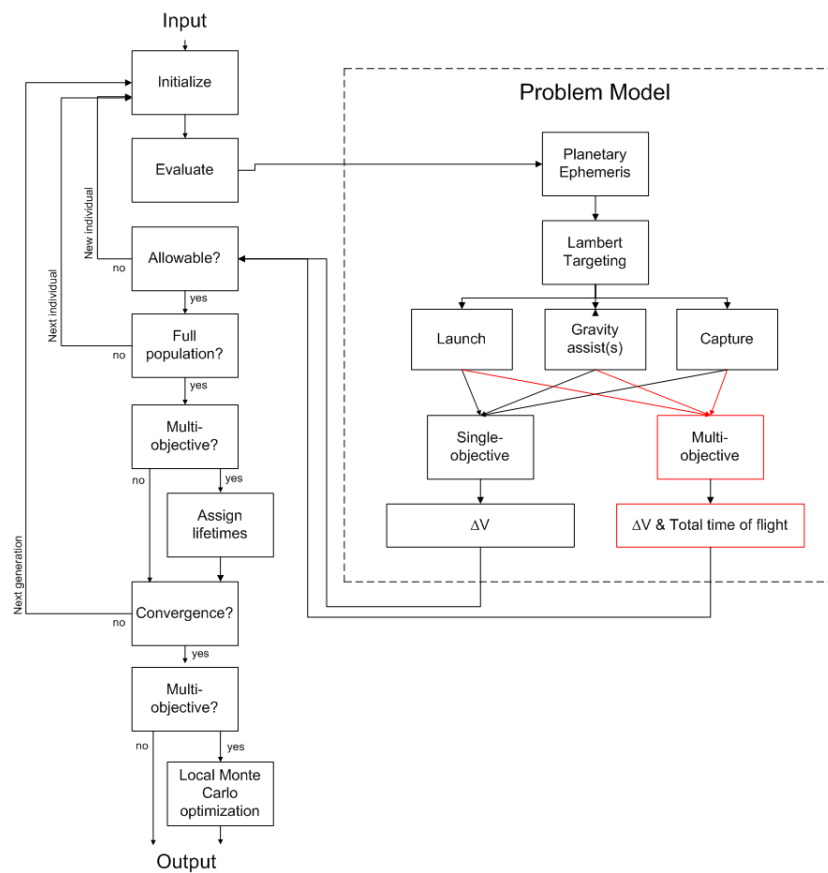


Figure 12.1 Flow diagram for GALOMUSIT, after [Heiligers, 2008].

operations. If convergence has been reached, the output is generated in the case of single-objective optimization. In the case of multi-objective optimization a local Monte Carlo search around the found minimum is applied.

12.2.2 Generation of individuals

In subroutine INITPOP individuals consisting of the launch date, the encounter dates with the swingby planets and the arrival date are created. For each individual the time of flight and the total ΔV are evaluated. If both these quantities are within the constraints, then the individual is allowed in the population. The population size is a very important parameter in the optimization process. In the GALOMUSIT manual a relationship is given between the number of (aero)gravity assists and the population size [Heiligers et al., 2009].

The process of creating individuals is done until the population for the first generation is filled. In this generation no genetic operations are executed on the individuals. For single-objective optimization the population size is constant throughout the optimization process.

<i>Number of gravity assists</i>	<i>Population size</i>
0	500
1	500
2	1000
3	1000
4	2000
5	4000

Table 12.1 Relation between the number of gravity assists and the population size in GALOMUSIT [Heiligers et al., 2009].

12.2.3 Creating new generations

For single-objective optimization, which is used in this thesis research, subroutine NEWPOPSINGLE is used to create a new population. The following genetic operations are performed in this subroutine: elitism, crossover, immigration and possibly mutation. The process can be summarized as follows:

- The individuals of the previous generation (a total number of NPOP individuals) are sorted according to their fitness value, the total ΔV .
- The best fraction of the previous generation (the NBEST individuals) are copied into the population of the new generation: elitism.
- Then new individuals are created through crossover. This is a total number of NBEST+1 up to NPOP-NRANDOM individuals, in which NRANDOM is the number of immigrants into the population of the new generation. Individuals of the previous generation are selected randomly for recombination.
- Completely newly generated individuals enter the population of the new generation (NRANDOM immigrants) to fill it up.
- Finally mutation could be added, but this is only applied to the newly generated immigrants.

After these steps, the process repeats itself again for the next generations until either convergence or the maximum amount of generations has been reached.

- For crossover, two individuals of the entire previous generation are selected randomly. They are not just chosen based on their fitness, an option that was mentioned in section 11.2. Good individuals (the ones with a low total ΔV) do not have a higher probability to be selected for crossover. A future user of GALOMUSIT might want to improve this.
- Mutations are possible only for the immigrants. This does not make any sense, since a random change is performed on a randomly created individual. This option should be improved by a future user.

12.2.4 Multi-objective optimization

The most significant addition to GALOMUSIT by *Heiligers* [2008] has been implementing multi-objective optimization. GA optimization with a variable population size is used when applying multi-objective optimization. Two subroutines are used to create new populations and subsequently determine the quality of each generated individual, NEWPOPMULTI and PARETO respectively. This quality of an individual is not just measured by the total ΔV , but instead the concept of Pareto optimality and Pareto ranking is used. Detailed information on Pareto optimality and ranking can be found in [*Heiligers*, 2008].

At the end of the first generation lifetimes are assigned to each individual in the population. The population is then transferred into the next generation, where the lifetime for each individual is decreased by one. New individuals are then created through immigration and mutation. When the population has been filled again, the Pareto fronts for the new population are determined. From these Pareto fronts, the lifetimes for the newly generated individuals are allocated. After this step the population is checked for convergence, see also section 12.2.5. If convergence is not reached, a new generation has to be created. However, before that can be done, the dead individuals (the ones with a lifetime of zero) have to be removed from the population. If a dead individual were to belong to the absolute Pareto front, it will not die but be preserved until it no longer belongs to the absolute Pareto front.

12.2.5 Convergence

For single-objective optimization, a run ends when either convergence has been reached or the maximum amount of generations has passed. Convergence is reached if the best and average total ΔV have not changed by more than a user defined value over a predefined number of generations.

In the case of multi-objective optimization convergence is reached if the absolute Pareto front does not change over a user-defined number of generations. This method of convergence implies a large computation time, because adding even one single individual to the absolute Pareto front means that the run will continue. Another option is that the area under the absolute Pareto front stays approximately the same. It was shown by *Heiligers* [2008] that this decreases the computational effort considerably without the loss of quality for the results. After reaching convergence, the user can choose to perform a local Monte Carlo optimization around the absolute Pareto front found by the GA.

12.3 Adaptations made to GALOMUSIT for this thesis

The objectives of this thesis were to develop a method with which interplanetary trajectories with DSMs can be analyzed and optimized using GALOMUSIT and to apply this method to a Uranus orbiter mission. It should therefore be stressed again that no modifications have been made to the already existing GA process

within GALOMUSIT.

In the following sections the adaptations that have been made to GALOMUSIT for this thesis research will be discussed. It is important to note that the structure of the program has remained the same as it was before this thesis started. Only the problem model for trajectories with DSMs is somewhat different from trajectories without DSMs, see figure 12.2.

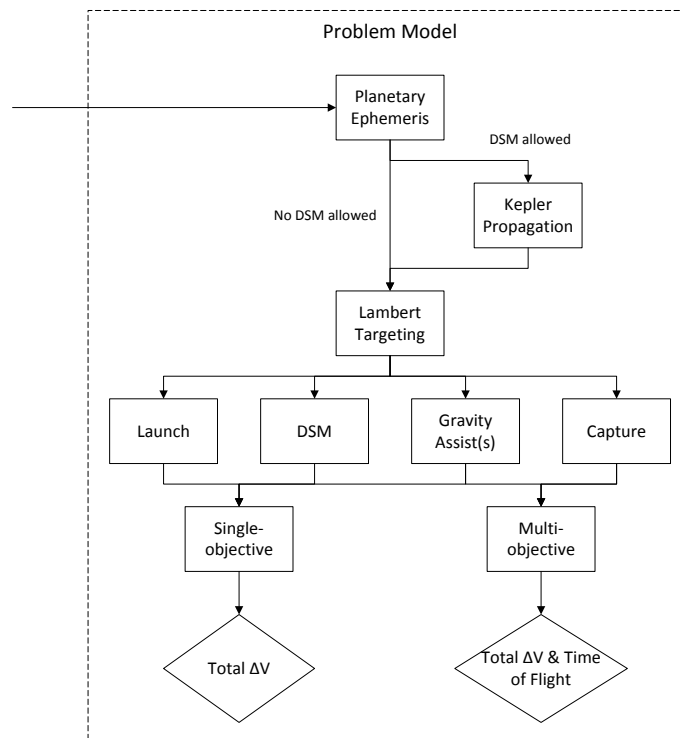


Figure 12.2 New problem model for GALOMUSIT, after the addition of DSMs.

If a DSM is allowed somewhere along the trajectory, Kepler propagation has to be applied. The end of the Kepler arc is also the starting point of the Lambert arc that connects the DSM position with the target planet. After the trajectory has been defined, the required ΔV components are calculated.

12.3.1 Adaptations prior to the thesis research

Before this thesis research was started, two changes to GALOMUSIT have been made in cooperation with *Corradini* [2008]. These were necessary changes and it provided the opportunity to get some experience with the program. The first change that was made had to do with the way in which a run in GALOMUSIT is started. Originally, the seed number for the random generator was a function of the internal clock time of the computer. Different runs with identical settings would produce different results. This has been adapted in such a way that the user

has to specify this seed number. This is advantageous because runs performed with identical settings and an identical seed number produce exactly the same results.

The second thing that has been changed before the thesis research was started was the addition of two new subroutines, namely `TIMEOFFLIGHT` and `CONSTRAINTS`. In subroutine `TIMEOFFLIGHT`, the time of flight is calculated for each individual. This is done for all available mission types. This is done so that no calculations are performed inside the optimization subroutines. The other subroutine, `CONSTRAINTS`, has been added to check whether or not the time of flight and the total ΔV violate the constraints. This is done at each part in the optimization process where new individuals are created. The output of this subroutine comes down to a boolean operator. If the constraints are violated, then a new individual must be created and the constraints have to be checked again. This subroutine has been created in such a way that new users can easily add new types of constraints, but with the same type of output.

12.3.2 Setting up the program

The next change that has been made to GALOMUSIT is that the user can now specify whether or not DSMs will be added to the trajectory and if so, on which legs they will be applied. This gives the user the flexibility of analyzing on which part of the trajectory the spacecraft can benefit from the DSM.

With the addition of this extra impulsive maneuver to the trajectory, a new constraint has been added to GALOMUSIT. The user can specify what the maximum allowable ΔV for a DSM is. If an individual is created that violates this constraint, it will not be allowed in the population and it will die.

12.3.3 Generating individuals for DSM trajectories

When the interplanetary trajectories using only Lambert targeting are optimized, an individual consists only of the launch epoch, the swingby epochs and the arrival epoch. The number of encounter epochs is defined as `NPARAM`. Adding DSMs to the trajectory increases the number of variables in the individual. The number of extra variables due to the addition of DSMs is `NPARAMDSM`. The new individual is then simply determined by adding the vector of DSM related variables to the vector containing the encounter epochs.

The new DSM related variables are generated by randomly selecting a value in the allowable search space for each of those variables. The user can specify the lower and upper bounds for each variable in the input part of the program (subroutine `INIT`). For example, for $|\vec{V}_{\infty L}|$, the lower and upper bounds are defined as `VINFLIMLOW` and `VINFLIMUPP` respectively. The same principle holds for θ , φ , η , h_p and ζ .

12.3.4 New subroutines added to GALOMUSIT

In order to incorporate DSMs on interplanetary trajectories three new subroutines have been added to GALOMUSIT, next to the addition of the DSM variables to the individuals. The new subroutines have to do with the following subjects:

- Calculating the ΔV that is needed at launch when a DSM is present on the first interplanetary leg
- Determining the position and velocity of the spacecraft at the end of a Kepler arc
- Determining the heliocentric velocity vector at the end of an unpowered swingby

ΔV at launch when a DSM is present on the first leg

Figure 12.3 shows the input that is needed for the new subroutine DSMLAUNCH and the output that it generates.



Figure 12.3 Input and output parameters for the newly created subroutine DSMLAUNCH.

If a DSM is present on the leg right after launch, the hyperbolic excess velocity vector has to be generated randomly. In DSMLAUNCH the random values for $|\bar{V}_{\infty L}|$, θ and φ are used to generate the hyperbolic excess velocity vector $\bar{V}_{\infty L}$. For the definition of the coordinate frame in which $\bar{V}_{\infty L}$ is defined, \bar{r}_{pl} and \bar{V}_{pl} are required (see also section 9.2.1). The required heliocentric velocity at the start of the interplanetary leg is then obtained by adding $\bar{V}_{\infty L}$ to \bar{V}_{pl} .

The impulsive maneuver ΔV_L is calculated in the same way as it is done as when the first leg were a Lambert arc. Equation 8.44 is applied using the parking orbit data and $|\bar{V}_{\infty L}|$.

Position and velocity at the end of a Kepler arc

An overview of the input and output of the new subroutine PROPAGATEKEPLER is shown in figure 12.4.

It was already outlined in chapter 10 that in order to propagate the orbit along a Kepler arc, the initial state (so \bar{r}_0 and \bar{V}_0) and the time of flight T is needed.



Figure 12.4 Input and output parameters for the newly created subroutine PROPAGATEKEPLER.

They are therefore also inputs for PROPAGATEKEPLER. The epoch at which the DSM is performed is $t_0 + \eta T$, so t_0 and η have to be put into the subroutine.

First of all the type of Kepler orbit is determined from the input position and velocity. Depending on the type of orbit the initial guess for the universal variable x is determined. The Laguerre iteration process (see equation 10.65) is then performed with the parameters tuned to the specific type of orbit. Once a converged value for x has been established, PROPAGATEKEPLER provides the position vector \bar{r} and velocity vector \bar{V} as output of the subroutine. Also the time of flight that remains for the subsequent Lambert arc is given as an output by the subroutine.

Heliocentric velocity vector at the end of an unpowered swingby

For the new subroutine UNPOWEREDSB the input and output variables are shown in figure 12.5.



Figure 12.5 Input and output parameters for the newly created subroutine UNPOWEREDSB.

In order to determine the incoming hyperbolic excess velocity at the unpowered swingby, the planet's velocity and the velocity at the end of the incoming Lambert arc are needed. The randomly selected pericenter altitude h_p is added to the planet's radius to get r_p . To calculate the swingby angle δ , $|\bar{V}_{\infty in}^-|$ and r_p are needed in UNPOWEREDSB. Together with the randomly generated value for ζ the new orientation of the hyperbolic velocity can be calculated. The frame with respect to which this is calculated needs \bar{r}_{pl} .

The output that is provided by UNPOWEREDSB is the heliocentric velocity vector right after the swingby. This velocity is needed for the subsequent propagation along the Kepler orbit until the application point of the DSM.

12.3.5 New output files

The previous version of GALOMUSIT provided output files in which the encounter epochs were shown, together with the required ΔV maneuvers and the GA settings. It was difficult to deduce the orbital elements of the trajectory or the relevant positions and velocities. Information on the distribution of feasible individuals within the search space was not available at all. Two new output files are therefore created.

The first new output file shows the values of all variables for each individual within the population. This is done for every generation, so the user can check the evolution of all variables during the optimization process. For example, the user can easily use this file to plot the distribution of the individuals in the population in a graph where the x- and y-axes represent the launch and arrival epoch. This can provide insight in locating a favorable launch window.

The second output file is for the best individual of the optimization run only. It shows the positions of the planetary encounters and, where relevant, the position of a DSM. The velocity at the start of each leg and right after performing a DSM is displayed as well. These positions and velocities are given in the inertial, heliocentric, equatorial reference frame. The file further contains the GA settings, the breakdown of the total ΔV and the values of the variables for the best individual.

Benchmark runs for GALOMUSIT

In order to test whether the changes to GALOMUSIT have been implemented correctly, a number of tests is performed for verification purposes. This is a crucial step when developing software, or in this case making additions to an existing piece of software. The optimization of the mission to Uranus can not start before it is certain that GALOMUSIT works correctly.

In section 13.1 some runs performed by previous users of GALOMUSIT will be reproduced in order to verify that the program still produces correct results after the modifications that have been outlined in chapter 12. Next, in section 13.2, an Earth-Mars transfer with a DSM somewhere along the trajectory is analyzed. Finally, a transfer from Earth to Mars with an unpowered swingby at Venus is discussed in section 13.3. In this test case a DSM is present on the leg between Venus and Mars.

13.1 Verification of results produced by previous users of GALOMUSIT

GALOMUSIT has been used by a number of students in the past. After the modifications to GALOMUSIT that were needed for this thesis research, the results of the previous users have to be verified. This has to be done in order to check that these parts of the program still work correctly. First, a Pluto flyby mission with a gravity assist at Jupiter is assessed, as done by *Schlijper* [2003] for his thesis research. Secondly, a trajectory to Neptune using multiple gravity assists, after the thesis work of *Melman* [2007], is discussed.

13.1.1 Pluto flyby with gravity assist at Jupiter

The best run, as found by *Schlijper* [2003] for his Pluto flyby mission, starts with a launch from a GTO on 1 January 2005. The maximum arrival date is set at 1 January 2020. The total ΔV for his best run was 5.644 km/s, associated with a time of flight of 14.7 years. For the current version of GALOMUSIT, when launching on the same date, the best total ΔV is 5.651 km/s with a time of flight of 14.4 years. The optimization was done five times, each time with a different seed number for

the random generator. The seed number producing the best result for the Pluto flyby mission was 250. A comparison between the original run and the best run with the current version of GALOMUSIT is given in table 13.1.

	Results from [Schlijper, 2003]	Current version of GALOMUSIT
Launch date	01/01/2005	01/01/2005
Swingby date	21/06/2006	19/06/2006
Flyby date	11/09/2019	07/06/2019
ΔV_L (km/s)	5.644	5.6475
ΔV_{SB} (km/s)	0.0003	0.0025
Time of flight (yr)	14.7	14.4

Table 13.1 Pluto flyby with a gravity assist at Jupiter. Results are given for the original run by *Schlijper* [2003] and for the current version of GALOMUSIT.

From this table it can be concluded that the launch date is the same for both runs. For the current version of GALOMUSIT, the value of the total ΔV is 7 m/s higher than for the best result from [Schlijper, 2003]. Because the seed number for the random generator was not known for the runs done by *Schlijper* [2003] the results can not be reproduced exactly. The gravity assist at Jupiter is practically unpowered for both cases and the swingby dates are similar. The second part of the journey, from Jupiter to Pluto, produces different flyby dates. This difference of about three months comes from the fact that the trajectory is optimized for the total ΔV , which is all used in the first leg of the mission. Therefore the arrival conditions are less stringent, as long as the flyby occurs before 1 January 2020. It can be concluded that GALOMUSIT is verified for this particular trajectory.

13.1.2 Trajectory to Neptune with multiple swingbys

The swingby sequence giving the lowest total ΔV for a trajectory to and capture around Neptune as found by *Melman* [2007] is VVEJS. The total ΔV corresponding to this best run was 5.819 km/s, with a total flight time of 17.6 years. For this run, the spacecraft was assumed to start from a GTO and the capture orbit was elliptic with a pericenter altitude of 4000 km and an apocenter altitude of 488,000 km. The launch date corresponding to the best VVEJS run was 12 May 2012. The spacecraft had to arrive before 1 January 2030. In terms of Genetic Algorithm settings *Melman* [2007] used 10% elitism, 10% immigration and no mutation. The population size used was 4000 individuals. Table 13.2 shows the results of the old version of GALOMUSIT and the results for the new version.

During the thesis work of *Melman* [2007] it was not possible yet to specify the seed number for the random generator in GALOMUSIT. Therefore the results can not be reproduced exactly. For the current version, the runs were executed 10 times, each time with a different seed number for the random generator (5, 10, 75, 250, 1000, 1050, 1100, 1150, 1200 and 1250). With table 13.2 it can be confirmed that GALOMUSIT is verified for this mission.

	<i>Results from [Melman, 2007]</i>	<i>Current version of GALOMUSIT</i>
Launch date	12/05/2012	16/05/2012
Swingby date 1	V: 08/11/2012	V: 08/11/2012
Swingby date 2	V: 16/12/2013	V: 15/12/2013
Swingby date 3	E: 25/09/2015	E: 24/09/2015
Swingby date 4	J: 28/12/2017	J: 07/02/2018
Swingby date 5	S: 14/06/2021	S: 28/06/2021
Arrival date	18/12/2029	23/12/2029
ΔV_L (km/s)	1.597	1.616
ΔV_{SB} (km/s)	0.632	0.449
ΔV_C	3.783	3.789
ΔV_{tot}	5.819	5.858
Time of flight (yr)	17.6	17.6

Table 13.2 Mission to Neptune with swingbys at Venus, Venus, Earth, Jupiter and Saturn. Results are given for the original run by *Melman* [2007] and for the current version of GALOMUSIT. The seed number producing the best result for the current version was 1100.

13.2 Verification of GAMOLUSIT for an Earth-DSM-Mars transfer

The following test case involves a transfer from Earth to Mars with a DSM somewhere along the trajectory [*Bernelli-Zazzera et al.*, 2007]. The objective function f that has to be minimized for this test case, which can be denoted by EdM, is as follows:

$$f = |\bar{V}_{\infty L}| + \Delta V_{DSM} + |\bar{V}_{\infty C}| \quad (13.1)$$

It should be stressed that *Bernelli-Zazzera et al.* [2007] used the hyperbolic excess velocity at launch and capture instead of the ΔV needed to get into a parking orbit. This is different from what has been used so far in this thesis research. However, this can be implemented easily in GALOMUSIT by specifically declaring that the ΔV at launch and capture are equal to the hyperbolic excess velocities. It poses no further problems for the optimization process.

13.2.1 Problem description and results from literature

The launch window and the bounds on the time of flight that are used by *Bernelli-Zazzera et al.* [2007] are given in table 13.3. The launch epoch and time of flight that correspond to the solution with the minimum value for f are shown as well.

The minimum launch epoch 1000 MJD2000 corresponds to the calendar date 27 September 2002 and the maximum launch epoch 2000 MJD2000 is equivalent to calendar date 23 June 2005. The maximum time of flight is 650 days, giving a

	t_0 (MJD2000)	T_{EM} (days)
Lower bound	1000	200
Upper bound	2000	650
For f_{best}	1243.2	606.2

Table 13.3 Lower and upper bounds for the launch epoch and the time of flight for the EdM test case of [Bernelli-Zazzera et al., 2007].

maximum arrival epoch of 2650 MJD2000, or calendar date 4 April 2007.

Aside from the launch and arrival epoch, *Bernelli-Zazzera et al.* [2007] have modeled the interplanetary trajectory with different parameters than the ones used in this thesis research. Therefore the remaining parameters of the solution found by *Bernelli-Zazzera et al.* [2007] can not be compared with the results found using GALOMUSIT. Comparisons have to be made through the objective function value corresponding to the best solution and the corresponding orbit.

The search space for the remaining decision variables is kept free by *Bernelli-Zazzera et al.* [2007], so it will also be done for the optimization using GALOMUSIT. It should be noted that the maximum bound of the search space for $|\bar{V}_{\infty L}|$ has been restricted to a constraint that has been set to the problem by *Bernelli-Zazzera et al.* [2007].

- $|\bar{V}_{\infty L}| \in [0, 3]$ km/s
- $\theta \in [0, 2\pi]$ rad
- $\phi \in [-\frac{\pi}{2}, +\frac{\pi}{2}]$ rad
- $\eta \in [0.10, 0.90]$

In the problem description constraints on the components of the objective function have been set, so also for $|\bar{V}_{\infty L}|$ as mentioned earlier [Bernelli-Zazzera et al., 2007].

- $|\bar{V}_{\infty L}| \leq 3.0$ km/s
- $\Delta V_{DSM} \leq 3.0$ km/s
- $|\bar{V}_{\infty C}| \leq 3.0$ km/s
- ΔV_{tot} or $f \leq 7.0$ km/s

Using the given launch window, bounds on the time of flight and the search space for the other variables, the best solution found by *Bernelli-Zazzera et al.* [2007] gives an objective function value $f_{best} = 5.632$ km/s. The components of the objective function for this best solution are listed below:

- $|\bar{V}_{\infty L}| = 2.77$ km/s

- $\Delta V_{DSM} = 2.77$ km/s
- $|\bar{V}_{\infty C}| = 0.07$ km/s

Obviously some typing error has been made by *Bernelli-Zazzera et al.* [2007], because the velocity components do not add up to 5.632 km/s. If the velocity components are correct, the objective function value should be 5.61 km/s. Depending on rounding errors this value can be slightly higher or lower. The error could also have been made in one of the velocity components. For the analysis in this section, the value of 5.632 km/s is assumed to be correct and results obtained with GALOMUSIT will be compared with this value. The orbit corresponding to this best solution found by *Bernelli-Zazzera et al.* [2007] is shown in figure 13.1.

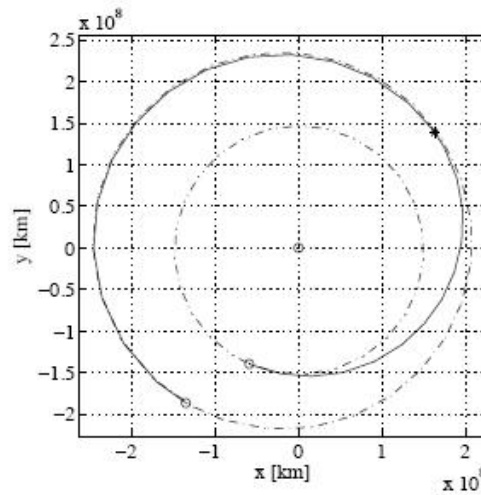


Figure 13.1 Orbit of the best solution for the EdM test case defined in [Bernelli-Zazzera et al., 2007]. Earth at launch and Mars at arrival are indicated by circles (Earth is the inner planet and Mars is the outer planet). The symbol '*' indicates the location of the DSM.

13.2.2 Results for the EdM test case using GALOMUSIT

The runs that were performed using GALOMUSIT with respect to this EdM test case used the complete search space for all decision variables.

- $t_0 \in [1000, 2000]$ MJD2000
- $T_{EM} \in [200, 650]$ days, so $t_1 \in [1200, 2650]$ MJD2000
- $|\bar{V}_{\infty L}| \in [0, 3]$ km/s
- $\theta \in [0, 2\pi]$ rad
- $\phi \in [-\frac{\pi}{2}, +\frac{\pi}{2}]$ rad
- $\eta \in [0.10, 0.90]$

The same constraints as in section 13.2.1 will be used. The optimization process has been performed 10 times, each time with a different seed number S for the random generator. The settings of the GA for this test case are:

- The best 15% of the individuals are copied into the next generation (elitism).
- 15% of the new population will consist of new randomly generated individuals (immigration).
- This means that the other 70% of the population will be created through crossover.
- Mutation is not used, since in GALOMUSIT it is only applied on immigrants.
- The (constant) population size N_{pop} is 500 individuals.

Table 13.4 shows the decision vectors for the best solutions for each run and the corresponding ΔV_{tot} .

S	t_0 MJD2000	t_1 MJD2000	$ \bar{V}_{\infty L} $ km/s	θ rad	φ rad	η -	ΔV_{tot} km/s
5	1216.7	1462.2	0.530	0.063	-0.257	0.193	5.654
10	1242.4	1470.4	2.198	6.270	-0.177	0.288	5.652
75	1243.1	1466.3	2.089	6.278	-0.122	0.229	5.651
250	1217.1	1463.3	0.614	0.082	-0.265	0.198	5.654
1000	1244.9	1462.5	2.228	0.012	-0.104	0.211	5.649
1050	1244.5	1510.5	2.671	0.038	-0.199	0.578	5.646
1100	1216.8	1461.7	0.488	0.061	-0.282	0.188	5.654
1150	1249.7	1467.1	2.601	6.243	-0.097	0.342	5.654
1200	1216.5	1458.1	0.126	0.103	-0.237	0.162	5.656
1250	1217.3	1462.7	0.625	0.083	-0.250	0.198	5.654

Table 13.4 Decision vectors and total ΔV the best individuals of 10 runs for the EdM test case [Bernelli-Zazzera *et al.*, 2007]. The time needed to complete these runs on the dutlruw.lr.tudelft.nl-server was 1409 s.

The best solution found by GALOMUSIT after the ten different runs is 5.646 km/s for seed number 1050, which is 14 m/s higher than the best solution found by Bernelli-Zazzera *et al.* [2007] (as mentioned earlier, the value found by Bernelli-Zazzera *et al.* [2007] is not certain). The launch epoch t_0 of the best individual in table 13.4 is 1244.5 MJD2000. This corresponds very well with the best solution found by Bernelli-Zazzera *et al.* [2007], which is 1243.2 MJD2000. The total time of flight for the best individual in table 13.4, however, is very different. GALOMUSIT finds a time of flight of 266 days, whereas Bernelli-Zazzera *et al.* [2007] find a time of flight of 606.2 days. The orbit corresponding to the best individual of table 13.4 is shown in figure 13.2.

It can be seen from table 13.4 that in terms of total ΔV the results for all runs are very similar. The same holds for the launch epoch t_0 and arrival

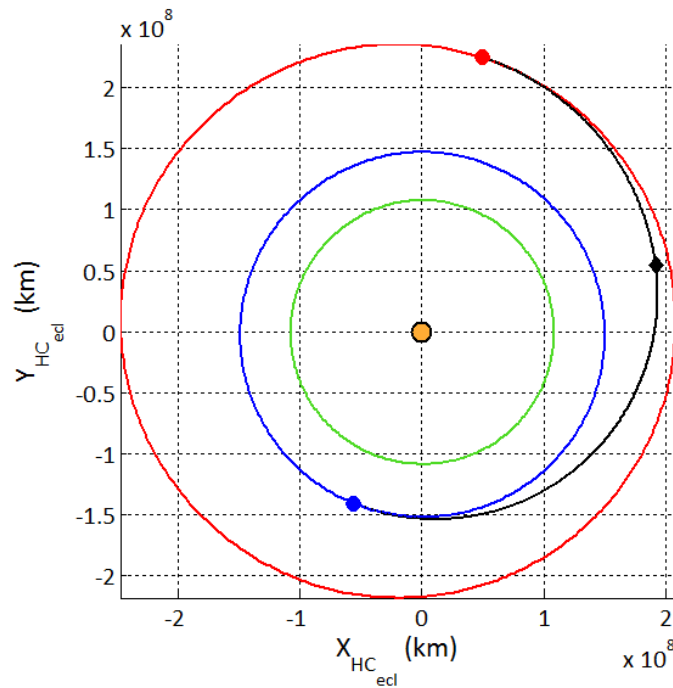


Figure 13.2 Orbit corresponding to the best solution obtained with GALOMUSIT for the EdM test case of [Bernelli-Zazzera *et al.*, 2007]. The seed number for the run was 1050. For each variable, the complete search space has been used. ●: Earth at launch, ◆: DSM, ●: Mars at arrival.

epoch t_1 , where only the best solution shows a distinctly higher value. There are significant differences, however, for $|\bar{V}_{\infty L}|$. For half of the individuals in table 13.4 $|\bar{V}_{\infty L}|$ is below 1 km/s, whereas the other half of the solutions has a $|\bar{V}_{\infty L}|$ that is over 2 km/s. The angles θ and φ on the other end are similar for all individuals, implying that regardless of the magnitude of the hyperbolic excess velocity at launch, the direction is practically the same for the launch epochs shown in table 13.4. Another feature that stands out from table 13.4 is that the value for η of the best individual differs significantly from the other values.

Because the spread of the total ΔV is very small, but $|\bar{V}_{\infty L}|$ is very different, it means that the components of the objective function are different for the different individuals. The objective function components are shown in table 13.5.

Table 13.5 shows that $|\bar{V}_{\infty C}|$ for all runs is similar, except for the best individual. Together with the observations that the time of flight and the value for η for the best individual are larger than for the individuals of the other runs leads to the hypothesis that the best solution might be improved by applying the global optimization method on a reduced search space.

The idea of search space reduction is reinforced when considering that the method used by Bernelli-Zazzera *et al.* [2007] includes search space pruning. This means that certain parts of the search space are removed that turned out to be not useful for the optimization process. For the best individual in table 13.4 the launch and arrival window is taken as an example. A distribution of the feasible

S	ΔV_{tot} (km/s)	$ \bar{V}_{\infty L} $ (km/s)	ΔV_{DSM} (km/s)	$ \bar{V}_{\infty C} $ (km/s)
5	5.654	0.530	2.533	2.592
10	5.652	2.198	1.065	2.389
75	5.651	2.089	1.054	2.508
250	5.654	0.614	2.466	2.574
1000	5.649	2.228	0.862	2.559
1050	5.646	2.671	1.697	1.278
1100	5.654	0.488	2.566	2.600
1150	5.654	2.601	0.590	2.462
1200	5.656	0.126	2.852	2.678
1250	5.654	0.625	2.454	2.576

Table 13.5 Breakdown of the objective function value for the best individuals out of the 10 runs for the EdM test case.

individuals in the initial population for the run with seed 1050 within the $t_0 - t_1$ search space is shown in figure 13.3. The initial population is taken, since this is the result of a purely randomly generated population and can therefore be considered a simple Monte Carlo search.

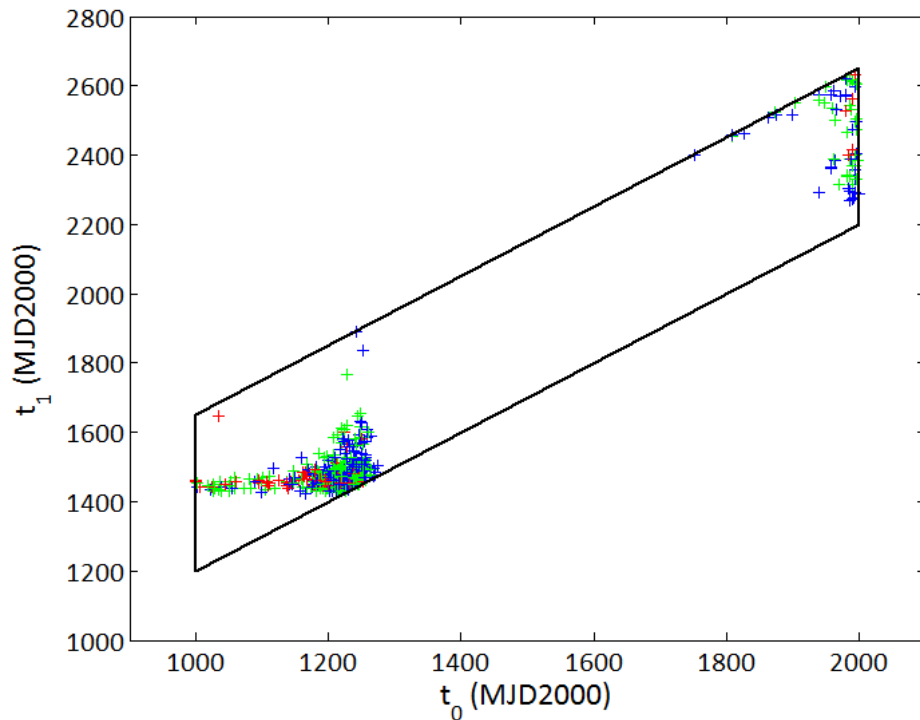


Figure 13.3 Distribution of the feasible individuals in the initial population for seed number 1050. For each variable, the complete search space has been used. The $t_0 - t_1$ search space is indicated by the solid line. $+$: $\Delta V_{tot} > 6.5$ km/s. $+$: $6.0 < \Delta V_{tot} \leq 6.5$ km/s. $+$: $\Delta V_{tot} \leq 6.0$ km/s.

Figure 13.3 shows several distinct features. The most obvious feature is the limited part of the search space where feasible individuals occur. One possible launch window is centered around $t_0 \approx 1250$ MJD2000. The next possible

launch window is located near the boundary of the t_0 search space, at $t_0 \approx 2000$ MJD2000. Since this launch window is cut off by the boundary of the t_0 search space it is highly likely that more possible solutions exist beyond this boundary, but they are not under consideration in this test case. This feature of subsequent launch windows can be related to the synodic period for the EdM transfer. In section 8.1.1 the synodic period for the Hohmann transfer was discussed briefly. For an Earth-Mars Hohmann transfer the synodic period is 2.135 years or 780 days [Cornelisse et al., 1979]. The difference between the centers of the launch windows in this test three-dimensional case corresponds to that value.

Another feature of figure 13.3 is that at both launch windows a range of flight times is possible. However, individuals with a flight time of 400 days or more are very hard to generate, especially for the launch window centered at 1250 MJD2000.

The individuals in the $t_0 - t_1$ search space are clustered close together. In order to assess whether or not this is also the case for the DSM related variables, some additional figures are required. Figure 13.4 shows the distribution of individuals in the $t_0 - |\bar{V}_{\infty L}|$ search space.

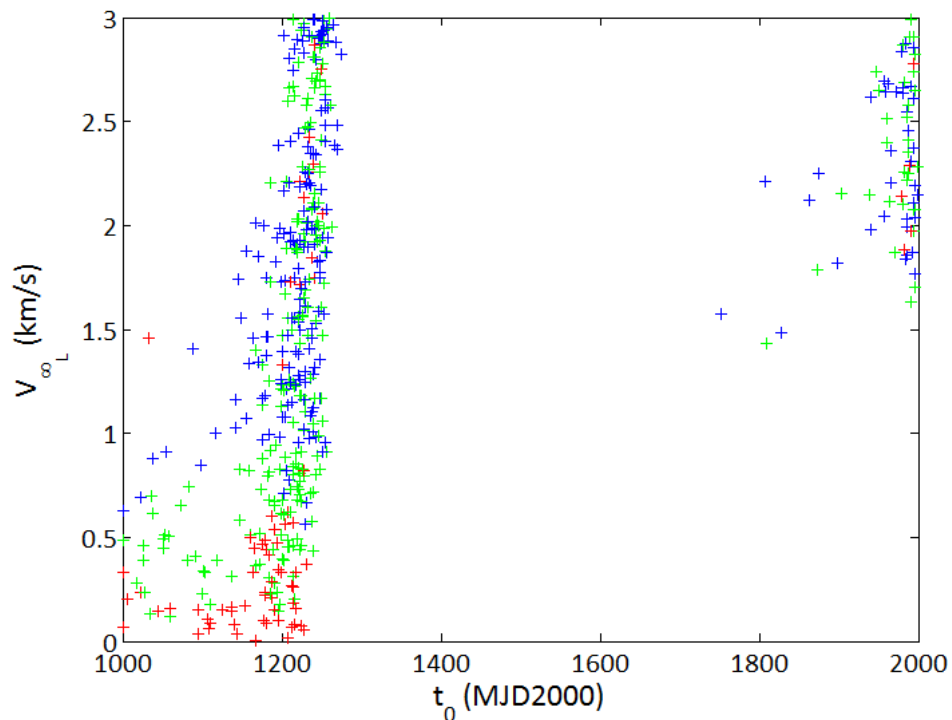


Figure 13.4 Distribution of the feasible individuals in the initial population for seed number 1050 in the $t_0 - |\bar{V}_{\infty L}|$ search space. For each variable, the complete search space has been used. $\color{blue}+$: $\Delta V_{tot} > 6.5$ km/s. $\color{green}+$: $6.0 < \Delta V_{tot} \leq 6.5$ km/s. $\color{red}+$: $\Delta V_{tot} \leq 6.0$ km/s.

Figure 13.4 shows that the distribution of $|\bar{V}_{\infty L}|$ is quite uniform in the initial population. The final values in table 13.4 show that the best individuals either have a value for $|\bar{V}_{\infty L}|$ below 1 km/s or above 2 km/s. In figure 13.4 it can be

seen that in the part of the search space between 1 km/s and 2 km/s that the worst individuals in the population dominate.

In figure 13.5 the distribution of individuals in the initial population is shown in the $\theta - \varphi$ search space.

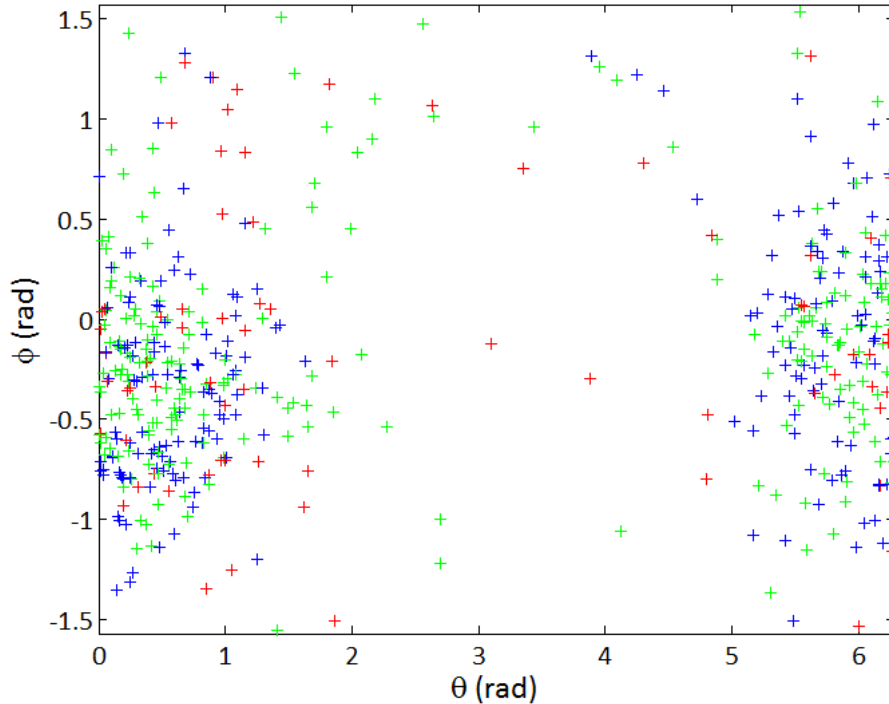


Figure 13.5 Distribution of the feasible individuals in the initial population for seed number 1050 in the $\theta - \varphi$ search space. For each variable, the complete search space has been used. + : $\Delta V_{tot} > 6.5$ km/s. + : $6.0 < \Delta V_{tot} \leq 6.5$ km/s. + : $\Delta V_{tot} \leq 6.0$ km/s.

From figure 13.5 it can be seen that the individuals in the initial population are not as clustered in the $\theta - \varphi$ search space as was the case in the $t_0 - t_1$ search space. However, it can be seen that a large part of the individuals are situated near $\theta = 0$ or $\theta = 2\pi$. For φ the individuals are spread out more across the search space, but it can be seen that there are bulges around $\varphi = 0$ at both ends of the search space for θ . All individuals in table 13.2 have values for θ and φ that correspond to this observation.

The final DSM related variable for this EdM test case is η . A distribution of the individuals in the initial population is shown in figure 13.6.

From figure 13.6 it can be concluded that the search space for η can be reduced. The maximum bound for η can be set to 0.65, since only 1 individual in the initial population has a value for η that is larger than that. This is also in

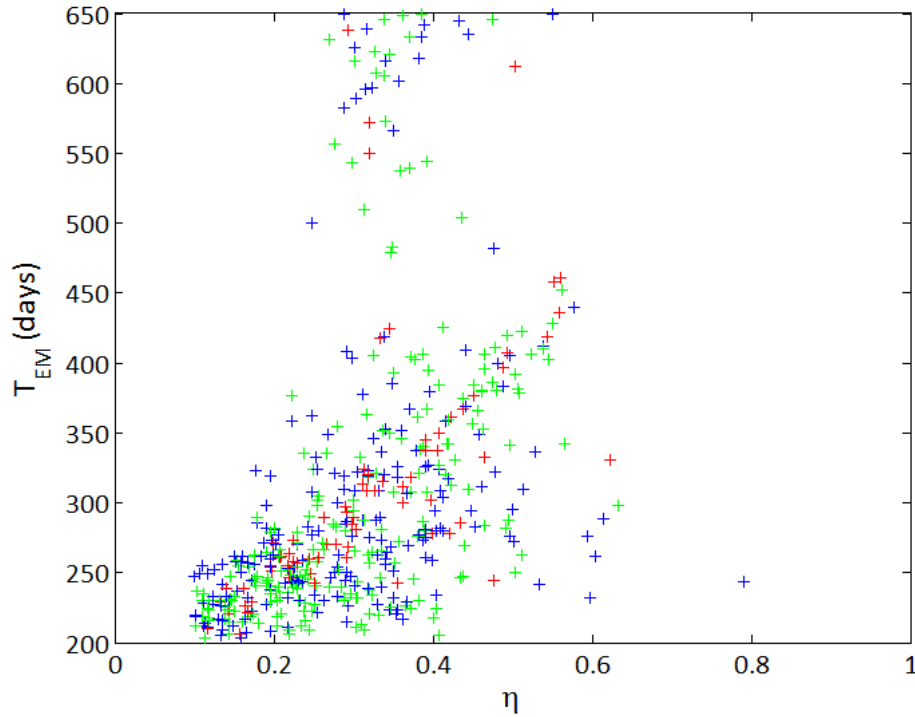


Figure 13.6 Distribution of the feasible individuals in the initial population for seed number 1050 in the $\eta - T_{EM}$ search space. For each variable, the complete search space has been used. $+$: $\Delta V_{tot} > 6.5$ km/s. $+$: $6.0 < \Delta V_{tot} \leq 6.5$ km/s. $+$: $\Delta V_{tot} \leq 6.0$ km/s.

accordance with the values of η for the individuals in table 13.4, where the largest value is 0.578.

From the discussion in this section it has become clear that applying the Genetic Algorithm optimization in GALOMUSIT on the complete search space results in a total ΔV that is close to the global optimum, but it has not reached it. As mentioned earlier, reducing the search space could improve the results. Therefore, in section 13.2.3 some additional tests are performed with reduced search spaces for all variables of this optimization problem.

13.2.3 Additional tests for the Earth-DSM-Mars test case

The test as it has been discussed in section 13.2 has been performed using the complete search space for all decision variables. A number of additional tests have been performed on this test case with constrained search spaces for the decision variables. Except for test VII, the launch window has been reduced to cover only the cluster around 1250 MJD2000. The additional tests that have been performed are given below:

- I ■ $t_0 \in [1100, 1300]$ MJD2000
 - For the other variables the complete search space is used
- II ■ $t_0 \in [1100, 1300]$ MJD2000

- $|\bar{V}_{\infty L}| \in [2.50, 2.90]$ km/s
 - For the other variables the complete search space is used
- III
- $t_0 \in [1100, 1300]$ MJD2000
 - $\theta \in [0, 0.10]$ rad
 - $\varphi \in [-0.30, 0]$ rad
 - For the other variables the complete search space is used
- IV
- $t_0 \in [1100, 1300]$ MJD2000
 - $\eta \in [0.40, 0.60]$
 - For the other variables the complete search space is used
- V
- $t_0 \in [1100, 1300]$ MJD2000
 - $|\bar{V}_{\infty L}| \in [2.75, 2.90]$ km/s
 - $\theta \in [0, 0.10]$ rad
 - $\varphi \in [-0.30, 0]$ rad
 - $\eta \in [0.40, 0.60]$
 - For the time of flight between Earth and Mars the complete search space is used.
- VI
- $t_0 \in [1100, 1300]$ MJD2000
 - $T_{EM} \in [600, 650]$ days
 - For the other variables the complete search space is used
- VII
- The complete search space for all variables is used
 - The population size N_{pop} is increased from 500 to 2000 individuals

The decision vectors of the best individuals for all runs, as well as the orbits of the best individuals and distributions of the individuals in the initial population for the best runs are given in appendix B.

Results for the additional simulations of the EdM test case

Table 13.6 shows the best and worst total ΔV within the runs for each additional test case. The original test is also included.

<i>Test</i>	Min. ΔV (km/s)	Max. ΔV (km/s)	Run time (s)
Original	5.646	5.656	1409
Test I	5.645	5.657	277
Test II	5.634	5.641	357
Test III	5.626	5.650	56
Test IV	5.638	5.652	539
Test V	5.622	5.626	29
Test VI	5.621	5.624	7541
Test VII	5.646	5.654	5277

Table 13.6 Comparison of the best and worst total ΔV for the 10 runs that were performed in each extra test for the EdM test case. The total computation time that was needed dutlruw.lr.tudelft.nl-server to complete the 10 runs is also shown.

From table 13.6 some important conclusions can be drawn:

- Constraining the launch window reduces the computation time significantly, but the best total ΔV only improves very slightly.
- Reducing the search space for $|\bar{V}_{\infty L}|$ around the best known solution in the constrained launch window increases the computation time, but it also improves the best total ΔV .
- Constraining the direction of the hyperbolic excess velocity vector at launch provides a drastic reduction in computation time. Furthermore, the total ΔV is also reduced significantly to a value that is lower than the best value found by *Bernelli-Zazzera et al.* [2007].
- Reducing the search space for η in the constrained launch window improves the results at the cost of an increase in computation time.
- Reduction of the search space for all DSM related variables in the constrained launch window gives a total ΔV that is 10 m/s lower than the best solution found by *Bernelli-Zazzera et al.* [2007]. The time to perform the 10 optimization runs in this case is about half of the time needed when only constraining the launch direction.
- The best solution found by *Bernelli-Zazzera et al.* [2007] has a time of flight of 606.2 days. Constraining the time of flight between 600 and 650 days (case VI) in GALOMUSIT does provide the overall best solution with 5.621 km/s. However, it takes more than 260 times as long to complete the 10 optimization runs with respect to the best result of test V. The gain in total ΔV is only 1 m/s.
- An increase of the population size with all variables in their complete search space only increases the computation time proportional to the population size. The best total ΔV does not improve for this EdM test case.

When the orbits corresponding to the best individuals of the extra tests in appendix B are examined, it can be seen that the initial part of the orbit and the location of the DSM are similar for all tests. The Lambert arc after the DSM can be quite different, however. The time of flight along the Lambert can vary significantly. For total flight times shorter than 300 days (tests II, IV and VII) the magnitude of the DSM is approximately 1.7 km/s and the subsequent $|\bar{V}_{\infty C}|$ is approximately 1.2 km/s. For flight times larger than 300 days the magnitude of the DSM is approximately 2.7 km/s and the subsequent $|\bar{V}_{\infty C}|$ is then approximately 0.2 km/s. In this case the DSM practically aligns the Lambert arc with the orbit of Mars. This feature is also visible in figure 13.1.

Concluding, the new version of GALOMUSIT can be verified for this EdM test case. It should be noted that after the initial optimization, the search space has to be reduced. When this is done, however, a lower total ΔV can be found than the best solution found by *Bernelli-Zazzera et al.* [2007].

13.3 Verification of GALOMUSIT for an Earth-Venus-DSM-Mars transfer

The following test case involves a transfer from Earth to Mars using a swingby at Venus. The swingby at Venus is unpowered and will be followed by a DSM on the leg towards Mars [Vasile et al., 2008].

13.3.1 Search space and results from literature

The first phase of the trajectory is a Lambert arc from Earth to Venus and is completely described by the respective encounter epochs t_0 and t_1 . The second part of the trajectory is described by four additional decision variables, namely t_2 , r_{pV} , ζ_V and η_{VM} . The search space for each of these decision variables is given below (the encounter epochs at Venus and Mars are derived implicitly from the flight times T_{EV} and T_{VM}) [Vasile et al., 2008]:

- $t_0 \in [3650, 9128.75]$ MJD2000
- $T_{EV} \in [50, 400]$ days
- $T_{VM} \in [50, 700]$ days
- $h_{pV} \in [0, 4]$ R_V , so $r_{pV} \in [1, 5]$ R_V
- $\zeta_V \in [0, 2\pi]$ rad
- $\eta_{VM} \in [0.10, 0.90]$

The objective function that is minimized in this EVdM test case is defined as follows [Vasile et al., 2008]:

$$f = |\bar{V}_{\infty L}| + \Delta V_{DSM} \quad (13.2)$$

This means that the ΔV or $|\bar{V}_{\infty}|$ needed for capture is not taken into account in this objective function. This choice of objective function is rather unusual. The total ΔV that is required to complete this mission should involve three different ΔV contributions. The first corresponds to overcoming the heliocentric velocity difference between Earth's orbit around the Sun and the required initial heliocentric velocity of the Lambert arc between Earth and Venus. The second contribution is the magnitude of the DSM, or ΔV_{DSM} . These two contributions are both present in the objective function of equation 13.2. However, the spacecraft also has to enter a parking orbit around Mars, which would result in an impulsive capture maneuver for.

The function value corresponding to the best result found by Vasile et al. [2008] is $f_{best} = 2.982$ km/s. The decision variables corresponding to this best solution are as follows:

- $t_{0_{best}} = 4472.0$ MJD2000
- $T_{1_{best}} = 172.9$ days
- $T_{2_{best}} = 697.6$ days
- $r_{pV_{best}} = 1 R_V$
- $\eta_{VM_{best}} = 0.5094$

The values for the time of flight between Venus and Mars and the pericenter radius at Venus are close to and on the boundaries of the search space. The plane change angle at the Venus swingby as defined by *Vasile et al.* [2008] is different from the plane change angle that is used in this thesis. Therefore these angles can not be compared, but the other variables and corresponding orbits provide plenty of comparison possibilities. The orbit corresponding to the best result found by *Vasile et al.* [2008] is shown in figure 13.7.

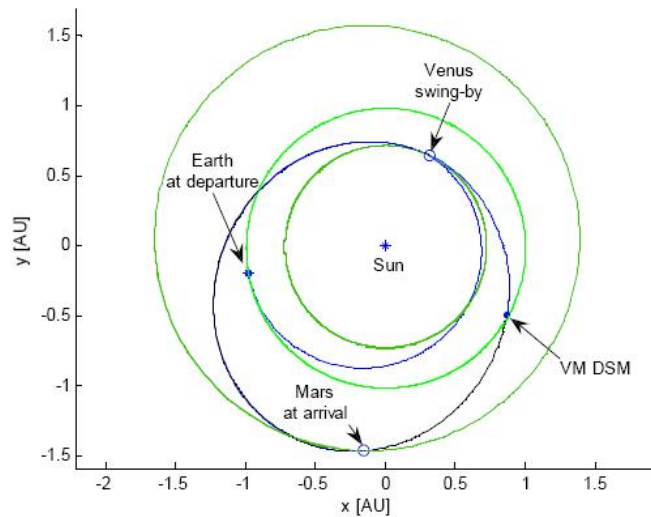


Figure 13.7 The orbit corresponding to the best result found by *Vasile et al.* [2008]. The orbit is shown in a top view of the inertial, heliocentric, ecliptic reference frame.

13.3.2 Results for the EVdM test case using GALOMUSIT

The following constraints in terms of ΔV are used in the optimization process in GALOMUSIT. These were not given by *Vasile et al.* [2008], but assigning values to these parameters ensures that GALOMUSIT will only take realistic solutions into account. In the same time, the constraints are not too tight with respect to the best solution found in [*Vasile et al.*, 2008]. Feasible individuals are more easily generated and the optimization process will run much faster than when extremely tight constraints are set.

- $\Delta V_{DSM} \leq 3.0$ km/s
- $\Delta V_{tot} \leq 10.0$ km/s

All decision variables are left free in their complete search space (see section 13.3.1). The optimization of this sequence is done for five different seed numbers for the random generator. The decision variables for the best solution in each run are shown in table 13.7, together with the objective function value, which is denoted as ΔV_{tot} (so the ΔV needed for capture is not included here).

S	t_0 MJD2000	t_1 MJD2000	t_2 MJD2000	h_{pV} km	ζ_V rad	η_{VM}	ΔV_{tot} km/s
5	6814.4	6983.2	7536.5	10099.2	0.970	0.508	3.381
10	6813.4	6981.6	7535.6	10284.0	0.951	0.518	3.387
75	6818.6	6986.6	7539.3	9642.5	1.021	0.493	3.383
250	6813.3	6981.0	7535.2	10386.4	0.951	0.551	3.396
1000	6812.3	6983.4	7536.7	10028.8	0.941	0.521	3.387
1050	6812.9	6981.6	7535.5	10299.8	0.947	0.497	3.391
1100	6815.1	6983.8	7537.1	10016.6	0.974	0.515	3.383
1150	6816.8	6986.8	7539.5	9559.2	0.996	0.498	3.385
1200	6813.4	6981.4	7535.3	10364.1	0.958	0.508	3.395
1250	6812.5	6980.7	7535.1	10363.7	0.936	0.492	3.395

Table 13.7 EVdM with the search space completely free. The population size was 500 individuals. The total time needed for these ten runs was 3850 sec on the dut1ruw.lr.tudelft.nl-server.

The best total ΔV when the complete search space is used for a population size of 500 individuals is 3.381 km/s, which is 400 m/s higher than the best result found by *Vasile et al.* [2008]. For all runs, the best solution is found near $t_0 \approx 6810$ MJD2000, whereas the best solution given by *Vasile et al.* [2008] is at $t_0 = 4472$ MJD2000. Figure 13.8 shows the distribution of individuals in the $t_0 - t_2$ search space of the initial population for the run with seed 5.

From this figure it can be clearly seen that there are a number of favorable launch windows within the complete search space for t_0 . This phenomenon was also found in section 13.2.2 with the EdM test case. The individuals in the initial population are spread out over the search space, forming several clusters. Two clusters stand out, namely at $t_0 \approx 4400$ MJD2000 and at $t_0 \approx 6800$ MJD2000. The best solution found by *Vasile et al.* [2008] is located in this first cluster. All solutions in table 13.7 are located in this second cluster. The best orbit found by GALOMUSIT when using the complete search space is shown in figure 13.9.

The orbit in figure 13.9 has a different orientation from the orbit corresponding to the best result found by *Vasile et al.* [2008]. This is no surprise since the launch windows are completely different.

The individuals in the initial population are clustered in a very compact manner when shown in the $t_0 - t_2$ space. To check the distribution of the DSM related variables some additional figures are required. Figure 13.10 shows the distribution

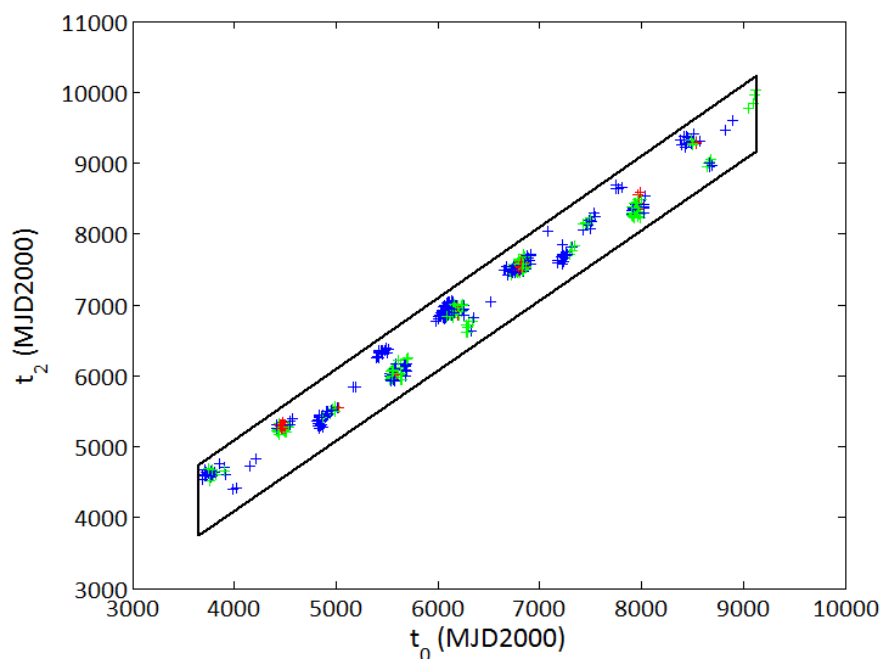


Figure 13.8 Distribution of the feasible individuals in the initial population for seed number 5. The $t_0 - t_2$ search space is indicated by the solid line. $\color{blue}+$: $\Delta V_{tot} > 8.0$ km/s. $\color{green}+$: $6.0 < \Delta V_{tot} \leq 8.0$ km/s. $\color{red}+$: $\Delta V_{tot} \leq 6.0$ km/s.

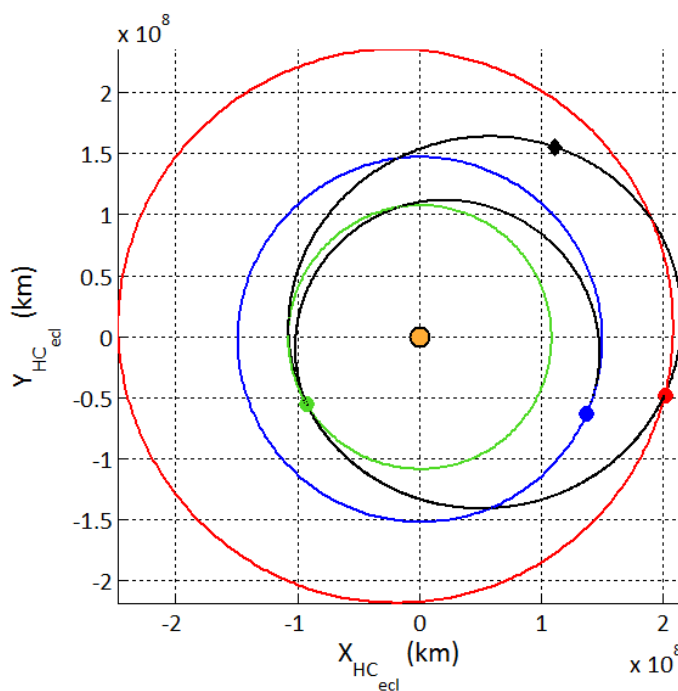


Figure 13.9 Orbit corresponding to the best individual of the run with seed number 5 for the EVdM test case. The complete search space was used for all variables. $\color{blue}\bullet$: Earth at launch, $\color{green}\bullet$: Venus swingby, \blacklozenge : DSM, $\color{red}\bullet$: Arrival at Mars.

of individuals in the $t_0 - h_p$ space.

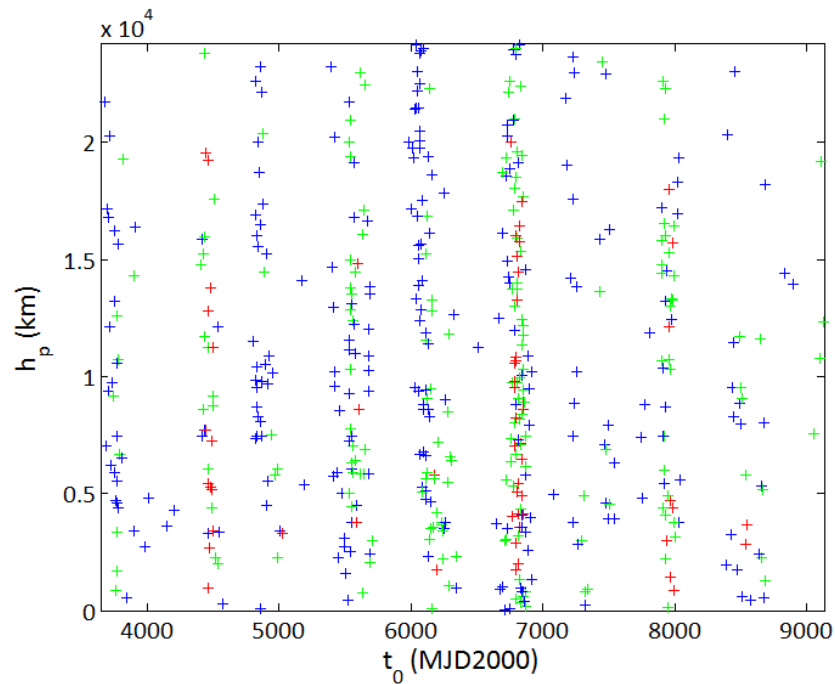


Figure 13.10 Distribution of individuals in the initial population in the $t_0 - h_p$ search space for the run with seed number 5 in the EVdM test case. The complete search space for all variables was used. $\color{blue}+$: $\Delta V_{tot} > 8.0$ km/s. $\color{green}+$: $6.0 < \Delta V_{tot} \leq 8.0$ km/s. $\color{red}+$: $\Delta V_{tot} \leq 6.0$ km/s.

Figure 13.10 clearly shows a banded structure at the values for t_0 where cluster occur. It can be seen that the cluster around 6800 MJD2000 is the strongest one, since it holds the most individuals. The cluster around 4400 MJD2000 does not have that many individuals. Most of the ones that are present, however, have a low total ΔV (this can be seen from the relative abundance of red crosses).

The distribution of the individuals in the initial population in the $t_0 - \zeta$ space is shown in figure 13.11.

Depending on t_0 , the swingby geometry is different. This is clearly visible in figure 13.11, where for the cluster at 4400 MJD2000 the values for ζ are above 4 radians. For the cluster around 6800 MJD2000 ζ is approximately in opposite direction, with values between 0 and 2 radians.

The final DSM related variable for the EVdM test case is η . The distribution of individuals in the initial population in the $t_0 - \eta$ space is shown in figure 13.12.

Figure 13.12 shows that depending on the launch epoch, certain values for η can be disregarded. For the cluster centered at 4400 MJD2000 the values for η

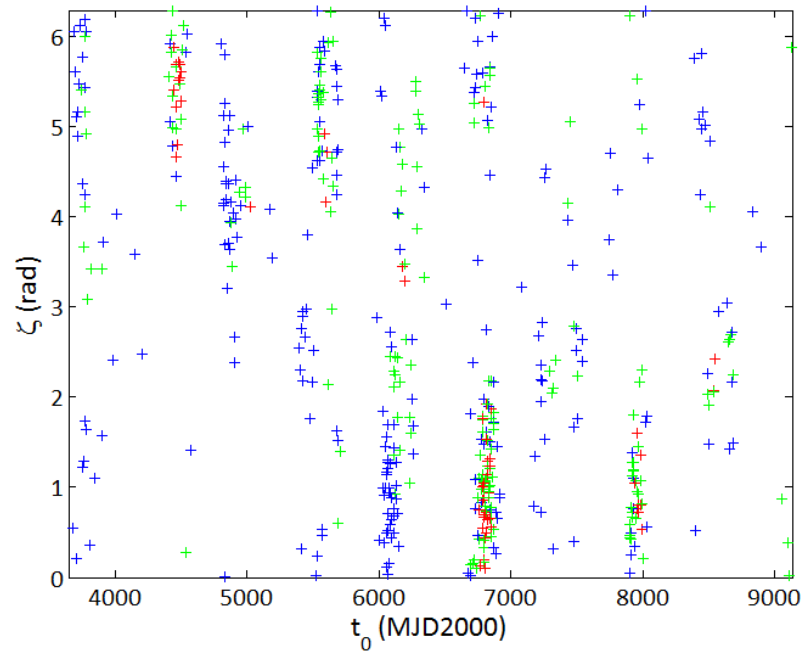


Figure 13.11 Distribution of individuals in the initial population in the $t_0 - \zeta$ search space for the run with seed number 5 in the EVdM test case. The complete search space for all variables was used.
 $\color{blue}+$: $\Delta V_{tot} > 8.0$ km/s. $\color{green}+$: $6.0 < \Delta V_{tot} \leq 8.0$ km/s. $\color{red}+$: $\Delta V_{tot} \leq 6.0$ km/s.

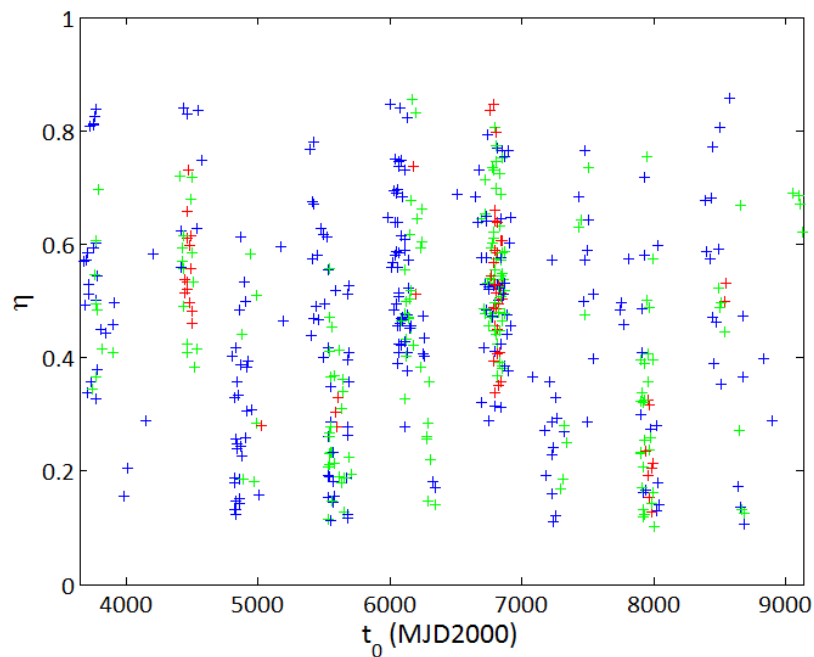


Figure 13.12 Distribution of individuals in the initial population in the $t_0 - \eta$ search space for the run with seed number 5 in the EVdM test case. The complete search space for all variables was used.
 $\color{blue}+$: $\Delta V_{tot} > 8.0$ km/s. $\color{green}+$: $6.0 < \Delta V_{tot} \leq 8.0$ km/s. $\color{red}+$: $\Delta V_{tot} \leq 6.0$ km/s.

vary from 0.40 to 0.80. For the cluster centered at 6800 MJD200 the range of values for η is a bit wider, from 0.30 to 0.80.

The above discussion has made one thing perfectly clear. The search space for the different variables has to be reduced if better solutions are to be found.

13.3.3 Additional tests for the EVdM test case

For the EVdM test case a number of additional optimization runs were performed with constrained search spaces for the decision variables. Also a test was performed with an increased population size for the same search space as was used in section 13.3.1. A description of the extra tests is provided below:

- I
 - $t_0 \in [4200, 4600]$ MJD2000
 - Complete search space for the other variables
- II
 - $t_0 \in [6600, 7000]$ MJD2000
 - Complete search space for the other variables
- III
 - $N_{pop} = 2000$
 - The complete search space for all variables is used
- IV
 - $t_0 \in [4200, 4600]$ MJD2000
 - $h_p \in [0, 0.75]$ R_V
 - For all other variables the complete search space is used
- V
 - $t_0 \in [4200, 4600]$ MJD2000
 - $\zeta \in [4.75, 6.00]$ rad
 - For all other variables the complete search space is used
- VI
 - $t_0 \in [4200, 4600]$ MJD2000
 - $\eta \in [0.45, 0.65]$
 - For all other variables the complete search space is used
- VII
 - $t_0 \in [4200, 4600]$ MJD2000
 - $h_p \in [0, 0.75]$ R_V
 - $\zeta \in [4.75, 6.00]$ rad
 - $\eta \in [0.45, 0.65]$
 - For the time of flight the complete search space is used

The results in terms of decision vectors, distribution of the initial population and orbits can be found in appendix C.

Results for the additional tests for the EVdM test case

Table 13.8 shows the best and worst total ΔV within the runs for each additional test case. The original test is also included.

<i>Test</i>	Min. ΔV (km/s)	Max. ΔV (km/s)	Run time (s)
Original	3.381	3.396	3850
Test I	2.994	3.226	3799
Test II	3.376	3.426	1405
Test III	3.231	3.391	16550
Test IV	2.987	3.185	2744
Test V	2.986	3.286	1324
Test VI	2.988	3.275	1792
Test VII	2.989	3.194	412

Table 13.8 Comparison of the best and worst total ΔV for the 10 runs that were performed in each extra test for the EVdM test case. The total computation time that was needed dutlruw.lr.tudelft.nl-server to complete the 10 runs is also shown.

Using table 13.8 and appendix C some important conclusions can be drawn about this test case:

- Constraining the launch window to fit the cluster of individuals centered around 4400 MJD2000 significantly improves the results. The total ΔV is now only 12 m/s higher than it is for the best solution found by *Vasile et al.* [2008]. The corresponding orbit, which is shown in figure C.2, resembles figure 13.7 very well. From these observations it can be concluded that indeed the global optimum is located in this launch window.
- When the launch window is constrained around the cluster at 6800 MJD2000 the results in total ΔV do not improve much with respect to the original runs. From the run time it can be concluded that this indeed is a strong local optimum with respect to the minimum near 4400 MJD2000. The run time for this minimum is less than half of the run time for the other constrained launch window.
- Increasing the population size and applying it to the complete search space improves the result. The best solution is located in the cluster where the global optimum is located, but still the value for the total ΔV is far from the best known value.
- When the DSM related variables h_p , ζ and η are constrained separately within the launch window around 4400 MJD2000, the best total ΔV decreases. The solutions are all very close to the best known solution and also the decision vectors (and thus the orbits) correspond very well. These runs can be considered as a local optimizations around the best solution.

For clarity, the decision vector and the orbit for the best found solution with GALOMUSIT are given. The decision vector belonging to the best solution is:

$$\bar{x}_{EVdM_{best}} = [t_0, t_1, t_2, h_{pV}, \zeta_V, \eta_V]$$

$$\bar{x}_{EVdM_{best}} = \begin{pmatrix} 4475.2 \\ 4646.6 \\ 5339.7 \\ 415.0 \\ 5.029 \\ 0.542 \end{pmatrix}$$

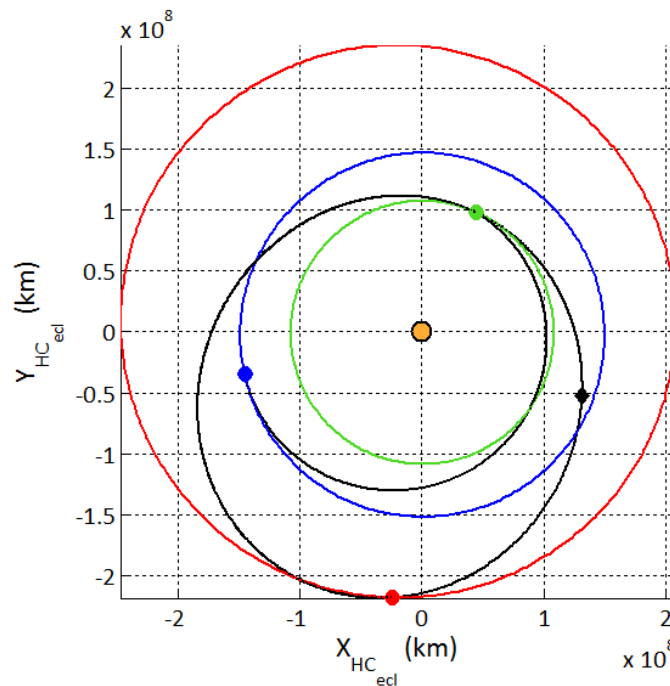


Figure 13.13 Orbit corresponding to the best individual for the EVdM test case found with GALOMUSIT. ●: Earth at launch, ●: Venus swingby, ◆: DSM, ●: Arrival at Mars.

Overall it can be concluded that GALOMUSIT is verified for this EVdM test case. The best solution that was found corresponds to the best solution found by *Vasile et al.* [2008]. One important note should be made here. When using large search spaces the program is sensitive to the strength of local minima. This could be clearly seen in the original test, where the optimization was executed 10 times, but each time the best solution that was found was located at a strong local minimum centered at 6800 MJD2000. After an increase in the population size (extra test III), GALOMUSIT was able to find that the best solution was in the cluster centered near 4400 MJD2000. This came at the price of a run time of more than 4.5 hours and even then it did not come close to the best value for the total ΔV . For the future runs that are done with GALOMUSIT, the complete search space will be examined first, but after that always some search space reduction will be done.

Part IV: Results for the Uranus orbiter mission

Results for the Uranus orbiter mission without DSMs

Before the results of the trajectories with DSMs are generated and discussed, first the results without DSMs are presented in this chapter. The method that is used is the same as used by *Melman* [2007] since the Uranus mission without DSMs shows striking similarities with the mission to Neptune studied in that thesis.

First the mission to Uranus will be analyzed in section 14.2, with the same possible swingby trajectories as used by *Melman* [2007]. Then, in section 14.3, a new range of possible trajectories is analyzed when a swingby at Venus is allowed after an Earth swingby.

14.1 Direct transfer from Earth to Uranus

The optimization of a direct transfer from Earth to Uranus without a DSM has two variables, t_0 and t_1 . Two impulsive maneuvers, one at launch and one at capture, make up the total ΔV for this mission. The optimization for the direct transfer was done 10 times using the settings in GALOMUSIT that are given in section 14.2.

The breakdown of the total ΔV for the best direct trajectory from Earth to Uranus is given in table 14.1.

ΔV_L	5.620 km/s
ΔV_C	1.053 km/s
ΔV_{tot}	6.673 km/s

Table 14.1 Breakdown of the total ΔV for the trajectory with the lowest total ΔV for a direct Earth-Uranus transfer without DSM. The seed number for this run was 1250.

The major contributor is ΔV_L , because the spacecraft has to gain such an amount of velocity at launch that the spacecraft is inserted into a highly elliptic orbit ($e = 0.90$) with a large semi-major axis ($a = 1.52 \cdot 10^9$ km which is

approximately 10 AU). For this best individual the launch date is 13 June 2015 (5641.5 MJD2000) and the arrival date is 30 May 2030 (11106.5 MJD2000), which gives a time of flight of 14.96 years.

Figure 14.1 shows the distribution of the individuals in the initial population.

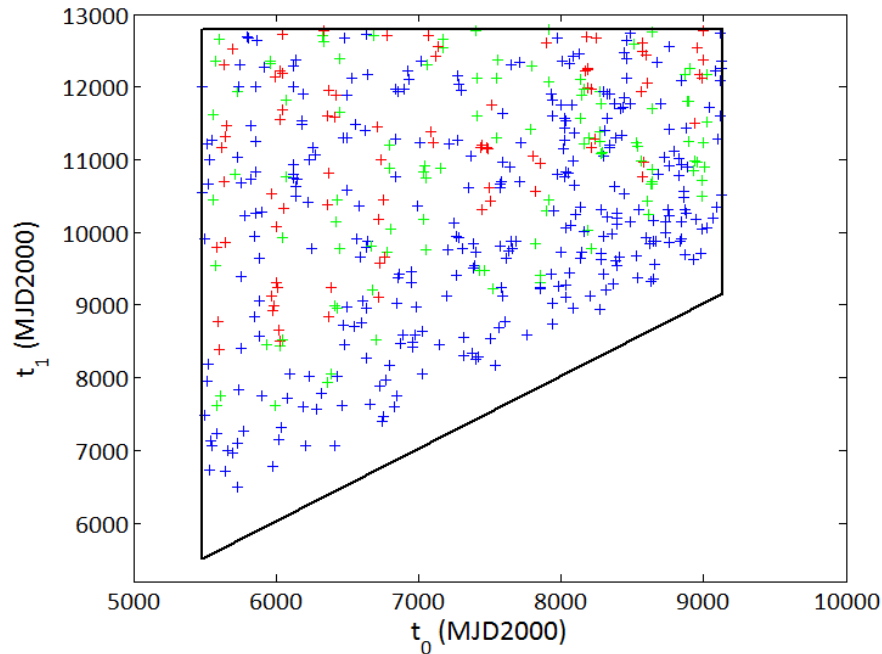


Figure 14.1 Distribution of the individuals in the initial population for the EU direct trajectory. The seed number for the run producing these individuals is 5. + : $\Delta V_{tot} \geq 20$ km/s, + : $12 \leq \Delta V_{tot} < 20$ km/s, + : $\Delta V_{tot} \leq 12$ km/s.

Because the constraint on the maximum allowable total ΔV is set to a very high value (75 km/s), almost the entire $t_0 - t_1$ search space contains possible solutions. If the constraint would have been set to 10 km/s, the distribution of individuals would look like figure 14.2.

In this figure the repetitive pattern of launch windows for a direct transfer from Earth to Uranus is clearly visible. Each possible launch opportunity is approximately a year after the previous one, which corresponds to the synodic period for an Earth-Uranus transfer. Tightening the constraint on the total ΔV has not improved the result, but it only confirmed it. The minimum total ΔV for a direct transfer from Earth to Uranus for this mission is 6.673 km/s.

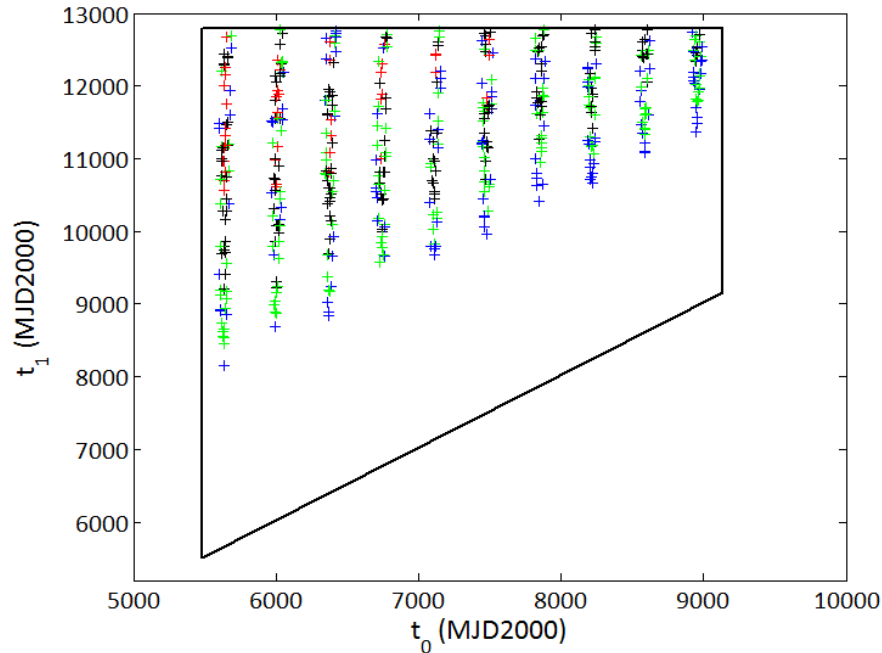


Figure 14.2 Distribution of the individuals in the initial population for the EU direct transfer trajectory is a constraint of $\Delta V_{tot} \leq 10$ km/s would be set. The seed number for the run producing these individuals is 5. $+$: $\Delta V_{tot} \geq 9$ km/s, $+$: $8 \leq \Delta V_{tot} < 9$ km/s, $+$: $7 \leq \Delta V_{tot} < 8$ km/s, $+$: $\Delta V_{tot} < 7$ km/s.

14.2 Results for trajectories from Earth to Uranus with swingbys

There are many possible planetary swingby sequences that the spacecraft can follow on its way to Uranus. In this section the same swingby sequences that were used by *Melman* [2007] will also be used for a mission to Neptune. There are 77 of them and they are shown in table 14.2.

V	E	M	J	S	VV	VE
VM	VJ	VS	EE	EM	EJ	ES
MJ	MS	JS	VVV	VVE	VVM	VVJ
VVS	VEE	VEM	VEJ	VES	VMJ	VMS
VJS	EEM	EEJ	EES	EMJ	EMS	EJS
MJS	VVVE	VVVM	VVVJ	VVVS	VVEE	VVEM
VVEJ	VVES	VVMJ	VVMS	VVJS	VEEM	VEEJ
VEES	VEMJ	VEMS	VEJS	VMJS	EEMJ	EEMS
EEJS	EMJS	VVVEE	VVVEM	VVVEJ	VVVES	VVVMJ
VVVMS	VVVJS	VVEEM	VVEEJ	VVEES	VVEMJ	VVEMS
VVEJS	VVMJS	VEEMJ	VEEMS	VEEJS	VEMJS	EEMJS

Table 14.2 Overview of the 77 different gravity assist sequences as defined in [*Melman*, 2007]. The initial planet is Earth and the final planet is Uranus for all sequences, so they are not shown in this table.

The following guidelines were used in order to come to this particular list of 77 sequences:

- A maximum of 5 swingbys is used per sequence. When looking at other missions to the outer planets in the solar system (see chapter 4), this upper limit of 5 swingbys is a practical one, since no missions have more than 5 swingbys.
- Mercury, the innermost planet in the solar system will not be used as a swingby planet. There are a number of reasons for this. The fact that Mercury is situated close to the Sun means that the satellite will have to cope with high heat loads. Furthermore, because of its proximity to the Sun, Mercury is too far in the wrong direction for a mission from Earth to Uranus.
- Two other planets in the solar system, Neptune and Pluto, are not used as a swingby planet either. They are located far beyond Uranus and are not of any use in this mission.
- Venus and Earth are planets that can be used for consecutive swingbys. Venus can be used three times for consecutive swingbys and Earth twice. The orbital periods of both planets are relatively short compared to the other planets that can be used for a gravity assist and the orbital period of Venus is about 0.62 times Earth's orbital period. So the revolutions of Venus about the Sun take almost the same amount of time as two revolutions for Earth.
- Mars, Jupiter and Saturn are used only once per sequence. Because of their long orbital periods compared to Venus and Earth, the time needed for consecutive flybys of these planets is large and not advantageous for the mission.
- Venus is used as final planet in a swingby sequence when it comprises swingbys at Venus only. After a swingby of Earth or any planet that is further away from the Sun, Venus will not be used.

14.2.1 Mission specific settings in GALOMUSIT

In the subsequent sections a number of optimization runs in GALOMUSIT have been executed for the mission to Uranus. The following mission specific settings are applied, which were derived from chapter 2:

- The starting point for the mission is Earth.
- The target planet of the mission is Uranus.
- It is a one-way orbiter mission.
- The spacecraft will either perform 1, 2, 3, 4 or 5 swingbys on its way to Uranus.
- No use is made of aerogravity assists.
- The launch window starts at 1 January 2015 and ends on 1 January 2025 [Molenaar, 2007].
- The maximum arrival date at Uranus is 1 January 2035, such that the total flight time is at most 20 years from the start of the launch window [Molenaar, 2007].
- The spacecraft will start its journey from a geostationary transfer orbit (GTO) with a perigee altitude of 185 km.

- The final parking orbit around Uranus is a highly elliptical orbit with a pericenter altitude of 2500 km and an eccentricity of 0.90.
- The positions and velocities of the planets at a particular epoch are derived from the JPL DE200 planetary ephemeris.

14.2.2 Initial GA settings in GALOMUSIT

Next to the mission specific parameters that need to be set in GALOMUSIT, also the settings for the GA (GA) optimization need to be set before any optimization run can be done. The first set of runs will optimize the 77 sequences as mentioned in table 14.2. The following GA settings will be used for this first set of runs:

- Each run will be done for five different seed numbers for the random generator: 5, 10, 75, 250 and 1000.
- The optimization will be single-objective, where the optimization parameter is the total ΔV . In his thesis work *Melman* [2007] assessed the population size for the different number of swingbys. Table 14.3 shows the population sizes for the trajectory optimization for a mission to Neptune:

<i>Number of swingby bodies</i>	<i>Population size</i>
1	500
2	1000
3	1000
4	2000
5	4000

Table 14.3 Population size for the different amount of swingby bodies in the single-objective GA optimization with constant population size [*Melman*, 2007].

Since the same swingby sequences are considered for the mission to Uranus, it is assumed that these values for the population size are sufficient for the current study.

- The maximum number of generations that can be reached during the GA optimization is 500.
- The number of generations that has to be reached before checks for convergence are performed is set to 10. This also means that convergence will be checked over 10 generations.
- The definition for convergence in this single-objective optimization process is that the maximum fitness value should be within 0.001 km/s over 10 generations and the average fitness value should be within 0.005 km/s [*Melman*, 2007].
- The amount of the best individuals (with respect to the optimization parameter, the total ΔV) that is copied into the next generation, expressed as a fraction of the total population has to be set. Elitism is set to 0.10 in the first set of runs.

- The amount of randomly generated new individuals that immigrate to the new generation, expressed as a fraction of the total population has to be set. Immigration is set to 0.05 in the first set of runs.
- The probability that one of the newly immigrated individuals is mutated. It should be stressed again that this is not the ideal implementation of mutation, since it does not makes much sense to mutate newly created random individuals. Later in this section mutation will be turned off.
- The lower limit on the time of flight in between consecutive planetary encounters is set to 30 days.
- The upper limit on the total ΔV for each created individual is set to 75 km/s.

14.2.3 Results for 10% elitism, 5% immigration and 0.1% mutation

As mentioned earlier, the optimization process was done for the 77 different swingby sequences that connect Earth and Uranus (see also table 14.2). Each run that was performed analyzed these sequences for one particular seed number for the random generator. Figure 14.3 shows a bar plot of the 20 sequences out of the 77, that produced the lowest total ΔV .

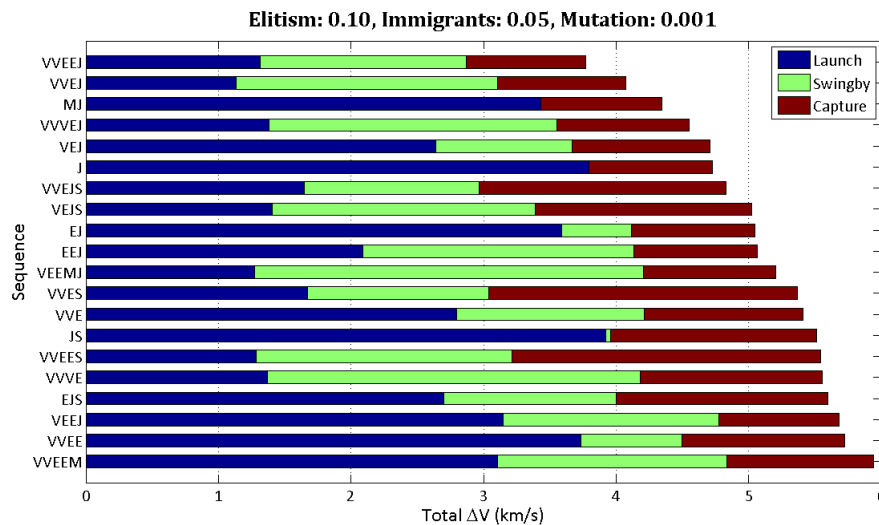


Figure 14.3 Schematic of the 20 best sequences for the first set of runs. Elitism: 10%, Immigration: 5% and Mutation: 0.1% for the configuration described in section 14.2. Only the best result out of the five different seed numbers for each sequence has been placed in this figure.

In this figure a clear distinction has been made between the ΔV needed for either launch, swingbys or capture in such a sequence. For each sequence only the best result (the lowest total ΔV) out of the five different seed numbers is shown. From figure 14.3 several observations can be made:

- It is advantageous to perform multiple swingbys on the trajectory from Earth to Uranus. Only one out of the best 20 sequences has a single swingby. It is no surprise that this trajectory involves a swingby at Jupiter, since this is the

largest and most powerful swingby planet in the solar system (see also figure 8.7).

- Many of the best 20 sequences have multiple swingbys in the inner solar system (so at Venus and Earth) to increase the velocity before traveling to the outer part of the solar system.
- Mars is hardly present as a swingby planet among the best 20 sequences. This can be explained using the rationale of section 8.4. Mars is not a massive planet and does not have a large capability to increase the total energy of a spacecraft during a swingby. It should be noted, however, that one of the best sequences, MJ, performs very well. This is most likely because the planets (Earth and Uranus included) are oriented in such a way that the total ΔV is quite low.
- Swingbys at Saturn cause the satellite to gain such an amount of velocity that the ΔV needed for capture around Uranus becomes quite high. This is the most important reason that Saturn can not be found among the best 6 sequences and is only represented in 5 of the best 20 sequences.

The best sequence for these GA settings is VVEEJ. This means that after launch from the GTO the satellite performs two swingbys at Venus, before performing consecutive swingbys at Earth and swinging by Jupiter in order to arrive at Uranus. The characteristics of this sequence are shown in table 14.4. The seed number that produced this best result was 250 and the total ΔV is 3.771 km/s.

<i>Launch</i>	<i>Date</i>	ΔV (km/s)	C_3 (km ² /s ²)	
	14/06/2015	1.3171	12.380	
<i>Swingbys</i>	<i>Date</i>	ΔV_{req} (km/s)	ΔV_{gained} (km/s)	<i>h</i> (km)
	V: 05/12/2015	0.0005	3.578	2562.6
	V: 20/02/2017	0.0002	-2.029	2292.0
	E: 27/04/2017	0.0019	5.856	2886.8
	E: 15/02/2019	1.4570	3.674	6066.0
J: 31/01/2022	0.0899	9.137	300209.2	
<i>Capture</i>	<i>Date</i>	ΔV (km/s)	C_3 (km ² /s ²)	V_{entry} (km/s)
	30/12/2034	0.9043	16.001	20.688

Table 14.4 The best sequence, VVEEJ, for elitism: 10%, immigration: 5% and mutation: 0.1%. The seed number for this run was 250.

Table 14.5 shows the total time it took for each run of 77 sequences to be completed.

From this table it can be concluded that for these initial settings of the GA it took more than 50 minutes to analyze all 77 sequences. In the subsequent sections a number of different GA settings is used to examine if the results improve. Only the best 20 sequences that have been shown in this section will be taken into account from now on.

<i>Seed</i>	<i>Run time (s)</i>
5	3069
10	3127
75	3033
250	3337
1000	3072

Table 14.5 Run time for the five different seed numbers of each of the 77 possible swingby sequences. Elitism: 10%, Immigrants: 5% and Mutation: 0.1%. The runs were executed on the `dutlruw.lir.tudelft.nl`-server.

14.2.4 Additional tests

For the next tests, mutation has been turned off since it is a random change of a variable in a randomly created new individual. The GA settings used in the next tests are:

- 10% elitism, 5% immigration
- 10% elitism, 20% immigration
- 15% elitism, 15% immigration
- 20% elitism, 5% immigration

For each of these four GA settings, the 20 best sequences of section 14.2.3 were optimized with GALOMUSIT. Each run was repeated 5 times, each time with a different seed number (the same seeds as used before). The bar charts and characteristics of the best individual for each swingby sequence can be found in appendix D. Table 14.6 shows the best total ΔV that was found for each sequence, together with the corresponding GA settings and seed number.

From table 14.6 it can be seen that the best individual that has been found has VVEJ as a swingby sequence. The total ΔV for this sequence is 2.892 km/s, with a total time of flight of 18.8 years. This is 3.781 km/s lower (56.7% improvement) than the result for the direct Earth-Uranus transfer. The characteristics of the best individual can be found in appendix D.3. The orbit for this VVEJ swingby sequence is shown in figures 14.4 and 14.5. These figures show the journey of the spacecraft in the inner part and outer part of the solar system separately. For the trajectory in the outer part of the solar system, only the part from the Earth swingby onwards is shown.

All swingby sequences in table 14.6 show improvements in the total ΔV with respect to the direct transfer. As already mentioned, VVEJ was the best sequence by far. The second best sequence, VVEEJ, is also far better than all other sequences (aside VVEJ of course). The total ΔV decreases with 2.907 km/s, which is an improvement of 43.6%.

Sequence	GA settings			Total ΔV (km/s)	Seed
	E (%)	I (%)	M (%)		
VVEJ	15	15	0	2.892	75
VVEEJ	15	15	0	3.766	250
MJ	20	5	0	4.348	1000
VVVEJ	15	15	0	4.453	1000
VVEJS	15	15	0	4.626	10
VEJ	20	5	0	4.640	1000
J	10	5	0	4.727	5
EJ	20	5	0	4.789	250
VEJS	20	5	0	4.914	250
VVES	15	15	0	5.011	250
EEJ	20	5	0	5.059	1000
VEEMJ	15	15	0	5.122	250
VVEE	15	15	0	5.368	250
VVE	20	5	0	5.399	1000
VVEES	10	20	0	5.502	1000
JS	10	5	0	5.514	250
VVVE	20	5	0	5.546	1000
EJS	10	5	0 </td <td>5.581</td> <td>250</td>	5.581	250
VEEJ	15	15	0	5.678	75
VVEEM	20	5	0	5.753	250

Table 14.6 Best total ΔV and the corresponding GA settings for each of the 20 best sequences in section 14.2.3.

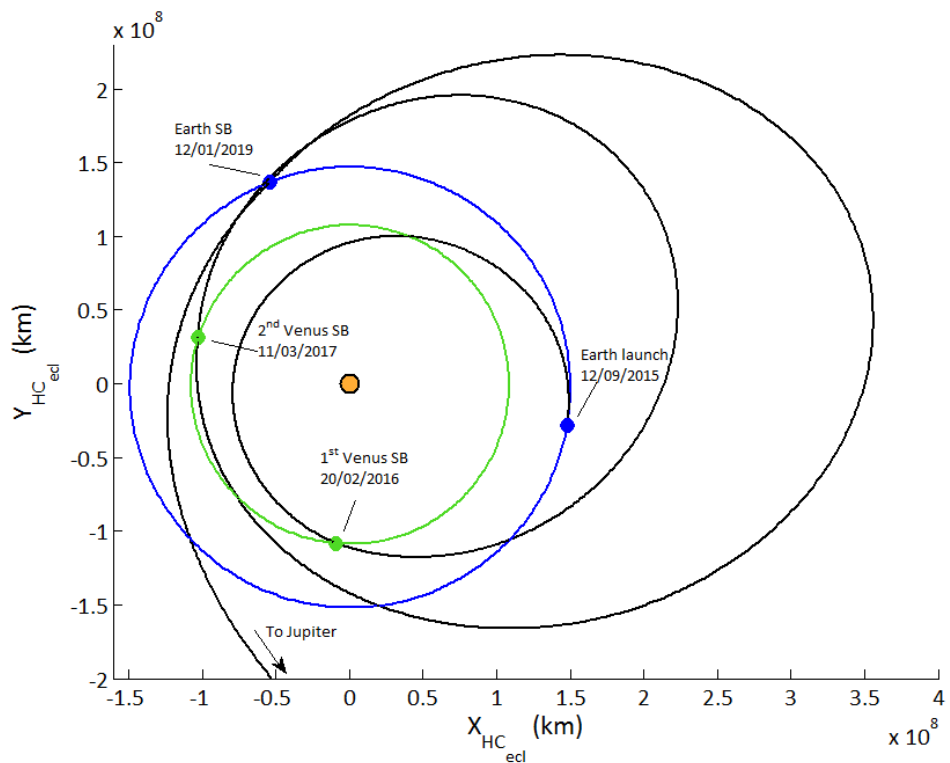


Figure 14.4 Trajectory of the spacecraft in the inner part of the solar system for the best swingby sequence: VVEJ.

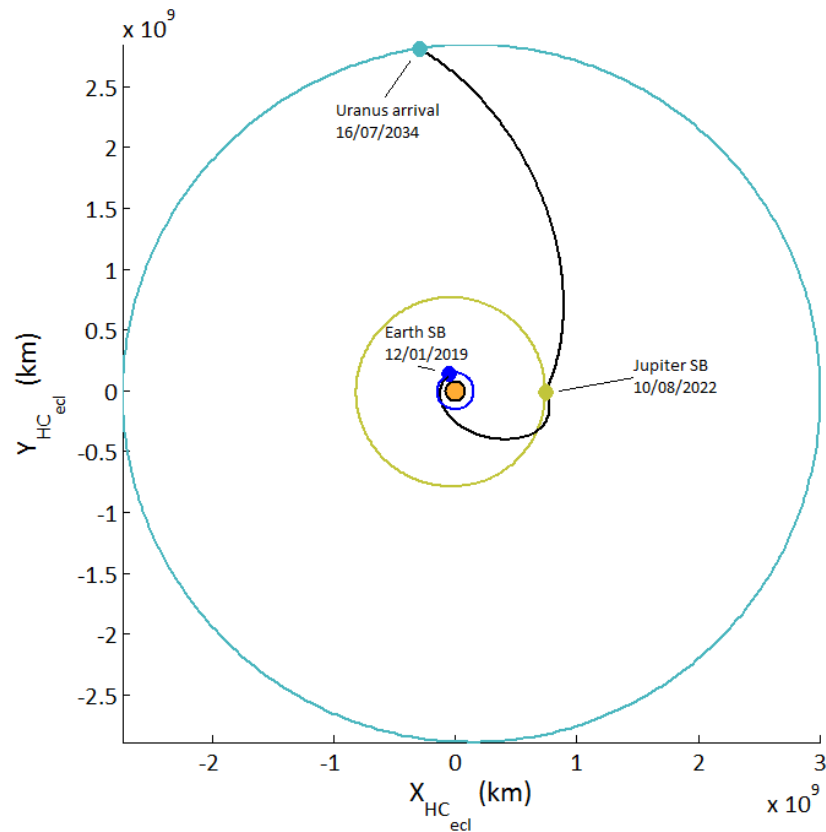


Figure 14.5 Trajectory of the spacecraft in the outer part of the solar system for the best swingby sequence: VVEJ.

From table 14.6 it can also be seen that two settings for the GA provide the majority of the best solutions. 15% Elitism with 15% immigration and 20% elitism with 5% immigration each produce the best result for 8 of the 20 swingby sequences. The best overall result total ΔV is produced with 15% elitism and 15% immigration, so therefore these GA settings are considered to be the best and will be used for the remainder of this thesis research.

14.3 Sequences when a Venus swingby is allowed after an Earth swingby

In the set of possible swingby sequences used in section 14.2, it was not allowed to perform a swingby at Venus after a swingby at Earth was performed. However, since the inner part of the solar system is used to gain velocity for the journey to the outer parts of the solar system, it might be that new swingby possibilities also provide trajectories with a low required total ΔV .

When generating these new sequences, the same rationale of section 14.2 is used. A maximum of 5 swinbys is still allowed. Venus can be used no more than three times within a swingby sequence. Earth can not be used more than twice and the other planets can be used only once. Using these guidelines the set of new

swingby sequences in table 14.7 was generated.

EV	VEV	EVV	EVE	EVM	EVJ	EVS
EEV	VVEV	VEVV	VEVE	VEVM	VEVJ	VEVS
VEEV	EVVV	EVVE	EVVM	EVVJ	EVVS	EVEV
EVEM	EVEJ	EVES	EVMJ	EVMS	EVJS	EEVV
EEVM	EEVJ	EEVS	VVEVE	VVEVM	VVEVJ	VVEVS
VVEEV	VEVVE	VEVVM	VEVVJ	VEVVS	VEVEV	VEVEM
VEVEJ	VEVES	VEVMJ	VEVMS	VEVJS	VEEVV	VEEVM
VEEVJ	VEEVS	EVVVE	EVVVM	EVVVJ	EVVVS	EVVEV
EVVEM	EVVEJ	EVVES	EVVMJ	EVVMS	EVVJS	EVEVV
EVEVM	EVEVJ	EVEVS	EVEMJ	EVEMS	EVEJS	EVMJS
EEVVV	EEVVM	EEVVJ	EEVVS	EEVMJ	EEVMS	EEVJS

Table 14.7 Overview of the 77 new gravity assist sequences that are obtained when a Venus swingby is allowed after an Earth swingby. The initial planet is Earth and the final planet is Uranus for all sequences, so they are not shown in this table.

14.3.1 Results for 15% elitism, 15% immigration

The idea behind the new set of possible swingby trajectories was that new ways were created to gain velocity in the inner part of the solar system. Figure 14.6 shows the breakdown of the total ΔV of the 10 best sequences of table 14.7.

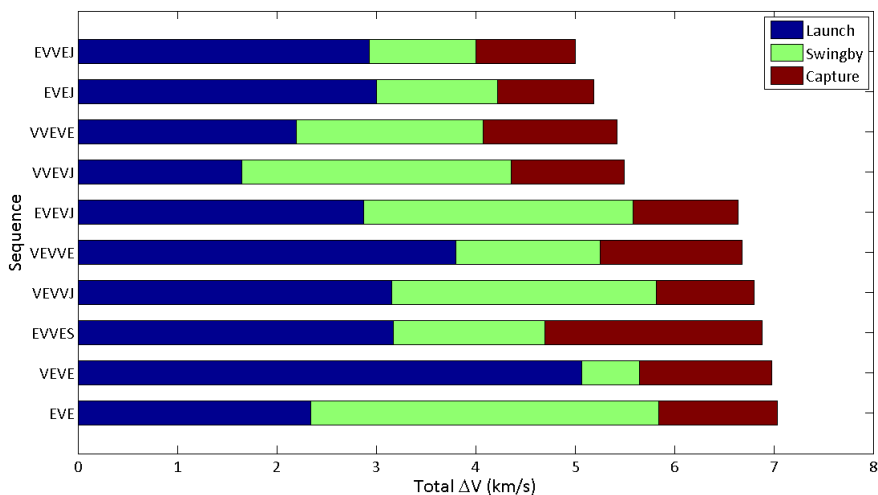


Figure 14.6 Schematic of the 10 best sequences out of the set of 77 new swingby possibilities when a swingby at Venus is allowed after an Earth swingby. Elitism was set to 15%, immigration to 15% as well and no mutation was used. Only the best result out of the five different seed numbers for each sequence has been placed in this figure.

The best result with the new set of swingby possibilities was obtained with EVVEJ as the swingby sequence. The total ΔV needed for this trajectory is 5.005 km/s. The seed number producing this result was 250. The characteristics of the

best result are shown in table 14.8.

<i>Launch</i>	<i>Date</i>	ΔV (km/s)	C_3 (km ² /s ²)	
	09/01/2017	2.9298	52.299	
<i>Swingbys</i>	<i>Date</i>	ΔV_{req} (km/s)	ΔV_{gained} (km/s)	<i>h</i> (km)
	E: 02/11/2018	0.0065	-7.155	306.2
	V: 02/03/2019	0.0050	2.929	3065.7
	V: 05/04/2020	0.0236	2.915	3157.4
	E: 01/06/2020	0.0262	3.234	4163.7
J: 24/04/2023	1.0163	9.242	322585.1	
<i>Capture</i>	<i>Date</i>	ΔV (km/s)	C_3 (km ² /s ²)	V_{entry} (km/s)
	15/11/2034	0.9971	19.849	20.781

Table 14.8 The best sequence, EVVEJ, when a swingby at Venus is allowed after an Earth swingby. The seed number for this run was 250.

From figure 14.6 it can be concluded that allowing a swingby at Venus after an Earth swingby does not improve the results for the mission to Uranus. In fact, the EVVEJ trajectory would not be in the best 5 results for the original set of possible swingby sequences.

Results for trajectories with DSMs

In this chapter the introduction of deep space maneuvers to trajectories for the Uranus mission is assessed. The minimum launch date of 1 January 2015 is equivalent to 5478.5 MJD2000, the maximum launch date of 1 January 2025 is equivalent to 9131.5 MJD2000 and the maximum arrival date of 1 January 2035 is equivalent to 12783.5 MJD2000. The parking orbits around Earth and Uranus are defined in chapter 2. For the Genetic Algorithm, the best settings found in chapter 14 will be used again for optimizing trajectories with DSMs. Elitism is set to 15%, immigration is set to 15% as well and mutation is turned off.

First of all, the trajectory from Earth to Uranus without swingbys is analyzed in section 15.1. In section 15.2 trajectories to Uranus with a single swingby will be assessed. Finally, section 15.3 will cover trajectories with two swingbys between Earth and Uranus.

15.1 Earth-Uranus transfer without swingbys

The first simulations that are done for the Uranus mission cover the direct transfer from Earth to Uranus. The results for the Lambert solution (so without the addition of a DSM) have already been presented in chapter 14.

15.1.1 Results of an EdU transfer with a complete search space

A DSM will now be added to the trajectory to examine whether or not a lower value for the total ΔV can be found than for the direct Earth-Uranus transfer. Since a DSM is added to the leg right after Earth launch, $|\bar{V}_{\infty_L}|$, θ , φ and η need to be generated randomly from a given search space. For each of these variables the complete search space that is used is:

- $|\bar{V}_{\infty_L}| \in [0, 12]$ km/s
- $\theta \in [0, 2\pi]$ rad
- $\varphi \in [-\frac{\pi}{2}, +\frac{\pi}{2}]$ rad
- $\eta \in [0.01, 0.90]$

The launch window and maximum arrival date are the same as before. Next to the constraint on the maximum allowable total ΔV (75 km/s), a constraint is set on the maximum allowable ΔV_{DSM} . If an individual would be generated with a DSM higher than 5.0 km/s, it will not be put into the population. The minimum time of flight for each generated individual is 30 days.

The optimization is repeated 10 times, each time with a different seed number for the random generator. Table 15.1 shows the decision vectors corresponding to the best individual for each run, as well as the seed number for each run and the total ΔV .

S	t_0 MJD2000	t_1 MJD2000	$ \bar{V}_{\infty L} $ km/s	θ rad	φ rad	η	ΔV_{tot} km/s
5	5641.3	11585.8	11.421	0.081	-0.022	0.184	6.682
10	5645.3	11931.1	11.428	0.053	0.057	0.103	6.718
75	5642.4	11664.2	11.420	0.066	0.047	0.134	6.690
250	6377.6	11945.8	11.464	0.083	0.087	0.160	6.744
1000	5646.6	11493.4	11.463	6.188	0.084	0.055	6.698
1050	6383.4	12193.4	11.405	6.260	-0.040	0.139	6.722
1100	6382.5	11986.2	11.408	6.226	0.015	0.132	6.696
1150	6005.5	11171.9	11.429	0.055	-0.031	0.066	6.722
1200	5643.8	11959.0	11.423	0.091	-0.028	0.172	6.711
1250	6011.4	11760.6	11.404	0.012	0.002	0.074	6.700

Table 15.1 Decision vectors and total ΔV for the best individuals of each run. The complete search space for all variables is used. Elitism was set to 15%, immigration was set to 15% and the population size was 500. The time needed on the dut1rww.lrw.tudelft.nl-server was 2538 s.

The best individual found by GALMUSIT using the complete search space for all decision variables has a total ΔV of 6.682 km/s, which is 9 m/s higher than the best solution found when no DSM was applied. Table 15.2 shows the breakdown of the total ΔV for the best individual.

ΔV_L	5.620 km/s
ΔV_{DSM}	0.023 km/s
ΔV_C	1.040 km/s
ΔV_{tot}	6.682 km/s

Table 15.2 Breakdown of the total ΔV for the trajectory with the lowest total ΔV for the EdU transfer. The complete search space for all variables was used. The seed number for this run was 1250.

Table 15.1 shows that for all the best solutions, the values for the DSM related variables are all close to each other. This means that the search space for these variables can be constrained, hopefully improving the results. In section 15.1.2 some extra optimization runs will be discussed where the search space for the decision variables has been reduced.

Figure 15.1 shows the initial population in the $t_0 - t_1$ space when the complete search space for all variables is used.

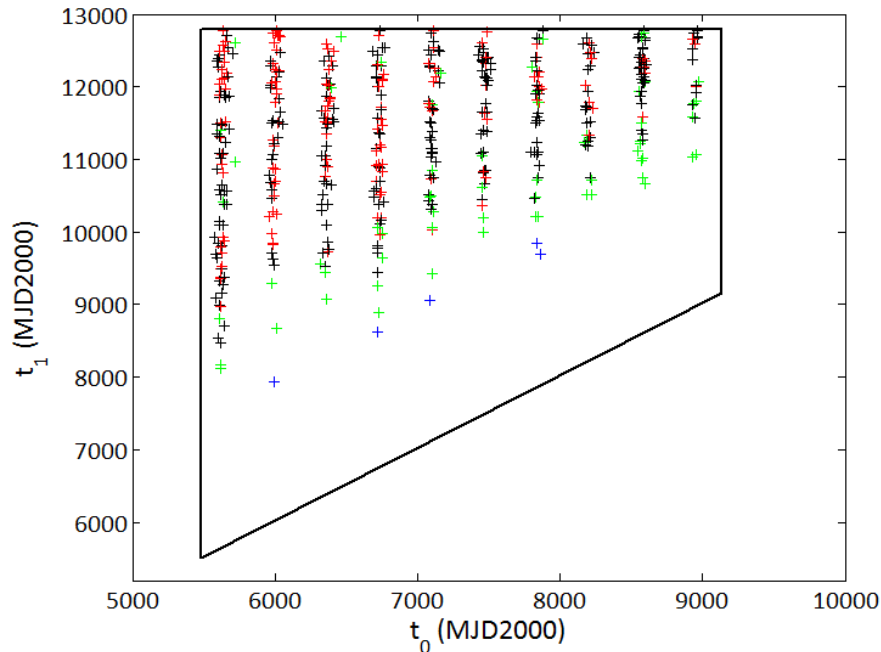


Figure 15.1 Distribution of the individuals in the initial population for the EdU trajectory using the complete search space for all variables. The seed number for the run producing these individuals is 5. \times : $\Delta V_{tot} \geq 15$ km/s, $+$: $12 \leq \Delta V_{tot} < 15$ km/s, \oplus : $10 \leq \Delta V_{tot} < 12$ km/s, \oplus : $\Delta V_{tot} \leq 10$ km/s.

The structure corresponding to the synodic period for an Earth-Uranus transfer is visible in figure 15.1. The launch epochs for the individuals in table 15.1 are located in one of the first three launch windows. The best individual is located in the first one.

The distribution of the DSM related variables in the initial population can be shown as well. The direction angles of the hyperbolic excess velocity, θ and φ , are plotted in figure 15.2.

From figure 15.2 it can clearly be seen that for this trajectory only a very small portion of the search space is interesting. The values for θ are either near 0 or 2π and for φ the values are all near 0. This means that it is most advantageous to have \vec{V}_{∞_L} point in the same direction as \vec{V}_{pl} . This makes sense because when these two velocity vectors point in the same direction, it results in the maximum increase in heliocentric velocity. A high velocity is required after the engine burn at Earth (see section 14.1), so only a small part of the search space for θ and φ can be used.

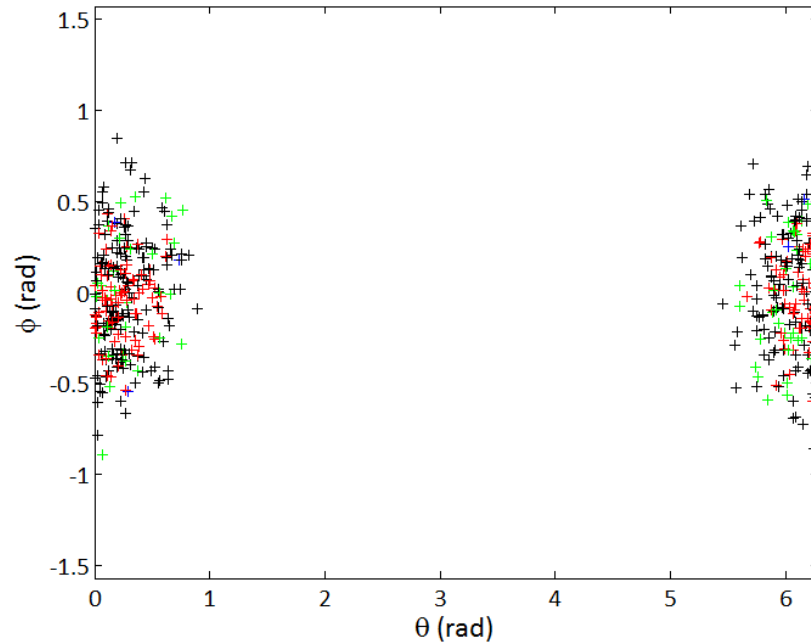


Figure 15.2 Distribution of the individuals in the initial population for the EdU trajectory in the $\theta - \varphi$ space. The complete search space for all variables was used. The seed number for the run producing these individuals is 5. $\color{blue}+$: $\Delta V_{tot} \geq 15$ km/s, $\color{green}+$: $12 \leq \Delta V_{tot} < 15$ km/s, $\color{black}+$: $10 \leq \Delta V_{tot} < 12$ km/s, $\color{red}+$: $\Delta V_{tot} \leq 10$ km/s.

One of the other DSM related variables is $|\bar{V}_{\infty L}|$. The values of $|\bar{V}_{\infty L}|$ are plotted against the launch epoch t_0 in figure 15.3.

From figure 15.3 it can be deduced that a large part of the search space for $|\bar{V}_{\infty L}|$ can be neglected. The majority of values is between 10 and 12 km/s. It is logical, based on the discussion on θ and φ , that the values for $|\bar{V}_{\infty L}|$ are high. The required velocity at the start of the heliocentric leg between Earth and Uranus should be very high in order to reach the outskirts of the solar system without swingbys.

The distribution of the final DSM related variable, η , is plotted against t_0 in figure 15.4. It is clear from figure 15.4 that values for η above 0.50 rarely occur for the EdU trajectory.

15.1.2 Results of an EdU transfer with a constrained search space

The previous optimization runs on the EdU trajectory were performed using the complete search space for all variables. In this section the search space for these variables will be reduced to examine what the influence is on the results. Before the search space for the different variables is reduced, the constraint on the maximum allowable total ΔV for each generated individual is tightened

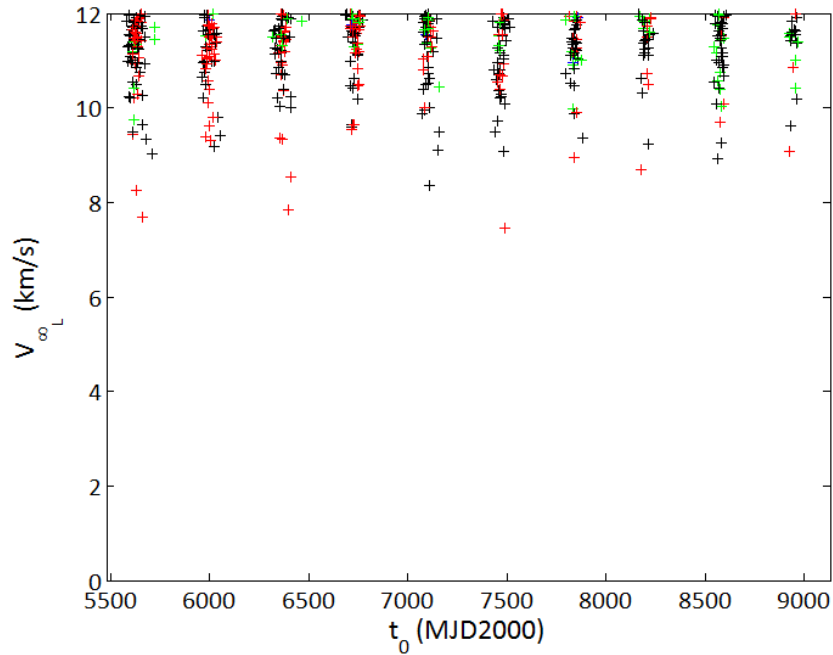


Figure 15.3 Distribution of the individuals in the initial population for the EdU trajectory in the $t_0 - |\bar{V}_{\infty L}|$ space. The complete search space for all variables was used. The seed number for the run producing these individuals is 5. $\color{blue}{+}$: $\Delta V_{tot} \geq 15$ km/s, $\color{green}{+}$: $12 \leq \Delta V_{tot} < 15$ km/s, $\color{black}{+}$: $10 \leq \Delta V_{tot} < 12$ km/s, $\color{red}{+}$: $\Delta V_{tot} \leq 10$ km/s.

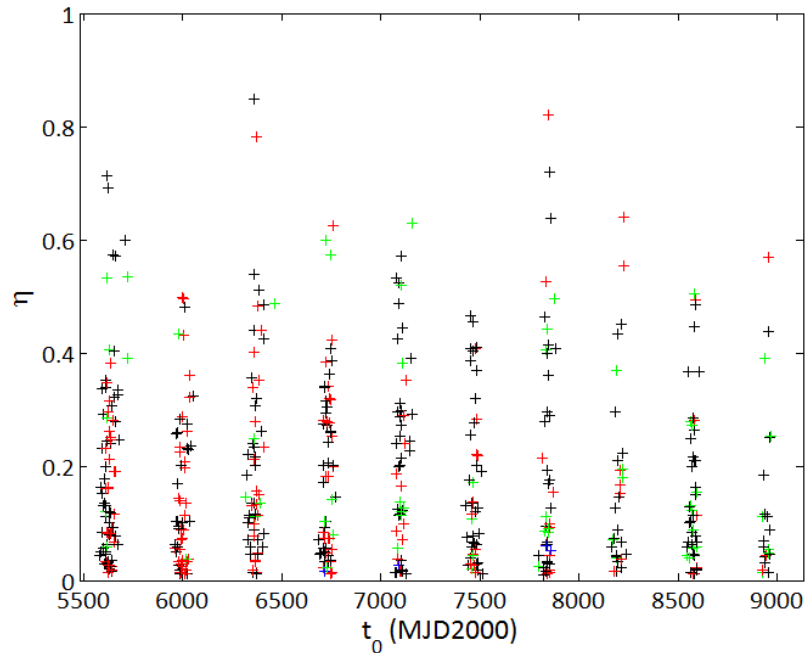


Figure 15.4 Distribution of the individuals in the initial population for the EdU trajectory in the $t_0 - \eta$ space. The complete search space for all variables was used. The seed number for the run producing these individuals is 5. $\color{blue}{+}$: $\Delta V_{tot} \geq 15$ km/s, $\color{green}{+}$: $12 \leq \Delta V_{tot} < 15$ km/s, $\color{black}{+}$: $10 \leq \Delta V_{tot} < 12$ km/s, $\color{red}{+}$: $\Delta V_{tot} \leq 10$ km/s.

Tightened constraint for the total ΔV

Using $\Delta V_{tot} \leq 10$ km/s, the results of 10 optimization runs are shown in table 15.3.

S	t_0 MJD2000	t_1 MJD2000	$ \bar{V}_{\infty L} $ km/s	θ rad	φ rad	η	ΔV_{tot} km/s
5	6381.6	12038.3	11.395	6.264	0.014	0.168	6.685
10	5643.1	11552.6	11.392	0.021	-0.002	0.114	6.664
75	5642.1	11470.9	11.399	0.032	-0.008	0.169	6.664
250	6014.1	11909.6	11.422	6.261	0.022	0.163	6.694
1000	5645.3	11646.1	11.395	6.262	0.005	0.200	6.664
1050	6384.6	12242.0	11.404	6.222	0.004	0.154	6.696
1100	6379.8	12241.8	11.430	0.083	-0.045	0.172	6.708
1150	5638.6	11376.4	11.455	0.112	-0.021	0.166	6.702
1200	6379.8	11878.7	11.399	6.281	0.014	0.207	6.689
1250	6380.3	12072.4	11.398	0.029	-0.004	0.215	6.688

Table 15.3 Decision vectors and total ΔV for the best individuals of each run, with $\Delta V_{tot} \leq 10$ km/s used as a new constraint. The complete search space for all variables is used. Elitism was set to 15%, immigration was set to 15% and the population size was 500. The time needed on the dutlruw.lr.tudelft.nl-server was 14890 s.

The best total ΔV that is found by GALOMUSIT using the tight constraint of 10 km/s is lower than the best total ΔV as it was found using the original constraint of 75 km/s. The value of 6.664 km/s is even 9 m/s lower than the best ΔV for the direct Earth-Uranus trajectory without DSM. The time needed for optimizing these 10 runs is more than 4 hours. The time that was needed to optimize the 10 runs using the original constraint was just over 40 minutes. Obtaining better results in this case comes at the price of a significant increase in computational time.

Figure 15.5 shows the initial population in the $t_0 - t_1$ space when the complete search space for all variables is used with $\Delta V_{tot} \leq 10$ km/s.

From figure 15.5 it can be seen that the same banded structure is present as in figure 15.1. So when the constraint for the maximum allowable total ΔV is tightened, no new information on the launch window is obtained, while the computation time has increased drastically. Without showing the plots, the same holds for search space of the DSM related variables. No new information is obtained on which parts of the search space can be neglected. Therefore it seems that tightly constraining the total ΔV is not the most efficient way to obtain information on possibilities for reducing the search space.

Constrained launch window

In figures 15.1 and 15.5 it could be seen that within the complete search space for t_0 there are a limited number of launch opportunities. The best solution

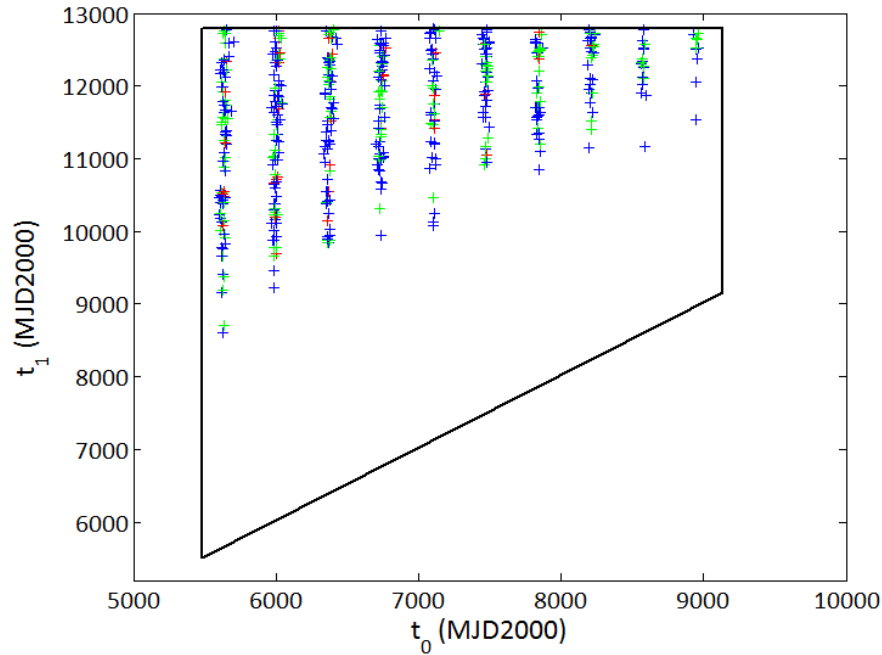


Figure 15.5 Distribution of the individuals in the initial population for the EdU trajectory, with $\Delta V_{tot} \leq 10$ km/s used as a new constraint. The seed number for the run producing these individuals is 10. $\color{blue}+$: $9 < \Delta V_{tot} \leq 10$ km/s, $\color{green}+$: $8 < \Delta V_{tot} \leq 9$ km/s, $\color{red}+$: $\Delta V_{tot} \leq 8$ km/s.

that was obtained in using the complete search space (see table 15.1) is located at the first launch possibility. It makes sense to constrain the search space for t_0 to only enclose this first launch opportunity. The results of 10 optimization runs are shown in table 15.4. For all variables except t_0 the complete search space is used.

S	t_0 MJD2000	t_1 MJD2000	$ \bar{V}_{\infty L} $ km/s	θ rad	φ rad	η	ΔV_{tot} km/s
5	5642.3	11134.9	11.414	6.226	-0.010	0.180	6.714
10	5643.1	11539.9	11.397	0.019	-0.021	0.145	6.664
75	5641.8	11282.8	11.408	0.001	0.037	0.148	6.676
250	5639.5	11259.1	11.407	0.057	0.003	0.073	6.683
1000	5641.2	11533.6	11.442	0.077	-0.066	0.407	6.715
1050	5641.2	11354.0	11.402	0.034	-0.007	0.162	6.667
1100	5643.3	11263.6	11.411	6.231	0.028	0.193	6.671
1150	5640.8	11457.2	11.425	0.073	0.032	0.104	6.693
1200	5644.3	11523.7	11.436	6.264	0.101	0.069	6.691
1250	5649.3	11819.2	11.452	6.186	0.044	0.111	6.720

Table 15.4 Decision vectors and total ΔV for the best individuals of each run, with $t_0 \in [5600, 5700]$ MJD2000. The complete search space for all other variables is used. The original constraint for the total ΔV is used. The time needed on the `dut1ruw.lnr.tudelft.nl`-server was 526 s.

The best result is 6.664 km/s, which is the same as the value obtained with a tight constraint on the maximum allowable total ΔV . The difference, however, is in the computation time. Using only a constrained launch window decreases

the computation time to just 526 seconds. It is therefore more efficient in terms of computation time to do a Monte Carlo search on the complete search space first and subsequently apply the global optimization on a more constrained search space, than to only allow very good individuals to enter the population.

Table 15.5 shows the breakdown of the total ΔV for the best individual for the constrained launch window.

ΔV_L	5.602 km/s
ΔV_{DSM}	0.021 km/s
ΔV_C	1.040 km/s
ΔV_{tot}	6.664 km/s

Table 15.5 Breakdown of the total ΔV for the trajectory with the lowest total ΔV for the EdU transfer. $t_0 \in [5600, 5700]$ MJD2000, the complete search space for all other variables is used. The seed number for this run was 10.

Constrained DSM related variables

It could be seen from figure 15.2 that all solutions are close to 0 and 2π for θ and close to 0 for φ . This is confirmed when looking at table 15.1 for example. Therefore it makes sense to put both θ and φ equal to 0 as a means of search space reduction. Furthermore, $|\bar{V}_{\infty L}|$ and η can also be constrained. In the following optimization runs the following reduced search space for $|\bar{V}_{\infty L}|$ and η are used:

- $|\bar{V}_{\infty L}| \in [11, 12]$ km/s
- $\eta \in [0.001, 0.20]$

The complete launch window will be used in the next optimization runs. The minimum time of flight for each generated individual is set to 1 day and the maximum ΔV_{DSM} is set to 0.5 km/s. The resulting decision vectors and total ΔV after 10 optimization runs are shown in table 15.6.

Constraining the search space for the DSM related variables improves the best result that was obtained up to this point. The value of 6.663 km/s is 10 m/s lower than the lowest total ΔV needed for the direct Earth-Uranus transfer without DSM and 1 m/s lower than the total ΔV when tightening the constraints or constraining the launch window. Table 15.7 shows the breakdown of the total ΔV for the best individual for the constrained launch window.

In table 15.6 it can be seen that there is still quite some difference between the values of η of the best individuals in each run. For $|\bar{V}_{\infty L}|$ the values are consistent. To examine what the behavior of the objective function is around the global minimum, $|\bar{V}_{\infty L}|$ and η are grid sampled. This grid sampling is done by

S	t_0 MJD2000	t_1 MJD2000	$ \bar{V}_{\infty L} $ km/s	θ rad	φ rad	η	ΔV_{tot} km/s
5	5644.0	11592.6	11.390	0	0	0.141	6.671
10	5642.6	11404.5	11.378	0	0	0.038	6.676
75	5643.1	11478.5	11.379	0	0	0.051	6.672
250	5641.5	11235.0	11.398	0	0	0.076	6.669
1000	5642.6	11382.6	11.399	0	0	0.084	6.669
1050	5644.4	11610.0	11.391	0	0	0.099	6.672
1100	5645.7	11797.2	11.391	0	0	0.136	6.669
1150	5640.3	11075.9	11.409	0	0	0.102	6.679
1200	5644.4	11640.2	11.390	0	0	0.199	6.666
1250	5643.5	11508.7	11.391	0	0	0.131	6.663

Table 15.6 Decision vectors and total ΔV for the best individuals of each run, with $\theta = \varphi = 0$, $|\bar{V}_{\infty L}| \in [11, 12]$ km/s and $\eta \in [0.001, 0.20]$. The complete launch window is used.

ΔV_L	5.598 km/s
ΔV_{DSM}	0.023 km/s
ΔV_C	1.041 km/s
ΔV_{tot}	6.663 km/s

Table 15.7 Breakdown of the total ΔV for the trajectory with the lowest total ΔV for the EdU transfer. $\theta = \varphi = 0$, $|\bar{V}_{\infty L}| \in [11, 12]$ km/s and $\eta \in [0.001, 0.20]$. The complete launch window is used. The seed number for this run was 1250.

choosing a domain for both variables as well as a step size. Based on table 15.6 the following grid is defined:

- $|\bar{V}_{\infty L}| \in [11.30, 11.43]$ km/s, with a step size of 0.01 km/s
- $\eta \in [0.01, 0.28]$ with a step size of 0.01

This grid is then 14×28 , resulting in 392 sample points. The optimization is done three time for each sample point, with seed numbers 5, 10 and 75. The maximum allowable ΔV_{DSM} is set to 0.75 km/s. It should be noted that θ and φ are still equal to zero and that t_0 and t_1 are free variables (so the complete $t_0 - t_1$ search space is used). Figure 15.6 shows the value of the total ΔV over the grid sampled search space for $|\bar{V}_{\infty L}|$ and η .

The plot was obtained by taking the best value for the total ΔV in each grid point out of the three optimization runs. By applying interpolation between the grid points a contour plot could be drawn. A two-dimensional view of the contour plot, including a color bar is shown in figure 15.7.

Figures 15.6 and 15.7 show that at $|\bar{V}_{\infty L}| = 11.393$ km/s, the global optimum is represented by quite a large valley structure. A wide range of values for η is contained by this valley. In order to see what the minimum total ΔV is for each

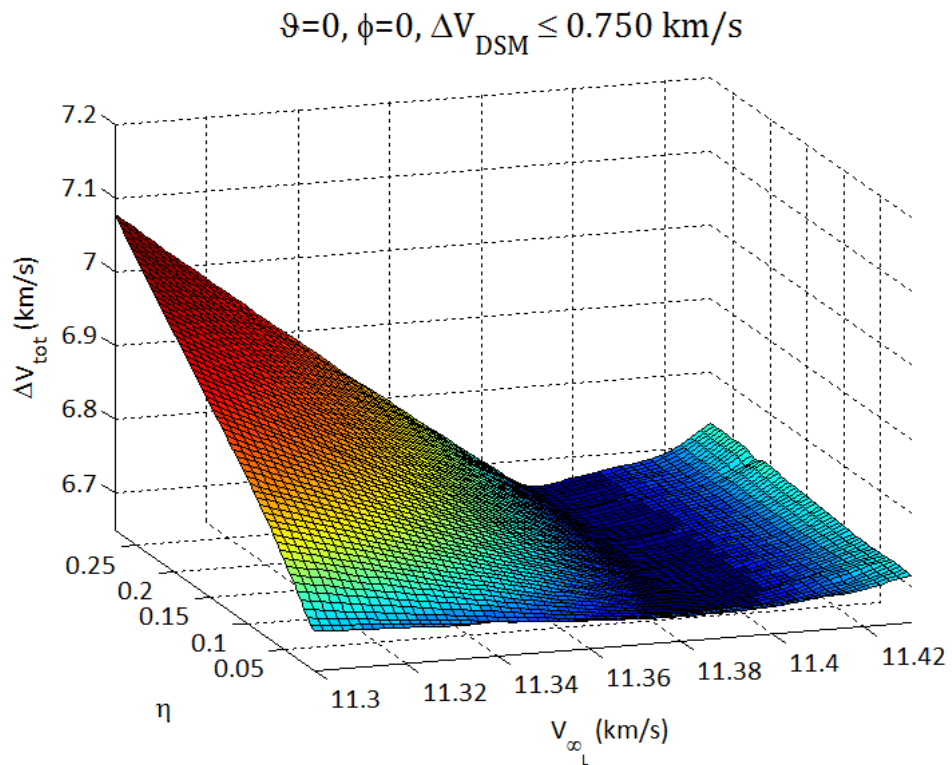


Figure 15.6 Contour plot of ΔV_{tot} , based on a grid sampled search space for $|\bar{V}_{\infty_L}|$ and η . $|\bar{V}_{\infty_L}| \in [11.30, 11.43]$ km/s, with a step size of 0.01 km/s and $\eta \in [0.01, 0.28]$ with a step size of 0.01. The complete $t_0 - t_1$ search space is used, while $\theta = \varphi = 0$.

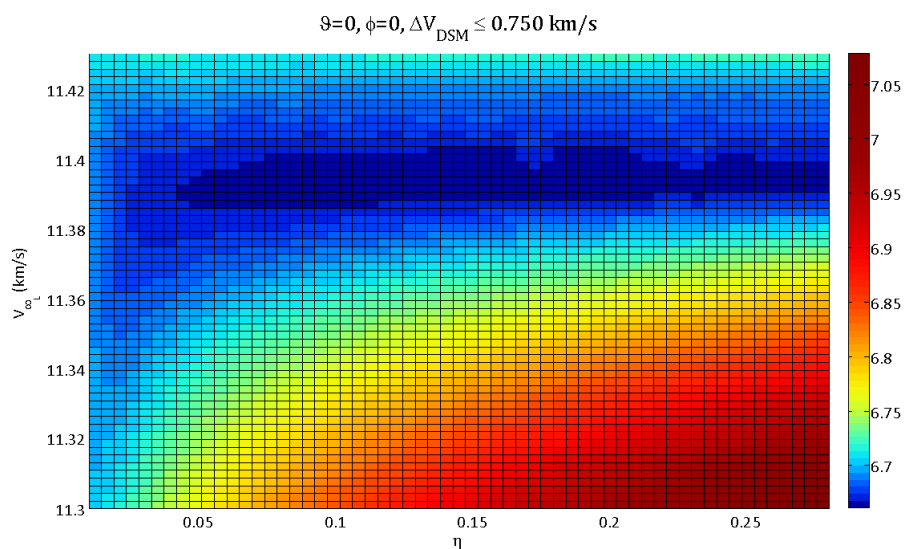


Figure 15.7 Two-dimensional view figure 15.6. The values of the total ΔV in km/s are indicated by the color bar.

value of η , figure 15.8 has been created.

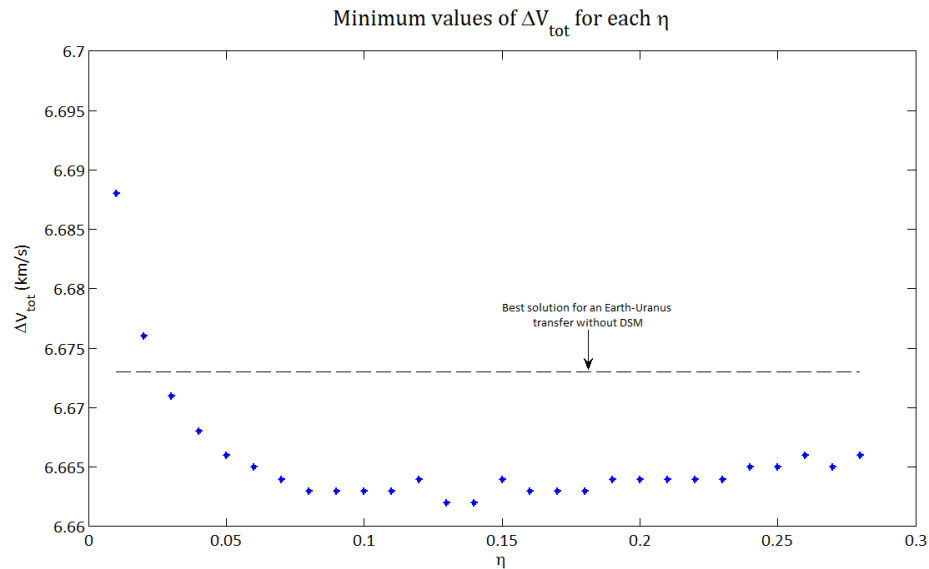


Figure 15.8 The lowest total ΔV for each value of η in the sampled grid for the Earth-Uranus transfer with DSM.

Figure 15.8 can be considered as a cross-section of the three-dimensional contour plot at $|\vec{V}_{\infty L}| = 11.393$ km/s. It shows that at $\eta \approx 0.13$ the minimum value for the total ΔV is obtained, which is 6.662 km/s. It should be noted that the line may have been a bit smoother, if more optimization runs were performed for each grid point. However, three runs were considered sufficient. For many values of η , the total ΔV is below the value obtained for the Earth-Uranus transfer without DSM. For how many values of η this holds it not known, since η was only sampled up to 0.28. The trend in figure 15.8 is that the ΔV increases as the value for η becomes larger.

It can be concluded that the results for the global optimization on the reduced search space (see table 15.6) are actually extremely close to the optimum value found by grid sampling around the global optimum (see figures 15.6, 15.7 and 15.8). The global optimization in this case performs well.

15.2 Trajectories to Uranus with one swingby

The direct transfer to Uranus, both with and without DSM, has been thoroughly discussed in section 15.1. The next step is to extend the analysis to trajectories with one swingby. The swingby planets that are considered are the same as used in the discussion on trajectories without DSMs.

- Venus
- Earth
- Mars

- Jupiter
- Saturn

In section 15.2.1 the single swingby trajectories will be analyzed without the addition of DSMs. After that, in section 15.2.2, a DSM will be added on the first leg of the trajectory. The next step is to only apply a DSM on the second leg of the trajectory. This situation will be discussed in section 15.2.3.

15.2.1 No DSM on trajectories to Uranus with one swingby

Trajectories to Uranus with a single swingby and without DSMs have been analyzed already in section 14.2.3, but then for different Genetic Algorithm settings. The best results out of 10 optimization runs for the five single swingby trajectories using 15% elitism and 15% immigration are shown in table 15.8.

	t_0	t_1	t_2	ΔV_{tot}	S
	MJD2000	MJD2000	MJD2000	km/s	
V	6197.0	6340.7	10967.3	8.251	75
E	5712.6	6379.6	11591.9	6.734	10
M	5679.5	8688.2	12664.7	7.447	1000
J	6201.4	7332.7	12679.4	4.745	1150
S	5501.1	7428.5	12636.6	6.280	1200

Table 15.8 Decision vectors and total ΔV for all trajectories without DSM to Uranus with a single swingby. The seed number producing the best result for each trajectory is also shown. 15% elitism and 15% immigration was used.

It should be noted that for the Jupiter swingby sequence already better results have been found in chapter 14 using different GA settings. A value of 4.727 was found for 10% elitism, 5% immigration and 0.1% mutation. The breakdown of the total ΔV for each of the individuals in table 15.8 is given in table 15.9.

	ΔV_L	ΔV_{SB}	ΔV_C	ΔV_{tot}
	km/s	km/s	km/s	km/s
V	1.158	5.881	1.212	8.251
E	2.794	2.866	1.074	6.734
M	4.520	1.560	1.366	7.447
J	3.796	0.001	0.948	4.745
S	4.846	0.221	1.214	6.280

Table 15.9 Breakdown of the total ΔV for all trajectories without DSM to Uranus with a single swingby. 15% elitism and 15% immigration was used.

The breakdown of the total ΔV can also be shown by means of the bar chart that is shown in figure 15.9.

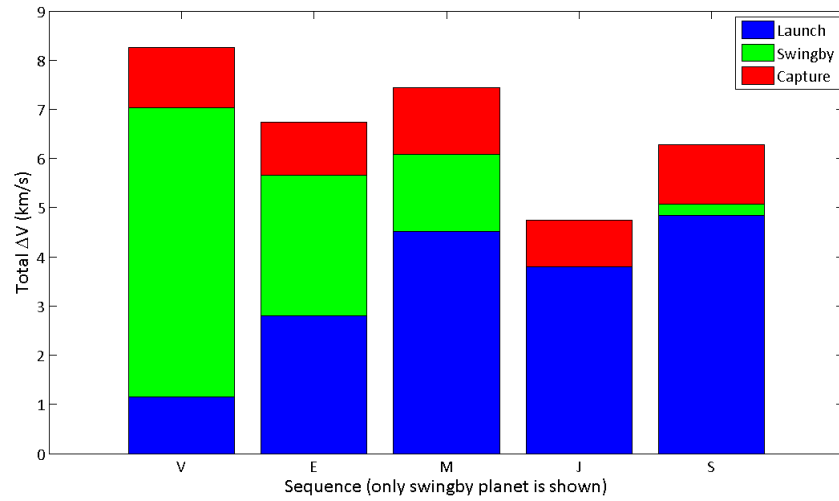


Figure 15.9 Bar chart indicating the breakdown of the total ΔV for all trajectories without DSM to Uranus with a single swingby. 15% elitism and 15% immigration was used.

15.2.2 DSM on the first leg of trajectories to Uranus with one swingby

A DSM on the first leg of the trajectory adds 4 variables to the decision vector. The search space that is used for the DSM related variables is given as follows.

- $|\bar{V}_{\infty L}| \in [0, 5]$ km/s, for the trajectories with a swingby at either Venus, Earth or Mars
- $|\bar{V}_{\infty L}| \in [0, 10]$ km/s, for the trajectory with a swingby at Jupiter
- $|\bar{V}_{\infty L}| \in [0, 12]$ km/s, for the trajectory with a swingby at Saturn
- $\theta \in [0, 2\pi]$ rad
- $\varphi \in [-\frac{\pi}{2}, +\frac{\pi}{2}]$ rad
- $\eta \in [0.01, 0.90]$

Performing the optimization for each trajectory 10 times, each time with a different number for the random generator, gives the following decision vectors and values for the total ΔV .

All values in table 15.10 are higher than the total ΔV for the Lambert solution (see table 15.8). The total ΔV for each of the best solutions in table 15.10 can be broken down into components for launch, DSM, swingby and capture. The different components, together with the seed number producing the best result, are shown in table 15.11.

The breakdown of the total ΔV can also be done graphically by means of a bar chart. This is shown in figure 15.9.

	t_0	t_1	t_2	$ \bar{V}_{\infty L} $	θ	φ	η	ΔV_{tot}
	MJD2000	MJD2000	MJD2000	km/s	rad	rad		km/s
dV	6203.2	6344.9	12318.5	3.188	3.171	-0.623	0.346	8.425
dE	6021.1	6740.0	12114.3	0.049	4.836	-0.195	0.546	6.743
dM	7474.7	8219.8	11718.5	3.748	0.569	0.200	0.325	8.722
dJ	6590.7	7437.9	12563.0	8.681	6.212	-0.002	0.187	4.798
dS	5499.0	7743.2	12779.2	10.336	0.167	0.139	0.128	6.318

Table 15.10 Decision vectors and total ΔV for trajectories to Uranus with a DSM on the first leg and a single swingby. The best result out of 10 optimization runs is shown for each swingby planet. The complete search space was used for all variables. The total ΔV is indicated in red, meaning that the results do not improve with respect to the Lambert solution.

	ΔV_L	ΔV_{DSM}	ΔV_{SB}	ΔV_C	ΔV_{tot}	S
	km/s	km/s	km/s	km/s	km/s	
dV	1.221	0.258	5.818	1.128	8.425	5
dE	0.769	0.023	4.885	1.066	6.743	1150
dM	1.389	2.617	3.127	1.589	8.722	75
dJ	3.778	0.089	0.002	0.930	4.798	75
dS	4.858	0.219	0.009	1.232	6.318	1000

Table 15.11 Breakdown of the total ΔV for all trajectories with a single swingby and a DSM on the first leg. The complete search space for all variables is used.

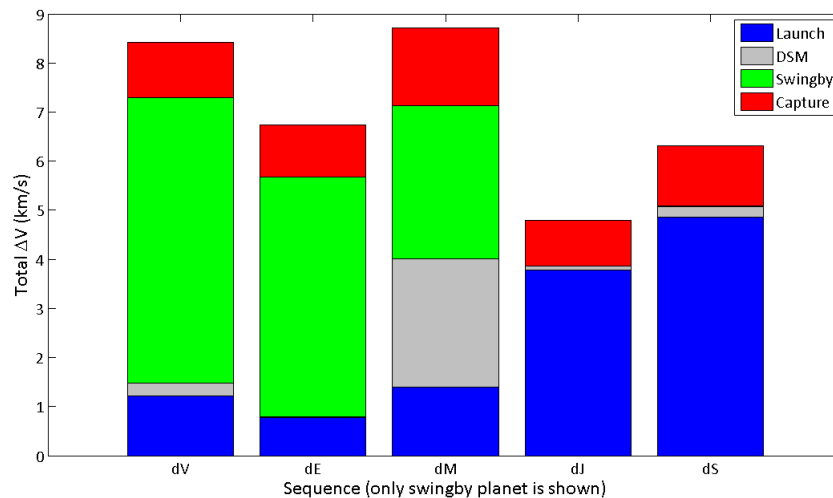


Figure 15.10 Bar chart indicating the breakdown of the total ΔV for all all trajectories with a single swingby and a DSM on the first leg. The complete search space for all variables is used.

For all sequences, performing the optimization with a complete search space for all variables leads to values for the total ΔV that are all higher than the values found for the trajectories without DSMs. Therefore the search space needs to be reduced. This will be done for two of the five possible trajectories, namely Venus and Saturn (arbitrarily chosen).

For both the Venus and Saturn trajectories, appendix E shows the decision vectors and total ΔV for each optimization run that was performed with the complete search space for all variables. The distribution of initial population individuals in the $t_0 - t_2$, $\theta - \varphi$ and $\eta - |\bar{V}_{\infty L}|$ space is also shown for both trajectories. For the EdVU transfer trajectory the distribution in the $t_0 - t_1$ and $t_1 - t_2$ space is shown too.

What immediately stands out is that for the trajectory with a swingby at Venus the complete search space is used for all DSM variables. This indicates that it is not possible to immediately neglect certain parts of the search space, based on the random generation of individuals for the initial population. For launch windows and arrival dates each leg should be considered separately, since the $t_0 - t_2$ space provides no information on possible launch window constraining.

The distribution of individuals for the trajectory with a swingby at Saturn shows a completely different behavior. In the $t_0 - t_2$ space the same banded structure can be seen that was present in the population distribution for the direct Earth-Uranus transfer. For a transfer from Earth to Saturn the synodic period is approximately a year. Figure E.6 confirms this value. When using Saturn as a swingby planet to go to the outer parts of the solar system, the configuration of the planets has to be just right. It is therefore logical that the synodic period comes back in the population distribution. The bands are wider than for the direct transfer because of the DSM and swingby that are performed. For θ , φ and $|\bar{V}_{\infty L}|$ only a small portion of the total search space is used. This can be clarified using the same rationale as for the direct Earth-Uranus transfer. To go to the outer parts of the solar system a large value for $|\bar{V}_{\infty L}|$ is required and the hyperbolic excess velocity vector should be approximately aligned with the planet's heliocentric velocity vector. For η , no values can be neglected based on the individuals in the initial population.

Search space reduction for the EdVU trajectory

The best EdVU trajectory in table 15.10 shows a value for θ that is almost equal to π , indicating a braking maneuver. The spacecraft will move inwards from Earth to Venus. In the next optimization runs the angle θ is constrained to π . Table 15.12 shows the decision vectors and total ΔV of the best individuals for each of the 10 optimization runs that were performed when $\theta = \pi$.

It can be seen in table 15.12 that two runs provide a lower total ΔV than the 8.425 km/s that was obtained using the complete search space for all variables.

S	t_0 MJD2000	t_1 MJD2000	t_2 MJD2000	$ \bar{V}_{\infty L} $ km/s	θ rad	φ rad	η	ΔV_{tot} km/s
5	6204.9	6341.7	12224.0	2.826	π	-0.443	0.386	8.385
10	6204.5	6341.5	12292.5	2.676	π	-0.316	0.438	8.413
75	6199.5	6337.9	11549.7	2.442	π	-0.422	0.419	8.740
250	6194.5	6354.0	11880.4	2.032	π	-0.254	0.478	9.850
1000	7244.0	7687.7	12131.6	2.883	π	0.075	0.513	8.428
1050	5487.9	5888.2	10999.0	3.229	π	-0.013	0.523	8.835
1100	6201.8	6342.1	11381.2	2.684	π	-0.476	0.452	8.667
1150	6198.8	6342.7	12054.9	2.372	π	-0.368	0.442	8.845
1200	6203.2	6341.3	12211.2	2.646	π	-0.404	0.397	8.481
1250	6583.8	7017.4	12329.4	2.761	π	-0.137	0.363	8.679

Table 15.12 Decision vectors and total ΔV for the 10 optimization runs done for EdVU with $|\bar{V}_{\infty L}| \in [0, 5]$ km/s, $\theta = \pi$, $\varphi \in [-\frac{\pi}{2}, +\frac{\pi}{2}]$ and $\eta \in [0.01, 0.90]$. The complete search space was used for time related variables.

The improvement, however is only marginal. It was noted earlier, that in the initial population, the complete $\theta - \varphi$ search space is used. Therefore, in the following optimization runs θ and φ are set equal to 0. This implies that the spacecraft will first travel outward (so farther away from the Sun than the orbit of Earth). Using the DSM the spacecraft will travel back to Venus to perform the swingby. Table 15.13 shows the decision vectors and total ΔV for the EdVU trajectory in this case.

S	t_0 MJD2000	t_1 MJD2000	t_2 MJD2000	$ \bar{V}_{\infty L} $ km/s	θ rad	φ rad	η	ΔV_{tot} km/s
5	6733.9	7251.1	12430.3	3.666	0	0	0.476	8.982
10	5621.9	6123.6	11939.2	3.312	0	0	0.511	8.936
75	6704.0	7237.0	12071.4	3.649	0	0	0.507	8.761
250	6001.1	6573.8	11823.2	4.412	0	0	0.406	8.621
1000	5990.6	6569.1	12532.9	4.593	0	0	0.381	8.890
1050	7884.1	8364.3	12433.9	3.796	0	0	0.480	9.093
1100	5988.5	6566.8	11346.9	4.398	0	0	0.424	8.852
1150	6358.3	7026.0	11518.6	4.869	0	0	0.482	8.490
1200	5999.5	6578.7	11719.1	4.289	0	0	0.470	8.546
1250	7817.5	8373.8	12719.3	4.106	0	0	0.458	9.040

Table 15.13 Decision vectors and total ΔV for the 10 optimization runs done for EdVU with $|\bar{V}_{\infty L}| \in [0, 5]$ km/s, $\theta = \varphi = 0$ and $\eta \in [0.01, 0.90]$. The complete search space was used for time related variables.

The best result from table 15.13, 8.490 km/s, is worse than the solution found when using the complete search space for all variables (see table 15.10). Nevertheless, in order to examine the behavior of the total ΔV for this case, $|\bar{V}_{\infty L}|$ and η were grid sampled around the values for the best individual in table 15.13.

- $|\bar{V}_{\infty L}| \in [4.500, 5.000]$ km/s, with a step size of 0.025 km/s

- $\eta \in [0.42, 0.58]$ with a step size of 0.01

This results in a grid that is 21×17 , yielding 357 grid points. At each grid point, the optimization was performed 5 times with seed numbers 5, 10, 75, 250 and 1000. So for each optimization, there were three variables, namely t_0 , t_1 and t_2 . The resulting contour plot is shown in figure 15.11.

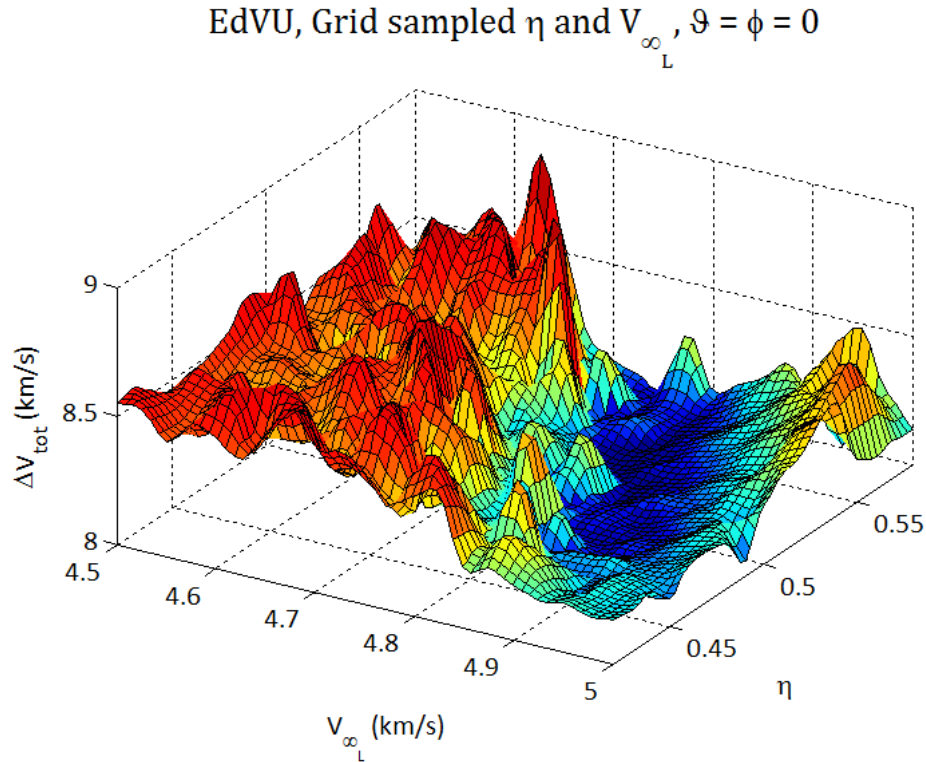


Figure 15.11 Contour plot for the EdVU trajectory. The total ΔV is plotted, based on a grid sampled search space for $|\bar{V}_{\infty L}|$ and η . $|\bar{V}_{\infty L}| \in [4.5000, 5.000]$ km/s, with a step size of 0.025 km/s and $\eta \in [0.42, 0.58]$ with a step size of 0.01. t_0 , t_1 and t_2 are free variables, while $\theta = \varphi = 0$.

Figure 15.11 shows a highly irregular behavior for the total ΔV . There is a large part of the grid above which the values of the total ΔV remain high, until suddenly a 'canyon' emerges in which the best solutions can be found. Figure 15.12 shows a two-dimensional view of the contour plot, where the values of the total ΔV are indicated by the color bar.

It can be seen that the best individual in table 15.13 has values for $|\bar{V}_{\infty L}|$ and η that are within the canyon feature. However, the value for the total ΔV is off by about 300 m/s from the value that it could have reached for those particular values of $|\bar{V}_{\infty L}|$ and η . So the global optimization does not find the values for the total ΔV that are found with the grid sampled search space. This is most likely because of differences in the planetary encounter epochs. This hypothesis is reinforced when performing the optimization process on the grid sampled search space only. The best solution after 10 optimizations (using the same seed numbers

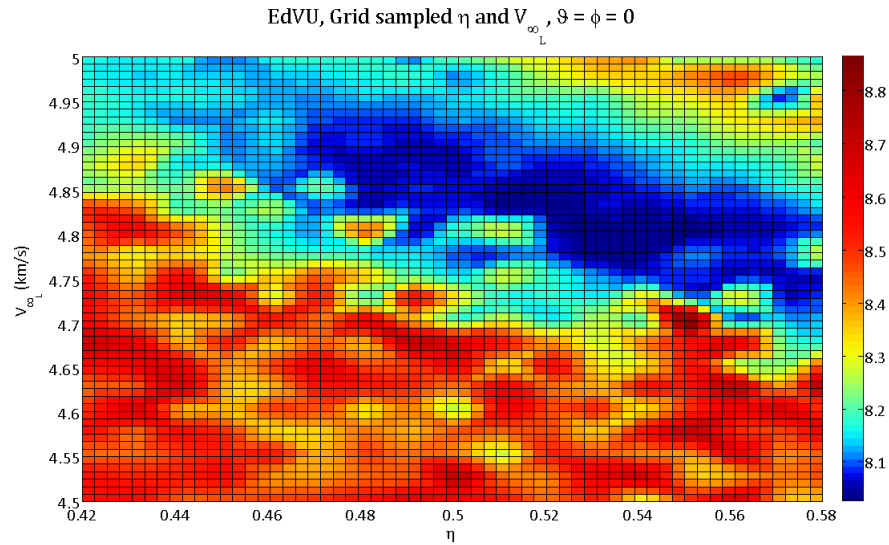


Figure 15.12 Two-dimensional view of the contour plot of figure 15.11. t_0 , t_1 and t_2 are free variables, while $\theta = \varphi = 0$. The values for the total ΔV are indicated by the color bar.

as before) gives a total ΔV of 8.057 km/s. For this individual $|\bar{V}_{\infty L}| = 4.793$ km/s and $\eta = 0.527$. This corresponds to the minimum value that can be seen in figure 15.12. The encounter epochs for this individual are $t_0 = 6358.3$ MJD2000, $t_1 = 7026.0$ MJD2000 and $t_2 = 11518.6$ MJD2000.

Search space reduction for the EdSU trajectory

It could be seen in figure E.7 that for the EdSU trajectory only very limited values for θ and φ are possible. Therefore both θ and φ will be put equal to zero. Also, based on figure E.8, the search space for $|\bar{V}_{\infty L}|$ can be constrained.

- $|\bar{V}_{\infty L}| \in [7, 13]$ km/s
- $\theta = \varphi = 0$ rad
- $\eta \in [0.01, 0.90]$

Table 15.14 shows the resulting decision vectors and total ΔV after 10 optimization runs using the aforementioned search space for the DSM related variables. For the planetary encounter epochs the complete search space was used.

The best value for the total ΔV found after the reduction of the search space is 6.246 km/s. This is better than the best solution found for the trajectory without the addition of a DSM. It is also better than the result that was found using the complete search space for all variables (see table 15.10). There is, however, still quite a spread in the total ΔV for the individuals in table 15.14. The values for $|\bar{V}_{\infty L}|$ and η are all close to each other. Therefore these parameters have been grid sampled around the values for the best individual in table 15.14 in order to

S	t_0 MJD2000	t_1 MJD2000	t_2 MJD2000	$ \bar{V}_{\infty L} $ km/s	θ rad	φ rad	η	ΔV_{tot} km/s
5	5885.7	8316.2	12551.7	10.225	0	0	0.183	6.607
10	5506.6	7788.0	12679.2	10.244	0	0	0.228	6.246
75	5884.8	8224.3	12720.0	10.259	0	0	0.209	6.755
250	5520.9	8524.5	12762.0	10.312	0	0	0.171	6.607
1000	5887.0	8345.2	12758.3	10.239	0	0	0.205	6.512
1050	5514.5	8188.2	12619.0	10.284	0	0	0.177	6.541
1100	5878.1	7771.0	12414.0	10.306	0	0	0.154	6.467
1150	6259.3	8524.2	12690.4	10.217	0	0	0.186	6.649
1200	5880.4	7970.5	12716.6	10.256	0	0	0.142	6.342
1250	6260.7	8680.5	12594.8	10.137	0	0	0.143	6.887

Table 15.14 Decision vectors and total ΔV for the 10 optimization runs done for EdSU with $|\bar{V}_{\infty L}| \in [7, 13]$ km/s, $\theta = \varphi = 0$ and $\eta \in [0.01, 0.90]$. The complete search space was used for time related variables.

examine the behavior of the total ΔV . The following grid was used.

- $|\bar{V}_{\infty L}| \in [10.000, 10.500]$ km/s, with a step size of 0.025 km/s
- $\eta \in [0.16, 0.28]$ with a step size of 0.01

This gives a grid of 21×13 , yielding 273 grid points. The optimization in each grid point has been performed 5 times, each time with a different seed number. The seed numbers that were used are 5, 10, 75, 250 and 1000. It should be stressed that at each grid point there are still three variables in the optimization process, namely t_0 , t_1 and t_2 . Figure 15.13 shows the resulting contour plot, indicating the total ΔV above the sampled grid.

The total ΔV above the sampled grid is very irregular. It can be seen that there are a number of local minima and it is not clear from the three-dimensional contour plot where the global minimum can be found. For that reason a two-dimensional view is shown in figure 15.14, where the values of the total ΔV are indicated by the color bar.

From the two-dimensional representation of the total ΔV for the sampled grid it can be seen that the global minimum can be found at $|\bar{V}_{\infty L}| \approx 10.24$ km/s and $\eta \approx 0.23$. The best individual that was found with the global optimization on the reduced search space (see table 15.14) is located at this global optimum. This was, however, the only run out of the 10 optimization runs that found the global minimum. The other runs got stuck in a local minimum. In figures 15.13 and 15.14 it can be seen that the values of the total ΔV in the local minima for the sampled grid can be off from the global minimum by a margin as large as 400 m/s.

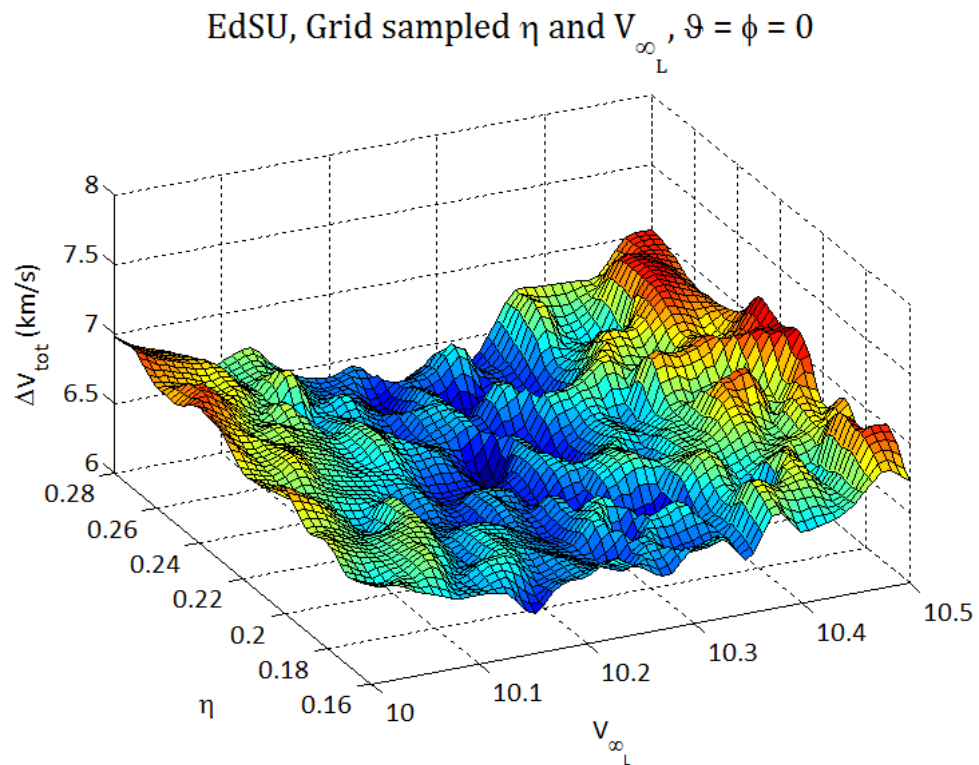


Figure 15.13 Contour plot for the EdSU trajectory. The total ΔV is plotted, based on a grid sampled search space for $|V_{\infty L}|$ and η . $|V_{\infty L}| \in [10.000, 10.500]$ km/s, with a step size of 0.025 km/s and $\eta \in [0.16, 0.28]$ with a step size of 0.01. t_0 , t_1 and t_2 are free variables, while $\theta = \varphi = 0$.

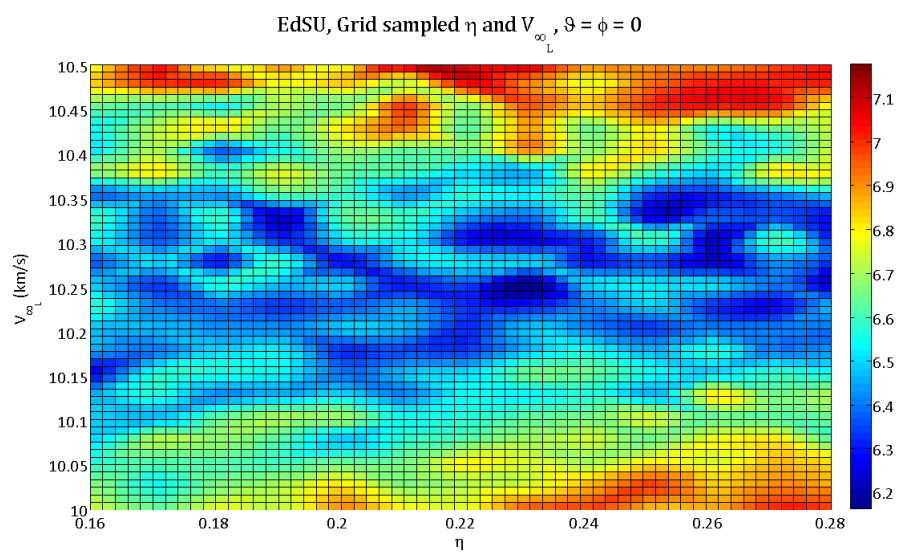


Figure 15.14 Two-dimensional view of the contour plot of figure 15.13. t_0 , t_1 and t_2 are free variables, while $\theta = \varphi = 0$. The values for the total ΔV are indicated by the color bar.

15.2.3 DSM on the second leg of trajectories to Uranus with one swingby

After the discussion on the addition of a DSM on the first leg of the trajectory, a DSM will now be added on the second leg of the trajectory. So the planetary swingbys are unpowered. For the DSM related variables the following search spaces are used.

- $(h_p)_V \in [0.047, 5] R_V$
- $(h_p)_E \in [0.048, 5] R_E$
- $(h_p)_M \in [0.076, 4] R_M$
- $(h_p)_J \in [0.600, 25] R_J$
- $(h_p)_S \in [0.342, 10] R_S$
- $\zeta \in [0, 2\pi]$ rad
- $\eta \in [0.01, 0.90]$

The minimum pericenter altitudes that are used in defining the search space are the same ones as used in GALOMUSIT based on mission heritage. The constraint that is set on the maximum allowable ΔV_{DSM} is 10 km/s for the next set of optimization runs. Table 15.15 shows the decision vectors and total ΔV of the best individuals for all five sequences. Each optimization run was done 10 times, with the seed numbers the same as before.

	t_0 MJD2000	t_1 MJD2000	t_2 MJD2000	h_p km	ζ rad	η	ΔV_{tot} km/s	S
Vd	7363.2	7465.4	12711.8	1996.6	1.574	0.272	10.889	1150
Ed	6082.2	7843.7	12477.1	598.6	3.149	0.020	7.048	10
Md	5666.0	7962.1	12675.8	1062.3	2.739	0.031	7.040	1100
Jd	6202.1	7347.3	12778.3	745598.2	1.134	0.106	4.742	1000
Sd	5506.8	7586.8	11992.4	42660.2	0.177	0.078	6.597	1000

Table 15.15 Decision vectors and total ΔV for trajectories to Uranus with a DSM on the second leg and a single swingby. The best result out of 10 optimization runs is shown for each swingby planet. The complete search space was used for all variables. Indicated in green are the results that are better than the Lambert solution and indicated in red are the solutions that do not improve.

Two of the five trajectories, the ones with swingbys at Mars and Jupiter, provide a total ΔV that is better than the best solution that was found with Lambert targeting only (indicated with green in table 15.15). For the trajectory with the Jupiter swingby the improvement is 3 m/s, where it should be noted that using some different Genetic Algorithm settings a value of 4.727 km/s was found in chapter 14. For the trajectory with the swingby at Mars the improvement is 407 m/s. With respect to the results of the trajectories with a DSM prior to the swingby, the Mars and Jupiter sequences are the only ones that improve as well.

The breakdown of the total ΔV for each sequence in table 15.15 is shown in table 15.16.

	ΔV_L km/s	ΔV_{DSM} km/s	ΔV_C km/s	ΔV_{tot} km/s
Vd	1.802	7.625	1.462	10.889
Ed	5.602	0.293	1.153	7.048
Md	4.202	1.700	1.138	7.040
Jd	3.794	0.017	0.930	4.742
Sd	4.910	0.035	1.653	6.597

Table 15.16 Breakdown of the total ΔV for all trajectories with a DSM after the unpowered swingby. The complete search space for all variables was used.

Like before, the breakdown of the total ΔV can also be shown by means of a bar chart. This is shown in figure 15.15.

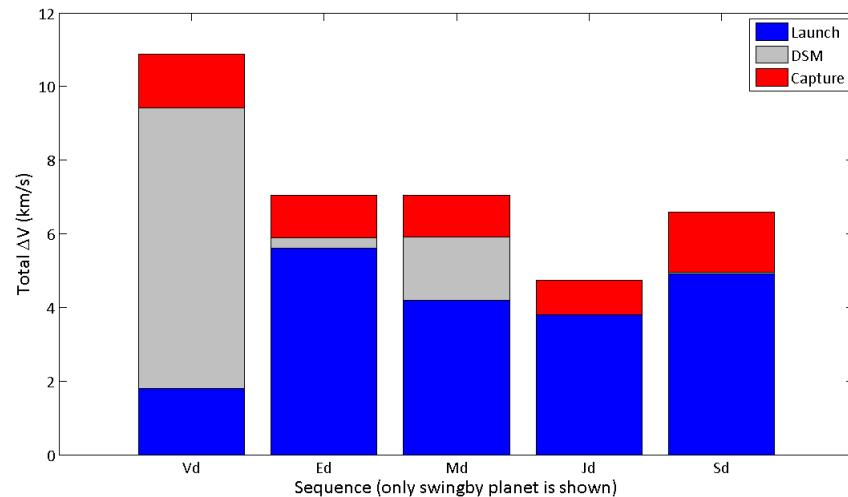


Figure 15.15 Breakdown of the total ΔV for all trajectories with a DSM after the unpowered swingby. The complete search space for all variables was used.

The trajectory with the Mars swingby will now be used for an analysis of the search space, since the total ΔV improves so significantly.

Constrained search space for the EMdU trajectory

Table 15.17 shows the decision vectors and total ΔV for the EMdU trajectory after 10 optimization runs using the complete search space for all variables. The best individual was already shown in table 15.15.

S	t_0 MJD2000	t_1 MJD2000	t_2 MJD2000	h_p km	ζ rad	η	ΔV_{tot} km/s
5	6011.8	7223.7	11972.4	2413.7	2.472	0.033	7.970
10	5656.1	7949.6	12405.1	3604.9	2.682	0.032	7.408
75	5660.3	7954.0	12558.8	6020.5	2.592	0.029	7.364
250	5651.2	7236.9	12321.3	5831.6	2.683	0.028	7.628
1000	5652.9	7238.2	12197.3	5057.4	2.536	0.028	7.586
1050	6015.9	7929.0	12341.2	10170.3	2.542	0.036	7.933
1100	5666.0	7962.1	12675.8	1062.3	2.739	0.031	7.040
1150	6386.8	7932.0	12580.8	3282.7	2.527	0.035	7.827
1200	5663.6	6550.9	11649.1	479.7	1.490	0.024	7.732
1250	5645.9	7237.4	12073.3	1739.6	2.675	0.032	7.635

Table 15.17 Decision vectors and total ΔV for the EMdU trajectory after 10 optimization runs using the complete search space for all variables. The best individual is indicated in red.

From table 15.17 it can be seen that 3 out of the 10 runs produce values for the total ΔV that are lower than the best solution obtained without DSMs. These are the runs with seed numbers 10, 75 and 1100. The values of the total ΔV for these runs are 39 m/s, 83 m/s and 407 m/s lower than the Lambert solution, respectively.

The distribution of the individuals in the initial population in the $t_0 - t_1$ space for the best individual is shown in figure 15.16. So the axes of this figure represent the launch date and the swingby date. The maximum time of flight between the two planetary encounters is 4 times the Hohmann transfer time between the two, which amounts to 258.6 days.

There are five distinct clusters that can be found in the complete launch window for the first leg of the trajectory. They are all spaced with intervals of 760 days, which corresponds to the synodic period for an earth-Mars transfer. When the distribution of individuals is shown in the search space for the second leg, the result is figure 15.17.

From figures 15.16 and 15.17 it can be deduced that some parts of the search space relating the encounter dates to each other can be ignored. The distribution of the initial population individuals in the $\zeta - h_p$ space and in the $\eta - h_p$ space are shown in appendix E.3.

The values for η in table 15.17 are all very close to 0.030. Therefore a grid sampling has been done for this value of η to examine the behavior of the ΔV for a selected set of values for h_p and ζ . The choice was made to create the grid around the best solution that was found in table 15.17.

- $h_p \in [900, 1200]$ km, with a step size of 25 km
- $\zeta \in [2.450, 2.950]$ rad, with a step size of 0.025 rad

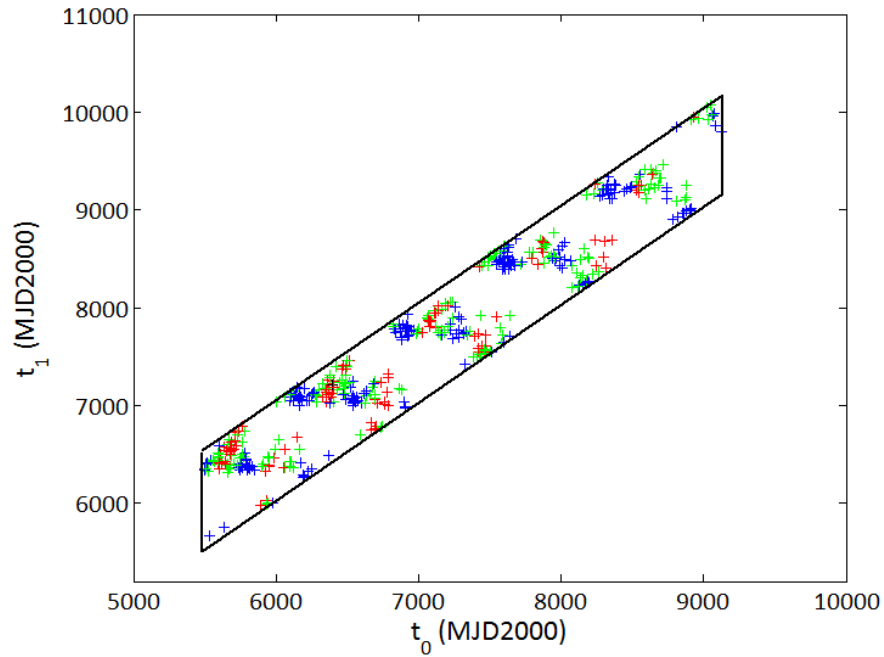


Figure 15.16 Distribution in the $t_0 - t_1$ space of the individuals in the initial population for the EMdU trajectory. The complete search space for all variables was used. The seed number for this run was 1100. $\color{blue}+$: $\Delta V_{tot} > 25$ km/s, $\color{green}+$: $15 < \Delta V_{tot} \leq 25$ km/s, $\color{red}+$: $\Delta V_{tot} \leq 15$ km/s, $\color{black}+$: $\Delta V_{tot} < 10$ km/s.

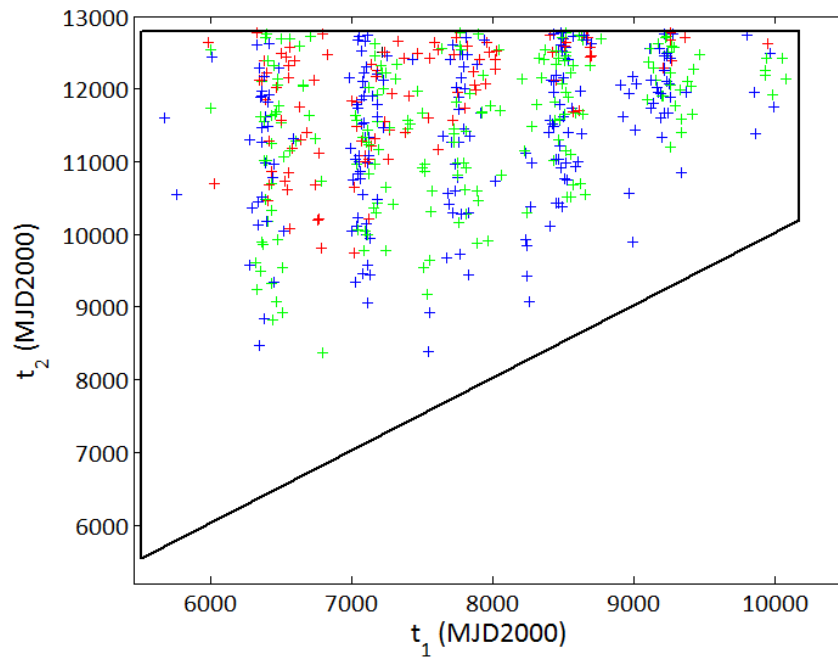


Figure 15.17 Distribution in the $t_1 - t_2$ space of the individuals in the initial population for the EMdU trajectory. The complete search space for all variables was used. The seed number for this run was 1100. $\color{blue}+$: $\Delta V_{tot} > 25$ km/s, $\color{green}+$: $15 < \Delta V_{tot} \leq 25$ km/s, $\color{red}+$: $\Delta V_{tot} \leq 15$ km/s, $\color{black}+$: $\Delta V_{tot} < 10$ km/s.

The resulting grid is 13×21 , yielding 273 grid points. The optimization was done 5 times at each grid point, with seed numbers 5, 10, 75, 250 and 1000. For the optimization at each grid point, there were three variables in the optimization process, namely t_0 , t_1 and t_2 . The resulting contour plot is shown in figure 15.18.

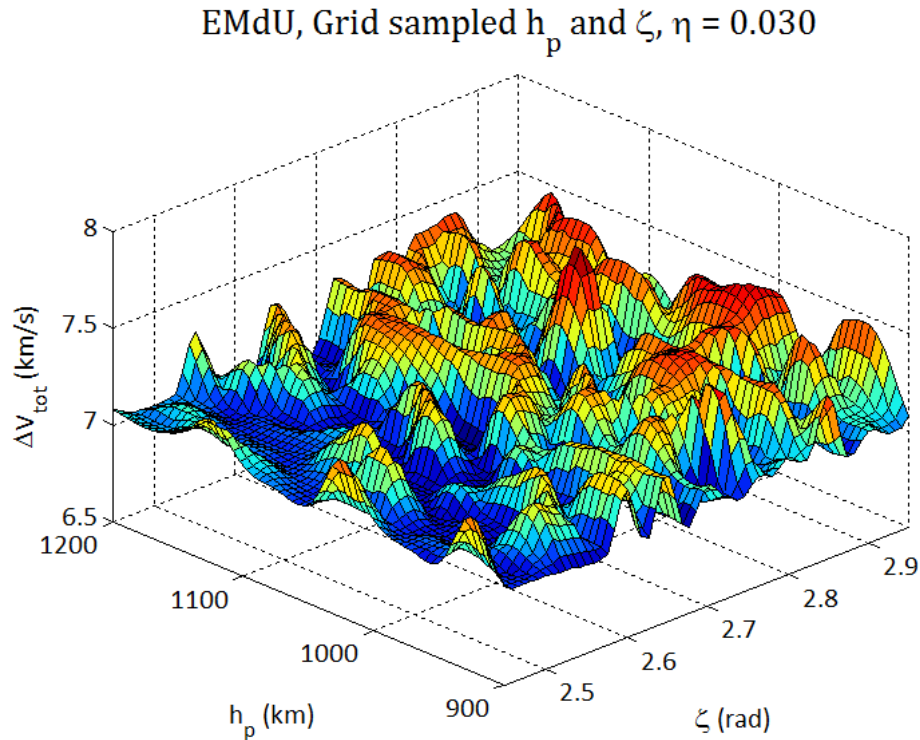


Figure 15.18 Contour plot for the EMdU trajectory. The total ΔV is plotted, based on a grid sampled search space for h_p and ζ . $h_p \in [900, 1200]$ km, with a step size of 25 km and $\zeta \in [2.450, 2.950]$ rad, with a step size of 0.025 rad. t_0 , t_1 and t_2 are free variables, while $\eta = 0.030$.

The value for the total ΔV above the grid shows a highly irregular pattern with many local minima. In order to see where exactly these local minima occur, a two-dimensional view of the contour plot is shown in figure 15.19, where the total ΔV is indicated by the color bar.

The best individual in table 15.17, on which the grid sampling was based, is not located in one of the local minima in figure 15.19. This may be because of the different value for η (0.030 for the grid sampled space and 0.031 for the complete search space). It is more likely, however, that GALOMUSIT is not able to find the best solutions.

A big portion of the grid sampled search space results in values for the total ΔV that are near 7.0 km/s, but based on the figure it can not be stated that the global minimum can be found within the grid sampled search space. The pericenter altitude is very different for each individual in table 15.17 for example,

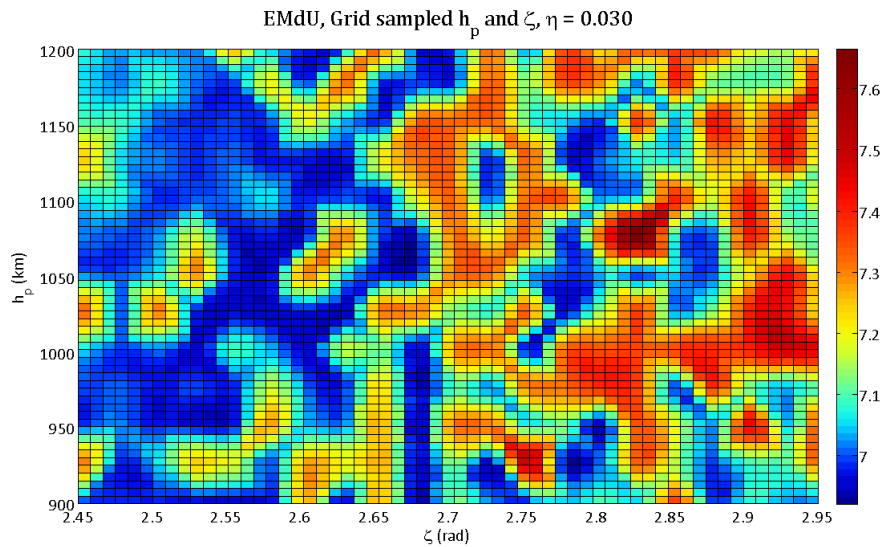


Figure 15.19 Two-dimensional view of the contour plot of figure 15.18. the values for the total ΔV are indicated by the color bar.

and most values there fall outside of the boundaries of the grid sampled space. For the angle ζ , however, the range of values is rather limited. Together with the fact that there also is a very limited range of values for η another set of optimization runs is performed with a constrained search space for all DSM related variables.

- $h_p \in [0.076, 2] R_M$
- $\zeta \in [2, 3]$ rad
- $\eta \in [0.001, 0.10]$

The results of 10 optimization runs for these search spaces are given in table 15.18.

S	t_0 MJD2000	t_1 MJD2000	t_2 MJD2000	h_p km	ζ rad	η	ΔV_{tot} km/s
5	6026.1	7941.0	12468.2	3491.6	2.678	0.034	7.616
10	5669.2	7971.4	12588.6	807.6	2.570	0.023	6.840
75	5673.8	7976.4	12626.3	962.2	2.609	0.020	6.803
250	6392.8	8645.1	12427.5	4042.2	2.742	0.040	7.922
1000	5678.7	8686.4	12752.6	399.5	2.652	0.014	6.780
1050	5673.5	8662.6	12262.8	1547.3	2.504	0.036	7.584
1100	5671.9	7281.5	12492.1	735.2	2.472	0.016	6.916
1150	5669.5	7972.1	12626.7	529.7	2.659	0.025	6.777
1200	6031.6	7960.5	12397.5	456.0	2.480	0.033	7.149
1250	5668.7	7966.3	12648.4	1138.6	2.608	0.026	6.934

Table 15.18 Decision vectors and total ΔV for the EMdU trajectory with constrained search spaces for all DSM related variables. $h_p \in [0.076, 2] R_M$, $\zeta \in [2, 3]$ rad and $\eta \in [0.001, 0.10]$ For the time related variables the complete search space is used.

From table 15.18 it can be concluded that indeed the best solution could not be found in the grid sampled search space used for figures 15.18 and 15.19.

15.3 Trajectories to Uranus with two swingbys

The final part of this chapter concerns trajectories to Uranus with two swingbys. Disregarding a swingby at Venus after an Earth swingby, there are 12 different sequences possible with two swingbys.

15.3.1 No DSMs on trajectories to Uranus with two swingbys

In the same way as it was done in the previous sections, first the swingby trajectories are optimized without the addition of DSMs. Table 15.19 shows the breakdown of the total ΔV for the best individual out of 10 optimization runs, that were performed with the same seed numbers as usual.

	ΔV_L km/s	ΔV_{SB} km/s	ΔV_C km/s	ΔV_{tot} km/s	S
VV	2.070	4.226	1.198	7.495	75
VE	1.276	3.518	1.534	6.328	1250
VM	1.731	7.316	1.470	10.517	1250
VJ	1.333	3.969	0.903	6.205	1100
VS	1.368	6.087	1.360	8.815	1000
EE	2.161	3.540	1.104	6.806	250
EM	3.185	3.318	1.328	7.832	250
EJ	3.216	0.607	0.982	4.806	1100
ES	2.262	3.535	1.480	7.276	10
MJ	3.435	0.000	0.925	4.360	5
MS	4.610	0.100	2.345	7.054	75
JS	3.922	0.053	1.541	5.517	1150

Table 15.19 Breakdown of the total ΔV for all trajectories with two swingbys. The best result out of 10 optimization runs is displayed, together with the seed number producing that result. No DSMs were allowed. Indicated in red is the sequence giving the lowest total ΔV .

The total ΔV for a direct Earth-Uranus transfer is 6.673 km/s (see chapter 14). The sequences VE, VJ, EJ, MJ and JS all have values for the total ΔV that are lower than 6.673 km/s. In the subsequent sections only one DSM will be added to a particular leg of the trajectory. The analysis will start with the addition of a DSM on the first leg of the interplanetary trajectory.

15.3.2 DSM on the first leg of trajectories with two swingbys

As a first step a DSM is added to the first leg of the interplanetary trajectory from Earth to Uranus with two swingbys. The following search spaces are used for all variables:

- For all sequences, except for dJS, $|\bar{V}_{\infty L}| \in [0, 5]$ km/s
- For dJS, $|\bar{V}_{\infty L}| \in [0, 10]$ km/s
- $\theta \in [0, 2\pi]$ rad
- $\varphi \in [-\frac{\pi}{2}, +\frac{\pi}{2}]$ rad
- $\eta \in [0.01, 0.90]$

The best results after 10 optimizations for each sequence are shown in table 15.20. The same seed numbers as before are used. The sequences that improve the total ΔV with respect to the sequence without DSM are indicated in green. The ones that do not improve are indicated in red.

	t_0	t_1	t_2	t_3	$ \bar{V}_{\infty L} $	θ	φ	η	ΔV_{tot}
dVV	5589.6	5723.6	6972.3	11501.6	2.887	3.797	-0.410	0.384	5.305
dVE	5949.5	6410.2	8535.5	12329.3	3.314	3.787	-0.447	0.434	4.773
dVM	5594.5	5748.3	7846.3	11465.2	3.006	3.743	0.247	0.476	9.933
dVJ	6749.6	6961.0	8047.9	12566.0	2.072	3.996	-0.797	0.289	7.809
dVS	6172.4	6321.3	9412.7	12562.2	3.402	3.882	0.151	0.404	9.440
dEE	5930.7	6460.0	8197.9	12281.5	0.057	2.970	-1.258	0.715	4.107
dEM	5543.9	6043.3	8663.0	11897.4	0.677	4.498	-0.408	0.721	6.676
dEJ	6031.1	6587.7	7815.8	12611.6	0.000	4.634	0.598	0.558	4.498
dES	5906.1	6287.0	8498.4	12618.0	0.139	4.620	0.335	0.708	6.563
dMJ	6684.9	6889.0	7760.2	12367.9	2.874	0.170	-0.573	0.461	8.349
dMS	5841.0	6554.8	8928.1	12771.0	2.547	0.244	0.204	0.396	10.917
dJS	5811.8	7143.2	9129.8	12735.7	8.931	0.086	-0.106	0.237	5.788

Table 15.20 Decision vectors and total ΔV for the trajectories with two swingbys and a DSM on the first interplanetary leg. The complete search space for each variable is used. The sequences that improve the total ΔV with respect to the sequence without DSM are indicated in green. The ones that do not improve are indicated in red.

The breakdown of the total ΔV is shown in table 15.21 together with the seed number that produced the best result.

It can be seen that 7 out of the 12 sequences provide better results than for the case when no DSM was applied to the trajectory. The improvements can be significant, even as large as 2.7 km/s (sequence dEE). One of the trajectories showing an immense improvement in terms of total ΔV is the one with a swingby at Venus and then at Earth. The trajectory in the inner part of the solar system of the EVEU sequence without DSMs is shown in figure 15.20.

The spacecraft moves inwards from launch at Earth towards Venus, where due to a large ΔV a transfer orbit between Earth and Venus is generated with a large semi-major axis. After the next encounter with Earth the spacecraft is injected into an orbit that will encounter Uranus.

	ΔV_{tot}	ΔV_L	ΔV_{DSM}	ΔV_{SB}	ΔV_{SB}	S
dVV	5.305	1.141	1.597	1.263	1.304	1000
dVE	4.773	1.256	1.943	0.107	1.468	75
dVM	9.933	1.172	1.857	5.212	1.691	1200
dVJ	7.809	0.962	1.831	4.053	0.963	1100
dVS	9.440	1.282	0.824	5.345	1.990	1000
dEE	4.107	0.769	0.167	1.858	1.312	1200
dEM	6.676	0.790	0.480	3.462	1.944	1150
dEJ	4.498	0.769	0.021	2.769	0.938	1200
dES	6.563	0.770	0.082	4.154	1.557	1150
dMJ	8.349	1.138	0.636	5.561	1.015	1050
dMS	10.917	1.060	2.955	5.315	1.587	75
dJS	5.788	3.934	0.032	0.135	1.688	5

Table 15.21 Breakdown of the total ΔV for the trajectories with two swingbys and a DSM on the first interplanetary leg.

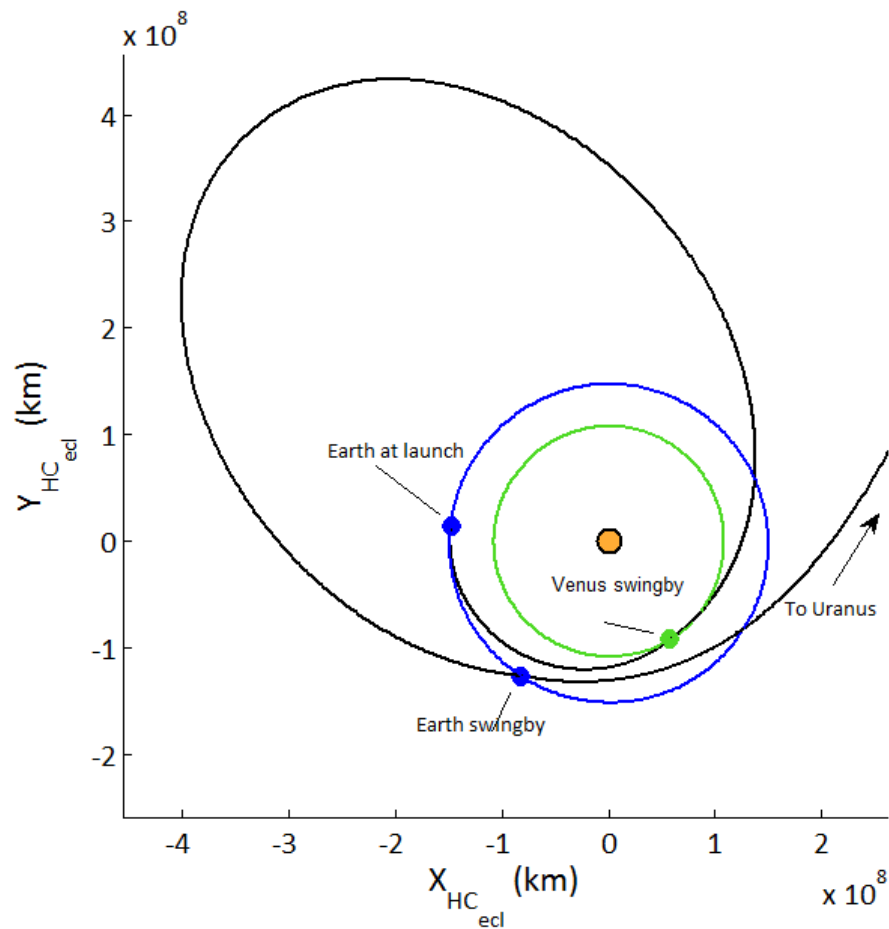


Figure 15.20 The EVEU trajectory in the inner part of the solar system.

When a DSM is added in the first leg of the interplanetary trajectory, the spacecraft's journey in the inner part of the solar system is very different. This is shown in figure 15.21.

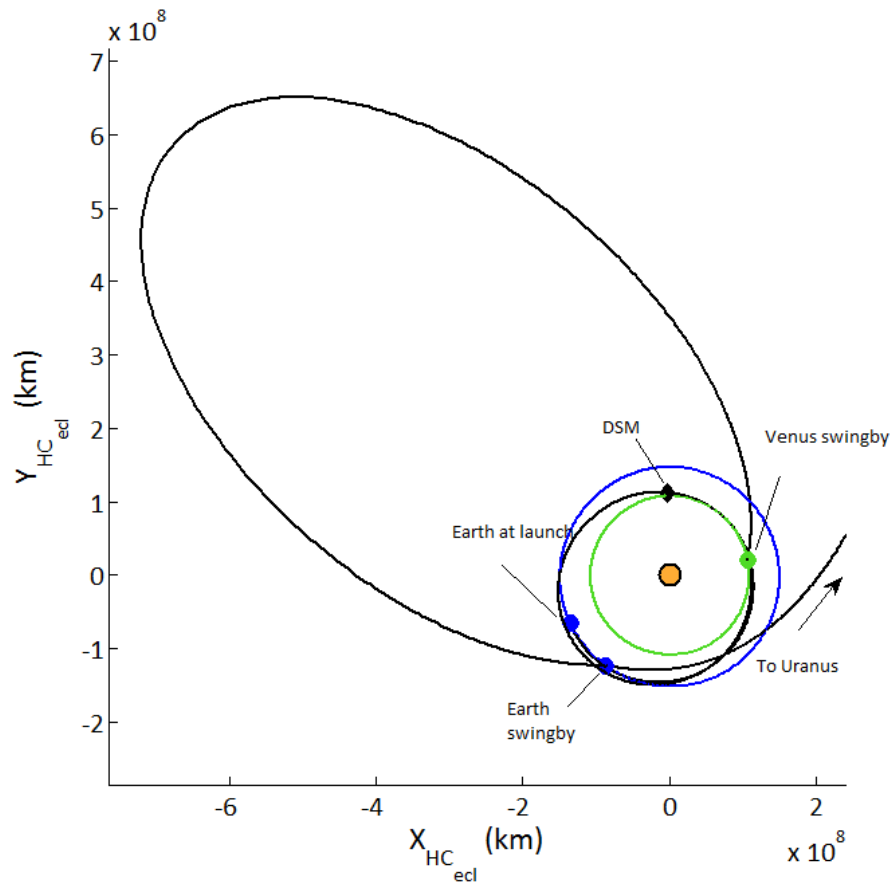


Figure 15.21 The EdVEU trajectory in the inner part of the solar system.

Because of the introduction of a DSM between Earth and Venus an extra revolution about the Sun can be done before the Venus swingby. This is due to the fact that only single-revolution Lambert arcs are allowed (see section 8.2). When the DSM is introduced, ΔV_{SB} is almost decreased to zero for the entire trajectory, which can be seen in table 15.21. The leg between the Venus and Earth swingby is more or less similar for both figure 15.20 and 15.21. Without the DSM between Earth and Venus, the part between the two swingbys is generated because of a large engine burn at the pericenter of the Venus swingby. Because of the DSM, the incoming heliocentric velocity at the swingby is more favorable than for the trajectory without the DSM in terms of a required pericenter burn. This is an important conclusion, because it shows the limitations of the single-revolution assumption.

In the following set of optimization runs, the angles θ and φ are assumed to be 0. This reduces the number of variables of the optimization problem from 8 to 6. For some sequences this could mean that the results do not improve due to

the fact that a braking maneuver at Earth would be better, but the purpose is to show what happens when constraining the direction.

Setting $\theta = \varphi = 0$ for all swingby sequences

The optimizations will be done for all swingby sequences. The search spaces for the variables in the optimization process are given as follows.

- For all sequences, except for dJS, $|\bar{V}_{\infty L}| \in [0, 5]$ km/s
- For dJS, $|\bar{V}_{\infty L}| \in [0, 10]$ km/s
- $\theta = \varphi = 0$
- $\eta \in [0.01, 0.90]$

Table 15.22 shows the decision vectors and total ΔV of the best individuals after the optimization when $\theta = \varphi = 0$. The sequences that improve the total ΔV with respect to the sequence without DSM are indicated in green. The ones that do not improve are indicated in red.

	t_0	t_1	t_2	t_3	$ \bar{V}_{\infty L} $	θ	φ	η	ΔV_{tot}
dVV	6085.7	6618.1	7896.0	11813.3	3.985	0	0	0.358	6.176
dVE	5807.2	6226.7	8142.2	12443.3	1.859	0	0	0.370	6.142
dVM	5672.1	6068.7	6157.1	11347.3	3.622	0	0	0.410	9.858
dVJ	6618.9	7185.9	8059.0	12478.5	4.122	0	0	0.462	6.504
dVS	5528.9	6062.0	8289.7	12516.0	3.904	0	0	0.397	8.599
dEE	6247.9	6827.2	8178.0	12516.4	0.450	0	0	0.591	4.130
dEM	5778.6	6451.1	8711.5	12504.7	0.110	0	0	0.482	6.729
dEJ	6015.0	6626.6	7831.6	12328.1	0.030	0	0	0.560	4.718
dES	5926.9	6681.9	8597.6	12636.0	0.089	0	0	0.598	6.658
dMJ	6005.2	6818.9	7425.5	12445.9	4.539	0	0	0.381	5.985
dMS	7509.4	7943.4	10028.8	12779.0	3.477	0	0	0.505	10.150
dJS	5823.5	7308.3	9334.4	12773.1	8.927	0	0	0.215	5.816

Table 15.22 Decision vectors and total ΔV for trajectories to Uranus with two swingbys and a DSM on the first leg. $\theta = \varphi = 0$ and for the other variables the complete search space is used. The sequences that improve the total ΔV with respect to the sequence without DSM are indicated in green. The ones that do not improve are indicated in red.

The total ΔV that is obtained when using the complete search space for θ and φ can be compared with the total ΔV when both these angles are equal to 0. This is done in figure 15.22.

From figure 15.22 it can be deduced that it depends on the swingby sequence whether or not adding a DSM on the first leg reduces the total ΔV . It can also be seen that constraining θ and φ to 0 does not necessarily improve results with respect to the best result obtained with a complete search space. On the one hand

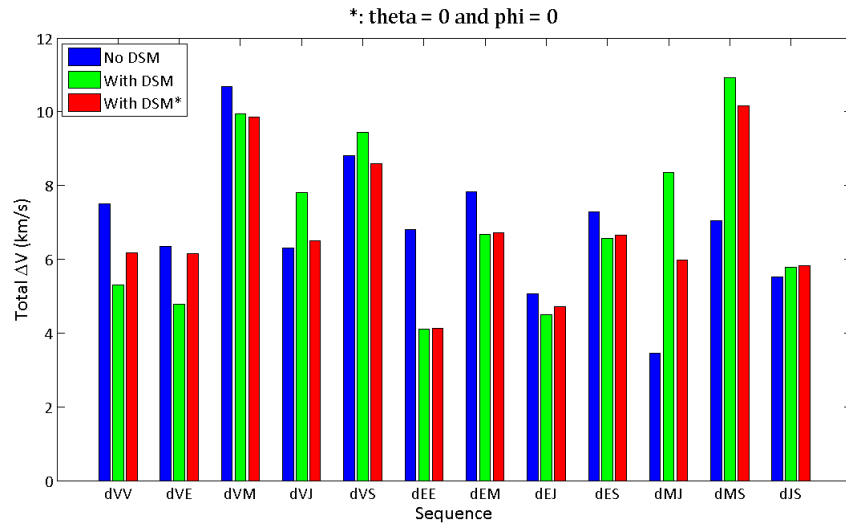


Figure 15.22 Comparison of the total ΔV for trajectories to Uranus with two swingbys. The blue bar indicates that no DSMs were allowed, the green bar indicates that the complete search space for θ and ϕ was used when a DSM is applied on the first leg and the red bar indicates that θ and ϕ are equal to 0.

this has to do with an unfavorable launch direction, as mentioned earlier. On the other hand it shows the inconsistency of the optimizations and the problems GALOMUSIT has tackling these problems. The EdMJU trajectory, for example does not benefit from adding a DSM on the first leg. This particular sequence will be analyzed in more detail in the next section.

Details for the EdMJU transfer

The best solution for the EdMJU trajectory using a full search space for the angles θ and ϕ is 8.349 km/s. When θ and ϕ are set to 0, the total ΔV decreases drastically to 5.985 km/s. This result was obtained after 10 optimization runs, the results of which are shown in table 15.23.

	t_0	t_1	t_2	t_3	$ \bar{V}_{\infty L} $	θ	ϕ	η	ΔV_{tot}
5	5973.2	6416.4	7784.8	12562.2	3.440	0	0	0.530	8.105
10	6003.8	6498.7	7602.3	12114.6	3.881	0	0	0.497	7.953
75	6005.2	6818.9	7425.5	12445.9	4.539	0	0	0.381	5.985
250	6007.9	6479.6	7978.8	12088.5	4.042	0	0	0.563	8.138
1000	6787.9	7406.0	7678.9	12002.3	3.177	0	0	0.197	7.388
1050	6714.7	7487.8	8260.4	12100.2	4.362	0	0	0.381	7.415
1100	5892.4	6138.2	7291.8	12253.5	2.265	0	0	0.306	7.896
1150	6016.1	6543.5	7693.0	11907.3	4.070	0	0	0.472	8.356
1200	5910.4	6710.7	7893.3	12255.8	4.409	0	0	0.484	8.138
1250	6002.2	6538.0	7741.4	12318.6	3.731	0	0	0.413	8.052

Table 15.23 Decision vectors and total ΔV of best solutions of the 10 optimization runs for the EdMJU trajectory. $\theta = \phi = 0$ and for the other variables the complete search space is used.

The values for the total ΔV show a large spread. The values for $|\bar{V}_{\infty L}|$ and η ,

on the other hand, do not show that much spread. Therefore the search space for $|\vec{V}_{\infty L}|$ and η is grid sampled.

- $|\vec{V}_{\infty L}| \in [2.50, 5.00]$ km/s, with a step size of 0.10 km/s
- $\eta \in [0.10, 0.56]$ with a step size of 0.02

The resulting grid is 26×24 , yielding 624 grid points. For each grid point the optimization was performed for five seed numbers (5, 10, 75, 250 and 1000). Each run had four time related variables in the optimization problem. The resulting contour plot above the sampled grid is shown in figure 15.23.

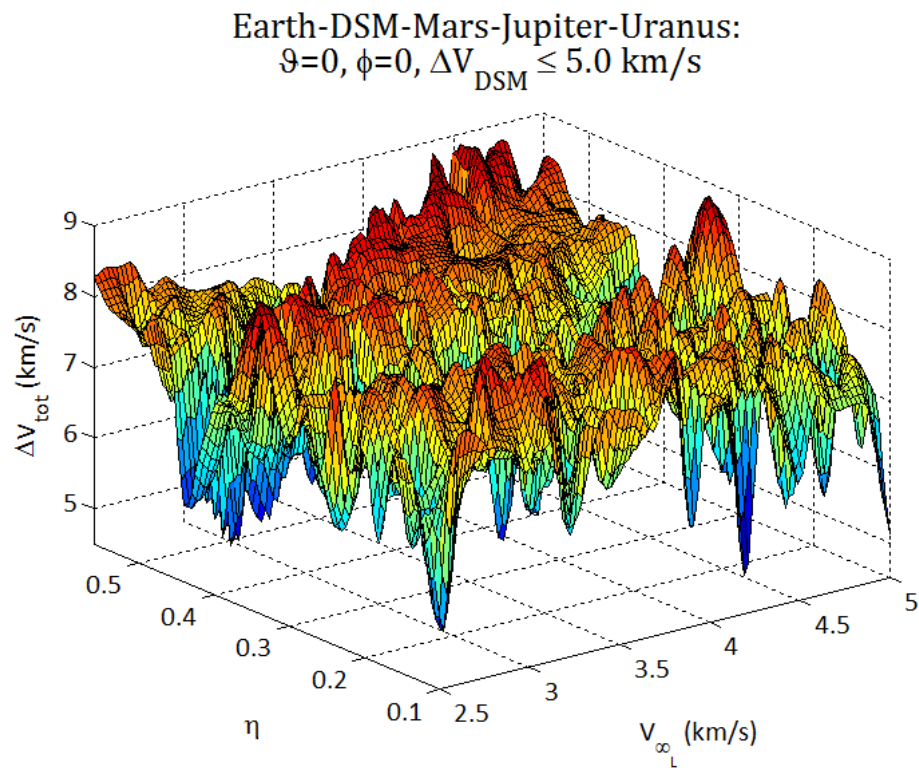


Figure 15.23 Contour plot for the EdSU trajectory. The total ΔV is plotted, based on a grid sampled search space for $|\vec{V}_{\infty L}|$ and η . $|\vec{V}_{\infty L}| \in [2.50, 5.00]$ km/s, with a step size of 0.10 km/s and $\eta \in [0.10, 0.56]$ with a step size of 0.02.

This plot shows very spectacular and extremely complex behavior of the total ΔV . There are countless peaks and valleys and the slopes are very steep. So, starting from a certain point on the contour, if the value for $|\vec{V}_{\infty L}|$ or η changes even slightly, the total ΔV can change with a few km/s. To examine the structure of the values of the total ΔV , a two-dimensional view of the contour plot has been created and it is shown in figure 15.24.

Figure 15.24 shows that the best value that was found, using the complete search space for $|\vec{V}_{\infty L}|$ and η and setting θ and φ equal to 0, is nowhere near

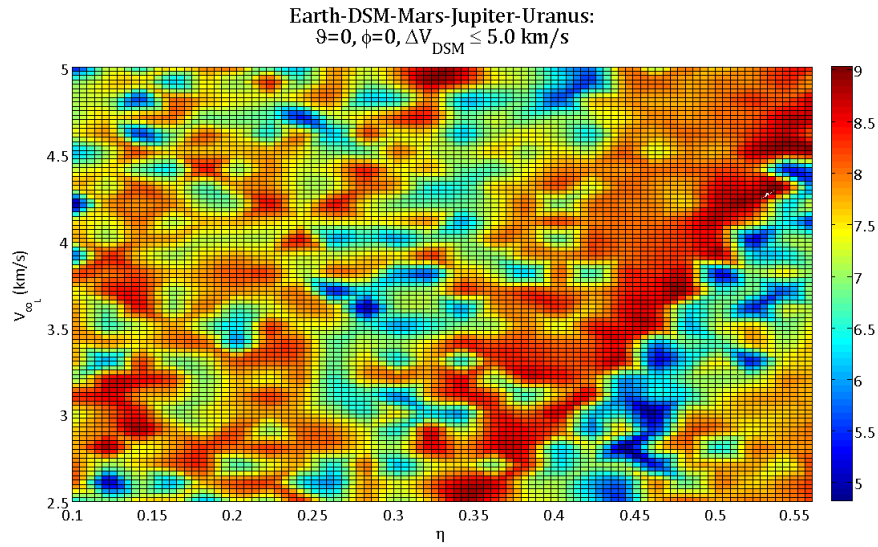


Figure 15.24 Two-dimensional view of the contour plot in figure 15.23. The values of the total ΔV are indicated by the color bar.

the lowest value of the contour plot above the grid sampled search space. It is located on a ridge, but there is a local minimum in the vicinity (at $\eta = 0.40$ and $|\bar{V}_{\infty L}| = 4.85$). The fact that GALOMUSIT can not find this local minimum indicates that it is not powerful enough to optimize such a relatively complex problem. The 10 optimization runs that have been done are not enough. Better results could be obtained if the optimization would be repeated 50 or maybe even 100 times. This, however, leads to large computation times, while the performance of GALOMUSIT is still very poor.

15.3.3 DSM on the second leg of trajectories with two swingbys

In the final part of this chapter a DSM on the second leg only and on the third leg only will be discussed briefly. First, the addition of a DSM to the second leg of the trajectory is analyzed. The search spaces for the different variables that are used in the optimization process are as follows:

- $(h_p)_V \in [0.047, 4] R_V$
- $(h_p)_E \in [0.048, 4] R_E$
- $(h_p)_M \in [0.076, 4] R_M$
- $(h_p)_J \in [0.600, 20] R_J$
- $(h_p)_S \in [0.342, 10] R_S$
- $\zeta \in [0, 2\pi]$
- $\eta \in [0.01, 0.90]$

Table 15.24 shows the best result out of 10 optimization runs for each sequence. Indicated in green are the sequences that provide better results than the case without DSMs and indicated in red are the results that are worse.

	t_0	t_1	t_2	t_3	h_p	ζ	η	ΔV_{tot}	S
VdV	6207.5	6303.6	6797.1	11135.0	3488.2	1.960	0.285	7.211	250
VdE	6841.4	7004.7	7499.1	12226.5	7620.7	1.114	0.378	7.580	1200
VdM	5945.0	6214.1	6816.0	12434.4	15229.6	4.327	0.011	12.688	1000
VdJ	6685.1	6936.5	7785.3	12418.9	2932.7	5.675	0.034	9.201	75
VdS	5675.2	5862.9	9423.1	12520.9	3953.5	1.439	0.241	10.765	250
EdE	5657.3	6732.9	7870.2	12347.5	21501.1	3.424	0.296	5.353	5
EdM	6055.6	7148.3	8242.8	12423.7	20760.8	2.985	0.334	8.862	250
EdJ	5548.9	6589.4	7644.1	12527.2	6116.2	3.326	0.144	4.909	1200
EdS	5612.3	6629.0	9160.9	12716.5	1043.9	3.283	0.071	7.333	1100
MdJ	5540.0	7000.3	8048.8	12595.3	5898.3	4.807	0.150	4.828	250
MdS	5894.1	5981.6	9306.3	12637.6	671.9	1.252	0.084	6.997	5
JdS	5824.0	7326.6	9394.1	12765.1	364324.6	3.186	0.161	5.946	10

Table 15.24 Decision vectors and total ΔV for the trajectories to Uranus with two swingbys and a DSM on the second leg. The best result out of 10 optimization runs is shown for each sequence.

Comparing table 15.20 with table 15.24 it can be deduced that the sequences that improve the total ΔV are not always the same. For example, the EdVEU trajectory benefited significantly from the addition of the DSM, with a decrease in the total ΔV of 1.6 km/s. The EVdEU trajectory, on the other hand, shows an increase in the total ΔV of 1.2 km/s.

15.3.4 DSM on the third leg of trajectories with two swingbys

The final set of optimization runs have a DSM after the second planetary swingby. The search spaces that were used for all variables are the same as the ones used in section 15.3.3. Table 15.25 shows the decision vectors and total ΔV for the next result out of 10 optimization runs for each sequence. The values that are indicated in green have improved the total ΔV with respect to the trajectory without DSMs, whereas the values that are indicated in red have not.

	t_0	t_1	t_2	t_3	h_p	ζ	η	ΔV_{tot}	S
VVd	6172.4	6384.5	8565.5	11823.6	9543.0	3.026	0.019	5.815	1050
VEd	6130.5	6331.9	6729.3	11019.9	24517.4	1.041	0.240	5.233	1000
VMd	6720.1	6921.5	6993.6	11779.4	2866.6	1.463	0.386	5.279	1100
VJd	5650.7	5782.0	7331.3	12696.5	804809.1	1.310	0.171	6.564	1050
VSd	5660.2	5830.8	8125.3	11900.8	54900.0	0.071	0.098	9.238	1200
EEd	5712.6	6433.5	7822.7	11911.2	2678.4	2.868	0.088	5.630	1700*
EMd	6741.5	7443.3	7529.1	11540.7	7119.1	0.777	0.046	3.834	1950*
EJd	5937.8	6987.2	8127.6	12395.8	227215.5	3.102	0.156	4.820	2550*
ESd	7801.6	8471.1	10448.9	12717.0	54967.0	3.115	0.040	7.511	3050*
MJd	5901.8	6993.4	8028.2	12010.7	485529.8	3.322	0.212	6.178	3600*
MSd	5976.1	8521.0	10430.5	12767.6	130657.3	3.081	0.107	7.134	4100*
JSd	5814.2	7166.5	8847.5	12739.6	29411.3	2.922	0.067	5.533	4550*

Table 15.25 Decision vectors and total ΔV for the trajectories to Uranus with two swingbys and a DSM on the third leg. The best result out of 10 optimization runs is shown for each sequence. * For the last 7 sequences, different seed numbers were used than ones ones used throughout the rest of this chapter.

Comparing tables 15.20, 15.24 and 15.25, it can be seen that three sequences improve the total ΔV for every case. These sequences are VV, EE and EJ. There are others, however, that never benefit from the addition of a DSM. There are four of these sequences, namely VJ, VS, MJ and JS. It appears that the Lambert solution is optimal for these particular sequences. An important note should be made here, however, because it turned out from the analysis of DSMs on trajectories with swingbys that GALOMUSIT has problems of finding the optimal solution. Therefore, it could very well be that better solutions exist, but GALOMUSIT can not find them.

Chapter 16

Conclusions

After the discussions in the preceding chapters it is time to reflect on the thesis objectives that were stated in chapter 1:

- I *Develop a method to optimize interplanetary trajectories with deep space maneuvers and integrate this method in the software package GALOMUSIT.*
- II *Apply the developed method to optimize the trajectory for a Uranus orbiter mission.*

In terms of developing the method to apply DSMs to GALOMUSIT, it meant that some changes had to be made to the program. First of all, a method had to be developed to propagate a spacecraft along a Kepler orbit. An interplanetary leg with a DSM can not be analyzed using Lambert targeting alone. The first part of the leg is now based on Kepler's problem, where both the initial position and velocity need to be known together with the time of flight. A universal formulation of Kepler's problem was implemented in GALOMUSIT that is the same for each type of conic section. The end of the Kepler arc is the location where the DSM is performed. The output parameters of the Kepler problem are the position and velocity at the end of the Kepler arc. The second part of the leg is then analyzed using Lambert targeting, which makes sure that the spacecraft encounters the next planet. The discontinuity in the velocity at the end of the Kepler arc and at the start of the Lambert arc is the DSM.

Adding DSMs to the trajectory introduces many additional variables besides the encounter epochs. If a DSM is added to the first leg of the trajectory, 4 variables are added to the problem. A DSM on a leg after an unpowered swingby introduces three new variables. All of the DSM related variables are generated randomly from a user defined search space. Finally, a new subroutine had to be created in GALOMUSIT to force the swingby to be unpowered. No engine burn is allowed at the pericenter of the planetocentric hyperbola.

In terms of optimizing the Uranus orbiter mission, first the trajectory was optimized without DSMs. The trajectory that produces the lowest total ΔV for trajectories in that case performs two swingbys at Venus, one swingby at Earth

and a final swingby at Jupiter before traveling onwards to Jupiter. The total ΔV that is required for this trajectory is 2.892 km/s. The launch date is 12 September 2015 and the arrival date is 16 July 2034, giving a total time of flight of 6882.2 days.

The VVEJ trajectory was present in a set of swingby sequences used by *Melman* [2007] for his thesis research. A new set of possible swingby sequences was created by allowing a swingby at Venus after a swingby at Earth. The best result out of the 77 new sequences is EVVEJ, with a total ΔV of 5.005 km/s. The launch date is 17 January 2017 and the arrival date is 15 November 2034. This results in a total time of flight of 6518.7 days. The new swingby sequences do not provide better results in terms of the total ΔV with respect to the original set of sequences.

For the optimization of the Uranus mission with DSMs the following conclusions can be drawn.

- From the benchmark runs in chapter 13 it could be concluded that the implementation of the method to analyze trajectories with DSMs was done correctly. The total ΔV and the orbits corresponding to the best solutions found in the literature could be reproduced. This was not directly, using the complete search space for all variables, but after one step where the search space was reduced.
- For the direct Earth-Uranus transfer the optimization on the complete search space produces a total ΔV that is slightly higher than the total ΔV for the Lambert solution. After an analysis of the search space it was found that a large part of the search space could be neglected and after search space reduction a value for the total ΔV was found that is 10 m/s lower than the best value for the Lambert solution. A grid sampling around the global optimum showed that the total ΔV behaves in a smooth way.
- When a DSM is added to a trajectory with a swingby, the behavior of the total ΔV changes from being smooth to being quite irregular. After an analysis of the search space the results can be improved when the search space has been reduced or certain variables have been given a fixed value.
- Adding a DSM may result in trajectories that have more than one revolution between planetary encounters. When only Lambert targeting was concerned, these multi-revolution transfers were not allowed. In this thesis only single-revolution Lambert arcs were allowed as well, but the addition of a Kepler arc in front of a Lambert arc opens up a new range of trajectories that otherwise would not be possible. A prime example of this could be seen in section 15.3.2, where the total ΔV for an EdVEU transfer was 1.6 km/s lower than for the Lambert solution.
- The examples with grid sampled search spaces have shown the need for a local optimization around the best known solution from the global optimization. At the moment no such method exists for single-objective optimization in GALOMUSIT.

From the discussion above it can finally be concluded that GALOMUSIT as it exists now is not powerful and sophisticated enough to find the optimal solution

at once when DSMs are added to the trajectory. The search space is too large and the objective function behaves very irregularly. After a first run on the complete search space, the search space itself has to be analyzed to determine if certain parts can be ignored. Right now, this still has to be done by hand, which is tedious work. If this process could be automated it will improve the performance of the program.

Chapter 17

Recommendations

Although much work has been done for this thesis research, there is only a limited amount of time available. Therefore there are still several recommendations for future work that can be done on the subject of DSMs and on the program GALOMUSIT itself.

Regarding the analysis of DSMs the following recommendations can be made:

- From chapters 13 and 15 it has become clear that the way in which DSMs are applied in GALOMUSIT has its shortcomings. In most of the cases that were considered the global optimum was found after reduction of the search space. This had to be done manually each time, however, after the results of the optimization using the complete search space was done. Because this is very time consuming it might prove useful to develop some sort of clustering algorithm. After a Monte Carlo search on the complete search space the clustering algorithm analyzes results of the Monte Carlo search and prunes the parts of the search space that do not provide solutions to the optimization problem. A good example of clustering of individuals could be seen in chapter 13, where two test cases with DSMs were benchmarked. After the random initialization of a population of possible solutions to the optimization problem, the clustering algorithm will search for commonalities for the different variables. The parts of the search space that can then be neglected are not considered anymore and the global optimization will be performed only on the constrained parts of the search space. It could be that the clustering takes a large amount of computation time, but the reduction in search space increases the probability of finding the global minimum.
- After the global optimization, a local optimization can also be applied to improve the results. In this thesis a number of examples with grid sampling around the best known solution were performed, which showed the irregular behavior of the total ΔV . Application of a local optimization could improve the ΔV significantly. For multi-objective optimization in GALOMUSIT such a local optimization is already present (a Monte Carlo search around the absolute Pareto front) and it is recommended to add a local optimization method to single-objective optimization as well.

It became clear in chapter 15 that the addition of a DSM to an interplanetary leg allows more than one revolution around the Sun between two planetary encounters. It proved that a large gain in total ΔV could be obtained in this way. Throughout this thesis it was assumed that only single-revolution transfers were possible for a Lambert problem. A future user may want to analyze multi-revolution Lambert arcs and examine whether or not large improvements can be made with respect to results obtained with single-revolution Lambert arcs.

With respect to the optimization in GALOMUSIT and the program itself the following recommendations are made:

- For single-objective optimization, the mutation option that exists now should be changed. Mutation is a random operation that can now only be applied to immigrants, which are randomly created themselves. This makes no sense and therefore mutation should be applied in another way. This could be done for example by applying mutation only on the individuals in the population that are not immigrants. The best individual may be immune to mutation in order to prevent the best individual from dying.
- The Genetic Algorithm process in GALOMUSIT could be improved by adding more sophisticated genetic operations. The process in GALOMUSIT in essence is quite simple. Selecting individuals for crossover, for example, is done randomly, instead of roulette wheel selection, where the individual's fitness is a measure of its probability for selection.
- It should be investigated whether or not other global optimization methods provide better results than Genetic Algorithm optimization. Other techniques, like Differential Evolution and Particle Swarm optimization have proven to be good methods for optimizing interplanetary trajectories.
- The program GALOMUSIT as it exists now is the result of the work of several students at the Faculty of Aerospace Engineering of Delft University of Technology in The Netherlands. GALOMUSIT as it exists now is made up of one single file only, in which several subroutines are present to keep the program structured. However, because the program has become so large (approximately 18000 lines of code and comments), it takes a long time for someone get familiar with it. A better overview of the program could be kept, if GALOMUSIT were to be built up in a modular fashion. Different files could then represent the different subroutines, making the endless scrolling in GALOMUSIT a thing of the past. The user would still have to familiarize him- or herself with the code.

Bibliography

- Allen, J.A. van (2003), Gravitational assist in celestial mechanics - a tutorial, *Am. J. Phys.*, 71(5), 448–451, May 2003.
- Bate, R.R., D. Mueller, and J.E. White (1971), *Fundamentals of Astrodynamics*, Dover Publications Inc.
- Battin, R.H. (1999), *An Introduction to the Mathematics and Methods of Astrodynamics*, AIAA Education Series.
- Beebe, R.F. (2004), Comparative study of the dynamics of the outer planets, *Space Science Reviews*, 116, 137–154.
- Bernelli-Zazzera, F., M. Lavagna, R. Armellin, P. Di Lizia, F. Topputo, M. Berz, and T. Vinkó (2007), Global Trajectory Optimisation: Can We Prune the Solution Space when Considering Deep Space Maneuvers?, Aerospace Engineering Department of Politecnico di Milano, Department of Physics and Astronomy of Michigan State University and ESA.
- Bertaux, J-L. *et al.*(2007), SPICAV on Venus Express: Three spectrometers to study the global structure and composition of the Venus atmosphere, *Planetary and Space Science*, 55, 1673, 1700 2007.
- Cornelisse, J.W., H.F.R. Schröyer, and K.F. Wakker (1979), *Rocket Propulsion and Spaceflight Dynamics*, Pitman Publishing Limited.
- Corradini, S. (2008), MSc thesis on exponential sinusoidal spacecraft trajectories, Delft University of Technology, Faculty of Aerospace Engineering, The Netherlands.
- Der, G.J. (1996), An elegant state transition matrix, *AIAA 96-3660*.
- Devitt, T. (2004), Keck zooms in on the weird weather on Uranus, 10 November 2004, Photograph: Courtesy Lawrence Sromovsky, UW-Madison Space Science and Engineering Center, <http://www.news.wisc.edu/10402>, Last accessed: 12/05/2009.
- Devitt, T. (2008), New images yield clues to seasons of Uranus, 13 October 2008, <http://www.news.wisc.edu/15776>, Last accessed: 12/05/2009.
- Dodge, R., and M.A. Boyles (2007), Key and Driving Requirements for the Juno Payload Suite of Instruments, *AIAA*.
- EADS (2009), NASA's Galileo Propulsion Module, http://cs.astrium.eads.net/sp/SpacecraftPropulsion/Showcase/Galileo_NASA.htm, Last accessed: 19/05/2009.
- Erdogan, N. (2005), Search for Manned Mars Mission Possibilities, Delft University of Technology, Faculty of Aerospace Engineering, The Netherlands.

- Evertsz, C.M. (2008), Multiple Asteroid Rendezvous, Delft University of Technology, Faculty of Aerospace Engineering, The Netherlands.
- Faure, G., and T.M. Mensing (2007), *Introduction to Planetary Science*, chapter 18, Springer Netherlands.
- Fortescue, P., and J. Stark (1995), *Spacecraft Systems Engineering*, John Wiley & Sons, 2nd edition.
- Gold, R.E. *et al.* (2001), The messenger mission to mercury: scientific payload, *Planetary and Space Science*, 49, 1467–1479.
- Goldberg, D.E. (1989), *Genetic Algorithms in Search, Optimization and Machine Learning*, Add-son-Wesley Publishing Company, Inc.
- Gooding, R.H. (1990), A procedure for the solution of Lambert’s orbital boundary-value problem, *Celestial Mechanics and Dynamical Astronomy*, 48, 145–165.
- Hamilton, C.J. (2001), The interior of Uranus, Copyright: Calvin J. Hamilton, <http://solarviews.com/cap/uranus/uranusint.htm>, Last accessed: 12/05/2009.
- Hammel H.B., M.D. Hofstadter, and M.J. Klein (2003), Understanding Uranus, Goldstone Apple Valley Radio Telescope Project, December 2003.
- Heiligers, M.J. (2008), Trajectory optimization for an asteroid/comet sample return mission, Delft University of Technology, Faculty of Aerospace Engineering, The Netherlands.
- Heiligers, M.J., S. Corradini, and S. Molenaar (2009), A manual to get acquainted with the ins and outs of GALOMUSIT, Delft University of Technology, Faculty of Aerospace Engineering, The Netherlands.
- HubbleSite (2005), NASA’s Hubble Discovers New Rings and Moons Around Uranus, HubbleSite NewsCenter, 22 December 2005, <http://www.hubblesite.org>, Last accessed: 20/09/2007.
- Jong, L.J. de (2004), The Aerogravity Assist, Bachelor’s thesis, INHOLLAND Hogeschool Haarlem and Delft University of Technology, The Netherlands, 3 February 2004.
- Kemble, S. (2006), *Interplanetary Mission Analysis and Design*, Springer-Verlag, Praxis Publishing Ltd.
- Lakdawalla, E. (2004), No Longer Boring: ‘Fireworks’ and Other Surprises at Uranus Spotted Through Adaptive Optics, The Planetary Society, http://www.planetary.org/news/2004/1111_No_Longer_Boring_Fireworks_and_Other.html, Last accessed: 27/05/2009.
- Larson, W.J., and J.R. Wertz (1999), *Space Mission Analysis and Design*, Microcosm, Inc., Kluwer Academic Press, 3rd edition.
- MAPSView (2006), MAPS Key Parameter Database, University of Michigan, http://mapsview.engin.umich.edu/data_descriptions/spacecraft_overview.php, Last accessed: 19/05/2009.
- MathWorld (2009a), Halley’s Method, <http://mathworld.wolfram.com>, Last accessed: 09/06/2009.
- MathWorld (2009b), Newton-Raphson, <http://mathworld.wolfram.com>, Last accessed: 11/06/2009.

- Melman, J.C.P. (2007), Trajectory Optimization for a Mission to Neptune and Triton: Thesis Report, Delft University of Technology, Faculty of Aerospace Engineering, The Netherlands.
- Michalewicz, Z. (1996), *Genetic Algorithms + Data Structures = Evolution Programs*, Springer, 3rd edition.
- Molenaar, S. (2007), Trajectory optimization for a Uranus polar orbiter mission: Literature Study, Delft University of Technology, Faculty of Aerospace Engineering, The Netherlands.
- Montenbruck, O., and E. Gill (2005), *Satellite Orbits: Models, methods and applications*, Springer-Verlag Berlin Heidelberg, 3rd edition.
- NASA/Cassini (2009), Cassini Equinox Mission, <http://saturn.jpl.nasa.gov>, Last accessed: 14/05/2009.
- NASA/Galileo (2007), Galileo Legacy Site, <http://solarsystem.nasa.gov/galileo/index.cfm>, Last accessed: 13/05/2009.
- NASA/GRC (2005), Stirling convertor for the stirling radioisotope generator tested as a prelude to transition to flight, <http://grc.nasa.gov>, Last accessed: 12/12/2007.
- NASA/GSFC (2007), Lunar and Planetary Science, <http://nssdc.gsfc.nasa.gov/planetary>, Last accessed: 12/05/2009.
- NASA/JHU-APL (2006), New Horizons Mission Guide, NASA/Johns Hopkins University Applied Physics Laboratory.
- NASA/JHU-APL (2009), New Horizons: NASA's Pluto-Kuiper Belt Mission, <http://pluto.jhuapl.edu>, Last accessed: 20/05/2009.
- NASA/JPL (2009), Solar System Exploration, <http://sse.jpl.nasa.gov>, Last accessed: 07/05/2009.
- NASA/Voyager (2009), Voyager: The interstellar mission, <http://voyager.jpl.nasa.gov>, Last accessed: 07/05/2009.
- NOAA (2007), Uranus' Moons - Miranda, Ariel, Umbriel, Titania, Oberon, http://sos.noaa.gov/datasets/solar_system/uranusmoons.html, Last accessed: 11/12/2007.
- Noomen, R. (2006), *Space Mission Design: Optimization*, Delft University of Technology, Faculty of Aerospace Engineering, The Netherlands, Lecture slides ae4-878, v.1.2, 21/02/2006.
- Noomen, R. *et al.*(2003), *Space Engineering and Technology III*, Delft University of Technology, Faculty of Aerospace Engineering, The Netherlands, Lecture notes ae3-803.
- Pater, I. de, and J. Lissauer (2007), *Planetary Sciences*, Cambridge University Press.
- Schatz, W.J., R.D. Cannova, R.T. Cowley, and D.D. Evans (1979), Development and Flight Experience of the Voyager Propulsion System.
- Schlijper, R.M.H. (2003), Genetic Algorithm Optimization of Planetary Gravity-Assist Missions to Pluto, Delft University of Technology, Faculty of Aerospace Engineering, The Netherlands.
- ScienceDaily (2006), Pluto Downgraded To 'Dwarf Planet' Status; Solar System Now Has Eight Planets, 24 August 2006, <http://www.sciencedaily.com/releases>.

- Sromovsky, L., P. Fry, H. Hammel, and K. Rages (2005), Hubble Discovers a Dark Cloud in the Atmosphere of Uranus, <http://www.physorg.com/news78676690.html>, Last accessed: 04/05/2009.
- Stanley, S., and J. Bloxham (2004), Convective-region geometry as the cause of Uranus' and Neptune's unusual magnetic fields, *Nature*, 428, 11 March 2004.
- Strange, N.J., and J.M. Longuski (2002), Graphical Method for Gravity-Assist Trajectory Design, *Journal of Spacecraft and Rockets*, 39(1).
- Turner, M.J.L. (2005), *Rocket and Spacecraft Propulsion*, chapter 6, Springer Berlin Heidelberg, 2nd edition.
- Vallado, D.A., and W.D. McClain (2007), *Fundamentals of Astrodynamics and Applications*, Microcosm Press, 3 edition.
- Vasile, M., and P. de Pascale (2006), Preliminary design of multiple gravity-assist trajectories, *Journal of Spacecraft and Rockets*, Volume 43-4.
- Vasile, M., M. Ceriotti, G. Radice, V. Becerra, S. Nasuto, J. Anderson, and C. Bombardelli (2008), Global Trajectory Optimisation: Can we Prune the Solution Space when Considering Deep Space Manoeuvres?, Department of Aerospace Engineering, University of Glasgow, United Kingdom and School of Systems Engineering, University of Reading, United Kingdom.
- Vinko, T., D. Izzo, and C. Bombardelli (2007), Benchmarking different global optimisation techniques for preliminary space trajectory design, *58th International Astronautical Congress, Hyderabad*.
- Wakker, K.F. (2002), *Astrodynamics I and II*, Delft University of Technology, Faculty of Aerospace Engineering, The Netherlands, Lecture notes AE4-873.
- Wertz, J.R. (2001), *Mission Geometry; Orbit and Constellation Design and Management*, Kluwer Academic Publishers, Microcosm, Inc.
- Wikipedia (2009), Wikipedia, the free encyclopedia, <http://en.wikipedia.org>, Last accessed: 26/05/2009.
- Zandbergen, B.T.C. (2004), *Thermal Rocket Propulsion*, Delft University of Technology, Faculty of Aerospace Engineering, The Netherlands, Lecture notes ae4-S01.

Appendix A

The Hohmann transfer to Uranus

The orbital velocity of the Earth around the Sun is given by:

$$V_E = \sqrt{\frac{\mu_S}{r_E}} = 29.78 \text{ km/s} \quad (\text{A.1})$$

In this equation μ_S is the gravitational parameter of the Sun ($1.3271 \cdot 10^{11} \text{ km}^3/\text{s}^2$) and r_E is the distance from the center of the Earth to the center of the Sun (which is 1 AU or $149.598 \cdot 10^6 \text{ km}$). The escape velocity at the parking orbit around the Earth can be calculated using equation 6.27:

$$V_{esc} = \sqrt{2}V_c = \sqrt{\frac{2\mu_E}{r_0}} = \sqrt{\frac{2\mu_E}{R_E + h}} = 11.02 \text{ km/s} \quad (\text{A.2})$$

Here $\mu_E = 3.986004 \cdot 10^5 \text{ km}^3/\text{s}^2$, $R_E = 6378.137 \text{ km}$ and $h = 185 \text{ km}$. The heliocentric velocity at leaving the Earth's orbit is calculated using the vis-viva equation:

$$V_1 = \sqrt{\mu_S \left(\frac{2}{r_E} - \frac{1}{a_H} \right)} = 41.06 \text{ km/s} \quad (\text{A.3})$$

The semi-major axis of the Hohmann orbit is $a_H = \frac{1}{2}(r_E + r_U)$, where the orbital radius of Uranus r_U is 19.191 AU. The hyperbolic excess velocity is then calculated as follows:

$$V_{\infty E} = V_1 - V_E = 41.06 - 29.78 = 11.28 \text{ km/s} \quad (\text{A.4})$$

The velocity after the impulsive shot is give in the parking orbit around Earth can then be calculated as follows:

$$V_0 = \sqrt{V_{esc0}^2 + V_{\infty E}^2} = 15.77 \text{ km/s} \quad (\text{A.5})$$

The only thing to determine now to calculate ΔV_0 is the velocity the spacecraft has in its parking orbit, V_{c0} .

$$V_{c0} = \sqrt{\frac{\mu_E}{r_0}} = 7.79 \text{ km/s} \quad (\text{A.6})$$

The magnitude of the impulsive shot in the parking orbit around the Earth becomes:

$$\Delta V_0 = V_0 - V_{c0} = 7.98 \text{ km/s} \quad (\text{A.7})$$

The next impulsive shot is needed to decelerate the spacecraft and go into orbit around Uranus. The velocity that Uranus has around the Sun is:

$$V_U = \sqrt{\frac{\mu_S}{r_U}} = 6.81 \text{ km/s} \quad (\text{A.8})$$

The heliocentric velocity at Uranus is calculated with the vis-viva equation:

$$V_2 = \sqrt{\mu_S \left(\frac{2}{r_U} - \frac{1}{a_H} \right)} = 2.15 \text{ km/s} \quad (\text{A.9})$$

The hyperbolic excess velocity at Uranus can then be obtained:

$$V_{\infty U} = V_2 - V_U = -4.66 \text{ km/s} \quad (\text{A.10})$$

It is assumed that the parking orbit around Uranus is at 1.1 times the radius of Uranus ($R_U = 25,559 \text{ km}$). The mass of Uranus is 14.6 times the mass of Earth, so its gravitational parameter is 14.6 times larger than Earth's. Now the velocity after the impulsive shot is calculated as follows:

$$V_3 = \sqrt{V_{esc3}^2 + V_{\infty U}^2} = \sqrt{\frac{2\mu_U}{r_3} + V_{\infty U}^2} = 20.87 \text{ km/s}$$

The velocity in the circular parking orbit around Uranus is:

$$V_{par3} = \sqrt{\frac{\mu_U}{r_3}} = 14.38 \text{ km/s} \quad (\text{A.11})$$

Then finally, the magnitude of the impulsive shot at Uranus can be calculated:

$$\Delta V_3 = V_3 - V_{par_3} = 6.49 \text{ km/s} \quad (\text{A.12})$$

So in order to perform a Hohmann transfer from a circular Low Earth Orbit (LEO) at 185 km altitude to a circular parking orbit around Uranus radius with radius $1.1R_U$ requires two large ΔV 's. The first one is 7.98 km/s and the second one is 6.49 km/s. The transfer time for such an orbit is half the orbital period of an ellipse with semi-major axis a_H . This comes down to:

$$T_H = \frac{1}{2} \cdot 2\pi \sqrt{\frac{a_H^3}{\mu_S}} = 5.04 \cdot 10^8 \text{ s} = 15.97 \text{ yr} \quad (\text{A.13})$$

Appendix B

Benchmark tests for the EdM test case

This appendix contains the results of the additional tests for EdM test case in section 13.2. For each extra test the following results will be given:

- The decision vectors for the best individual in each run.
- The orbit corresponding to the best individual.
- The distribution of the individuals in the initial population.

All optimization runs are performed 10 times, each time with a different seed number for the random generator. The Genetic Algorithm settings are the same as used in section 13.2.2.

B.1 EdM test case, extra test I

Table B.1 shows the decision vectors for the best solutions for each run and the corresponding ΔV_{tot} .

S	t_0 MJD2000	t_1 MJD2000	$ \bar{V}_{\infty L} $ km/s	θ rad	φ rad	η -	ΔV_{tot} km/s
5	1217.0	1463.1	0.643	0.071	-0.259	0.202	5.654
10	1216.6	1463.8	0.642	0.078	-0.259	0.204	5.654
75	1216.5	1457.2	0.011	6.283	-0.288	0.155	5.657
250	1215.8	1460.4	0.328	0.082	-0.285	0.181	5.655
1000	1245.7	1684.5	2.789	0.066	-0.073	0.467	5.645
1050	1247.5	1839.9	2.769	6.169	-0.093	0.341	5.649
1100	1216.7	1461.4	0.457	0.065	-0.270	0.186	5.654
1150	1216.2	1460.7	0.409	0.060	-0.252	0.184	5.655
1200	1241.9	1466.3	1.960	6.278	-0.139	-0.139	5.653
1250	1216.4	1464.7	0.693	0.070	-0.265	0.211	5.655

Table B.1 Decision vectors and total ΔV the best individuals of 10 runs for extra test I of the EdM test case [Bernelli-Zazzera *et al.*, 2007]. The launch window is constrained to $t_0 \in [1100, 1300]$ MJD2000. The time needed to complete these runs on the `dutlrw.lr.tudelft.nl`-server was 277 s.

The best solution found by GALOMUSIT after the ten different runs is 5.645 km/s for seed number 1000, which is 13 m/s higher than the best solution found by Bernelli-Zazzera *et al.* [2007]. The orbit corresponding to this best individual is shown in figure B.1.

The distribution of feasible individuals in the initial population within the $t_0 - t_1$ search space is shown in figure B.2.

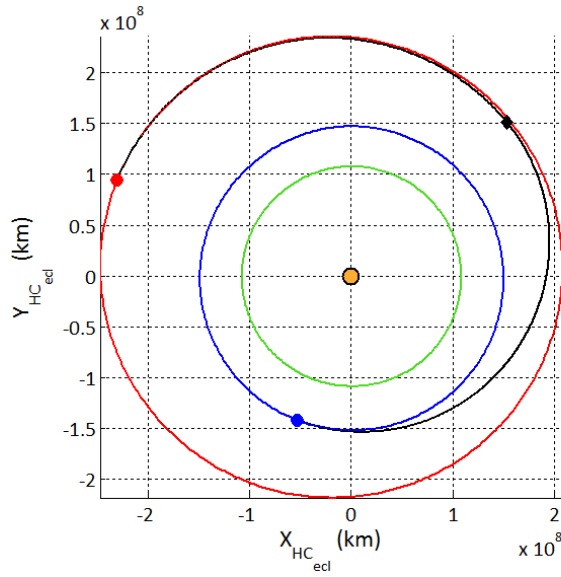


Figure B.1 Orbit corresponding to the best solution obtained with GALOMUSIT for extra test I of the EdM test case of [Bernelli-Zazzera *et al.*, 2007]. The seed number for the run was 1000. The launch window was constrained to $t_0 \in [1100, 1300]$ MJD2000. For the other variables, the complete search space has been used. ●: Earth at launch, ◆: DSM, ●: Mars at arrival.

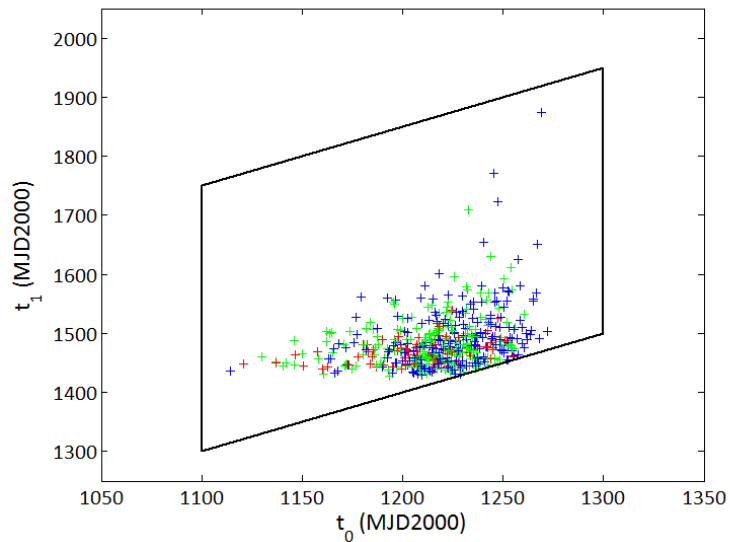


Figure B.2 Distribution of the feasible individuals in the initial population for seed number 1000 for extra test I of the EdM test case. The launch window was constrained to $t_0 \in [1100, 1300]$ MJD2000. For the other variables, the complete search space has been used. The $t_0 - t_1$ search space is indicated by the solid line. "●": $\Delta V_{tot} > 6.5$ km/s. "●": $6.0 < \Delta V_{tot} \leq 6.5$ km/s. "●": $\Delta V_{tot} \leq 6.0$ km/s.

B.2 EdM test case, extra test II

Table B.2 shows the decision vectors for the best solutions for each run and the corresponding ΔV_{tot} .

S	t_0 MJD2000	t_1 MJD2000	$ \bar{V}_{\infty L} $ km/s	θ rad	φ rad	η -	ΔV_{tot} km/s
5	1246.7	1539.5	2.684	6.244	-0.145	0.586	5.635
10	1245.8	1476.5	2.608	0.026	-0.031	0.474	5.640
75	1244.2	1479.8	2.577	0.040	-0.144	0.492	5.641
250	1244.0	1492.1	2.612	0.040	-0.141	0.556	5.639
1000	1245.1	1485.7	2.640	0.038	-0.137	0.550	5.638
1050	1247.9	1506.3	2.731	6.281	-0.130	0.629	5.634
1100	1246.2	1475.1	2.611	0.016	-0.131	0.471	5.640
1150	1245.9	1477.2	2.633	0.038	-0.126	0.494	5.640
1200	1246.2	1486.0	2.646	0.006	-0.138	0.557	5.637
1250	1245.7	1487.3	2.716	0.068	-0.124	0.603	5.639

Table B.2 Decision vectors and total ΔV the best individuals of 10 runs for extra test II of the EdM test case [Bernelli-Zazzera *et al.*, 2007]. The launch window is constrained to $t_0 \in [1100, 1300]$ MJD2000 and $|\bar{V}_{\infty L}| \in [2.50, 2.90]$ km/s. The time needed to complete these runs on the dut1ruw.lir.tudelft.nl-server was 357 s.

The best solution found by GALOMUSIT after the ten different runs is 5.634 km/s for seed number 1050, which is 2 m/s higher than the best solution found by Bernelli-Zazzera *et al.* [2007]. The orbit corresponding to this best individual is shown in figure B.3.

The distribution of feasible individuals in the initial population within the $t_0 - t_1$ search space is shown in figure B.4.

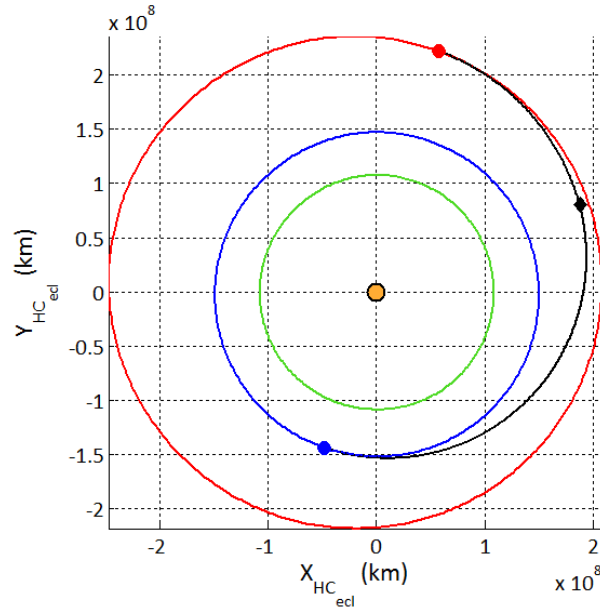


Figure B.3 Orbit corresponding to the best solution obtained with GALOMUSIT for extra test II of the EdM test case of [Bernelli-Zazzera *et al.*, 2007]. The seed number for the run was 1000. The launch window was constrained to $t_0 \in [1100, 1300]$ MJD2000 and $|\vec{V}_{\infty L}| \in [2.50, 2.90]$ km/s. For the other variables, the complete search space has been used. \bullet : Earth at launch, \blacklozenge : DSM, \bullet : Mars at arrival.

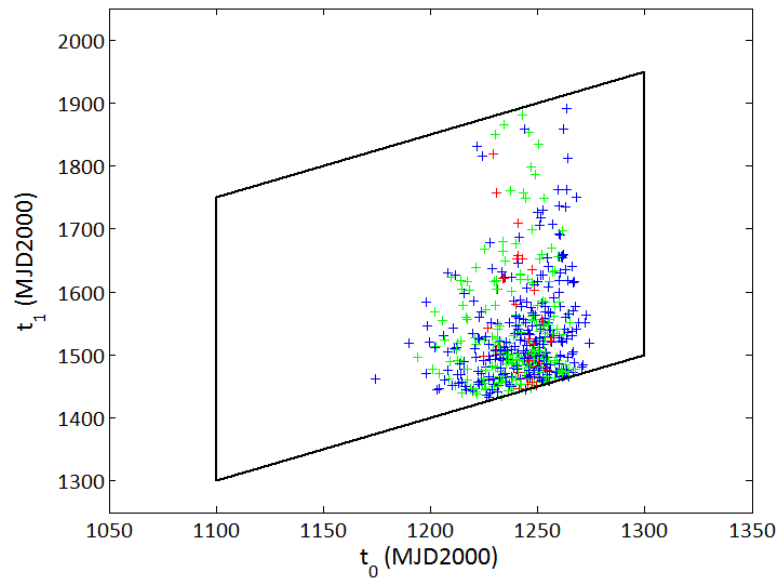


Figure B.4 Distribution of the feasible individuals in the initial population for seed number 1000 for extra test II of the EdM test case. The launch window was constrained to $t_0 \in [1100, 1300]$ MJD2000 and $|\vec{V}_{\infty L}| \in [2.50, 2.90]$ km/s. For the other variables, the complete search space has been used. The $t_0 - t_1$ search space is indicated by the solid line. " $+$ ": $\Delta V_{tot} > 6.5$ km/s. " $+$ ": $6.0 < \Delta V_{tot} \leq 6.5$ km/s. " $+$ ": $\Delta V_{tot} \leq 6.0$ km/s.

B.3 EdM test case, extra test III

Table B.3 shows the decision vectors for the best solutions for each run and the corresponding ΔV_{tot} .

S	t_0 MJD2000	t_1 MJD2000	$ \bar{V}_{\infty L} $ km/s	θ rad	φ rad	η -	ΔV_{tot} km/s
5	1245.6	1467.4	2.471	0.009	-0.126	0.339	5.645
10	1245.0	1465.2	2.415	0.034	-0.108	0.275	5.647
75	1216.5	1458.4	0.121	0.069	-0.277	0.162	5.656
250	1244.0	1465.9	2.365	0.041	-0.127	0.283	5.647
1000	1245.2	1468.8	2.441	0.011	-0.124	0.325	5.645
1050	1242.4	1464.8	2.094	0.028	-0.130	0.221	5.650
1100	1248.4	1497.3	2.775	0.003	-0.152	0.634	5.642
1150	1245.7	1464.1	2.399	0.025	-0.108	0.254	5.647
1200	1244.3	1467.9	2.407	0.031	-0.122	0.314	5.645
1250	1247.7	1625.6	2.823	0.037	-0.115	0.523	5.626

Table B.3 Decision vectors and total ΔV the best individuals of 10 runs for extra test III of the EdM test case [Bernelli-Zazzera et al., 2007]. The launch window is constrained to $t_0 \in [1100, 1300]$ MJD2000, $\theta \in [0, 0.10]$ rad and $\varphi \in [-0.30, 0]$. The time needed to complete these runs on the dutlruw.lir.tudelft.nl-server was 56 s.

The best solution found by GALOMUSIT after the ten different runs is 5.626 km/s for seed number 1250, which is 6 m/s lower than the best solution found by Bernelli-Zazzera et al. [2007]. The orbit corresponding to this best individual is shown in figure B.5.

The distribution of feasible individuals in the initial population within the $t_0 - t_1$ search space is shown in figure B.6.

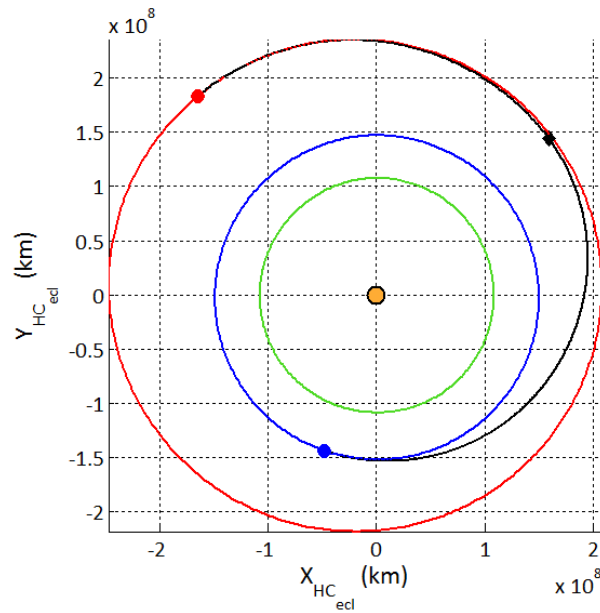


Figure B.5 Orbit corresponding to the best solution obtained with GALOMUSIT for extra test III of the EdM test case of [Bernelli-Zazzera et al., 2007]. The seed number for the run was 1250. The launch window was constrained to $t_0 \in [1100, 1300]$ MJD2000, $\theta \in [0, 0.10]$ rad and $\varphi \in [-0.30, 0]$ rad. For the other variables, the complete search space has been used. \bullet : Earth at launch, \blacklozenge : DSM, \bullet : Mars at arrival.

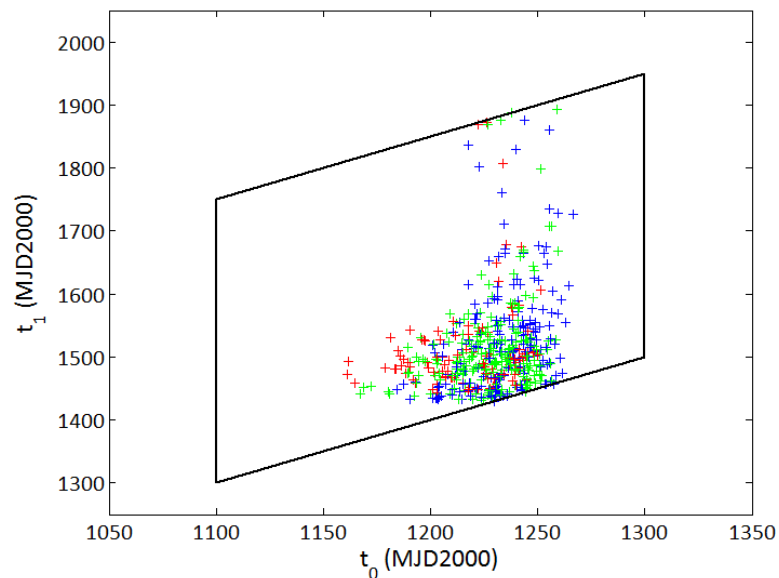


Figure B.6 Distribution of the feasible individuals in the initial population for seed number 1250 for extra test III of the EdM test case. The launch window was constrained to $t_0 \in [1100, 1300]$ MJD2000, $\theta \in [0, 0.10]$ rad and $\varphi \in [-0.30, 0]$ rad. For the other variables, the complete search space has been used. The $t_0 - t_1$ search space is indicated by the solid line. "+" : $\Delta V_{tot} > 6.5$ km/s. "+" : $6.0 < \Delta V_{tot} \le 6.5$ km/s. "+" : $\Delta V_{tot} \le 6.0$ km/s.

B.4 EdM test case, extra test IV

Table B.4 shows the decision vectors for the best solutions for each run and the corresponding ΔV_{tot} .

S	t_0 MJD2000	t_1 MJD2000	$ \bar{V}_{\infty L} $ km/s	θ rad	φ rad	η -	ΔV_{tot} km/s
5	1244.1	1481.0	2.567	0.037	-0.135	0.490	5.641
10	1244.5	1485.3	2.561	0.010	-0.146	0.506	5.640
75	1241.9	1478.6	2.449	0.047	-0.150	0.425	5.647
250	1241.6	1487.3	2.371	6.247	-0.166	0.443	5.652
1000	1243.6	1483.2	2.526	0.022	-0.149	0.480	5.642
1050	1242.4	1477.9	2.480	0.042	-0.159	0.438	5.645
1100	1244.3	1499.4	2.609	0.015	-0.152	0.566	5.638
1150	1242.1	1479.9	2.493	0.053	-0.149	0.455	5.646
1200	1245.6	1476.7	2.618	0.034	-0.129	0.484	5.640
1250	1242.3	1479.6	2.513	0.068	-0.142	0.456	5.647

Table B.4 Decision vectors and total ΔV the best individuals of 10 runs for extra test IV of the EdM test case [Bernelli-Zazzera *et al.*, 2007]. The launch window is constrained to $t_0 \in [1100, 1300]$ MJD2000 and $\eta \in [0.40, 0.60]$. The time needed to complete these runs on the dutlrw.lr.tudelft.nl-server was 539 s.

The best solution found by GALOMUSIT after the ten different runs is 5.640 km/s for seed number 1100, which is 8 m/s higher than the best solution found by Bernelli-Zazzera *et al.* [2007]. The orbit corresponding to this best individual is shown in figure B.7.

The distribution of feasible individuals in the initial population within the $t_0 - t_1$ search space is shown in figure B.8.

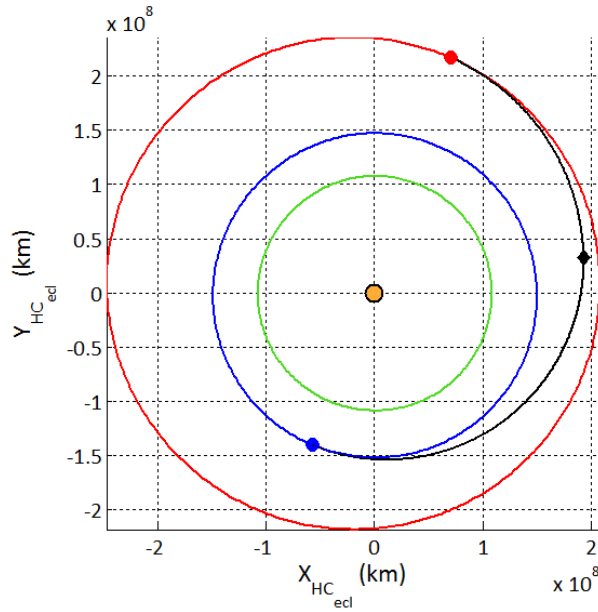


Figure B.7 Orbit corresponding to the best solution obtained with GALOMUSIT for extra test IV of the EdM test case of [Bernelli-Zazzera et al., 2007]. The seed number for the run was 1100. The launch window was constrained to $t_0 \in [1100, 1300]$ MJD2000 and $\eta \in [0.40, 0.60]$. For the other variables, the complete search space has been used. ●: Earth at launch, ◆: DSM, ●: Mars at arrival.

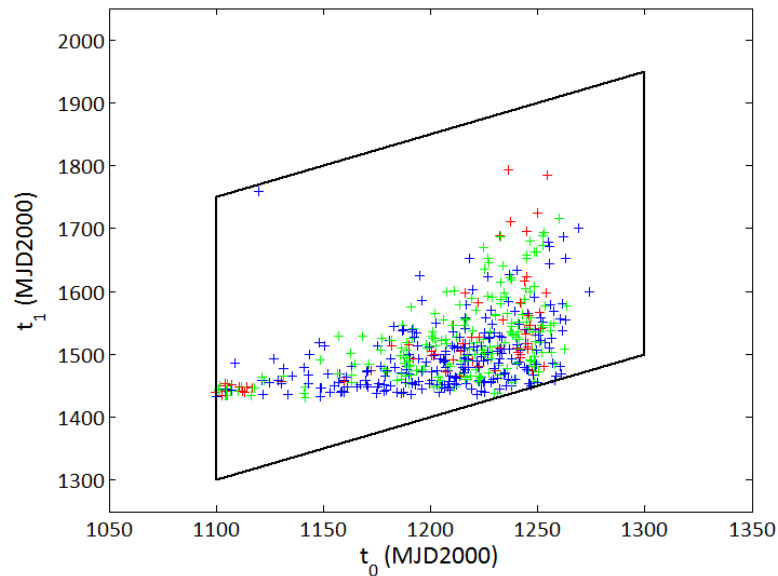


Figure B.8 Distribution of the feasible individuals in the initial population for seed number 1100 for extra test IV of the EdM test case. The launch window was constrained to $t_0 \in [1100, 1300]$ MJD2000 and $\eta \in [0.40, 0.60]$. For the other variables, the complete search space has been used. The $t_0 - t_1$ search space is indicated by the solid line. "+" : $\Delta V_{tot} > 6.5$ km/s. "+" : $6.0 < \Delta V_{tot} \leq 6.5$ km/s. "+" : $\Delta V_{tot} \leq 6.0$ km/s.

B.5 EdM test case, extra test V

Table B.5 shows the decision vectors for the best solutions for each run and the corresponding ΔV_{tot} .

S	t_0 MJD2000	t_1 MJD2000	$ \bar{V}_{\infty L} $ km/s	θ rad	φ rad	η -	ΔV_{tot} km/s
5	1247.2	1706.3	2.813	0.024	-0.107	0.435	5.623
10	1247.3	1678.7	2.833	0.047	-0.113	0.465	5.626
75	1245.2	1716.9	2.768	0.018	-0.136	0.422	5.622
250	1247.2	1647.6	2.793	0.013	-0.124	0.491	5.623
1000	1247.2	1616.6	2.795	0.024	-0.124	0.526	5.625
1050	1245.9	1618.7	2.764	0.027	-0.136	0.518	5.625
1100	1245.3	1634.7	2.771	0.045	-0.142	0.504	5.626
1150	1246.2	1603.4	2.775	0.036	-0.134	0.539	5.625
1200	1246.6	1618.3	2.777	0.020	-0.132	0.521	5.624
1250	1247.3	1621.9	2.787	0.014	-0.124	0.520	5.624

Table B.5 Decision vectors and total ΔV the best individuals of 10 runs for extra test V of the EdM test case [Bernelli-Zazzera *et al.*, 2007]. All variables are constrained, except the time of flight. The time needed to complete these runs on the dut1ruw.lr.tudelft.nl-server was 29 s.

The best solution found by GALOMUSIT after the ten different runs is 5.622 km/s for seed number 75, which is 10 m/s lower than the best solution found by Bernelli-Zazzera *et al.* [2007]. The orbit corresponding to this best individual is shown in figure B.9.

The distribution of feasible individuals in the initial population within the $t_0 - t_1$ search space is shown in figure B.10.

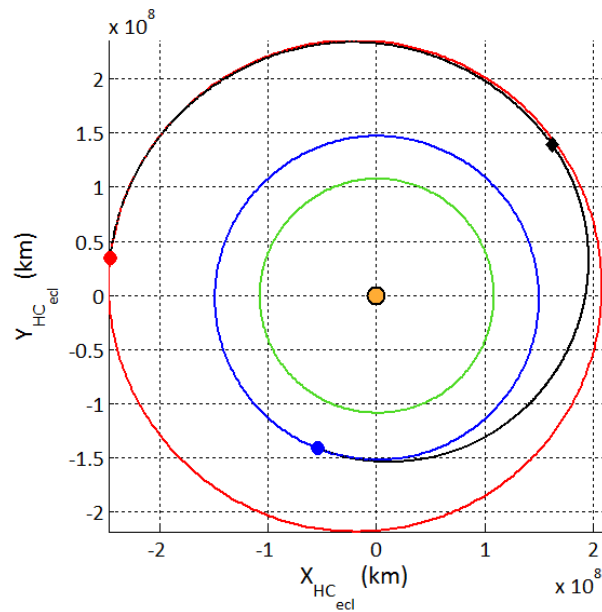


Figure B.9 Orbit corresponding to the best solution obtained with GALOMUSIT for extra test V of the EdM test case of [Bernelli-Zazzera et al., 2007]. The seed number for the run was 75. All variables are constrained, except the time of flight. ●: Earth at launch, ◆: DSM, ●: Mars at arrival.

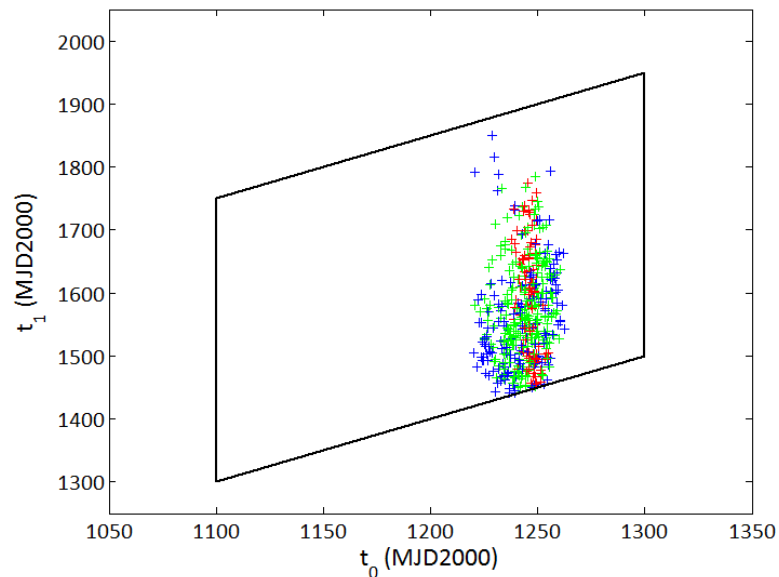


Figure B.10 Distribution of the feasible individuals in the initial population for seed number 75 for extra test V of the EdM test case. All variables are constrained, except the time of flight. The $t_0 - t_1$ search space is indicated by the solid line. " + ": $\Delta V_{tot} > 6.5$ km/s. " + ": $6.0 < \Delta V_{tot} \leq 6.5$ km/s. " + ": $\Delta V_{tot} \leq 6.0$ km/s.

B.6 EdM test case, extra test VI

Table B.6 shows the decision vectors for the best solutions for each run and the corresponding ΔV_{tot} .

S	t_0 MJD2000	t_1 MJD2000	$ \bar{V}_{\infty L} $ km/s	θ rad	φ rad	η -	ΔV_{tot} km/s
5	1243.1	1878.2	2.782	0.024	-0.119	0.322	5.621
10	1243.1	1873.9	2.786	0.036	-0.118	0.325	5.622
75	1245.1	1892.3	2.795	6.272	-0.103	0.315	5.621
250	1243.8	1879.2	2.769	6.265	-0.119	0.321	5.621
1000	1244.3	1871.4	2.773	6.251	-0.127	0.322	5.623
1050	1245.0	1860.7	2.785	6.270	-0.107	0.330	5.621
1100	1243.1	1890.4	2.774	0.006	-0.117	0.316	5.621
1150	1242.5	1883.3	2.776	0.017	-0.133	0.319	5.621
1200	1241.6	1875.1	2.763	0.024	-0.142	0.322	5.624
1250	1244.6	1877.3	2.792	0.007	-0.102	0.324	5.621

Table B.6 Decision vectors and total ΔV the best individuals of 10 runs for extra test VI of the EdM test case [Bernelli-Zazzera et al., 2007]. The launch window is constrained to $t_0 \in [1100, 1300]$ MJD2000 and $T_{EM} \in [600, 650]$ days. For the other variables, the complete search space has been used. The time needed to complete these runs on the `outlrw.lr.tudelft.nl`-server was 7541 s.

The best solution found by GALOMUSIT after the ten different runs is 5.621 km/s for seed number 1050. The best total ΔV is the same for 6 of the 10 individuals, but the individual for seed number 1050 has the lowest time of flight. The total ΔV is 11 m/s lower than the best solution found by Bernelli-Zazzera et al. [2007]. The orbit corresponding to this best individual is shown in figure B.9.

The distribution of feasible individuals in the initial population within the $t_0 - t_1$ search space is shown in figure B.12.

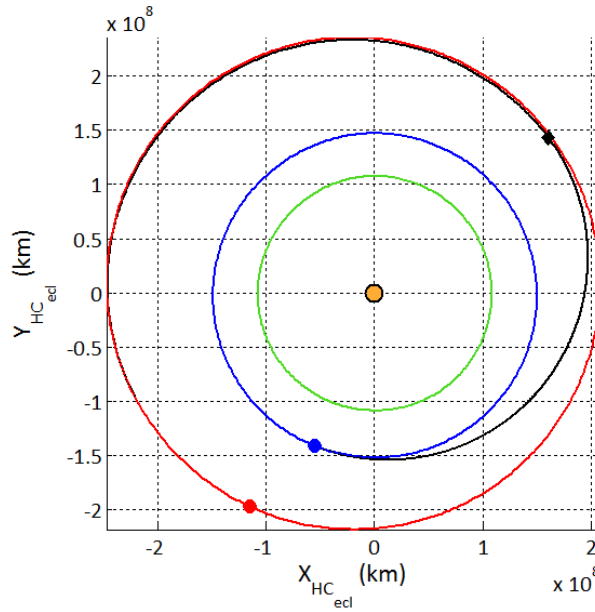


Figure B.11 Orbit corresponding to the best solution obtained with GALOMUSIT for extra test VI of the EdM test case of [Bernelli-Zazzera *et al.*, 2007]. The seed number for the run was 1050. The launch window was constrained to $t_0 \in [1100, 1300]$ MJD2000, and $T_{EM} \in [600, 650]$ days. For the other variables, the complete search space has been used. ●: Earth at launch, ◆: DSM, ●: Mars at arrival.

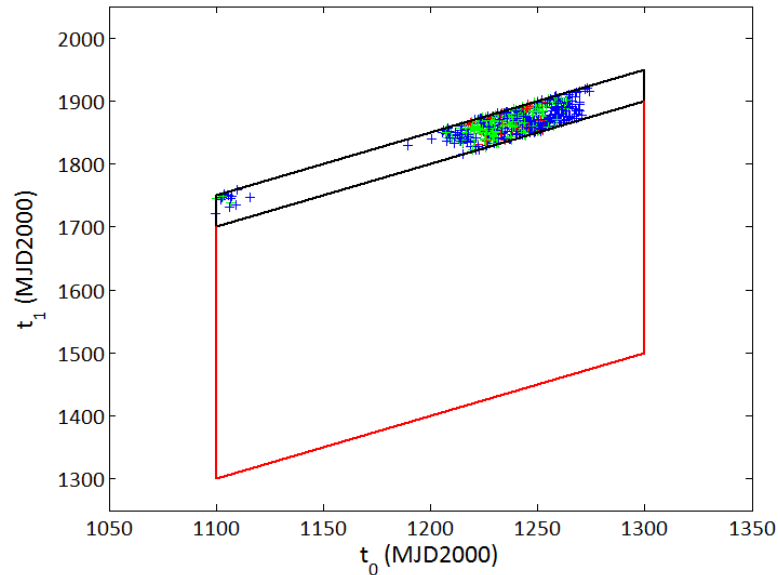


Figure B.12 Distribution of the feasible individuals in the initial population for seed number 1050 for extra test VI of the EdM test case. The launch window was constrained to $t_0 \in [1100, 1300]$ MJD2000 and $T_{EM} \in [600, 650]$ days. For the other variables, the complete search space has been used. The $t_0 - t_1$ search space is indicated by the solid black line. The red line indicates the boundary of the complete search space for T_{EM} . " + ": $\Delta V_{tot} > 6.5$ km/s. " + ": $6.0 < \Delta V_{tot} \leq 6.5$ km/s. " + ": $\Delta V_{tot} \leq 6.0$ km/s.

B.7 EdM test case, extra test VII

Table B.7 shows the decision vectors for the best solutions for each run and the corresponding ΔV_{tot} .

S	t_0 MJD2000	t_1 MJD2000	$ \bar{V}_{\infty L} $ km/s	θ rad	φ rad	η -	ΔV_{tot} km/s
5	1216.723	1464.367	0.679	0.056	-0.260	0.207	5.654
10	1216.821	1463.797	0.651	0.059	-0.261	0.205	5.654
75	1216.536	1461.848	0.487	0.059	-0.266	0.190	5.654
250	1245.135	1532.427	2.674	6.266	-0.139	0.590	5.646
1000	1243.418	1463.497	2.158	0.026	-0.125	0.217	5.649
1050	1244.525	1510.517	2.671	0.038	-0.199	0.578	5.646
1100	1216.924	1461.774	0.502	0.062	-0.266	0.189	5.654
1150	1241.473	1727.879	2.721	0.034	-0.187	0.416	5.649
1200	1216.648	1462.278	0.509	0.078	-0.270	0.190	5.654
1250	1216.658	1463.630	0.646	0.066	-0.258	0.205	5.654

Table B.7 Decision vectors and total ΔV the best individuals of 10 runs for extra test VII of the EdM test case [Bernelli-Zazzera et al., 2007]. For the decision variables, the complete search space has been used. The population size was 2000. The time needed to complete these runs on the dutlrw.lr.tudelft.nl-server was 5277 s.

The best solution found by GALOMUSIT after the ten different runs is 5.646 km/s for seed number 1050. The best total ΔV is the same for 2 of the 10 individuals, but the individual for seed number 1050 has the lowest time of flight. The total ΔV is 14 m/s higher than the best solution found by Bernelli-Zazzera et al. [2007]. It actually had the same decision vector as the best solution found in section 13.2.2.

The distribution of feasible individuals in the initial population within the $t_0 - t_1$ search space is shown in figure B.13.

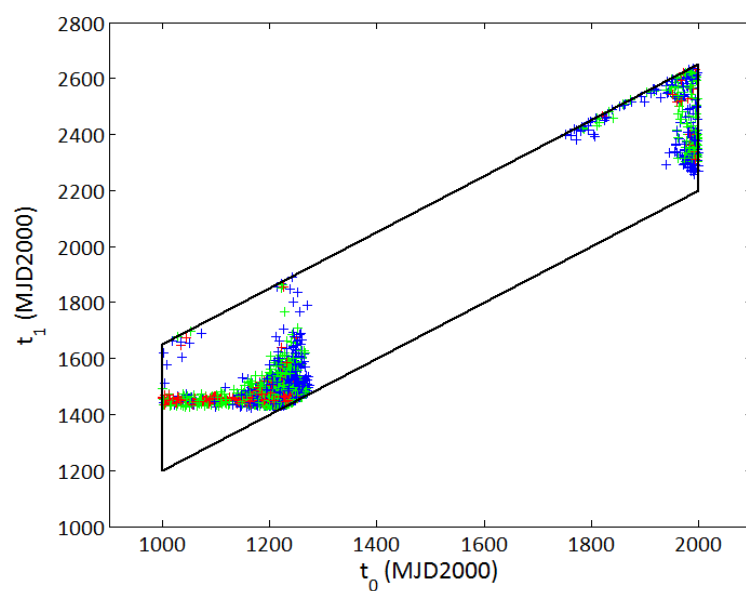


Figure B.13 Distribution of the feasible individuals in the initial population for seed number 1050 for extra test VII of the EdM test case. For all variables, the complete search space has been used. The population size N_{pop} was 2000. The $t_0 - t_1$ search space is indicated by the solid line. " $+$ ": $\Delta V_{tot} > 6.5$ km/s. " $+$ ": $6.0 < \Delta V_{tot} \leq 6.5$ km/s. " $+$ ": $\Delta V_{tot} \leq 6.0$ km/s.

Appendix C

Benchmark tests for the EVdM test case

This appendix contains the results for the additional tests for EVdM test case in section 13.3. For each extra test the following results will be given:

- The decision vectors for the best individual in each run.
- The distribution of the individuals in the initial population.
- The orbit corresponding to the best individual. It should be noted that for extra tests II, V, VI and VII the orbits are not shown since they are all similar to the orbit obtained in extra test I.

All optimization runs are performed 10 times, each time with a different seed number for the random generator. The Genetic Algorithm settings are the same as used in section 13.2.2.

C.1 Extra test I: $t_0 \in [4200, 4600]$ MJD2000

S	t_0 MJD2000	t_1 MJD2000	t_2 MJD2000	h_{pV} km	ζ_V rad	η_{VM}	ΔV_{tot} km/s
5	4481.5	4657.4	5284.3	3181.1	5.602	0.554	3.226
10	4476.0	4647.7	5340.1	643.05	4.990	0.537	2.994
75	4475.9	4648.0	5339.6	769.1	4.980	0.542	3.016
250	4474.5	4644.8	5343.1	52.6	5.134	0.544	2.996
1000	4480.4	4657.3	5284.2	3128.9	5.610	0.539	3.220
1050	4480.6	4656.7	5285.8	1628.8	5.674	0.518	3.179
1100	4481.1	4658.1	5284.4	3235.6	5.610	0.546	3.215
1150	4481.1	4657.6	5285.0	2694.9	5.637	0.554	3.188
1200	4481.8	4657.6	5284.8	2917.6	5.617	0.516	3.209
1250	4477.4	4647.5	5339.0	999.4	5.010	0.516	3.084

Table C.1 EVdM with $t_0 \in [4200, 4600]$ MJD2000. For the other variables the complete search space was used. The total time needed for these ten runs was 3799 sec on the `dutlruw.lr.tudelft.nl-server`.

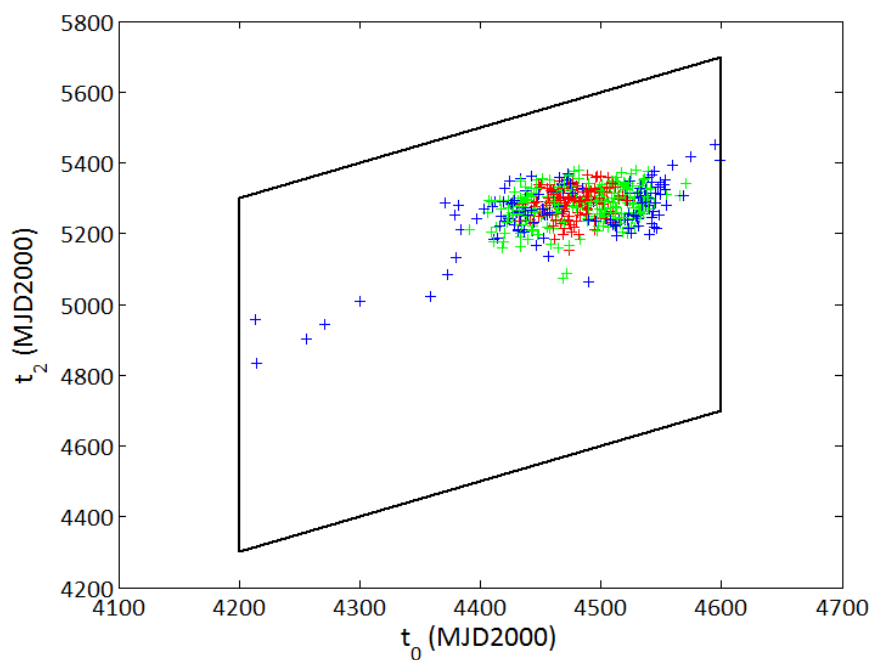


Figure C.1 Distribution of the feasible individuals in the initial population for seed number 10 when $t_0 \in [4200, 4600]$ MJD2000. The $t_0 - t_2$ search space is indicated by the solid line. $\color{blue}+$: $\Delta V_{tot} > 8.0$ km/s. $\color{green}+$: $6.0 < \Delta V_{tot} \leq 8.0$ km/s. $\color{red}+$: $\Delta V_{tot} \leq 6.0$ km/s.

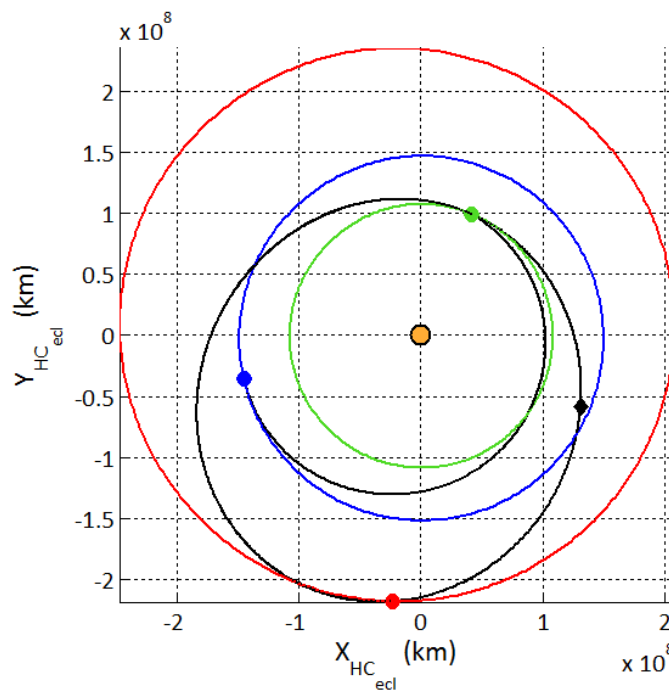


Figure C.2 Orbit corresponding to the best individual of extra test I for the EVdM test case. The seed number for this run was 10. $\color{blue}\bullet$: Earth at launch, $\color{green}\bullet$: Venus swingby, \blacklozenge : DSM, $\color{red}\bullet$: Arrival at Mars.

C.2 Extra test II: $t_0 \in [6600, 7000]$ MJD2000

S	t_0 MJD2000	t_1 MJD2000	t_2 MJD2000	h_{pV} km	ζ_V rad	η_{VM}	ΔV_{tot} km/s
5	6807.513	6977.450	7534.837	9723.0	0.809	0.498	3.426
10	6814.840	6983.919	7537.000	10044.9	0.978	0.507	3.383
75	6812.620	6982.787	7536.410	10046.9	0.939	0.542	3.389
250	6818.135	6987.479	7540.010	9398.4	1.011	0.533	3.383
1000	6815.467	6983.499	7536.780	10076.2	0.983	0.556	3.379
1050	6817.258	6985.891	7538.747	9695.6	1.000	0.555	3.378
1100	6812.333	6982.431	7536.342	10077.0	0.930	0.496	3.391
1150	6819.450	6987.617	7540.136	9423.0	1.026	0.538	3.376
1200	6812.562	6982.640	7536.209	10121.4	0.942	0.516	3.384
1250	6811.994	6980.436	7535.100	10313.9	0.924	0.517	3.397

Table C.2 EVdM with $t_0 \in [6600, 7000]$ MJD2000. For the other variables the complete search space was used. The total time needed for these ten runs was 1405 sec on the `outlruw.lr.tudelft.nl`-server.

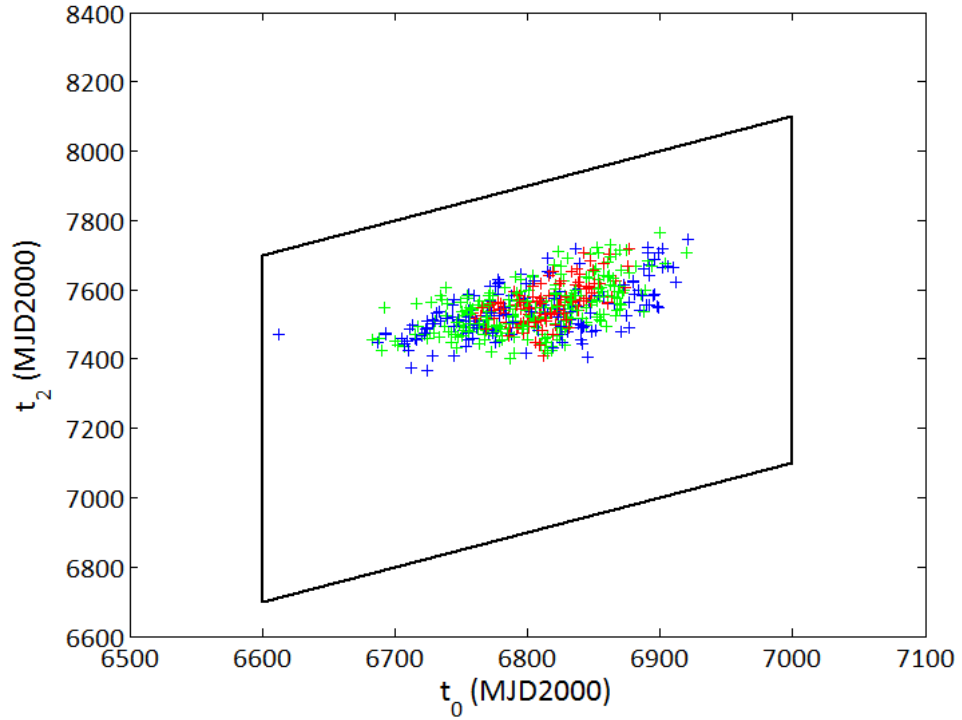


Figure C.3 Distribution of the feasible individuals in the initial population for seed number 1150 when $t_0 \in [6600, 7000]$ MJD2000. The $t_0 - t_2$ search space is indicated by the solid line. $+$: $\Delta V_{tot} > 8.0$ km/s. $+$: $6.0 < \Delta V_{tot} \leq 8.0$ km/s. $+$: $\Delta V_{tot} \leq 6.0$ km/s.

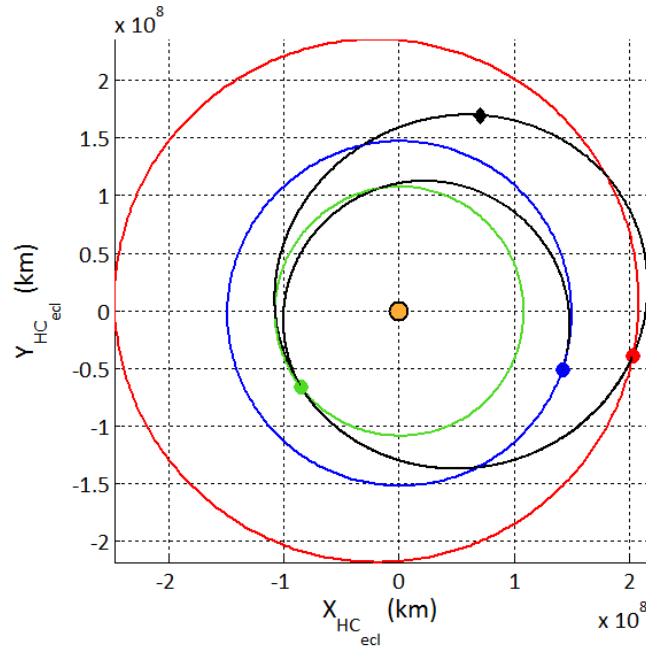


Figure C.4 Orbit corresponding to the best individual of extra test II for the EVdM test case. The seed number for this run was 1150. ●: Earth at launch, ●: Venus swingby, ◆: DSM, ●: Arrival at Mars.

C.3 Extra test III: Complete search space, $N_{pop} = 2000$

S	t_0 MJD2000	t_1 MJD2000	t_2 MJD2000	h_{pV} km	ζ_V rad	η_{VM}	ΔV_{tot} km/s
5	6811.5	6981.3	7535.5	10230.9	0.920	0.528	3.391
10	6812.6	6982.7	7536.3	10103.9	0.941	0.470	3.384
75	6815.5	6984.4	7537.4	9930.0	0.982	0.548	3.375
250	6817.5	6986.1	7538.7	9686.2	1.007	0.477	3.374
1000	6814.7	6984.0	7537.2	9964.0	0.972	0.519	3.375
1050	6816.9	6985.9	7538.7	9687.2	0.998	0.495	3.373
1100	6818.8	6986.5	7539.0	9630.3	1.024	0.557	3.380
1150	4483.0	4658.6	5355.2	3553.5	4.928	0.546	3.341
1200	6814.7	6984.6	7537.6	9872.3	0.971	0.509	3.377
1250	4471.6	4648.8	5342.0	1059.6	4.955	0.501	3.231

Table C.3 EVdM with the complete search space used for all variables. The population size is 2000 individuals. The total time needed for these ten runs was 16550 sec on the `outlrw.lr.tudelft.nl`-server.

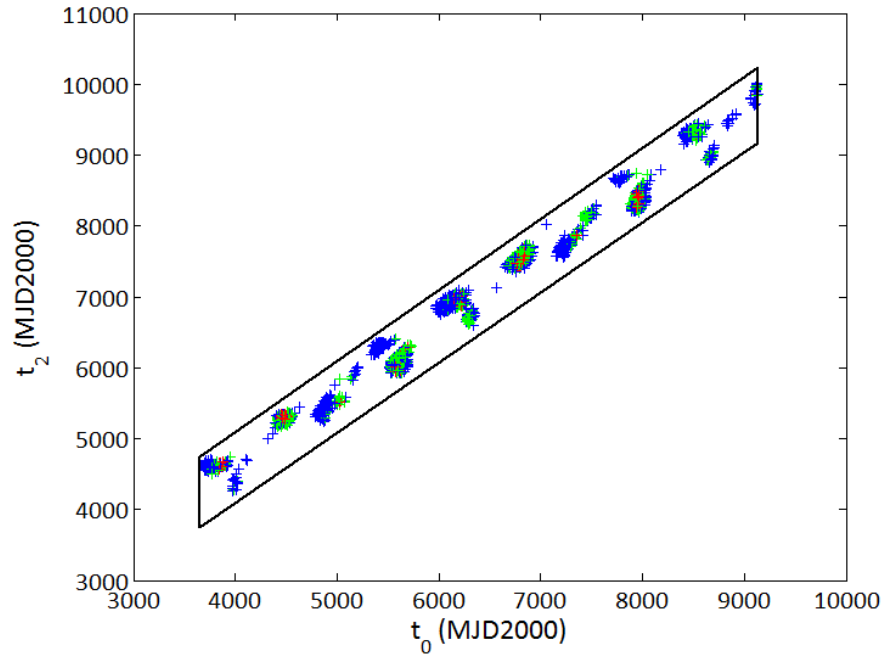


Figure C.5 Distribution of the feasible individuals in the initial population for seed number 1250. The complete search space was used for all variables and the population size was 2000. The $t_0 - t_2$ search space is indicated by the solid line. \times : $\Delta V_{tot} > 8.0$ km/s. \times : $\Delta V_{tot} > 8.0$ km/s. \times : $6.0 < \Delta V_{tot} \leq 8.0$ km/s. \times : $\Delta V_{tot} \leq 6.0$ km/s.

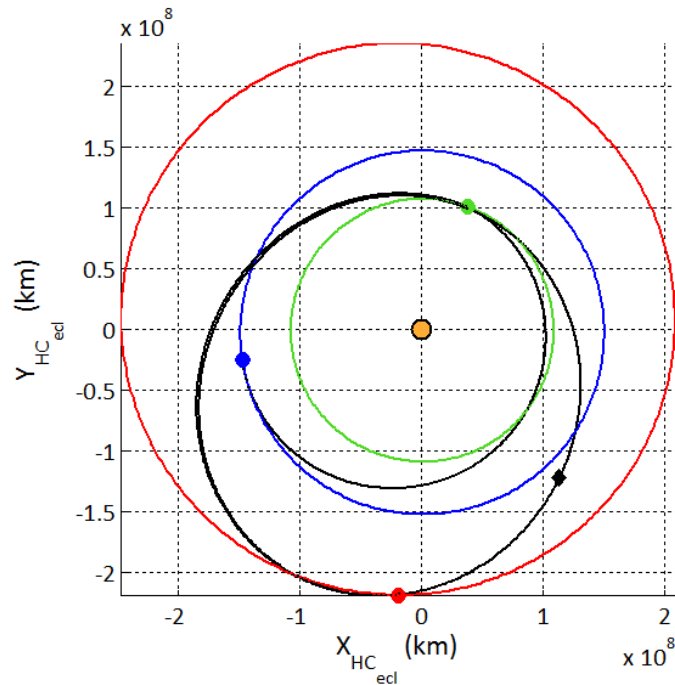


Figure C.6 Orbit corresponding to the best individual of extra test III for the EVdM test case. The seed number for this run was 1250. \bullet : Earth at launch, \bullet : Venus swingby, \blacklozenge : DSM, \bullet : Arrival at Mars.

C.4 Extra test IV: $h_p \in [0, 0.75]$ R_V , $t_0 \in [4200, 4600]$ MJD2000

S	t_0 MJD2000	t_1 MJD2000	t_2 MJD2000	h_{pV} km	ζ_V rad	η_{VM}	ΔV_{tot} km/s
5	4481.2	4657.3	5285.2	8519.7	5.643	0.566	3.185
10	4482.2	4657.3	5285.5	8236.8	5.654	0.558	3.179
75	4481.1	4657.0	5286.5	7512.0	5.681	0.565	3.164
250	4475.7	4646.8	5338.5	6636.9	5.018	0.544	3.020
1000	4477.3	4646.1	5334.7	7017.9	5.060	0.514	3.172
1050	4476.4	4647.0	5337.8	6755.4	5.009	0.547	3.040
1100	4480.3	4654.7	5351.9	7918.8	4.890	0.568	3.177
1150	4477.3	4648.1	5338.8	7012.2	4.978	0.533	3.050
1200	4478.1	4648.9	5341.2	7094.0	4.960	0.697	3.023
1250	4476.0	4646.2	5340.0	6407.6	5.045	0.532	2.987

Table C.4 EVdM with $h_p \in [0, 0.75]$ R_V in the launch window centered at 4400 MJD2000. The complete search space is used for the other variables. The population size is 500 individuals. The total time needed for these ten runs was 2744 sec on the `outlruw.lir.tudelft.nl`-server.

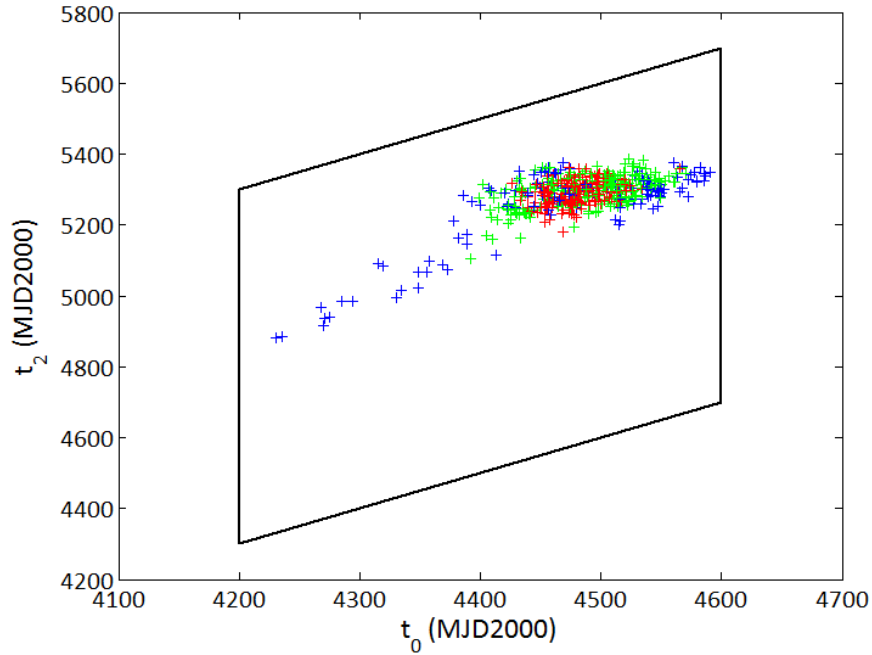


Figure C.7 Distribution of the feasible individuals in the initial population for seed number 1250. $h_p \in [0, 0.75]$ R_V in the launch window centered at 4400 MJD2000. The complete search space is used for the other variables. The $t_0 - t_2$ search space is indicated by the solid line. $+$: $\Delta V_{tot} > 8.0$ km/s. $+$: $6.0 < \Delta V_{tot} \leq 8.0$ km/s. $+$: $\Delta V_{tot} \leq 6.0$ km/s.

C.5 Extra test V: $\zeta \in [4.75, 6.00]$ rad, $t_0 \in [4200, 4600]$ MJD2000

S	t_0 MJD2000	t_1 MJD2000	t_2 MJD2000	h_{pV} km	ζ_V rad	η_{VM}	ΔV_{tot} km/s
5	4480.4	4650.9	5344.1	1395.6	4.934	0.575	3.037
10	4476.3	4647.2	5333.5	1134.5	4.993	0.537	3.144
75	4479.9	4656.0	5285.2	1938.4	5.652	0.510	3.201
250	4482.0	4657.7	5285.1	2697.8	5.634	0.563	3.189
1000	4475.6	4646.6	5337.5	592.4	5.019	0.549	3.035
1050	4481.4	4657.9	5284.7	3026.7	5.620	0.539	3.202
1100	4481.6	4657.3	5283.2	3850.6	5.550	0.531	3.286
1150	4475.2	4646.6	5339.7	415.0	5.029	0.542	2.986
1200	4473.1	4645.0	5332.5	499.3	5.056	0.538	3.124
1250	4475.9	4646.3	5341.1	706.0	5.096	0.541	3.147

Table C.5 EVdM with $\zeta \in [4.75, 6.00]$ rad in the launch window centered at 4400 MJD2000. The complete search space is used for the other variables. The population size is 500 individuals. The total time needed for these ten runs was 1324 sec on the `outlrw.lr.tudelft.nl`-server.

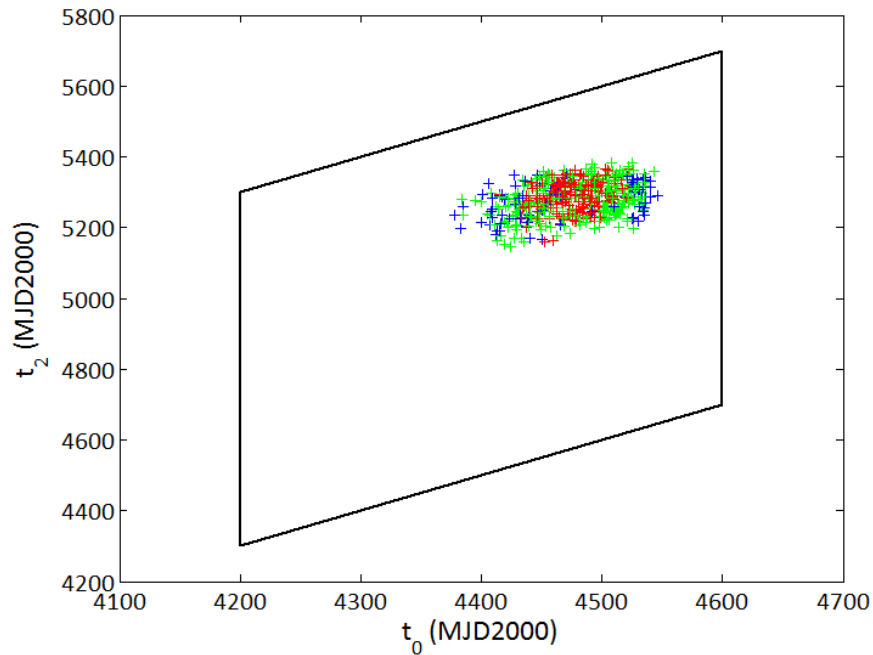


Figure C.8 Distribution of the feasible individuals in the initial population for seed number 1150. $\zeta \in [4.75, 6.00]$ in the launch window centered at 4400 MJD2000. The complete search space is used for the other variables. The $t_0 - t_2$ search space is indicated by the solid line. $+$: $\Delta V_{tot} > 8.0$ km/s. $+$: $6.0 < \Delta V_{tot} \leq 8.0$ km/s. $+$: $\Delta V_{tot} \leq 6.0$ km/s.

C.6 Extra test VI: $\eta \in [0.45, 0.65]$, $t_0 \in [4200, 4600]$ MJD2000

S	t_0 MJD2000	t_1 MJD2000	t_2 MJD2000	h_{pV} km	ζ_V rad	η_{VM}	ΔV_{tot} km/s
5	4477.2	4648.2	5333.7	1688.7	4.983	0.535	3.198
10	4475.6	4646.8	5339.8	467.6	5.018	0.529	2.988
75	4476.9	4648.7	5339.5	970.4	4.964	0.540	3.039
250	4476.4	4647.5	5340.1	611.1	4.996	0.540	2.994
1000	4480.6	4655.6	5284.0	2891.3	5.597	0.532	3.249
1050	4480.9	4657.5	5284.2	3202.0	5.604	0.546	3.223
1100	4477.9	4648.8	5334.9	1682.4	4.962	0.541	3.182
1150	4480.4	4656.1	5282.9	3488.8	5.570	0.548	3.275
1200	4481.9	4658.3	5284.7	3154.2	5.614	0.553	3.207
1250	4476.3	4646.8	5337.9	682.3	5.020	0.534	3.042

Table C.6 EVdM with $\eta \in [0.45, 0.65]$ in the launch window centered at 4400 MJD2000. The complete search space is used for the other variables. The population size is 500 individuals. The total time needed for these ten runs was 1324 sec on the `dut1ruw.lir.tudelft.nl`-server.

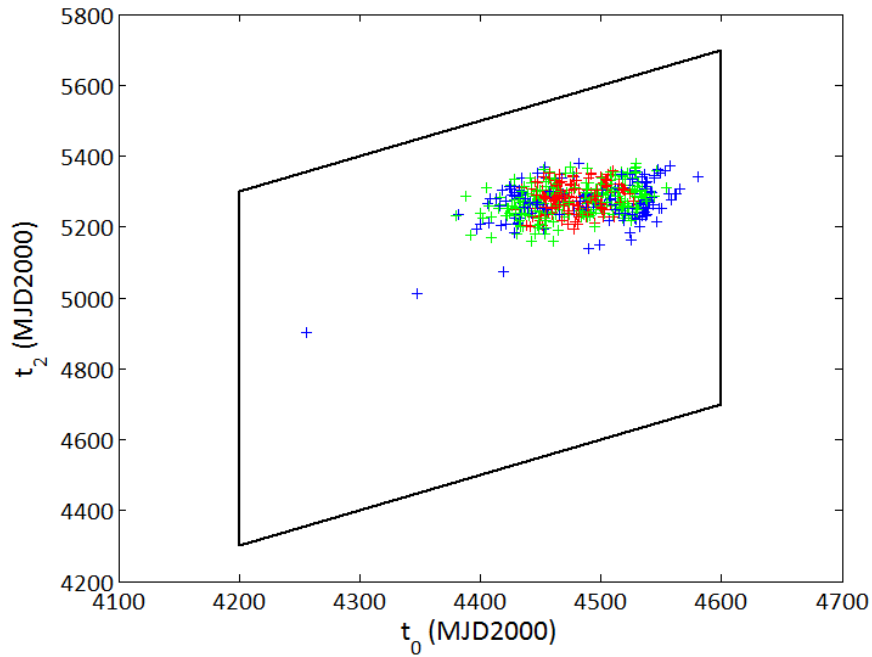


Figure C.9 Distribution of the feasible individuals in the initial population for seed number 10. $\eta \in [0.45, 0.65]$ in the launch window centered at 4400 MJD2000. The complete search space is used for the other variables. The $t_0 - t_2$ search space is indicated by the solid line.
 + : $\Delta V_{tot} > 8.0$ km/s. + : $6.0 < \Delta V_{tot} \leq 8.0$ km/s. + : $\Delta V_{tot} \leq 6.0$ km/s.

C.7 Extra test VII Combination of extra tests IV, V and VI

S	t_0 MJD2000	t_1 MJD2000	t_2 MJD2000	h_{pV} km	ζ_V rad	η_{VM}	ΔV_{tot} km/s
5	4478.2	4650.2	5343.0	1170.7	4.938	0.537	3.026
10	4476.7	4647.1	5337.4	752.2	5.004	0.550	3.052
75	4475.7	4647.1	5339.9	503.2	5.011	0.549	2.991
250	4476.0	4646.4	5340.0	376.6	5.038	0.568	2.989
1000	4477.6	4649.2	5341.9	958.8	4.955	0.547	3.015
1050	4481.8	4658.0	5284.9	2897.5	5.626	0.525	3.194
1100	4475.3	4645.9	5335.1	771.2	5.053	0.530	3.108
1150	4477.6	4648.4	5340.8	796.2	4.975	0.518	3.003
1200	4474.8	4645.6	5337.6	419.3	5.054	0.551	3.034
1250	4479.4	4651.2	5344.5	1437.6	4.927	0.541	3.038

Table C.7 EVdM with $h_p \in [0, 0.75]$ R_V , $\zeta \in [4.75, 6.00]$ and $\eta \in [0.45, 0.65]$ in the launch window centered at 4400 MJD2000. The population size is 500 individuals. The total time needed for these ten runs was 412 sec on the dutlruw.lr.tudelft.nl-server.

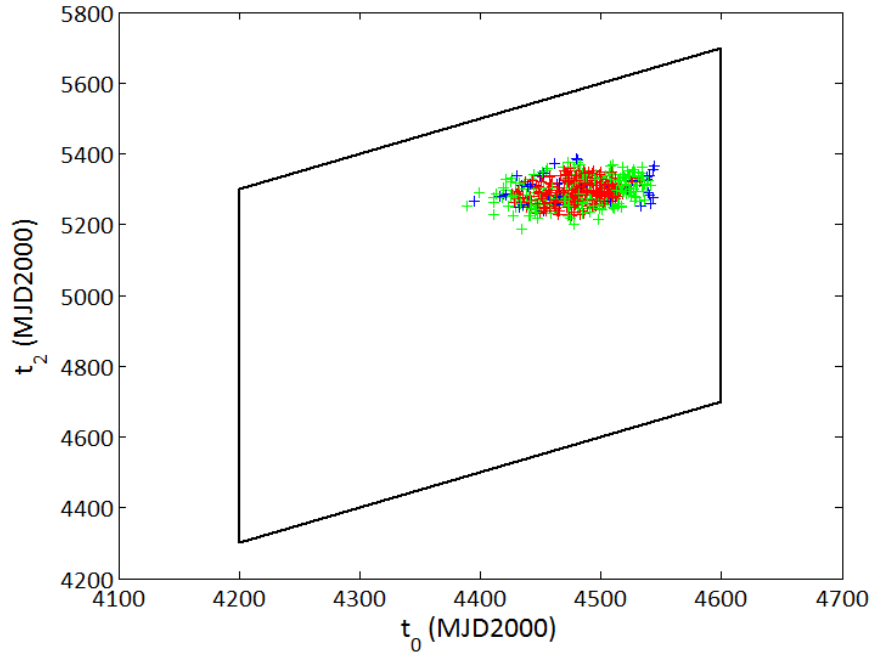


Figure C.10 Distribution of the feasible individuals in the initial population for seed number 250. $h_p \in [0, 0.75]$ R_V , $\zeta \in [4.75, 6.00]$ and $\eta \in [0.45, 0.65]$ in the launch window centered at 4400 MJD2000. The $t_0 - t_2$ search space is indicated by the solid line. $+$: $\Delta V_{tot} > 8.0$ km/s. $+$: $6.0 < \Delta V_{tot} \leq 8.0$ km/s. $+$: $\Delta V_{tot} \leq 6.0$ km/s.

Appendix D

Results for trajectories to Uranus without DSMs

...

D.1 Elitism: 0.10, Immigration: 0.05, No Mutation

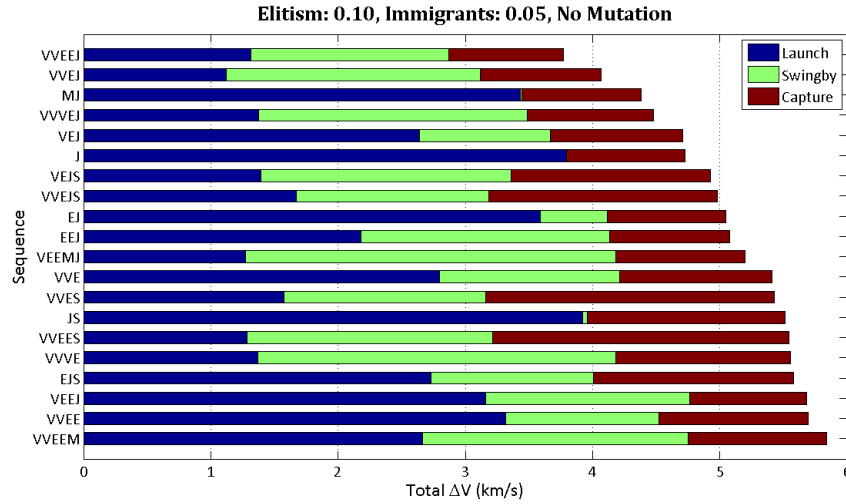


Figure D.1 Schematic of the 20 best sequences for the first set of runs. Elitism: 10%, Immigration: 5% and no Mutation for the configuration described in section 14.2.3. Only the best result out of the five different seed numbers for each sequence has been placed in this figure.

<i>Launch</i>	<i>Date</i>	ΔV (km/s)	C_3 (km ² /s ²)	
	14/06/2015	1.3171	12.380	
<i>Swingbys</i>	<i>Date</i>	ΔV_{req} (km/s)	ΔV_{gained} (km/s)	h (km)
	V: 05/12/2015	0.0005	3.578	2562.6
	V: 20/02/2017	0.0005	-2.029	2292.0
	E: 27/04/2017	0.0002	5.856	2886.8
	E: 15/02/2019	1.4570	3.674	6066.0
J: 31/01/2022	0.0899	9.137	300209.2	
<i>Capture</i>	<i>Date</i>	ΔV (km/s)	C_3 (km ² /s ²)	V_{entry} (km/s)
	14/03/2034	1.0091	20.347	20.793

Table D.1 The best sequence, VVEEJ, for elitism: 10%, immigration: 5% and no mutation. The seed number for this run was 250.

D.2 Elitism: 0.10, Immigration: 0.20, No Mutation

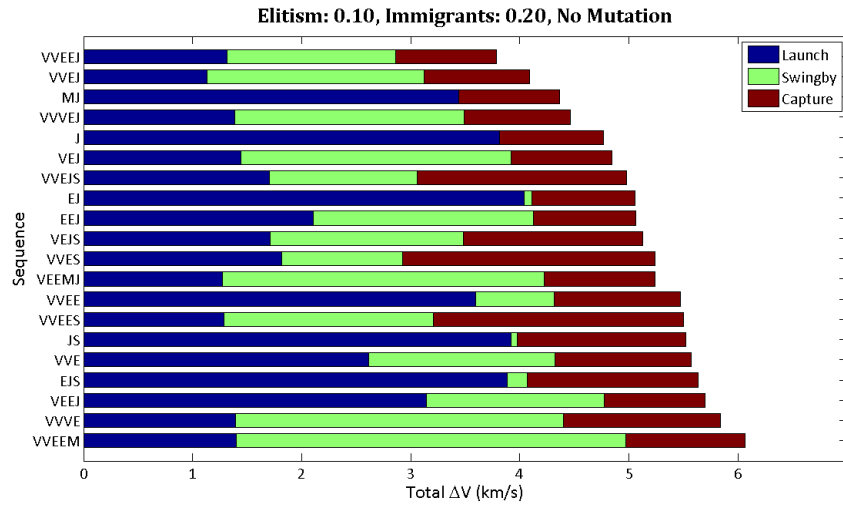


Figure D.2 Schematic of the 20 best sequences for the first set of runs. Elitism: 10%, Immigration: 20% and no Mutation for the configuration described in section 14.2.3. Only the best result out of the five different seed numbers for each sequence has been placed in this figure.

	Date	ΔV (km/s)	C_3 (km ² /s ²)
Launch	13/06/2015	1.3154	12.341

	Date	ΔV_{req} (km/s)	ΔV_{gained} (km/s)	h (km)
Swingbys	V: 05/12/2015	0.0008	3.576	2567.1
	V: 20/02/2017	0.0019	-1.972	2513.9
	E: 26/04/2017	0.0064	5.775	3079.9
	E: 13/02/2019	1.4026	3.665	5714.1
	J: 23/12/2021	0.1377	9.256	336268.5

	Date	ΔV (km/s)	C_3 (km ² /s ²)	V_{entry} (km/s)
Capture	17/10/2034	0.9209	16.687	20.705

Table D.2 The best sequence, VVEEJ, for elitism: 10%, immigration: 20% and no mutation. The seed number for this run was 75.

D.3 Elitism: 0.15, Immigration: 0.15, No Mutation

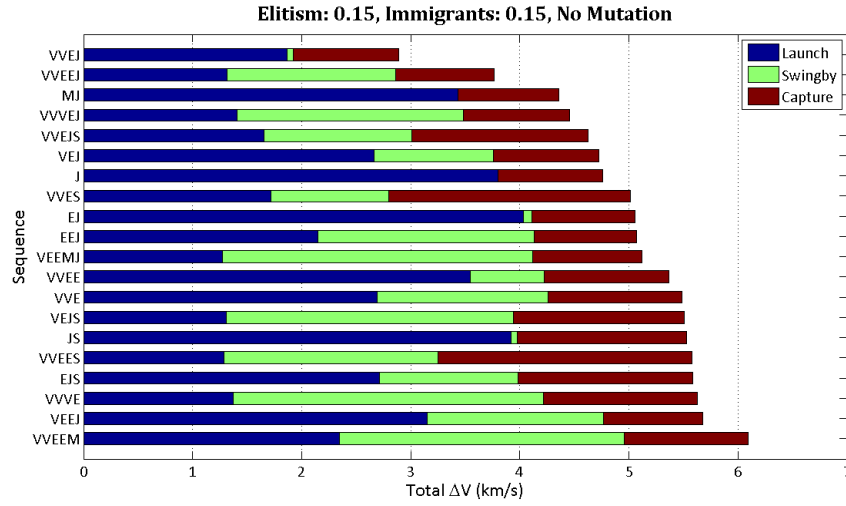


Figure D.3 Schematic of the 20 best sequences for the first set of runs. Elitism: 15%, Immigration: 15% and no Mutation for the configuration described in section 14.2.3. Only the best result out of the five different seed numbers for each sequence has been placed in this figure.

<i>Launch</i>	<i>Date</i>	ΔV (km/s)	C_3 (km ² /s ²)	
	12/09/2015	1.8680	25.431	
<i>Swingbys</i>	<i>Date</i>	ΔV_{req} (km/s)	ΔV_{gained} (km/s)	h (km)
	V: 20/02/2016	0.0088	4.814	1537.3
	V: 11/03/2017	0.0080	2.590	5085.2
	E: 12/01/2019	0.0030	3.802	22066.8
J: 10/08/2022	0.0348	8.789	115123.3	
<i>Capture</i>	<i>Date</i>	ΔV (km/s)	C_3 (km ² /s ²)	V_{entry} (km/s)
	16/07/2034	0.9692	18.690	20.753

Table D.3 The best sequence, VVEJ, for elitism: 15%, immigration: 15% and no mutation. The seed number for this run was 75.

D.4 Elitism: 0.20, Immigration: 0.05, No Mutation

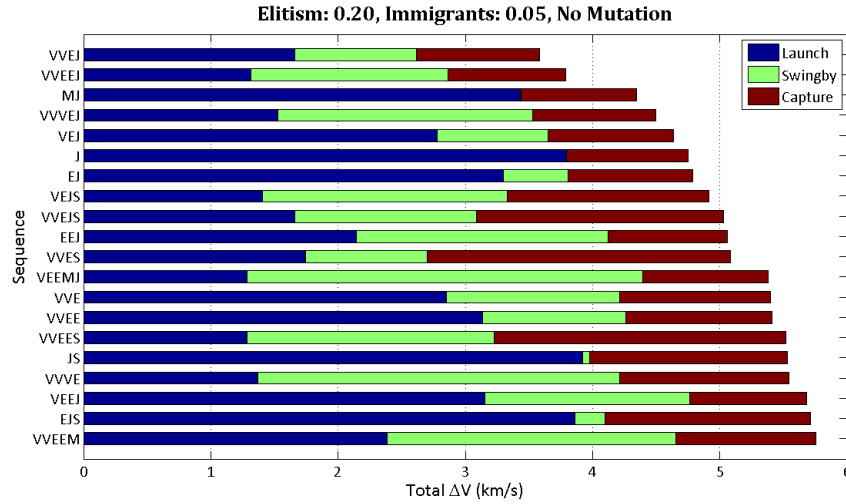


Figure D.4 Schematic of the 20 best sequences for the first set of runs. Elitism: 20%, Immigration: 5% and no Mutation for the configuration described in section 14.2.3. Only the best result out of the five different seed numbers for each sequence has been placed in this figure.

<i>Launch</i>	<i>Date</i>	ΔV (km/s)	C_3 (km ² /s ²)	
	24/08/2015	1.6615	20.468	
<i>Swingbys</i>	<i>Date</i>	ΔV_{req} (km/s)	ΔV_{gained} (km/s)	h (km)
	V: 02/02/2016	0.6445	4.484	1833.1
	V: 09/03/2017	0.0008	2.471	5656.4
	E: 28/12/2018	0.0015	3.688	2844.7
J: 16/10/2021	0.3052	9.885	249024.2	
<i>Capture</i>	<i>Date</i>	ΔV (km/s)	C_3 (km ² /s ²)	V_{entry} (km/s)
	14/04/2034	0.9719	18.802	20.756

Table D.4 The best sequence, VVEJ, for elitism: 20%, immigration: 5% and no mutation. The seed number for this run was 75.

Appendix E

Trajectories with DSMs and one swingby

E.1 EdVU, complete search space for all variables

S	t_0 MJD2000	t_1 MJD2000	t_2 MJD2000	$ \bar{V}_{\infty L} $ km/s	θ rad	φ rad	η	ΔV_{tot} km/s
5	6203.2	6344.9	12318.5	3.188	3.171	-0.623	0.346	8.425
10	6573.8	7014.0	12154.3	2.977	3.444	-0.012	0.397	8.696
75	6566.0	7014.5	11985.4	2.630	3.741	-0.330	0.594	9.176
250	6188.5	6338.7	11722.1	2.929	3.606	-0.311	0.373	8.706
1000	6165.5	6340.8	11682.3	2.082	3.790	-0.325	0.425	9.445
1050	6577.8	7016.0	12215.2	3.792	3.810	-0.195	0.433	8.676
1100	6140.3	6349.8	10312.2	4.589	4.186	0.096	0.467	9.893
1150	6189.5	6333.5	10709.8	2.890	3.562	-0.211	0.434	8.885
1200	6179.1	6338.9	11964.1	2.945	3.679	-0.473	0.412	8.715
1250	6190.3	6340.7	10885.6	2.570	3.485	-0.346	0.362	8.672

Table E.1 Decision vectors and total ΔV for the 10 optimization runs done for EdVU. The complete search space was used for all variables.

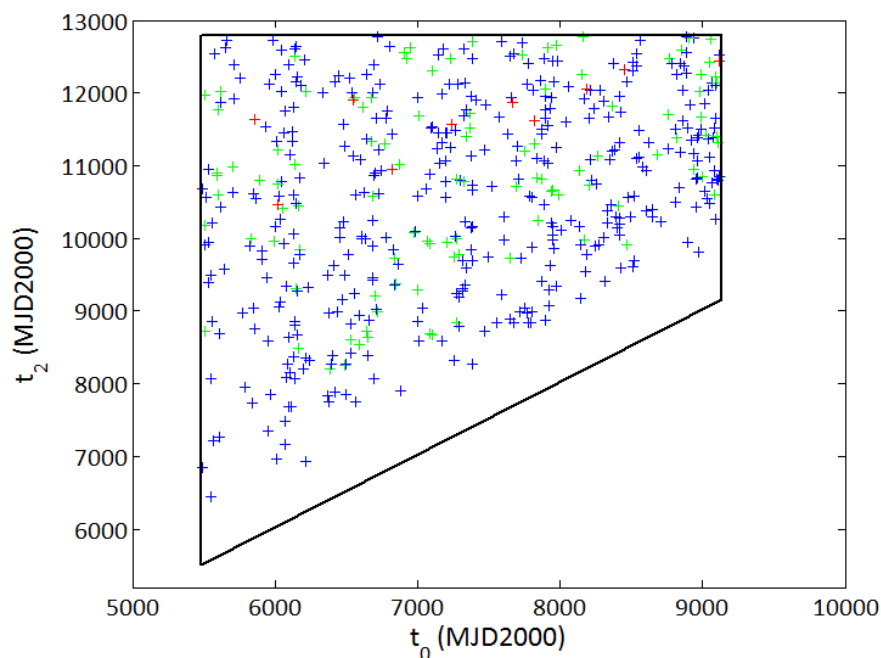


Figure E.1 Distribution of the individuals in the initial population for the EdVU trajectory. The seed number for the run producing these individuals is 5. + : $\Delta V_{tot} > 30$ km/s, + : $15 < \Delta V_{tot} \leq 30$ km/s, + : $\Delta V_{tot} \leq 15$ km/s.

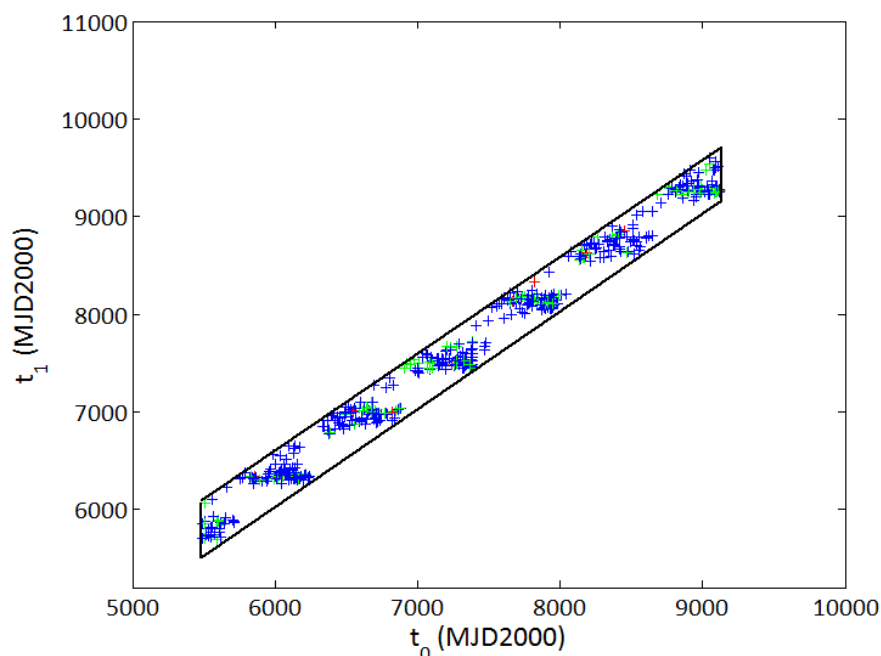


Figure E.2 Distribution in the $t_0 - t_1$ space of the individuals in the initial population for the EdVU trajectory. The seed number for the run producing these individuals is 5. + : $\Delta V_{tot} > 30$ km/s, + : $15 < \Delta V_{tot} \leq 30$ km/s, + : $\Delta V_{tot} \leq 15$ km/s.

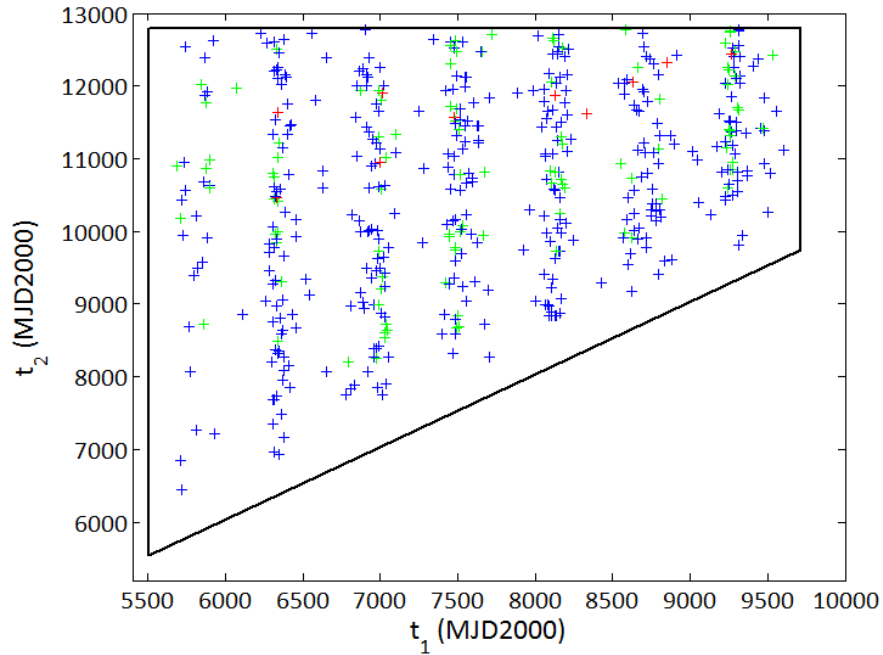


Figure E.3 Distribution in the $t_1 - t_2$ space of the individuals in the initial population for the EdVU trajectory. The seed number for the run producing these individuals is 5. + : $\Delta V_{tot} > 30$ km/s, + : $15 < \Delta V_{tot} \leq 30$ km/s, + : $\Delta V_{tot} \leq 15$ km/s.

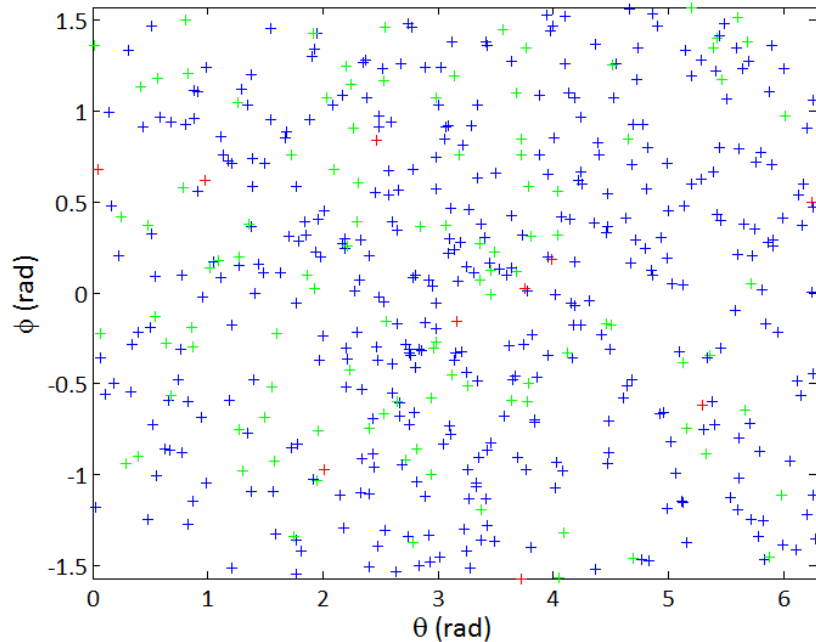


Figure E.4 Distribution of the individuals in the initial population for the EdVU trajectory in the $\theta - \varphi$ space. The complete search space for all variables was used. The seed number for the run producing these individuals is 5. + : $\Delta V_{tot} > 30$ km/s, + : $15 < \Delta V_{tot} \leq 30$ km/s, + : $\Delta V_{tot} \leq 15$ km/s.

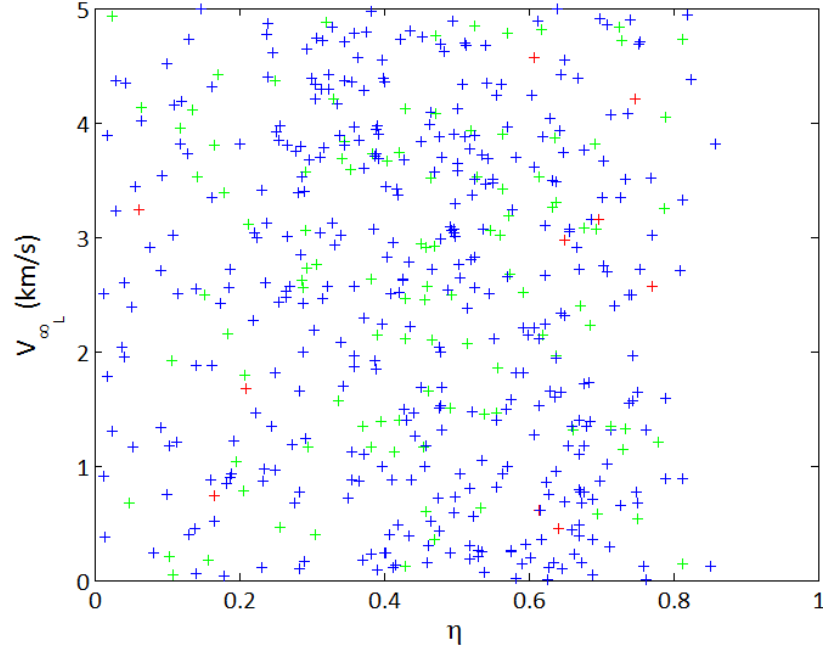


Figure E.5 Distribution of the individuals in the initial population for the EdVU trajectory in the $\eta - |\bar{V}_{\infty L}|$ space. The complete search space for all variables was used. The seed number for the run producing these individuals is 5. + : $\Delta V_{tot} > 30$ km/s, + : $15 < \Delta V_{tot} \leq 30$ km/s, + : $\Delta V_{tot} \leq 15$ km/s.

E.2 EdSU, complete search space for all variables

S	t_0 MJD2000	t_1 MJD2000	t_2 MJD2000	$ \bar{V}_{\infty L} $ km/s	θ rad	φ rad	η	ΔV_{tot} km/s
5	5524.9	8833.2	12619.8	10.481	0.078	0.158	0.199	7.277
10	5887.9	8647.3	12662.3	10.464	0.160	0.171	0.178	6.830
75	5888.8	8375.0	12702.7	10.386	6.243	-0.140	0.165	6.694
250	6255.8	8546.1	12707.0	10.307	0.131	0.044	0.180	6.689
1000	5499.0	7743.2	12779.2	10.336	0.167	0.139	0.128	6.318
1050	5869.6	7904.0	12712.3	10.631	0.296	0.018	0.155	6.576
1100	5870.4	7828.1	12656.7	10.432	0.219	-0.001	0.136	6.471
1150	5893.9	8563.3	12618.6	10.319	6.137	0.105	0.131	6.844
1200	5890.0	8487.2	12588.7	10.246	6.241	0.040	0.192	6.705
1250	5879.1	8400.7	12708.6	10.489	0.252	0.048	0.171	6.690

Table E.2 Decision vectors and total ΔV for the 10 optimization runs done for EdSU. The complete search space was used for all variables.

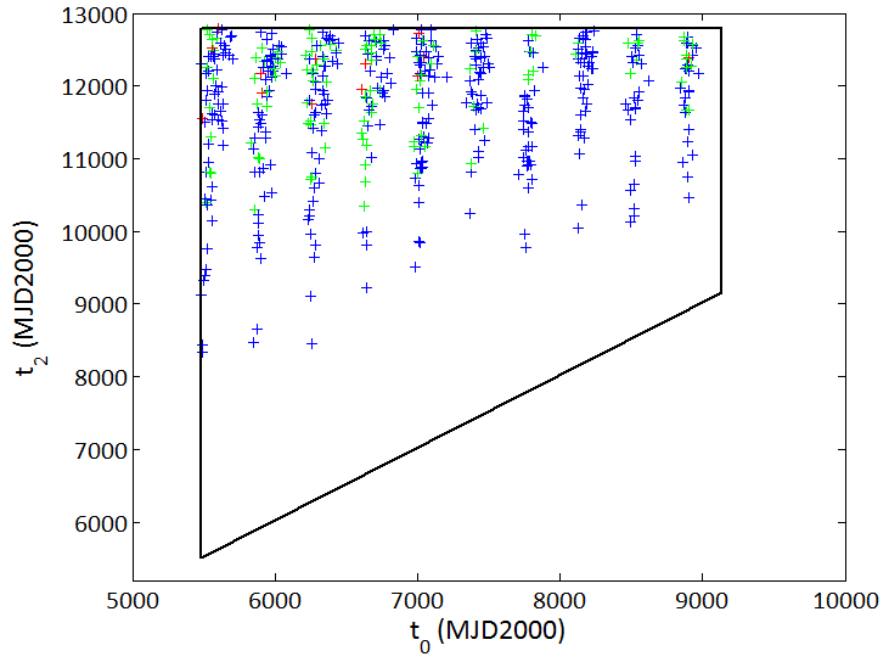


Figure E.6 Distribution of the individuals in the initial population for the EdSU trajectory. The seed number for the run producing these individuals is 1000. $\color{blue}+$: $\Delta V_{tot} \geq 20$ km/s, $\color{green}+$: $12 \leq \Delta V_{tot} < 20$ km/s, $\color{red}+$: $\Delta V_{tot} \leq 12$ km/s.

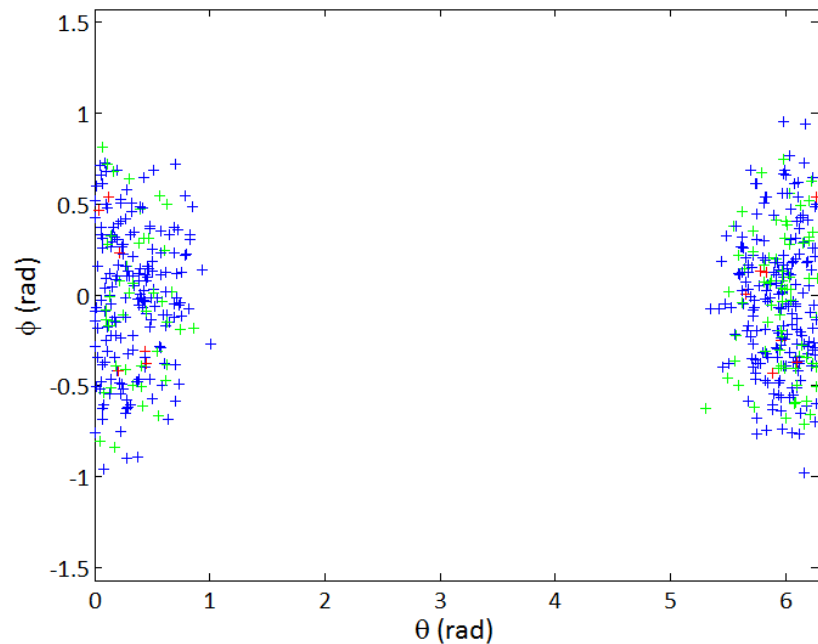


Figure E.7 Distribution of the individuals in the initial population for the EdSU trajectory in the $\theta - \phi$ space. The complete search space for all variables was used. The seed number for the run producing these individuals is 1000. $\color{blue}+$: $\Delta V_{tot} \geq 20$ km/s, $\color{green}+$: $12 \leq \Delta V_{tot} < 20$ km/s, $\color{red}+$: $\Delta V_{tot} \leq 12$ km/s.

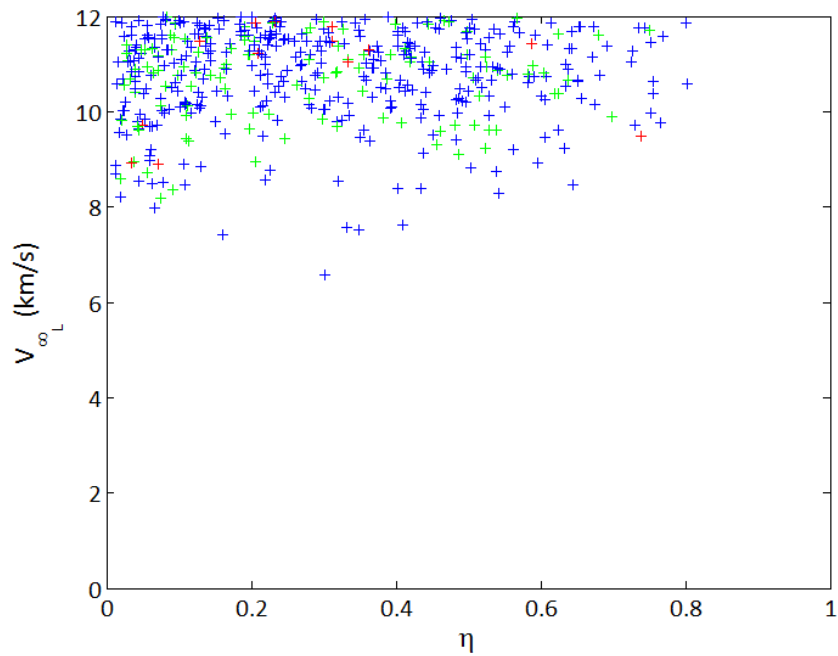


Figure E.8 Distribution of the individuals in the initial population for the EdSU trajectory in the $\eta - |\bar{V}_{\infty_L}|$ space. The complete search space for all variables was used. The seed number for the run producing these individuals is 1000. $+$: $\Delta V_{tot} \geq 20$ km/s, $+$: $12 \leq \Delta V_{tot} < 20$ km/s, $+$: $\Delta V_{tot} \leq 12$ km/s.

E.3 EMdU, complete search space for all variables

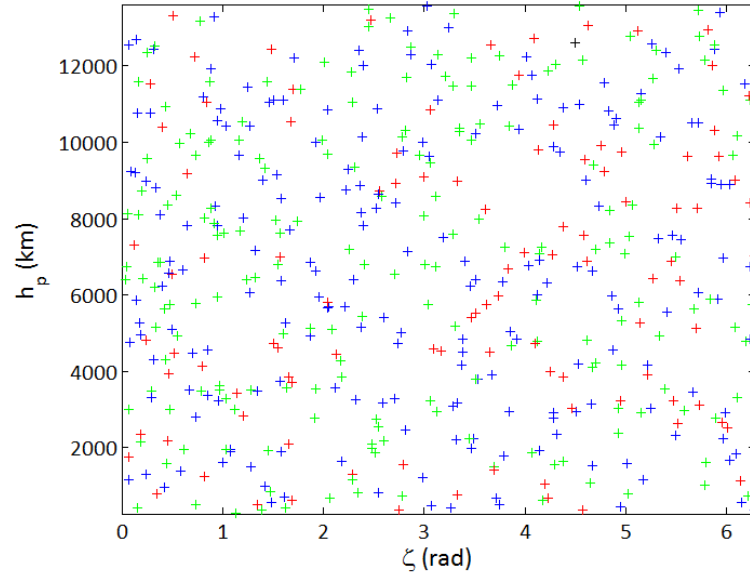


Figure E.9 Distribution of the individuals in the initial population for the EMdU trajectory in the $\zeta - h_p$ space. The complete search space for all variables was used. The seed number for the run producing these individuals is 1100. $\color{blue}+$: $\Delta V_{tot} > 25$ km/s, $\color{green}+$: $15 < \Delta V_{tot} \leq 25$ km/s, $\color{red}+$: $\Delta V_{tot} \leq 15$ km/s, $\color{black}+$: $\Delta V_{tot} < 10$ km/s.

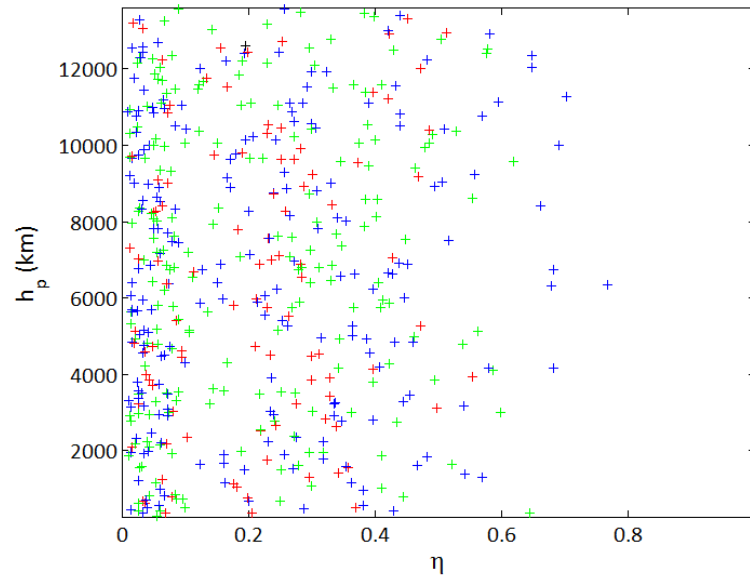


Figure E.10 Distribution of the individuals in the initial population for the EMdU trajectory in the $\eta - h_p$ space. The complete search space for all variables was used. The seed number for the run producing these individuals is 1100. $\color{blue}+$: $\Delta V_{tot} > 25$ km/s, $\color{green}+$: $15 < \Delta V_{tot} \leq 25$ km/s, $\color{red}+$: $\Delta V_{tot} \leq 15$ km/s, $\color{black}+$: $\Delta V_{tot} < 10$ km/s.